Investigation of Advanced Modulation and Multiplexing Schemes for High-Capacity Optical Transmission Systems

by

An Li

Submitted in total fulfilment of

The requirements of the degree of

Doctor of Philosophy

Department of Electrical and Electronic Engineering

The University of Melbourne

VIC 3010, Melbourne, Australia

July 2012

Printed on archival quality paper.

Abstract

Investigation of Advanced Modulation and Multiplexing Schemes for High-Capacity Optical Transmission Systems

by **An Li**

Space-division multiplexed (SDM) transmission based on multi-core (MCF) or multi-mode fibre (MMF) emerges as one of the promising solutions for overcoming the capacity limit of standard single mode fibre (SSMF). However, to unleash the full potential of the high data rate SDM transmission, brand-new research on the device to system level is required. In this thesis, we elucidate the overall system architecture, critical components and sub-system modules for mode-division multiplexed (MDM) transmission and report our latest demonstration of MDM superchannel transmission based on few-mode fibre (FMF). We envisage that the combination of MDM and OFDM modulation could provide a viable pathway to the future Tb/s and beyond optical transports.

We first review the basic concepts and principles of conventional optical OFDM system. We introduce two novel variants of coherent optical OFDM (CO-OFDM) system, namely the wavelet packet transform based OFDM (WPT-OFDM) and discrete Fourier transform based OFDM (DFTS-OFDM). The performance of the two new systems are analysed and compared with conventional CO-OFDM system. We next look at the most basic but important element for the SDM transmission system – FMF few-mode fibre (FMF).We then show an experimental demonstration of characterization of physical property of a custom-designed TMF fibre. After that we investigate a broad range of issues on SDM -especially the MDM based on MMF or FMF - from its fundamentals to some of the critical FMF components including mode stripper, mode converter, mode combiner and few-mode amplifiers. With these few-mode components and subsystem module available, we then show experimental demonstrations of MDM transmission over TMF fibre under three different unique MDM schemes:(1) LP_{01}/LP_{11} mode, (2) dual-LP_{11} mode, and (3) triple-mode ($LP_{01}+LP_{11a}+LP_{11b}$). Finally, the research outcome in this thesis is summarized and a few research directions toward future work are presented.

This is to certify that

(i) the thesis comprises only my original work,

(ii) due acknowledgement has been made in the text to all other material used,

(iii) the thesis is less than 100,000 words in length, exclusive of table, maps, bibliographies, appendices and footnotes.

Signature_____

Date_____

Declaration

I hereby declare that this thesis comprises only my original work. No material in this thesis has been previously published and written by another person, except where due reference is made in the text of the thesis. I further declare that this thesis contains no material which has been submitted for a degree or diploma or other qualifications at any other university. Finally, I declare that the thesis is less than 100,000 words in length, exclusive of tables, figures, bibliographies, appendices and footnotes.

Acknowledgements

Although this thesis consists of academic achievements as a summarization of my PhD study, more precisely it is teamwork from everyone who has ever helped me including my supervisors, collaborators, friends and also my family. The work cannot be fulfilled without their great support.

First I would like to express my sincere gratitude to my supervisor, Prof. William Shieh and co-supervisor Prof. Rod Tucker, for their patient supervision and advice throughout my entire PhD candidature. Their high- quality academic guidance and meticulous attention to detail helped me develop my skills quickly and lead me to the cutting-edge research topics. In addition, I would also like to express my thanks to Dr. Fred Buchali at Bell labs, Alcatel-Lucent Germany for providing me an invaluable opportunity to undertake an internship, where I have learned a lot from you and other experts in Bell labs. It is such a wonderful time that I will never forget in my life.

My second thanks are given to the other members in Prof. William Shieh's group. Xi Chen, Guanjun Gao, Simin Chen and Abdullah Al Amin, my best research partners and friends I have ever had. I never get bored when I was doing experiment in the lab as long as they are around. We are the best team together to have so many OFC postdeadline papers for years. Without their contribution, I could never win the award of Corning's Outstanding Student Paper in OFC 2012. The other newly joined members - Jia Ye, Jiayuan He, and Qian Hu, have also helped me a lot during my thesis writing.

I am also grateful to The University of Melbourne and Department of Electrical & Electronic Engineering for providing me the MIFRS and MIRS scholarships, as well as friendly study environment and facilities. Furthermore, I am grateful to the Centre for Energy Efficient Telecommunications (CEET) for providing me the PhD top-up scholarship for the last year of my study.

Last but not least, I would like to give my special thanks to my dearest parents and sister. You are my spiritual strength and anchor when I am abroad. I love you from the deepest of my heart! There are many people who have helped me but I forget to mention here, thank you so much and wish you all the best for the future!

Contents

List of Figures

List of Tables

1 Introduction

1.1 Overview

1.1.1 Optical communications and fibre optics

There is a long history of using light for communication ever since the ancient time. Similar to any other forms of telecommunication systems, an optical communication system consists of a transmitter that encodes data and modulates them onto an optical signal, a channel (optical fibre or air) which carries the optical signal to the destination, and a receiver which detects and recovers the data from the received optical signal. The prototype of modern optical communication systems can be traced back to 1880 when Alexander Graham Bell invented his 'Photophone', which transmitted a voice signal on a beam of light [1]. The obstacle to Bell's further research is that many things such as fog or raindrops could interfere with the Photophone. Even then, scientists had been in the long seeking for the best material for light communications until the introduction of fibre optics, a contained transmission of light through long optical fibres. Although there were uncladded glass fibres fabricated earlier in the 1920s [2]–[4], the field of fibre optics was not born until the 1950s when the use of a cladding layer led to considerable improvement in the fibre characteristics [5]-[8]. Since 1960s the field of fibre optics has been well-developed. However, the early fibres (such as bundle of glass fibres) were very lossy (>1000 dB/km) compared to modern telecommunication fibres. This situation changed in 1970 followed an earlier Nobel Prize work and suggestion by K. C. Kao in [9] that the losses of silica fibre span be reduced to below 20 dB/km. The progress in fibre fabrication technology [10] in 1979 results in a loss of as low as 0.2 dB/km in the 1.55 μm wavelength window [11], which has been standardized as the C-band in modern telecommunication systems. Typically optical fibres consist of a transparent core surrounded by a transparent cladding material with a lower index of refraction. This makes fibre a waveguide where light is kept in the core by total internal reflection [12].

Although there are other types of channels used such as air in free-space optical communication (FSO) [13], optical fibre is the most commonly used channel in modern optical communication systems. The advantage of using optical fibres, compared with metal media such as copper wires, is that silica fibres can transmit

infrared optical signals with small attenuation over long distance, and are also immune to electromagnetic interference.

1.1.2 High speed optical communication systems

Since the arrival of internet in early 1980, the data traffic growth on the internet has lead to a higher and higher data transmission speeds over optical fibre networks from 1-Gb/s, to 10-Gb/s, to today's 100-Gb/s. The internet has been continuously growing and in order to satisfy the demand on the capacity, intensive study has been made on the long-haul high-capacity optical communication systems. The backbone and metropolitan area network (MAN) should be scaled up accordingly in anticipation of the upsurge of the traffic. Nowadays, single-channel data transmission rate over 100-Gb/s has become a commercial reality, thanks to re-emergence of coherent detection technologies in combination with high-speed electronic digital-to-analogue and analogue-to-digital converter (DAC/ADC) and digital signal processing (DSP). Together with wavelength-division multiplexing (WDM), polarization-division multiplexing (PDM) and high order modulation schemes, the highest reported single optical fibre data transmission capacity has reached over 100-Tb/s [14]-[15].

State-of-the-art digital communication systems can be grouped into two categories, single-carrier modulation (SCM) and multi-carrier modulation (MCM). For SCM systems, as the name suggests, the data is carried with a single optical carrier, which has been the dominant modulation format for optical communications over three decades. However, with the increase of network data rate and reach, the optical signal is extremely sensitive to the chromatic dispersion (CD), polarization mode dispersion (PMD), reconfigurable optical add/drop multiplexer (ROADM) filtering effects, and imperfections of the electric-optics components. These place significant challenges on the conventional SCM system. For MCM systems, the data is divided and carried by a large number of low symbol rate carriers (called sub-carriers). Orthogonal frequency-division multiplexing (OFDM) is a frequency-division multiplexing (FDM) scheme by which a large number of closely-spaced orthogonal subcarriers are used to carry data. With OFDM, each sub-carrier is modulated with a conventional modulation scheme (such as quadrature amplitude modulation or phase-shift keying) at a low symbol rate, maintaining total data rates similar to conventional single-carrier modulation schemes in the same bandwidth. OFDM has been adopted for broad range of applications in wideband digital communications, wireless or over copper wires,

such as digital television and audio broadcasting, wireless networking and broadband internet access [16]. In fibre-optic communications, optical orthogonal frequency division multiplexing (O-OFDM) has recently attracted many interests from the optical communication community [17-18] because of its high spectral efficiency and robustness against impairments such as CD and PMD. Direct-detection optical OFDM (DDO-OFDM) was first proposed with a simple architecture and has been actively pursued by several groups [17, 19-23]. Coherent optical OFDM (CO-OFDM) was also proposed with coherent detection, which shows benefits of high spectral efficiency (SE) and high receiver sensitivity [18]. The advantage of CO-OFDM is prominent. It has the highest performance in receiver sensitivity, SE and robustness against linear channel impairments. By appropriately choosing the length of cyclic prefix (CP) and insert training symbols at the transmitter, both inline CD and PMD can be fully compensated via digital signal processing (DSP). However, the disadvantages of CO-OFDM also cannot be ignored. It requires a local oscillator (LO) at the receiver, and is more sensitive to phase noise. CO-OFDM receiver also needs two pairs of balanced receivers therefore it is more costly and complex than DDO-OFDM. In addition, CO-OFDM also suffers from high peak-to-average-power ratio (PAPR) that leads to inferior nonlinearity tolerance than single-carrier system.

1.2 Motivation

The highest reported single optical fibre data transmission speed has reached over 100 Tb/s [14]-[15]. However, there is a need to continue enhancing the total data transmission capacity while keeping the signals within the available optical spectrum of the conventional Erbium doped fibre amplifier (EDFA), which translates into the requirement for increased SE (expressed in b/s/Hz). Although Shannon's theory predicts SE to increase with higher received SNR as a result of increased transmission power, fibre nonlinearity imposes a hard limit on improving channel capacity [24].

We intend to explore various modulation and multiplexing schemes to improve the transmission performance. First we study two new variants of the CO-OFDM systems for SMF fibres, namely the wavelet packet transform based OFDM (WPT-OFDM) and discrete Fourier transform spread OFDM (DFTS-OFDM). The incentive to use WPT-OFDM is to provide better spectral roll-off and to remove the need for CP [25]. In addition, wavelets can provide more freedom in system design. DFTS-OFDM, also called single-carrier frequency-division multiplexing (SC-FDM),is

proved to have much reduced PAPR than conventional OFDM with many interesting features [26-28], which has been widely adopted in the wireless communication and is the recommended uplink format in the 3GPP-LTE standard for the next generation mobile system [26]. Furthermore, benefited from the sub-band or sub-wavelength accessibility of CO-OFDM, properly designed multiband DFTS-OFDM (MB-DFTS-OFDM) can potentially have better nonlinearity tolerance over either conventional CO-OFDM or SC system for ultra-high speed transmission. On the other hand, space-division multiplexed (SDM) transmission based on multi-core (MCF) [29-34] or multi-mode fibre (MMF) [35-38] was proposed for overcoming the barrier of capacity limit of SSMF. Information theory reveals that by adding another degree of freedom, namely the spatial mode, the fibre capacity of MMF or few-mode fibre (FMF) can be increased in the form of multiple-input multiple-output (MIMO) transmission. Compared with the standard MMF that supports a few tens or hundreds modes which make it extremely difficult to receive and process, FMF has been proposed to significantly reduce the system complexity to a manageable level by supporting a small number of modes (e.g., 3 or 5 modes). It has the advantage of better mode selectivity and easier management of the mode impairments. By utilizing mode-division multiplexing (MDM) and multiple-input multiple-output (MIMO) digital signal processing (DSP) technique, it is expected that *N* spatial modes in a FMF can support *N* times the capacity of a SSMF. In this thesis, we constraint our focus to two-mode fibre (TMF) based MDM transmission and try to answer the following questions

- Whether FMF such as TMF can offer capacity beyond that of SSMF in a cost effective manner?
- Is MDM transmission a feasible solution for the future Terabit and beyond optical networks?
- Is MDM an industry-transforming technology?

1.3 Thesis outline

The content of the report is structured as follows.

Chapter 1 Introduction This chapter gives a literature review of the optical OFDM systems, describe important variations include wavelet packet transform based OFDM (WPT-OFDM) system and DFT-Spread OFDM (DFTS-OFDM) system, discuss

evolution of telecommunication fibres and novel fibre design, new fibre based devices, and finally present experimental demonstration and recent progress of spatial mode multiplexed systems for the future network.

Chapter2 Literature Review This chapter reviews the relevant literature on high-speed optical transmission technologies including the CO-OFDM scheme, few-mode transmission from device to system level, and experimental demonstration of space division multiplexing (SDM).

Chapter3 Principle of Optical OFDM System In this chapter the principle of OFDM systems and coherent optical OFDM (CO-OFDM) systems are given and discussed. OFDM fundamentals including its basic mathematical formulation, discrete Fourier transform implementation and cyclic prefix are first presented. The coherent optical OFDM technique including the system architecture, optical spectral efficiency, coherent optical MIMO-OFDM models and signal processing will also be discussed.

Chapter 4 Variations of OFDM System In this chapter the advantages and drawbacks of CO-OFDM are discussed. We show that conventional OFDM systems have disadvantages of the need for cyclic prefix (CP) that proportionally increases with chromatic dispersion, and high peak-to-average power ratio (PAPR) which exacerbates its performance of nonlinearity tolerance. In order to solve these problems two new types of OFDM systems are proposed, one is WPT-OFDM and the other DFT-S OFDM. We show investigation of WPT-OFDM and system modelling in the presence of fibre impairments including chromatic dispersion (CD) and polarization mode dispersion (PMD). Then we look at the other variant called DFTS-OFDM. The prominent advantage of nonlinear tolerance of DFT-S-OFDM is discussed. We demonstrate experimentally two transmission schemes: (1) 1.0-Tb/s PDM-QPSK UW-DFTS-OFDM superchannel signal transmission over 8,000-km SSMF and (2) 1.63-Tb/s PDM-16QAM UW-DFTS-OFDM superchannel transmission over 1,010-km SSMF, with 80-km span engineering and EDFA-amplification using QPSK modulation compatible with most of the deployed links.

Chapter 5 Few-Mode and Two-Mode Fibre In this chapter we study the principle of optical waveguides and mode theory, and its application into fibre design. The unique characteristics of different silica-based fibres such as single mode fibre (SMF), multimode fibre (MMF), few mode fibre (FMF) and especially two-mode fibre are

discussed. Their pros and cons are also presented. The major parameters and constraints in designing a practical fibre for communication system are included. A step-index of a two-mode fibre (TMF) model will be presented with rigorous analysis on the key parameters.

Chapter 6 Fundamentals of Space-Division Multiplexing (SDM) and Design of Few-Mode Components This chapter studies the fundamentals of spatial-mode multiplexing. The two main implementations: SDM systems based on multi-core fibres and mode-division-multiplexed (MDM) based on multimode fibres are given and discussed. Then the enabling technique will be discussed. A few experimental demonstrations of the SDM and MDM systems will be presented and compared. The individual pros and cons of the two systems will be also analysed, followed by a simulation and discussion. As the design and fabrication of FMF has now become readily available, various FMF based passive or active components can be designed. Among the FMF based devices, a mode stripper (MS) is presented first. Then a long period fibre grating (LPFG) based mode converter (MC) is shown. The mechanism, fabrication and key design parameters are given, and the performance is analysed and compared with simulation. After that a mode stripper is proposed to strip out higher order modes, which is very useful in a mode multiplexed system. The third useful TMF based component is the spatial mode combiner/splitter (SMC/SMS), which can be the critical multiplexing/de-multiplexing components in a mode multiplexed system. Two types of SMC/SMS are discussed: first one is free-space based coupling system and the second one is fused fibre coupler based mode combiner. The mechanism, design and implementation in real system are presented thereafter. A few experimental demonstrations and figures are also shown. At last the concept and recent progress of TMF based amplifiers are shown and discussed.

Chapter 7 Transmission of Mode-Division Multiplexed CO-OFDM (MDM-CO-OFDM)Signal over Two-Mode Fibre In this chapter a few transmission demonstrations of mode-division multiplexed (MDM)CO-OFDM signal over few-mode fibre are given. Three following experiments will be presented and discussed,

1) Transmission of LP_{01}/LP_{11} mode multiplexed OFDM signal over two-mode fiber
2) Transmission of dual-LP_{11}mode multiplexed OFDM signal over Two-Mode fiber

3) Transmission of triple (LP_{01}+LP_{11a}+LP_{11b}) mode multiplexed OFDM signal over two-mode fiber

The system setup will be shown and the key components, parameters, enabling techniques and digital signal processing will be revealed. The experiment result will be also given and discussed.

Chapter 8 Conclusions In this chapter the main results of the thesis are reviewed and summarized.

1.4 Contributions

The contributions of this work in thesis are listed as follows,

Chapter 4 We have proposed two new variants of CO-OFDM systems, namely WPT-OFDM and DFTS-OFDM, for the potential application in future high-speed optical networks. We show that WPT-OFDM have advantages in system flexibility and spectral roll-off, whilst DFTS-OFDM has better nonlinear tolerance over the conventional CO-OFDM.

Chapter 5 We design a two-mode fibre (TMF) for the application of SDM. The design parameters and major characteristics of the TMF are simulated. This fibre provides an insight to the future fibre design for high-speed SDM transmission systems.

Chapter 6 We have introduced various few-mode components for the application of SDM based systems. The proposed mode stripper, mode converter, mode combiner, optical add/drop multiplexer and few-mode fibre amplifier have been widely used in SDM based transmission systems which demonstrates their great feasibility.

Chapter 7 We have shown a few proof-of-principle experimental demonstrations of MDM transmissions based on two-mode fibre. The up-to-date experimental results provide good references for the MDM system design.

1.5 Publications related to this thesis

1. **A. Li**, X. Chen, A. Al Amin and W. Shieh, “Fused Fiber Mode Couplers for Few-Mode Transmission,” Photonic Technology Letters, IEEE, vol. **24**, no. 21, pp. 1953-1956 (2012).
2. **A. Li**, X. Chen, A. Al. Amin, J. Ye and W. Shieh, "Space-Division Multiplexed High-Speed Superchannel Transmission over Few-Mode Fiber, (Invited Paper)" J.

Lightwave Technol., DOI: 10.1109/JLT.2012.2206797 (in press, July 2012).

3. **A. Li**, X. Chen, G. Gao and W. Shieh, "Transmission of 1-Tb/s Unique-Word DFT-Spread OFDM Superchannel over 8000-km EDFA-only SSMF link," J. Lightwave Technol., DOI: 10.1109/JLT.2012.2206369, (in press, July 2012).
4. **A. Li**, A. Al. Amin, and W. Shieh, "Mode Converters and Couplers for Few-Mode Transmission," Photonics Society Summer Topical Meeting, 2012 IEEE, July 2012 (invited talk).
5. **A. Li**, A. Al. Amin, X. Chen, S. Chen, G. Gao and W. Shieh, "Transmission of 1.63-Tb/s PDM-16QAM Unique-word DFT-Spread OFDM Signal over 1,010-km SSMF," in Optical Fiber Communication Conference (OFC), 2012, pp.OW4C.1.
6. **A. Li**, A. Al. Amin, X. Chen, S. Chen, G. Gao and W. Shieh, "Reception of Dual-Spatial-Mode CO-OFDM Signal over a Two-Mode Fiber," J. Lightwave Technol., vol. **30**, no. 4, pp. 634–640 (2012).
7. **A. Li**, X. Chen, G. Gao and W. Shieh, "Transmission of 1-Tb/s Unique-word DFT-Spread OFDM Superchannel over 8,000-km SSMF," in Communications and Photonics Conference and Exhibition, 2011. ACP. Asia , vol., no., pp.1–7, 13–16 Nov. 2011.
8. **A. Li**, A. Al. Amin, and W. Shieh, "Design of a Broadband LP11 Spatial Mode Combiner," in Communications and Photonics Conference and Exhibition, 2011. ACP. Asia , vol., no., pp.1–6, 13–16 Nov. 2011.
9. **A. Li**, A. Al. Amin, X. Chen, and W. Shieh, "Transmission of 107-Gb/s mode and polarization multiplexed CO-OFDM signal over a two-mode fiber," Opt. Express, vol. **19**, pp. 8808–8814 (2011).
10. **A. Li**, A. Al. Amin, X. Chen, and W. Shieh, "Reception of Mode and Polarization Multiplexed 107-Gb/s CO-OFDM Signal over a Two-Mode Fiber," in Optical Fiber Communication Conference (OFC), 2011, paper PDPB8.
11. **A. Li**, W. Shieh, and R. S. Tucker, "Wavelet Packet Transform-Based OFDM for Optical Communications," J. Lightwave Technol., vol. **28**, no. 24, pp. 3519–3528 (2010).
12. **A. Li**, W. Shieh, and R. S. Tucker, "Impact of polarization-mode dispersion on wavelet transform based optical OFDM systems," in Optical Fiber Communication Conference (OFC), 2010, paper JThA5 (2010).

13. W. Shieh, **A. Li**, A. Al Amin, and X. Chen, "Space-Division Multiplexing for Optical Communications," Research Highlights, Photonics Society Newsletter 26, 5, October 2012.
14. A. Al Amin, **A. Li**, X. Chen and W. Shieh, "Mode Division Multiplexing MIMO-OFDM Optical Transmission," in 17th OptoElectronics and Communications Conference (OECC), 2012, pp. 555–556.
15. X. Chen, **A. Li**, J. Ye, A. Al. Amin, and W. Shieh, "Reception of mode-division multiplexed superchannel via few-mode compatible optical add/drop Multiplexer," Opt. Express, vol. **20**, pp. 14302–14307 (2012).
16. X. Chen, **A. Li**, G. Gao, A. Al. Amin, and W. Shieh, "Characterization of Fiber Nonlinearity and Analysis of Its Impact on Link Capacity Limit of Coherent Optical OFDM Systems for Two-Mode Fibers," IEEE Photonics Journal, vol.**4**, no.2, pp. 455–460 (2012).
17. X. Chen, **A. Li**, J. Ye, A. Al. Amin, and W. Shieh, "Reception of Dual-LP11-Mode CO-OFDM Signals through Few-mode Compatible Optical Add/Drop Multiplexer," in Optical Fiber Communication Conference (OFC), 2012, paper PDPB5.4.
18. W. Shieh, **A. Li**, A. Al. Amin, X. Chen, S. Chen, and G. Gao, "Spatial Mode-Division Multiplexing for High-Speed Optical Coherent Detection Systems," ZTE Communications, vol. **10**, no. 1 (2012).
19. X. Chen, **A. Li**, G. Gao, and W. Shieh, "Study of Fiber Nonlinearity Impact on the System Capacity of Two-mode Fibres," in Optical Fiber Communication Conference (OFC), 2012, paper JW2A.40.
20. X. Chen, **A. Li**, G. Gao, and W. Shieh, "Experimental demonstration of improved fiber nonlinearity tolerance for unique-word DFT-spread OFDM systems," Opt. Express **19**, 26198–26207 (2011).
21. A. Al. Amin, **A. Li**, X. Chen, and W. Shieh, "Spatial mode division multiplexing for overcoming capacity barrier of optical fibers," in 16th OptoElectronics and Communications Conference (OECC), 2011, pp. 415–416.
22. A. Al. Amin, **A. Li**, S. Chen, X. Chen, G. Gao, and W. Shieh, "Dual-LP11 mode 4x4 MIMO-OFDM transmission over a two-mode fiber," Opt. Express, vol. **19**, pp. 16672–16679 (2011).

23. A. Al. Amin, **A. Li**, X. Chen, and W. Shieh, "LP01/LP11 dual-mode and dual-polarisation CO-OFDM transmission on two-mode fibre," Electron. Lett., vol. **47**, pp. 606–607 (2011).

2 Literature Review

2.1 Introduction

The fast growth of bandwidth-rich internet applications such as online mobile applications and cloud computing has led to a huge demand on the bandwidth of optical transports. To satisfy the ever increasing bandwidth demand from back-bone all the way down to access networks, extensive studies have been conducted to increase the SE in the state-of-the-art optical transmission systems by means of polarization-division multiplexing (PDM), coherent optical OFDM (CO-OFDM) [39], and high order quadrature amplitude modulation (QAM), etc. CO-OFDM has become one of the promising candidates due to its high SE and resilience to linear channel impairments such as chromatic dispersion (CD). Experimental demonstration at data rate of 1-Tb/s [40-43] and beyond [44-51] has been achieved using either single carrier (SC) system or CO-OFDM. Since there's motivation to continue enhancing the data capacity within a certain bandwidth, the investigation of advanced modulation and multiplexing schemes are a feasible pathway towards the future high-capacity optical networks. In this chapter, a few currently existing multiplexing schemes in optical communications will be introduced, including the wavelength-division multiplexing (WDM), optical time-domain multiplexing (OTDM), CO-OFDM and direct detection optical OFDM (DDO-OFDM), with a focus on the CO-OFDM and its new variants. The pioneer work of our group and other groups in the novel area of space-division multiplexing (SDM) will also be reviewed.

2.2 Advanced multiplexing schemes for high-capacity optical transmission

2.2.1 WDM transmission systems

Wavelength-division multiplexing (WDM) is a technology in fibre optic communications which multiplexes many optical carrier signals onto a single optical fibre by using different wavelengths, in order to increase the fibre transmission capacity [52-5354]. WDM is also a kind of frequency-division multiplexing (FDM) scheme, where the term WDM is commonly applied to the optical carrier, whereas the term FDM is typically applied to the radio carrier. A WDM system usually consists of an optical multiplexer (MUX) at the transmitter to combine the signal at different wavelength together, and an optical de-multiplexer (DEMUX) at the receiver to split

them apart. In addition, there is also a device that can do both simultaneously, which is the optical add-drop multiplexer (OADM).

The concept of WDM was first proposed in 1970s, and the actual system has been realized in laboratory in 1978. The first WDM system only combined two signals at different wavelength channels. Nevertheless, state-of-art system can support more than one hundred signals, which can greatly enhance the data rate of the transmission system to be over Terabit/s, even though the basic data rate of a signal is low (e.g., 10-Gb/s). WDM systems can be divided into two major categories, coarse WDM (CWDM) and dense WDM (DWDM). The ITU standardized a channel spacing grid for use with CWDM (ITU-T G.694.2) in 2002. The suggested wavelengths range from 1270 nm to 1610 nm with a channel spacing of 20nm (250GHz). In 2003, it was revised to 1271 nm to 1611 nm [55]. However, many CWDM wavelengths below 1470 nm are "unusable" on old G.652 fibres due to the increased attenuation (water peak) in the 1270-1470 nm region. With the improved fibre fabrication process, new G.652 fibres which conform to G.652.C and G.652.D such as Corning® SMF-28e has very low water peak and therefore allow full operation of all 18 ITU-CWDM channels. For the most commonly used transmission window of C-band (1525-1565 nm), CWDM provides up to 8 WDM channels. As a comparison, DWDM also uses C-band but with much denser channel spacing. ITU standardizes DWDM channel grid in either multiple or fraction of 100 GHz, and the reference frequency is fixed at 193.10THz (1552.52 nm). Typical DWDM systems would use 40 channels at 100 GHz spacing or 80 channels with 50 GHz spacing. A basic DWDM system normally consists of the following important components: A DWDM terminal multiplexer, an intermediate line repeater, a DWDM terminal de-multiplexer, and/or optical supervisory channel (OSC).

A basic configuration for WDM system is illustrated in Fig.2.1. At the transmitter, N WDM channels generated from N are multiplexed by a WDM MUX and fed into a single fibre. In the transmission link, the signal is periodically amplified with the Erbium Doped Fibre Amplifier (EDFA) chain. The EDFA has a very broad gain bandwidth of 40 nm between 1525-1575 nm (C band), and can be extended to the longer wavelength window of 1570-1610 nm (L-band). At the receiver, the signal is first split into N channels with a WDM DEMUX, then received and detected separately. Before the advent of coherent detection, each WDM channel used a single

carrier (SC) modulation with simple generation and detection methods, but going to higher data rates such as 40 Gb/s or 100 Gb/s became problematic due to inter-symbol-interference (ISI) from chromatic and polarization mode dispersion (CD/PMD), which required precise dispersion management. With the arrival of full-field optical signal capture by coherent detection and subsequent digital signal processing (DSP), the concept of coherent WDM [56] is proposed, where the LO laser selects the target WDM channel thus only the channel that has a central frequency close to the LO laser frequency gives a beating frequency within the bandwidth of the receiver. Through coherent detection and digital signal processing (DSP), the ISI from chromatic and polarization mode dispersion (CD/PMD) in WDM can be effectively mitigated.

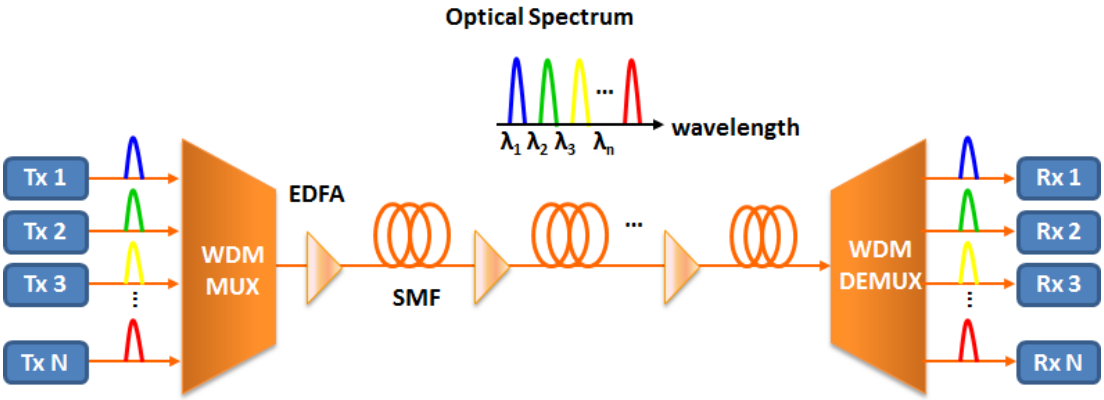

Fig.2.1 Conceptual diagram of a WDM transmission system.

2.2.2 OTDM transmission systems

Time-division multiplexing (TDM) is a kind of multiplexing technique that has been widely adopted in telecommunication networks. Optical time-division multiplexing (OTDM) is similar as electrical time-division multiplexing (ETDM) where a channel is divided into *N* individual tributary channels (time-slots) and each channel is occupied by an ultra-short optical pulse that carries the baseband signal. Through this technique, the N tributary channels at low bit rate can be multiplexed onto a single multiplexed channel with *N* times the bit rate of individual tributary channels. Therefore OTDM can drastically increase the transmission date rate beyond the limitation of electronic components.

There are two major advantages of using OTDM: (i) OTDM can solve much problem in WDM such as the non-flatness of spectrum due to the cascading of multiple optical amplifiers in the link, crosstalk due to the non-ideal filters and

wavelength conversion, limitation due to fibre nonlinearity, excessive demands on the wavelength stabilizer, and expensive tuneable filters; and (ii) To satisfy the ever increasing bandwidth demand from new internet and mobile applications, the future optical network will be all-optical network (AON) with all-optical switches and routers. OTDM may be a promising solution in the AON because:

(1) It can provide very high line rate (few hundred Gbit/s);

(2) The tributary channel can have variable data rate, which can be compatible with the existing techniques such as synchronous digital hierarchy (SDH);

(3) The amplifier and dispersion management are greatly simplified because of single wavelength transmission;

(4) Although the network link is working at very high data rates, at the network node, the electronic components can work at low data rate, therefore releases the demand of expensive high speed electronics.

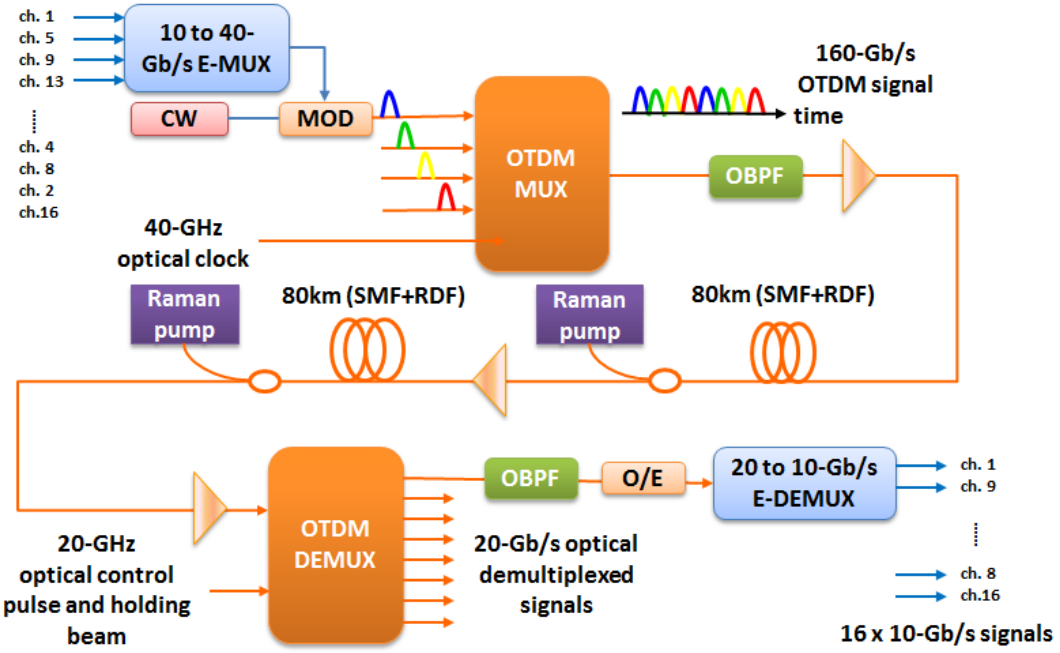

Fig.2.2 Experimental setup of a 160-Gb/s OTDM transmission system with all-channel independent modulation MUX and all-channel simultaneous DEMUX. E-MUX: electrical MUX. CW: continuous-wave laser source. MOD: $LiNbO_3$ intensity modulator. OBPF: optical bandpass filter. SMF: single-mode fibre. RDF: reverse dispersion fibre. O/E: optoelectronic converter. E-DEMUX: electrical DEMUX.

Figure 2.2 shows the experimental setup of a 160-Gb/s OTDM transmission system [57]. The critical components in the OTDM system are the OTDM-MUX and

OTDM-DEMUX. At the transmitter, an E-MUX multiplexes four 10-Gb/s electrical signals to a 40-Gb/s signal. The signal is then modulated onto the optical domain with NRZ modulation format by a $LiNbO_3$ intensity modulator. A 40-GHz optical clock is also generated by using a mode-locked laser diode and supercontinuum techniques. By filtering the supercontinuum spectrum, the pulse train is converted to the appropriate wavelength and pulse width. Four independently generated 40-Gb/s optical signals and the optical clock are then fed into the OTDM-MUX, which consists of two 4×1 couplers, a 2×1 coupler and periodically poled lithium niobate (PPLN) waveguides and integrated on a planar lightwave circuit (PLC). After the OTDM-MUX, a 160-Gb/s OTDM signal is obtained. The multiplexed signals have the same polarization in this experiment due to the polarization dependence of PPLN. However, alternative polarization is possible in other implementations. A 10-GHz optical clock is also transmitted with 160-Gb/s OTDM signal for clock recovery. After 160-km SMF+RDF transmission, at the receiver, the OTDM-DEMUX accepts the 160-Gb/s OTDM signal and 20-GHz optical control pulse (generated from the recovered 10-GHz clock). The OTDM-DEMUX consists of two 1×8 couplers, 8 WDM couplers and a SOA array. The FWM of SOA yield all-optical de-multiplexing. A linear polarized pump with polarization controller is also used to de-multiplex the OTDM signal. The relaxation time of SOAs imposes a limit on the base bit rate of OTDM-DEMUX, which is 20Gb/s. The eight 20-Gb/s signals are then optically filtered and converted back to electrical domain through an O/E converter. They are then electrically de-multiplexed again to 2×10-Gb/s each. Finally, the 16×10-Gb/s signals are received and processed. It is worth noting that reverse dispersion fibres (RDFs) are used in the link to compensate the chromatic dispersion (CD) of SMF, therefore CD is no longer a problem. There are also many challenges in OTDM systems. For example, at transmitter side, the pulse source must provide a well-controlled repetition frequency and wavelength [57], e.g., the pulse width should be significantly shorter than the bit period of the multiplexed data signal and the timing jitter should be much less than the pulse width. At the receiver side, High quality and low cost techniques are also needed for the recovery of optical clock and optical de-multiplexing. For the transmission link, OTDM is very susceptible to dispersions such as CD and polarization-mode dispersion (PMD), therefore dispersion compensation must be carefully done (or using optical solitons).

2.2.3 Coherent optical OFDM (CO-OFDM)

CO-OFDM represents the ultimate performance in receiver sensitivity, spectral efficiency and robustness against polarization dispersion, but requires high complexity in transceiver design. In the open literature, CO-OFDM was first proposed by Shieh and Athaudage [18], and the concept of the coherent optical MIMO-OFDM was formalized by Shieh et al. in [58]. The early CO-OFDM experiments were carried out by Shieh et al. for a 1000 km SSMF transmission at 8 Gb/s [59], and by Jansen et al. for 4160 km SSMF transmission at 20 Gb/s [60]. The principle and transmitter/receiver design for CO-OFDM are given below.

(i) Principle of CO-OFDM

The synergies between coherent optical communications and OFDM are two-fold. OFDM enables channel and phase estimation for coherent detection in a computationally efficient way. Coherent detection provides linearity in RF-to-optical (RTO) up-conversion and optical-to-RF (OTR) down-conversion, much needed for OFDM. Consequently, CO-OFDM is a natural choice for optical transmission in the linear regime. A generic CO-OFDM system is depicted in Fig.2.3. In general, a CO-OFDM system can be divided into five functional blocks including (i) RF OFDM transmitter, (ii) RTO up-converter, (iii) the optical channel, (iv) the OTR down-converter, and (v) the RF OFDM receiver. The detailed architecture for RF OFDM transmitter/receiver has already been shown in Fig.2.3, which generates/recovers OFDM signals either in baseband or an RF band. Let us assume for now a linear channel where optical fibre nonlinearity is not considered. It is apparent that the challenges for CO-OFDM implementation are to obtain a linear RTO up-converter and linear OTR down-converter. It has been proposed and analysed that by biasing the Mach-Zehnder modulators (MZMs) at null point, a linear conversion between the RF signal and optical field signal can be achieved [18, 61]. It has also been shown that by using coherent detection, a linear transformation from optical field signal to RF (or baseband electrical) signal can be achieved [18, 61-63]. Now by putting together such a composite system cross RF and optical domain [18, 59-60], a linear channel can be constructed where OFDM can perform its best role of mitigating channel dispersion impairment in both RF domain and optical domain. In this section, we use the term ‘RF domain’ and ‘electrical domain’ interchangeably.

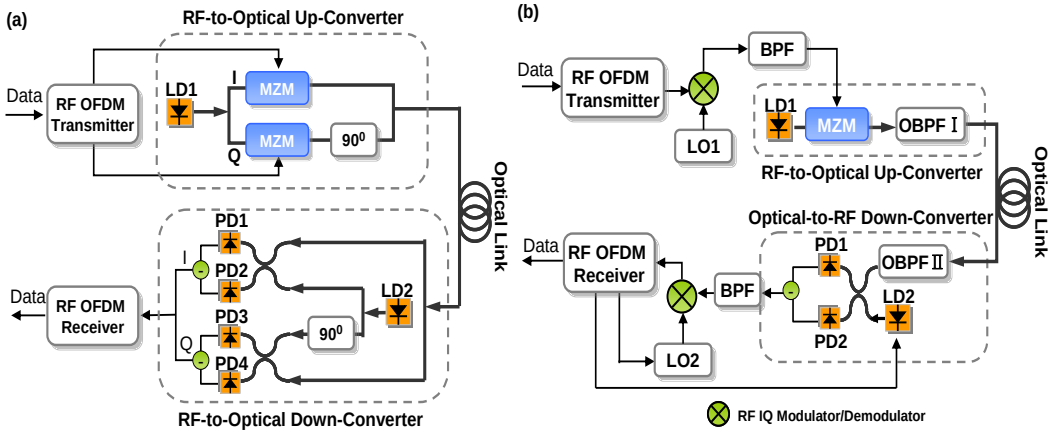

Fig.2.3 A CO-OFDM system in (a) direct up/down conversion architecture, and (b) intermediate frequency (IF) architecture.

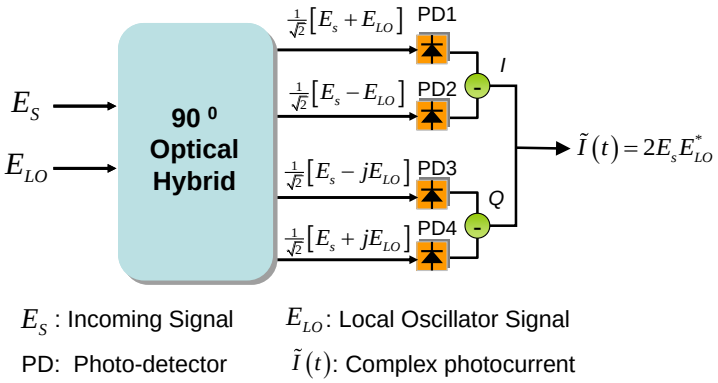

E_S : Incoming Signal E_{LO}: Local Oscillator Signal

PD: Photo-detector $\tilde{I}(t)$: Complex photocurrent

Fig.2.4 Coherent detection using an optical hybrid and balanced photo-detection.

(ii) Coherent detection for linear down-conversion and noise suppression

As shown in Fig.2.4, coherent detection uses a six-port 90 ° optical hybrid and a pair of balanced photo-detectors. The main purposes of coherent detection are (i) to linearly recover the *I* and *Q* components of the incoming signal, and (ii) to suppress or cancel the common mode noise. Using a six-port 90 ° hybrid for signal detection and analysis has been practiced in RF domain for decades [64-65], and its application to single-carrier coherent optical systems can be also found in [62-63]. In what follows, in order to illustrate its working principle, we will perform an analysis of down conversion via coherent detection assuming ideal condition for each component shown in Fig.2.4.

The purpose of the four output ports of the 90 ° optical hybrid is to generate a 90 ° phase shift between I and Q components, and 180 ° phase shift between balanced detectors. Ignoring imbalance and loss of the optical hybrid, the output signals E_{1-4} can be expressed as

$$E_1 = \tfrac{1}{\sqrt{2}}\left[E_s + E_{LO}\right], \qquad E_2 = \tfrac{1}{\sqrt{2}}\left[E_s - E_{LO}\right]$$
$$E_3 = \tfrac{1}{\sqrt{2}}\left[E_s - jE_{LO}\right], \qquad E_4 = \tfrac{1}{\sqrt{2}}\left[E_s + jE_{LO}\right] \tag{2.1}$$

where E_s and E_{LO} are respectively the incoming signal and local oscillator (LO) signal. We further decompose the incoming signal into two components: (i) the received signal when there is no amplified spontaneous noise (ASE), $E_r(t)$ and (ii) the ASE noise, $n_o(t)$, namely

$$E_s = E_r + n_o \tag{2.2}$$

We first study how the *I* component of the photo-detected current is generated, and the *Q* component can be derived accordingly. The *I* component is obtained by using a pair of the photo-detectors, PD1 and PD2 in Fig.2.4, whose photocurrent I_{1-2} can be described as

$$I_1 = |E_1|^2 = \frac{1}{2}\left\{|E_s|^2 + |E_{LO}|^2 + 2\,\mathrm{Re}\left\{E_s E_{LO}^*\right\}\right\} \tag{2.3}$$

$$I_2 = |E_2|^2 = \frac{1}{2}\left\{|E_s|^2 + |E_{LO}|^2 - 2\,\mathrm{Re}\left\{E_s E_{LO}^*\right\}\right\} \tag{2.4}$$

$$|E_s|^2 = |E_r|^2 + |n_o|^2 + 2\,\mathrm{Re}\left\{E_r n_o^*\right\} \tag{2.5}$$

$$|E_{LO}|^2 = I_{LO}\left(1 + I_{RIN}(t)\right) \tag{2.6}$$

where I_{LO} and $I_{RIN}(t)$ are the average power and relative intensity noise (RIN) of the LO laser, and '*Re*' or '*Im*' denotes the real or imaginary part of a complex signal. For simplicity, the photo-detection responsivity is set to unity. The three terms at the right hand of (2.5) represent signal-to-signal beat noise, signal-to-ASE beat noise, and ASE-to-ASE beat noise. Because of the balanced detection, using (2.3) and (2.4), the *I* component of the photocurrent becomes

$$I_I(t) = I_1 - I_2 = 2\,\mathrm{Re}\left\{E_s E_{LO}^*\right\} \tag{2.7}$$

Now the noise suppression mechanism becomes quite clear because the three noise terms in (2.5) and the RIN noise in (2.6) from a single detector are completely cancelled via balanced detection. Nevertheless, it has been shown that coherent detection can be performed by using a single photo-detector, but at the cost of reduced dynamic range [66].

In a similar fashion, the *Q* component from the other pair of balanced detectors can be derived as

$$I_Q(t) = I_3 - I_4 = 2\,\mathrm{Im}\left\{E_s E_{LO}^*\right\} \tag{2.8}$$

Using the results of (2.7) and (2.8), the complex detected signal $\tilde{I}(t)$ consisting of both *I* and *Q* components becomes

$$\tilde{I}(t) = I_I(t) + jI_Q(t) = 2E_s E_{LO}^* \tag{2.9}$$

From (2.9), the linear down-conversion process via coherent detection becomes quite clear; the complex photocurrent $\tilde{I}(t)$ is in essence a linear replica of the incoming complex signal that is frequency down-converted by a local oscillator frequency. Thus with linear coherent detection at receiver and linear generation at transmitter, complex OFDM signals can be readily transmitted over the optical fibre channel.

2.2.4 Direct detection optical OFDM (DDO-OFDM)

A DDO-OFDM aim for simpler transmitter/receiver than CO-OFDM for lower costs. It has many variants which reflect the different requirements in terms of data rates and costs from a broad range of applications. For instance, the first report of the DDO-OFDM [67] takes advantage of the fact the OFDM signal is more immune to the impulse clipping noise seen in CATV networks. Another example is single-side-band (SSB)-OFDM which has been recently proposed by Lowery et al. and Djordjevic et al. for long-haul transmission [22, 68]. Tang et al. have proposed an adaptively modulated optical OFDM (AMO-OFDM) that uses bit and power loading showing promising results for both multimode fibre and short-reach SMF fibre links [20, 69-70]. The common feature for DDO-OFDM is use of a simple square-law photodiode at the receiver. DDO-OFDM can be divided into two categories according to how optical OFDM signal is being generated: (i) linearly-mapped DDO-OFDM (LM-DDO-OFDM) where the optical OFDM spectrum is a replica of baseband OFDM, and (ii) nonlinearly-mapped DDO-OFDM (NLM-DDO-OFDM) where the optical OFDM spectrum does not display a replica of baseband OFDM. In what follows, we discuss the principles and design choices for these two classes of direct-detection OFDM systems.

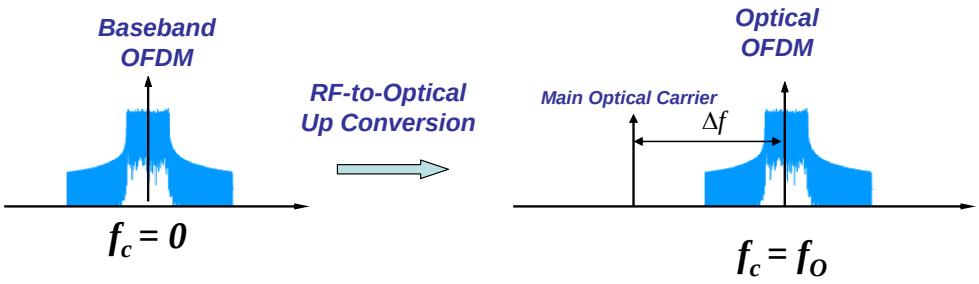

Fig.2.5 Illustration of linearly-mapped DDO-OFDM (LM-DDO-OFDM) where the optical OFDM spectrum is a replica of the baseband OFDM spectrum.

(i) Linearly-mapped DDO-OFDM

As shown in Fig.2.5, the optical spectrum of an LM-DDO-OFDM signal at the output of the O-OFDM transmitter is a linear copy of the RF OFDM spectrum plus an optical carrier that is usually 50 % of the overall power. The position of the main optical carrier can be one OFDM spectrum bandwidth away [68, 71] or right at the end of the OFDM spectrum [72-73]. Formally, such type of DDO-OFDM can be described as

$$s(t) = e^{j2\pi f_0 t} + \alpha e^{j2\pi(f_0+\Delta f)t} \cdot s_B(t) \tag{2.10}$$

where $s(t)$ is the optical OFDM signal, f_0 is the main optical carrier frequency, Δf is guard band between the main optical carrier and the OFDM band (Fig.2.5), and α is the scaling coefficient that describes the OFDM band strength related to the main carrier. $s_B(t)$ is the baseband OFDM signal given by

$$s_B = \sum_{k=-\frac{1}{2}N_{sc}+1}^{\frac{1}{2}N_{sc}} c_k e^{j2\pi f_k t} \tag{2.11}$$

where c_k and f_k are respectively the OFDM information symbol and the frequency for the k^{th} subcarrier. For explanatory simplicity, only one OFDM symbol is shown in (2.11). After the signal passing through fibre link with chromatic dispersion, the OFDM signal can be approximated as

$$r(t) = e^{j\left(2\pi f_0 t + \Phi_D(-\Delta f) + \phi(t)\right)} + \alpha e^{j\left(2\pi(f_0+\Delta f)t + \phi(t)\right)} \cdot \sum_{k=-\frac{1}{2}N_{sc}+1}^{\frac{1}{2}N_{sc}} c_{ik} e^{\left(j2\pi f_k t + \Phi_D(f_k)\right)} \tag{2.12}$$

$$\Phi_D(f_k) = \pi \cdot c \cdot D_t \cdot f_k^2 / f_O^2 \tag{2.13}$$

where $\Phi_D(f_k)$ is the phase delay due to chromatic dispersion for the k^{th} subcarrier. D_t is the accumulated chromatic dispersion in unit of ps/pm, and f_O is the centre

frequency of optical OFDM spectrum, and c is the speed of light. At the receiver, the photodetector can be modelled as a square-law detector and the resultant photo-current signal is

$$I(t) \propto |r(t)|^2 = 1 + 2\alpha \,\mathrm{Re}\left\{ e^{j2\pi\Delta f t} \sum_{k=-\frac{1}{2}N_{sc}+1}^{\frac{1}{2}N_{sc}} c_{ik} e^{\left(j2\pi f_k t + \Phi_D(f_k) - \Phi_D(-\Delta f)\right)} \right\} + |\alpha^2| \sum_{k_1=-\frac{1}{2}N_{sc}+1}^{\frac{1}{2}N_{sc}} \sum_{k_2=-\frac{1}{2}N_{sc}+1}^{\frac{1}{2}N_{sc}} c_{k_2}^{*} c_{k_1} e^{\left(j2\pi(f_{k1}-f_{k_2})t + \Phi_D(f_{k_1}) - \Phi_D(f_{k_2})\right)} \quad (2.14)$$

The first term is a DC component that can be easily filtered out. The second term is the fundamental term consisting linear OFDM subcarriers that are to be retrieved. The third term is the second-order nonlinearity term that needs to be removed.

There are several approaches to minimize the penalty due to the second-order nonlinearity term:

(A) Offset SSB-OFDM. Sufficient guard band is allocated such that the second-term and third-term RF spectra are non-overlapping. As such, the third term in Eq. (2.14) can be easily removed using a RF or DSP filter, as proposed by Lowery et al. in [68].

(B) Baseband Optical SSB-OFDM. α coefficient is reduced as much as possible such that the distortion as result of the third-term is reduced to an acceptable level. This approach has been adopted by Djordjevic et al. [22] and Hewitt et al. [72].

(C) Subcarrier interleaving. From Eq. (2.14), it follows that if only odd subcarriers are filled, i.e., c_k is nonzero only for the odd subcarriers, the second-order intermodulation will be at even subcarriers, which are orthogonal to the original signal at the odd subcarrier frequencies. Subsequently, the third-term does not produce any interference. This approach has been proposed by Peng et al. [74].

(D) Iterative distortion reduction. The basic idea is to go through a number of iterations of estimation of the linear term, and compute the second-order term using the estimated linear term, and removing the second-order term from the right side of Eq. (2.14). This approach has been proposed by Peng et al. [73].

There are advantages and disadvantages among all these four approaches. For instance, Approach B has the advantage of better spectral efficiency, but at the cost of

sacrificing receiver sensitivity. Approach D has both good spectral efficiency and receiver sensitivity, but has a burden of computational complexity.

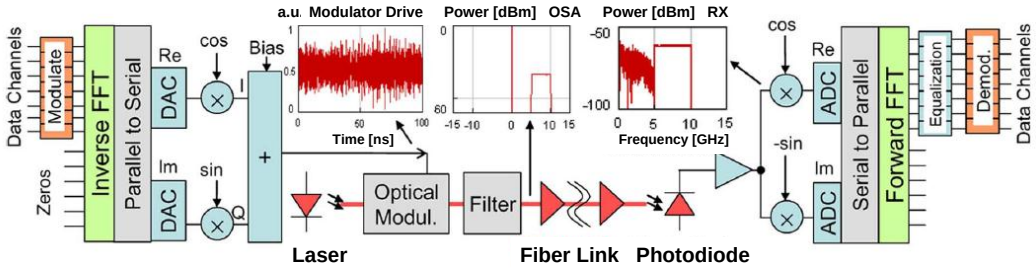

Fig.2.6 Direct-detection optical OFDM (DDO-OFDM) long-haul optical communication systems. After Ref. [75]

Fig.2.6 shows one offset SSB-OFDM proposed by Lowery et al. in [75]. They show that such DDO-OFDM can mitigate enormous amount of chromatic dispersion up to 5000 km standard SMF (SSMF) fibre. The proof-of-concept experiment was demonstrated by Schmidt et al. from the same group for 400 km DDO-OFDM transmission at 20 Gb/s [71].The simulated system is 10 Gb/s with 4-QAM modulation with a bandwidth around 5 GHz [75]. In the electrical OFDM transmitter, the OFDM signal is up-converted to an RF carrier at 7.5 GHz generating an OFDM band spanning from 5 to 10 GHz. The RF OFDM signal is fed into an optical modulator. The output optical spectrum has the two side OFDM bands that are symmetric across the main optical subcarrier. An optical filter is then used to filter out one OFDM side band. This single-side band (SSB) is critical to ensure there is one-to-one mapping between the RF OFDM signal and the optical OFDM signal. The power of main optical carrier is optimized to maximize the sensitivity. At the receiver, only one photo-detector is used. The RF spectrum of the photocurrent is depicted as an inset in Fig.2.6. It can be seen that the second-order inter-modulation, the third-term in Eq. (2.14) is from DC to 5 GHz whereas the OFDM spectrum, the second term in Eq. (2.14) spans from 5 GHz to 10 GHz. As such, the RF spectrum of the intermodulation does not overlap with the OFDM signal, signifying that the intermodulation does not cause detrimental effects after proper electrical filtering.

(ii) Nonlinearly-mapped DDO-OFDM (NLM-DDO-OFDM)

The second class of DDO-OFDM is nonlinearly-mapped OFDM, which means that there is no linear mapping between the electric field (baseband OFDM) and the optical field. Instead, NLM-DD-OFDM aims to obtain a linear mapping between

baseband OFDM and optical intensity. For simplicity, we assume generation of NLM-DDO-OFDM using direct modulation of a DFB laser, the waveform after the direct modulation can be expressed as [76]

$$E(t) = e^{j2\pi f_o t} A(t)^{1+jC} \tag{2.15}$$

$$A(t) \equiv \sqrt{P(t)} = A_0 \sqrt{1 + \alpha \,\mathrm{Re}\left(e^{j(2\pi f_{IF} t)} \cdot s_B(t)\right)} \tag{2.16}$$

$$s_B(t) = \sum_{k=-\frac{1}{2}N_{sc}+1}^{\frac{1}{2}N_{sc}} c_k e^{j2\pi f_k t} \tag{2.17}$$

$$m \equiv \alpha \sqrt{\sum_{k=-\frac{1}{2}N_{sc}+1}^{\frac{1}{2}N_{sc}} |c_k|^2} \tag{2.18}$$

where $E(t)$ is the optical OFDM signal, *A(t)* and *P(t)*are the instantaneous amplitude and power of the optical OFDM signal, c_k is the transmitted information symbol for the k^{th} subcarrier, *C* is the chirp constant for the direct modulated DFB laser [76], f_{IF} is the IF frequency for the electrical OFDM signal for modulation, *m* is the optical modulation index, α is a scaling constant to set an appropriate modulation index *m* to minimize the clipping noise, and $s_B(t)$ is the baseband OFDM signal. Assuming the chromatic dispersion is negligible, the detected current is

$$I(t) = |E(t)|^2 = |A|^2 = A_0 \left(1 + \alpha \,\mathrm{Re}\left(e^{j(2\pi f_{IF} t)} \cdot s_B(t)\right)\right) \tag{2.19}$$

Eq. (2.19) shows that the photocurrent contains a perfect replica of the OFDM signal $s_B(t)$ with a DC current. We also assume that modulation index *m* is small enough that clipping effect is not significant. Eq. (2.19) shows that by using NLM-DDO-OFDM with no chromatic dispersion, the OFDM signal can be perfectly recovered. The fundamental difference between the NLM- and LM-DDO-OFDM can be gained by studying their respective optical spectra. Fig.2.7 shows the optical spectra of NLM-DDO-OFDM using (a) direct modulation of a DFB laser with the chirp coefficient *C* of 1 in (2.15) and modulation index *m* of 0.3 in (2.18) and (b) offset SSB-OFDM. It can be seen that, in sharp contrast to SSB-OFDM, NLM-DDO-OFDM has a multiple of OFDM bands with significant spectral distortion. Therefore there is no linear mapping from the baseband OFDM to the optical OFDM. The

consequence of this nonlinear mapping is fundamental, because when any type of the dispersion, such as chromatic dispersion, polarization dispersion, or modal dispersion occurs in the link, the detected photocurrent can no longer recovers the linear baseband OFDM signal. Namely, any dispersion will cause the nonlinearity for NLM-DD-OFDM systems. In particular, unlike SSB-OFDM, the channel model for direct-modulated OFDM is no longer linear under any form of optical dispersion. Subsequently, NLM-DD-OFDM is only fit for short-haul application such as multimode fiber for local-area networks (LAN), or short-reach single-mode fibre (SMF) transmission. This class of optical OFDM has attracted attention recently due to its low cost. Some notable works of NLM-DD-OFDM are experimental demonstrations and analysis of optical OFDM over multimode fibres [69, 70,77] and compatible SSB-OFDM (CompSSB) proposed by Schuster et al. to achieve higher spectral efficiency than offset SSB-OFDM [78].

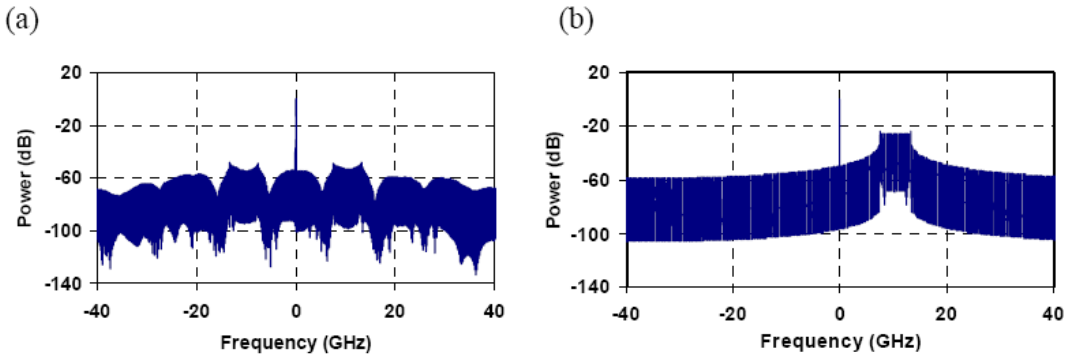

Fig.2.7 Comparison of optical spectra between (a) NLM-DDO-OFDM through direct-modulation of DFB laser, and (b) externally modulated offset SSB DDO-OFDM. The chirp constant C of 1 and the modulation index m of 0.3 are assumed for direct-modulation in (a). Both OFDM spectrum bandwidths are 5 GHz comprising 256 subcarriers.

2.2.5 Variants of CO-OFDM transmission systems

Conventional OFDM systems are based on Fourier transforms (FTs). In these OFDM systems, low rate subcarriers are orthogonally transformed into time domain signals, and the orthogonality between subcarriers can prevent inter-carrier interference (ICI). It has been shown that OFDM modulation/demodulation can be efficiently implemented using inverse discrete Fourier transform (IDFT)/discrete Fourier transform (DFT) electronically. Wavelet transforms (WTs), or wavelet packet transforms (WPTs) in particular [79-81], are relatively new concepts in transmission systems by which a signal is expanded in an orthogonal set called ‘wavelets’ [79-92].

Similarly to Fourier transform, wavelet transforms can provide orthogonality between OFDM subcarriers, however the basic functions are wavelets instead of sinusoids. Unlike sinusoids that are infinitely long in the time domain, wavelets have finite length. Therefore WTs have both frequency and time localization. The incentive to use WPTs rather than FTs in OFDM is to provide better spectral roll-off and to remove the need for CP [25].It has been proposed that wavelet packet transform-based optical OFDM (WPT-OFDM) be applied as an alternative approach to conventional Fourier transform based optical OFDM (FT-OFDM), with better performance in short haul. It is shown that WPT-OFDM can mitigate a CD of 3,380 ps/nm at 112 Gb/s rate, a remarkable result without the need of CP [25].

Despite many promising features, CO-OFDM system also suffers from high peak-to-average power ratio (PAPR) which leads to inferior tolerance to fibre nonlinearity compared with single-carrier (SC) system and has become an obstacle to its practical implementation in long-haul transmission systems. Although specialty fibres such as ultra-large area fibre (ULAF) [41, 47-48, 93] or low-loss low-nonlinearity pure silica core fibre (PSCF) [94] with Raman amplification has been suggested to further extend the reach of transmission systems, it could be either more expensive than or not compatible with the deployed links. To solve the nonlinear tolerance problem, discrete-Fourier-transform spread OFDM (DFTS-OFDM) has recently been proposed with an attractive feature of much reduced PAPR [26]. DFTS-OFDM is also called single-carrier frequency-division multiplexing (SC-FDM) that has been incorporated into the 3GPP-LTE standard in uplink for the next generation mobile system with many interesting features [27]. Furthermore, benefited from the sub-band or sub-wavelength accessibility of CO-OFDM, properly designed multiband DFTS-OFDM (MB-DFTS-OFDM) can potentially have better nonlinearity tolerance over either conventional CO-OFDM or SC system for ultra-high speed transmission [95-96]. The nonlinearity advantage of MB-DFTS-OFDM has been verified through simulation in [95-96]. In addition, optical transmission experiments utilizing the DFTS-OFDM or SC-FDM have been demonstrated very recently by several groups [94, 97-101] which shows a potential advantage of better nonlinear tolerance and high SE. The ROADM functionally has also been demonstrated on SC-FDM superchannel [100].

2.2.6 Space-division multiplexing (SDM)

Traditionally, high data rates can be obtained by using higher order modulation constellations or higher symbol rates which result in a large signal bandwidth. However, the available bandwidth of channel, no matter in wireless or optical communications, is limited due to the increased loss and/or constraints such as more costly RF/optical components (circuits, lasers, amplifiers, etc). In addition, transmit more bits per second will drastically decrease the Eb/No, and high sampling rates imply higher sensitivity to inter-symbol interference (ISI). To combat these problems, space-division multiplexing (SDM) was proposed as a promising solution for the increase of bandwidth efficiency and capacity. SDM, namely a multiplexing scheme that utilizes the space domain, is a method by which metallic, radio, or optical transmission media are physically separated by insulation, waveguides, or space in order to maintain channel separations. The space domain is an additional dimension that is orthogonal to the frequency/time domain. Within each space channel, the frequency/time/wavelength division multiplexing can be applied. SDM has been widely adopted in wireless communications, usually in combination with code/time/frequency division multiplexing (CDM/TDM/FDM). The multipath propagation in SDM system results in multipath fading, ISI and inter-channel interference (ICI), which needs to be dealt with for minimum penalty. OFDM is an efficient modulation scheme for mitigating the effects of multipath channel with excellent transmission performance since the ISI can be eliminated through insertion of CP, as will be discussed in Section 3.1.

In optical communications, SDM can be achieved through either a multi-core fibre (MCF) or a multi-mode fibre (MMF). For MMF (or more specifically, few-mode fibre (FMF)) based SDM transmission, mode-division multiplexing (MDM) is used. It is known that in a MMF or FMF, many orthogonal spatial (transverse) modes can be guided and transmitted simultaneously. By multiplexing the *N* different spatial modes, theoretically we can obtain a channel capacity that is *N* times of SMF. The feasibility of using MDM and MIMO in FMF transmission has recently been demonstrated by several groups [102-113]. In these experiments, MDM is achieved in FMF or two-mode fibre (TMF) with different combinations of supported modes, e.g., LP_{01} and LP_{11} modes [102-103], two degenerate LP_{11} modes (LP_{11a}+LP_{11b}) [104], and even all three modes (LP_{01}+LP_{11a}+LP_{11b}) [109-113]. These advances into few-mode

transmission require brand new research in a wide range of topics from device to system level, including FMF design, FMF compatible component design, FMF transmission and FMF amplification, among others. There have already been many designs of FMF in [103-115] with either step-index or graded-index profile. The step-index profile is normally considered to be easier to fabricate without the need for sophisticated doping and drawing process, while graded-index profile could significantly reduce the differential modal delay (DMD) between the modes. The trend of future FMF design will be first to further reduce the DMD to a low value comparable with the chromatic dispersion, but large enough to mitigate the fibre nonlinearity, and second to maintain the loss on par with the standard single-mode fibre (SSMF). In MDM transmission systems, mode multiplexer/de-multiplexer (MUX/DEMUX) components play a critical role. A few reliable components have been proposed such as mode stripper (MS) [103-107, 116], mode converter (MC) [102-107], mode combiner [104-113], and optical add/drop multiplexer (OADM) [107]. Significant effort has been made to demonstrate the feasibility of these components by either simulation analysis or experiments. These components fall into two major categories: free-space based or fibre based. One of the free-space components is a phase mask based MC using either liquid-crystal-on-silicon (LCoS) spatial light modulator (SLM) [104] or specially-fabricated glass plate [109], as shown in Fig.2.7.

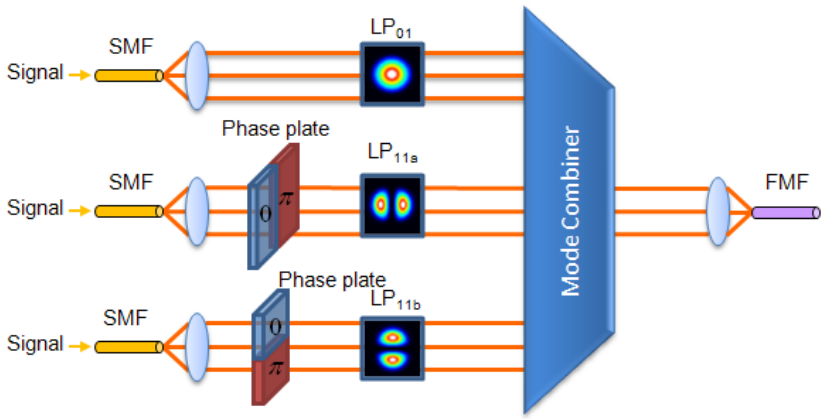

Fig.2.8 Schematic of a free-space 3×1 mode combiner using phase-plate based mode converters [109].

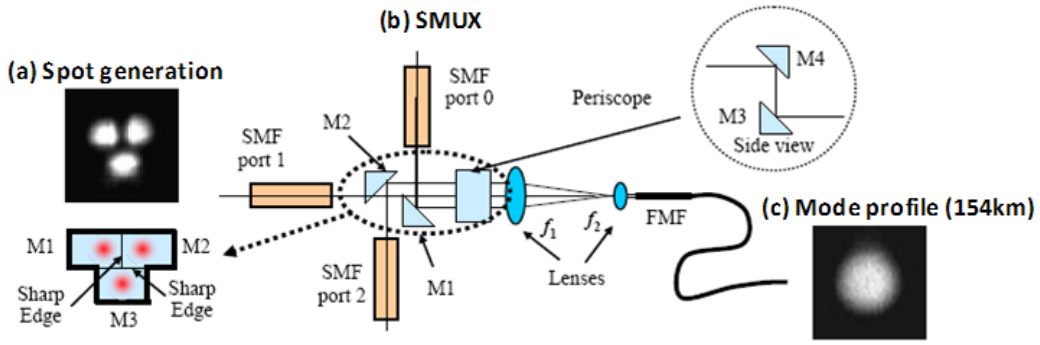

Fig.2.9. (a) Spot generation using mirrors with sharp edges. (b) Experimental setup of the low-loss mode coupler. (c) Mode profile at the end facet of 154-km hybrid FMF [113].

The above-mentioned MC can be readily implemented with commercially available free-space components. However, the insertion loss is often high due to the BSs, and especially when a phase plate is used (typically 9-10 dB for a 3×1 SMC). Recently an improved low-loss mode coupler has been proposed in [113] by illuminating the end facet of the TMF with three appropriately-placed spots, as shown in Fig.2.9. Each spot generally excites multiple modes. Nevertheless, as long as the three spots are symmetrically placed around the center and the amount of power coupled from a single spot into LP_{01} and the alternative LP_{11a} + LP_{11b} is exactly the same, the coupling matrix between the three spots and the true FMF modes is unitary, which guarantees no capacity loss after MIMO digital signal processing. In practice, insertion losses of 3.95, 3.85, and 3.7 dB for the 3 ports of the SMUX are reported [113]. Such a mode coupler can be scaled up to support more modes by using larger number of appropriately-placed spots, but meticulous coupling from each spot to each mode needs to be engineered to guarantee that the coupling matrix is still unitary.

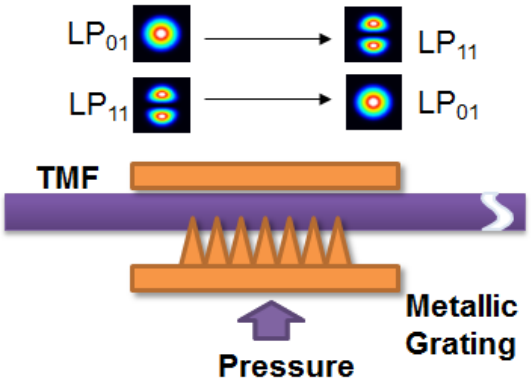

Fig.2.10 Schematic diagram of a LPFG based LP_{01}/LP_{11} mode converter [102-106].

Similarly, one of the fibre-based components is the long period fibre grating (LPFG) based MC [102-106] as shown in Fig.2.10. We proposed the use of LPFG-

based MC as a practical solution for MMUX/MDEMUX in MDM transmission. Its mechanism, fabrication and characterization will be discussed in Section 6.2. Experimental demonstration of MDM transmission utilizing the LPFG-based MC will be further shown in Chapter 7. The advantage of fibre based components over their free-space counterparts is the compactness and easiness of integration.

Beside the mode MUMX/MDEMUX components, few-mode amplifier for FMF transmission is also very important if there is significant accumulation of loss. The loss could come from the mode MUX/DEMUX or fibre loss. The feasibility of few-mode amplification using EDFA or Raman pump has recently been demonstrated [117-120] with the inclusion of aforementioned MCs. FMF compatible EDFA opens a gate to the long-haul FMF transmission [112, 117-119]. As is well known, the nonlinear effects in silica fibre impose a hard constraint on the achievable channel capacity. For FMF based transmission, there is strong field overlapping between different modes thus it is important to analyse the FMF systems taking into account potential inter-modal nonlinearity [121]. There have already been many theoretical studies on the nonlinear propagation modelling and simulation of FMF based transmission systems [121-122], but the experimental result is lacking. In a recent work [123] we have shown for the first time the experimental characterization of nonlinear parameters in a FMF. We have also proposed a method to mitigate the nonlinear noise on subsystem level, namely the unique-word DFT-Spread OFDM (UW-DFTS-OFDM) [95-99] which could fit well for future Terabit/s SDM superchannel transmission.

3 Principle of Optical OFDM System

3.1 Principle of OFDM system

OFDM is a special form of a broader class of multi-carrier modulation (MCM). The principle of OFDM is to transmit the information through a large number of orthogonal subcarriers. The OFDM signal in time domain consists of a continuous stream of OFDM symbols with a regular period T_s. The OFDM baseband signal *s(t)* is written as [124-125]

$$s(t)=\sum_{i=-\infty}^{+\infty}\sum_{k=-Nsc/2+1}^{k=N_{sc}/2} c_{ki}\exp(j2\pi f_k(t-iT_s))\,f(t-iT_s) \tag{3.1}$$

$$f_k=\frac{k-1}{t_s},\Delta f=\frac{1}{t_s} \tag{3.2}$$

$$f(t)=\begin{cases}1,(-\Delta_G<t\le t_s)\\0,(t\le-\Delta_G,t>t_s)\end{cases} \tag{3.3}$$

where c_{ki} is the *i*-th information symbol at the *k*-th subcarrier, $f(t)$ is the pulse waveform of the symbol, f_k is the frequency of the subcarrier, and Δf is the subcarrier spacing, T_s, ΔG and t_s are the OFDM symbol period, guard interval length and observation period, respectively.

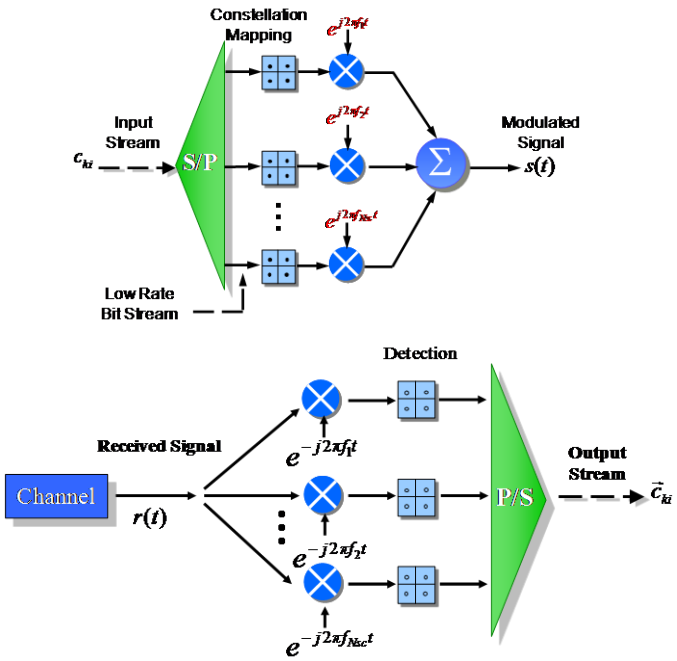

Fig.3.1 Conceptual diagram for a generic multi-carrier modulation (MCM) system.

The optimum detector for each subcarrier could use a filter that matches the subcarrier waveform, or a correlator matched to the subcarrier as shown in Fig.3.1. Therefore, the detected information symbol $\vec{c}_{ki}$ at the output of the correlator is given by

$$\vec{c}_{ki} = \int_0^{T_s} r(t - iT_s) s_k^* dt = \int_0^{T_s} r(t - iT_s) \exp(-j2\pi f_k t) dt \tag{3.4}$$

where $r(t)$ is the received time-domain signal. The classical MCM uses non-overlapped band limited signals, and can be implemented with a bank of large number of oscillators and filters at both transmit and receive end. The major disadvantage of MCM is that it requires excessive bandwidth. This is because in order to design the filters and oscillators cost-efficiently, the channel spacing has to be multiple of the symbol rate, greatly reducing the spectral efficiency. On the contrary, OFDM employs overlapped yet orthogonal signal set [126-127]. This orthogonality originates from the straightforward correlation between any two subcarriers, given by

$$\begin{aligned} \delta_{kl} &= \frac{1}{T_s} \int_0^{T_s} s_k s_l^* dt = \frac{1}{T_s} \int_0^{T_s} \exp(j2\pi(f_k - f_l)t) dt \\ &= \exp(j\pi(f_k - f_l)T_s) \frac{\sin(\pi(f_k - f_l)T_s)}{\pi(f_k - f_l)T_s} \end{aligned} \tag{3.5}$$

If the following condition

$$f_k - f_l = m \frac{1}{T_s} \tag{3.6}$$

is satisfied, then the two subcarriers are orthogonal to each other. This signifies that these orthogonal subcarrier sets, with their frequencies spaced at multiple of inverse of the symbol rate can be recovered with the matched filters (Eq. (3.4)) without inter-carrier interference (ICI), in spite of strong signal spectral overlapping.

One of the enabling techniques for OFDM is the insertion of cyclic prefix [124-125]. Cyclic prefix was proposed to resolve the channel dispersion induced inter-symbol interference (ISI) and ICI [124-125, 128]. Fig.3.2 shows insertion of a cyclic prefix by cyclic extension of the OFDM waveform into the guard interval, Δ_G. As shown in Fig.3.2, the waveform in the guard interval is essentially an identical copy of that in the DFT window, with time-shifted by 't_s' behind.

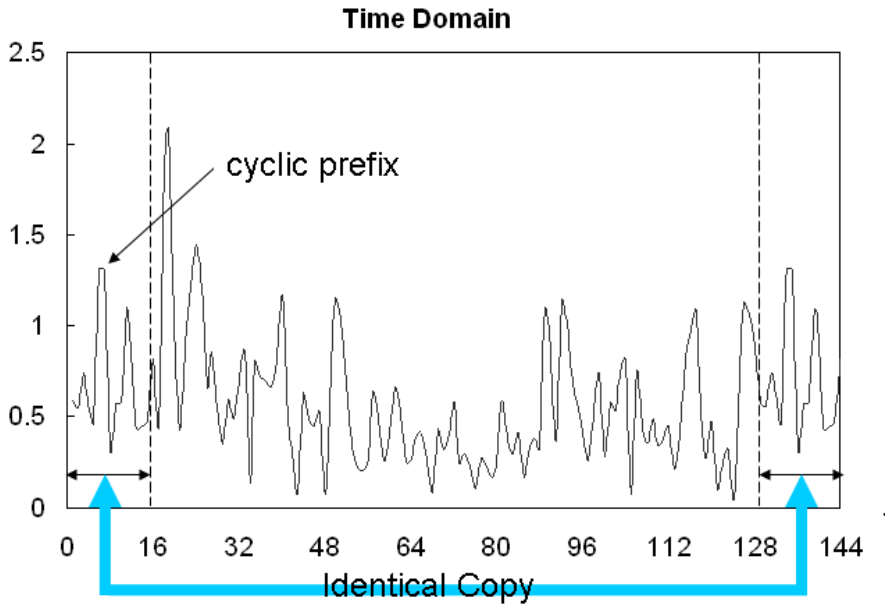

Fig.3.2 OFDM symbol in time domain.

It can be seen that, if the maximum delay spread of multi-path fading is smaller than the guard time Δ_G, the cyclic prefix can perfectly eliminate the ISI. In the context of optical transmission, the delay spread due to the chromatic dispersion among the subcarriers should not exceed the guard time, and the fundamental condition for complete elimination of ISI in optical medium is thus given by

$$\frac{c}{f^2}|D_t| \cdot N_{SC} \cdot \Delta f \leq \Delta_G \tag{3.7}$$

where f is the frequency of the optical carrier, c the speed of light, D_t the total accumulated chromatic dispersion in units of ps/km, and N_{sc} the number of subcarriers.

3.2 Principle of CO-OFDM

In the chapter 2 we have already introduced the concept of CO-OFDM with focus on the principle of coherent detection. Here we revisit the principle of CO-OFDM from experimental and signal processing point of view. Fig.3.3 shows a conceptual diagram of a complete CO-OFDM system [18, 59-60, 129-]. The function of the OFDM transmitter is to map the data bits into each OFDM symbol, and generate the time series by inverse discrete Fourier transform (IDFT) expressed in (Eq. (3.1)), including insertion of the guard interval, The digital signal is then converted to analogue one through digital-to-analogue converter (DAC), and filtered with a low-pass filter (LPF)

to remove the alias signal. In Fig.3.3, direct-up conversion architecture is used where radio-frequency (RF) OFDM transmitter outputs a baseband OFDM signal. The subsequent RF-To-Optical (RTO) up-converter transforms the baseband signal to the optical domain using an optical IQ modulator comprising a pair of Mach-Zehnder modulators (MZM) with a 90^{o} phase offset. The baseband OFDM signal is directly up-converted to the optical domain given by

$$E(t)=\exp\left(j\omega_{LD1}t+\phi_{LD1}\right)\cdot s_B(t) \tag{3.8}$$

where ω_{LD1} and ϕ_{LD1} respectively are the angular frequency and phase of the transmitter laser. The up-converted signal $E(t)$ traverses the optical medium with impulse response $h(t)$, and the received optical signal becomes

$$E(t)=\exp\left(j\omega_{LD1}t+\phi_{LD1}\right)s_B(t)\otimes h(t) \tag{3.9}$$

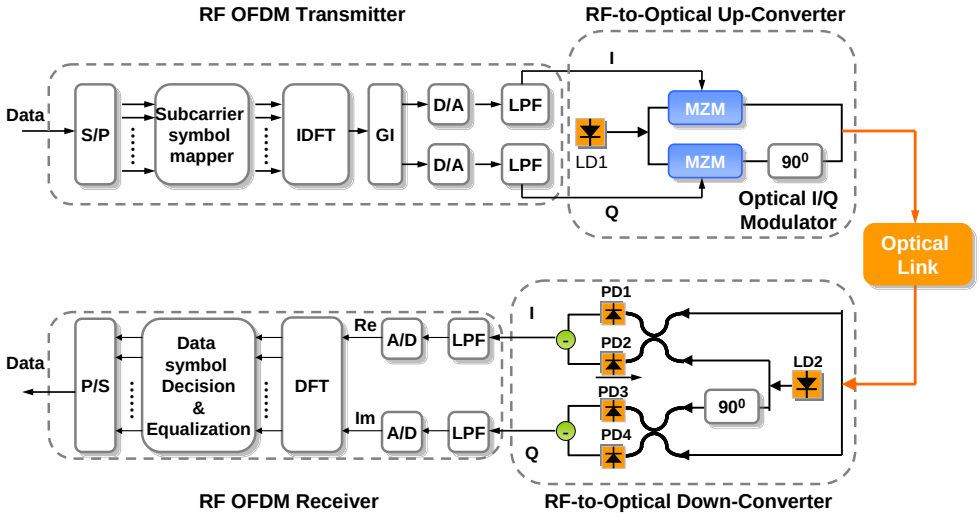

Fig.3.3 Conceptual diagram of CO-OFDM system. S/P: Serial-to-parallel, GI: Guard Interval, (I)DFT: (Inverse) Discrete Fourier Transform, LPF: Low Pass Filter, MZM: Mach-Zehnder Modulator, PD: Photodiode.

where '$\otimes$' stands for convolution. The optical OFDM signal is then fed into the Optical-To-RF (OTR) down-converter where the optical OFDM signal is converted to RF OFDM signal. There are two ways to do the down-conversion. One is direct down-conversion architecture where the intermediate frequency (IF) is near DC. The other is that we first down-convert the signal to RF domain with an intermediate frequency then down-convert to baseband. The IF signal can be expressed as

$$r(t)=\exp\left(j\omega_{off}t+\Delta\phi\right)r_0(t),\quad r_0(t)=s_B(t)\otimes h(t) \tag{3.10}$$

$$\omega_{off} = \omega_{LD1} - \omega_{LD2}, \quad \Delta\phi = \phi_{LD1} - \phi_{LD2} \tag{3.11}$$

where $\Delta\omega_{off}$ and $\Delta\phi$ are respectively the angular frequency offset and phase offset between transmit and receive lasers. In the RF OFDM receiver, the down-converted OFDM signal is first sampled with an analogue-to-digital converter (ADC). Then the signal needs to go through sophisticated three levels of synchronizations before the symbol decision can be made. The three levels of synchronizations are (i) FFT window synchronization where OFDM symbol is properly delineated to avoid inter-symbol-interference, (ii) frequency synchronization, namely, frequency offset ω_{off} needs to be estimated and compensated, and (iii) the subcarrier recovery, where each subcarrier channel is estimated and compensated. Assuming successful completion of DFT window synchronization and frequency synchronization, the RF OFDM signal through DFT of the sampled value of Eq. (3.10) becomes

$$r_{ki} = e^{\phi_i} h_{ki} c_{ki} + n_{ki} \tag{3.12}$$

where r_{ki} is the received information symbol, ϕ_i is the OFDM symbol phase (OSP) or common phase error (CPE), h_{ki} is the frequency domain channel transfer function, n_{ki} is the noise. The third synchronization of subcarrier recovery involves estimation of OSP ϕ_i and the channel transfer function h_{ki}. Once they are known, an estimated value of c_{ki}, $\hat{c}_{ki}$ is given by zero-forcing method as

$$\hat{c}_{ki} = \frac{h_{ki}^*}{|h_{ki}|^2} e^{-i\phi_i} r_{ki} \tag{3.13}$$

$\hat{c}_{ki}$ is used for symbol decision or to recover the transmitter value c_{ki}, which is subsequently be mapped back to the original transmitted digital bits.

The above description of CO-OFDM processing has so far leaved out the pilot-subcarrier or training-symbol insertion where a proportion of the subcarriers or all the subcarriers in one OFDM symbol are known values to the receiver. The purpose of these pilot subcarrier or training symbol is to assist the above-mentioned three-level synchronization. Another important aspect of the CO-OFDM signal processing that is not discussed is the error-correction coding involving error-correction encoder/decoder, and interleaver/de-interleaver.

3.3 PMD supported transmission in CO-OFDM system

It is well-known that optical fibre can support two polarization modes. The propagation of an optical signal is influenced by the polarization effects including polarization coupling and polarization dependent loss (PDL).

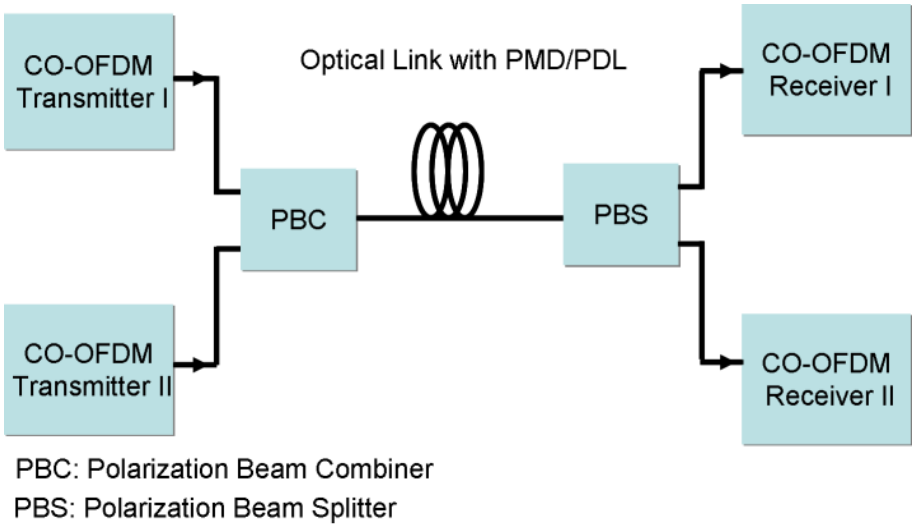

Fig.3.4 A variation of CO-MIMO-OFDM system: two-input two-output (TITO) [130].

As shown in Fig 2.4, a two-input-two-output (TITO) scheme of CO-OFDM is usually applied to support polarization-division multiplexed (PDM) transmission in the presence of polarization-mode dispersion (PMD) [58, 128-130, 131]. It consists of two set of CO-OFDM transmitters and receivers, each transmitter and receiver pair for a single polarization. In such a scheme, because the transmitted OFDM information symbol $\vec{c}_{ki}$ can be considered as polarization modulation or polarization multiplexing, the capacity is thus doubled compared with single-input-single-output (SISO) scheme. As the impact of the PMD is to simply rotate the subcarrier polarization, and can be treated with channel estimation and constellation reconstruction, and therefore the doubling of the channel capacity will not be affected by PMD. Secondly, due to the polarization-diversity receiver employed at the receive end, TITO scheme does not need polarization tracking at the receiver.

Similar to the single-polarization OFDM signal model described in Section 3.2, the OFDM time-domain signal, $\boldsymbol{s}(t)$ is described using Jones vector given by [129]

$$\mathbf{s}(t) = \sum_{i=-\infty}^{+\infty} \sum_{k=-N_{sc}/2+1}^{N_{sc}/2} \mathbf{c}_{ik} \prod (t - iT_s) \exp\left(j2\pi f_k (t - iT_s) \right) \tag{3.14}$$

$$\mathbf{s}(t) = \begin{bmatrix} s_x \\ s_y \end{bmatrix}, \quad \mathbf{c}_{ik} = \begin{bmatrix} c_{ik}^x \\ c_{ik}^y \end{bmatrix} \tag{3.15}$$

$$f_k = \frac{k-1}{t_s} \tag{3.16}$$

$$\prod(t) = \begin{cases} 1, (-\Delta_G < t < t_s) \\ 0, (t \le -\Delta_G, t > t_s) \end{cases} \tag{3.17}$$

where s_x and s_y are the two polarization components in the time-domain, $\boldsymbol{c}_{ik}$ is the transmitted OFDM symbol in the form of Jones vector for the k-th subcarrier in the i-th OFDM symbol, c_{ik}^x and c_{ik}^y are the two polarization elements for $\boldsymbol{c}_{ik}$, f_k is the frequency for the k-th subcarrier, N_{sc} is the number of OFDM subcarriers, T_s, Δ_G, and t_s are the OFDM symbol period, guard interval length and observation period respectively. The Jones vector $\boldsymbol{c}_{ik}$ is employed to describe generic OFDM information symbol regardless the methods of the OFDM transmitter polarization configuration. In particular, the $\boldsymbol{c}_{ik}$ encompasses various modes of the polarization generation including single-polarization, polarization multiplexing and polarization-modulation, as they all can be represented by the two-element Jones vector $\boldsymbol{c}_{ik}$. The difference of the transmitted information symbol in Jones vector is automatically dealt with in initiation phase of OFDM signal processing by sending known training symbols.

We select a guard interval long-enough to handle the fibre dispersion including PMD and CD. This time margin condition is given by

$$\frac{c}{f^2}\left|D_t\right| \cdot N_{SC} \cdot \Delta f + DGD_{\max} \le \Delta_G \tag{3.18}$$

Where f is the frequency of the optical carrier, c is the speed of light, D_t is the total accumulated chromatic dispersion in units of ps/pm, Nsc is the number of the subcarriers, Δf is the subcarrier channel spacing, and $DGD_{\max}$ is the maximum budgeted differential-group-delay (DGD), which is about 3.5 times of mean PMD to have sufficient margin.

Following the same procedure as in [18], assuming using long-enough symbol period, we arrive at the received symbol given by

$$\vec{c}'_{ik} = e^{j\phi_i} \cdot e^{j\Phi_D(f_k)} \cdot T_k \cdot \vec{c}_{ik} + \vec{n}_{ik} \tag{3.19}$$

$$T_k = \prod_{i=1}^{N} \exp\left\{(-\frac{1}{2} j\vec{\beta}_l f_k - \frac{1}{2}\vec{\alpha}_l)\vec{\sigma}\right\} \tag{3.20}$$

$$\Phi_D(f_k) = \pi \cdot c \cdot D_t \cdot f_k^2 / f_{LD1}^2$$

where $\boldsymbol{c}'_{ik} = [c'^{x}_{ik} \quad c'^{y}_{ik}]^T$ is the received information symbol in the form of the Jones vector for the *k*-th subcarrier in the *i*-th OFDM symbol, $\boldsymbol{n}_{ik} = [n^x_{ik} \quad n^y_{ik}]^T$ is the noise including two polarization components, $\boldsymbol{T}_k$ is the Jones matrix for the fibre link, $\Phi_D(f_k)$ is the phase dispersion owing to the fibre chromatic dispersion, and ϕ_i is the OFDM symbol phase noise owing to the phase noises from the lasers and RF local oscillators (LO) at both the transmitter and receiver [18]. ϕ_i is usually dominated by the laser phase noise.

4 Novel Variants of Coherent Optical OFDM System for Future High-Speed Optical Networks

4.1 Introduction

4.2 Wavelet packet transform based OFDM system (WPT-OFDM)

4.2.1 Fourier transform (FT) and wavelet transform (WT)

Fourier transform is an operation that transforms one complex-valued function into another. Since the domain of the original function is typically time and the new function is frequency, the Fourier transform is often called the frequency domain representation of the original function. The definition of Fourier transform is given as below

$$F(k) = \mathrm{F}_x\{f(x)\} = \int_{-\infty}^{\infty} f(x)e^{-2\pi ikx}dx \tag{4.1}$$

is called the forward Fourier transform, and

$$f(x) = \mathrm{F}_k^{-1}\{F(k)\} = \int_{-\infty}^{\infty} F(k)e^{2\pi ikx}dk \tag{4.2}$$

is called the inverse Fourier transform. Discrete Fourier transform (DFT) is a specific kind of Fourier transform that requires the input function be discrete, which means its non-zero values have a finite duration. Mathematically, forward and inverse DFTs are defined as

$$X(k) = DFT\{x(n)\} = \sum_{n=0}^{N-1} x(n)e^{-j2\pi nk/N} \tag{4.3}$$

$$x(n) = DFT^{-1}\{X(k)\} = \frac{1}{N}\sum_{k=0}^{N-1} X(k)e^{j2\pi nk/N} \tag{4.4}$$

It is known that DFT only have frequency localization, and its basic function, the sinusoids are infinitely long in time domain.

In comparison, wavelet transform is the representation of a function by an orthogonal set called ‘wavelets’. It is a form of time-frequency representation for the original function. Wavelets have finite length in time domain and can be designed to have different frequency localization. A concept diagram to compare time-frequency representation between FT and WT is given in Fig.4.1.

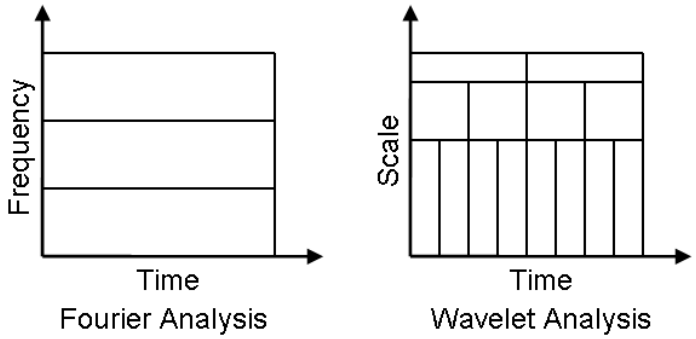

Fig.4.1 Time-Frequency representation of Fourier transform and wavelet transform.

Denoting the wavelet basis as $\varphi_{a,b}(t)$, forward and inverse WTs are defined as

$$W_f(a,b) = WT\{x(t)\} = \int_{-\infty}^{\infty} x(t)\varphi_{a,b}(t)dt \tag{4.5}$$

$$x(t) = WT^{-1}\{W_f(a,b)\} = \frac{1}{C}\int_0^{\infty}\int_{-\infty}^{\infty} W_f(a,b)\varphi_{a,b}(t)db\frac{da}{a^2} \tag{4.6}$$

where $\varphi_{a,b}(t) = \frac{1}{\sqrt{a}}\varphi(\frac{t-b}{a})$, and $C = \int_{-\infty}^{\infty}\frac{|\varphi(\omega)|^2}{\omega}d\omega < \infty$.

In order to best understand wavelet and wavelet transform, we start by defining the scaling function and its time shift set given by [85]

$$\varphi_k(t) = \varphi(t-k), \quad k \in Z, \quad \varphi \in L^2 \tag{4.7}$$

where Z is the set of all integers, and $L^2(R)$ is the vector space of square integrable function. v_0 is a space spanned by these scaling functions that defined as

$$v_0 = \overline{\underset{k}{Span}\{\varphi_k(t)\}}, \qquad k \in Z \tag{4.8}$$

The overbar means closure, namely

$$f(t) = \sum_{k=-\infty}^{\infty} a_k\varphi_k(t), \quad f(t) \in v_0 \tag{4.9}$$

By changing the time scale of the scaling functions, one can increase the size of the subspace, for example, from v_0 to v_j by a two-dimensional parameterization (time and scale) of scaling function $\varphi(t)$

$$\varphi_{j,k}(t) = 2^{j/2}\varphi(2^j t - k) \quad , \quad j,k \in Z \tag{4.10}$$

The expanded subspace v_j is spanned by the new function as

$$v_j = \overline{\underset{k}{Span}\{\varphi_k(2^j t)\}} = \overline{\underset{k}{Span}\{\varphi_{j,k}(t)\}} \tag{4.11}$$

for all $k \in Z$. In this expanded subspace, if $f(t) \in v_j$, it can be expressed as

$$f(t) = \sum_{k=-\infty}^{\infty} a_k \varphi(2^j t + k) \tag{4.12}$$

For $j > 0$ the span is larger since $\varphi_{j,k}(t)$ has finer scale and thus can represent finer detail, and vice versa for $j < 0$. This change of scale can be considered as a change of resolution. Wavelet satisfies a so-called multiresolution formulation requirement [82-85,85] which is designed to represent signals where a single event is decomposed into finer and finer detail.

The basic requirement of multiresoultion analysis (MRA) has the form given by

$$... \subset v_{-2} \subset v_{-1} \subset v_0 \subset v_1 \subset v_2 \subset ... \subset L^2 \tag{4.13}$$

with $v_{-\infty} = \{0\}$ and $v_{\infty} = L^2$, which means a space containing higher resolution will also contain those of lower resolution. Therefore if $f(t) \in v_j$, then $f(2t) \in v_{j+1}$. The nesting of v_j (spans of $\varphi(2^j t - k)$) can be achieved by requiring that $\varphi(t) \in v_1$. This means that if $\varphi(t)$ is in v_0 it's also in v_1 (spans of $\varphi(2t)$). Namely, $\varphi(t)$ can be expressed by a weighted sum of time-shifted $\varphi(2t)$ as

$$\varphi(t) = \sum_{n=-\infty}^{\infty} h(n)\sqrt{2}\varphi(2t - n), \ n \in Z \tag{4.14}$$

where $h(n)$ is a sequence of real or complex numbers called the scaling function coefficients (or scaling filter).

Since v_{j+1} is an expanded space of v_j, we define a new set of spaces w_j as the orthogonal complement of v_j in v_{j+1}, that is

$$v_{j+1} = v_j \oplus w_j, \quad j \in Z \tag{4.15}$$

It follows from Eq. (4.15) that

$$v_{j+1} = v_0 \oplus w_0 \oplus w_1 \oplus ... \oplus w_j \tag{4.16}$$

which is shown in Fig.4.2. It follows that

$$L^2 = v_0 \oplus w_0 \oplus w_1 \oplus \ldots \tag{4.17}$$

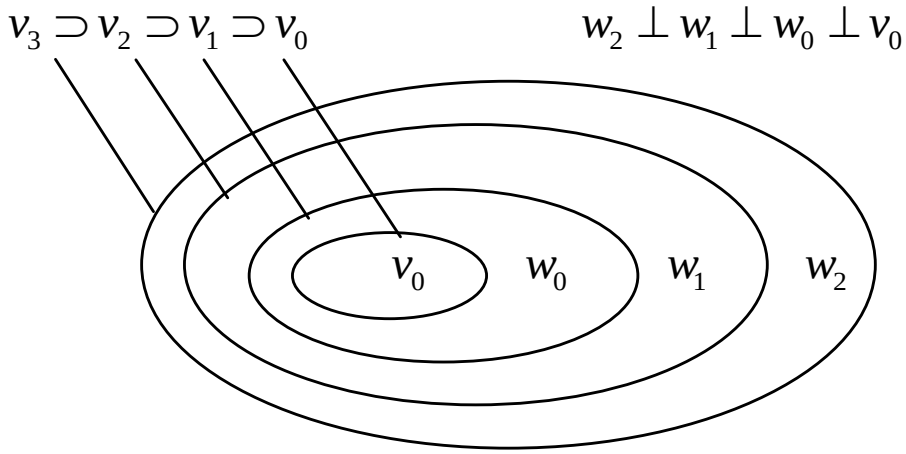

Fig.4.2 Scaling function and wavelet vector spaces.

Now we will define the wavelet function $\psi(t)$. Similarly to the scaling space v_0, let w_0 be spanned by a wavelet function $\psi_k(t)$, and for the expanded space w_j spanned by $\psi_{j,k}(t)$ using expressions equivalent to Eq. (4.8)-(4.11). Since w_j is orthogonal to v_j, orthogonality between scaling function $\psi(t)$ and $\varphi(t)$ is required, which means

$$\left\langle \varphi_{j,k}(t), \psi_{j,k}(t) \right\rangle = \int_{-\infty}^{\infty} \varphi_{j,k}(t)\psi_{j,l}(t)dt = 0 \tag{4.18}$$

Because these wavelets are in the space spanned by the next finer scaling function, or $w_0 \in v_1$, similar to the scaling function $\varphi(t)$, $\psi(t)$ can also be expressed by a weighted sum of time-shifted $\varphi(2t)$ as

$$\psi(t) = \sum_{n=-\infty}^{\infty} g(n)\sqrt{2}\varphi(2t-n), \ n \in Z \tag{4.19}$$

where $g(n)$ is called the wavelet function coefficients (or wavelet filter). The relationship between these two coefficients are restricted by the orthogonality condition Eq. (4.15), given by

$$g(n) = (-1)^n h(1-n) \tag{4.20}$$

If $h(n)$ has a finite even length N,

$$g(n) = (-1)^n h(N-1-n) \tag{4.21}$$

In addition, for the wavelet coefficients $g(n)$, an orthonormal perfect reconstruction (PR) requirement usually applies. PR means that in the absence of encoding, quantization and transmission errors, the reconstructed signal can be perfectly reassembled at the receiver, which is critical for transmission system. The orthonormality condition and the perfect reconstruction condition of the orthonormal two bands PR filter are [82]

$$g^T g = 1 \tag{4.22}$$

and

$$\sum_{n=-\infty}^{\infty} g(n)g(n+2k) = \delta(k) \tag{4.23}$$

where g in Eq. (4.22) is the vector form of $g(n)$.

We now use Haar wavelet to explain the wavelet and scaling coefficients. Haar wavelet function $\psi(t)$ is

$$\psi(t) = \begin{cases} 1 & 0 \le t < 1/2, \\ -1 & 1/2 \le t < 1, \\ 0 & otherwise. \end{cases} \tag{4.24}$$

and its scaling function is

$$\phi(t) = \begin{cases} 1 & 0 \le t < 1, \\ 0 & otherwise. \end{cases} \tag{4.25}$$

The filter coefficients of Haar wavelet can be obtained by applying Eqs. (4.14) and (4.19) given by

$$h(n) = \frac{1}{\sqrt{2}}(-1, 1)\ ,\ g(n) = \frac{1}{\sqrt{2}}(1, 1) \tag{4.26}$$

Now we have defined scaling and wavelet function as well as scaling and wavelet coefficients. From the wavelet theory we know that for any arbitrary signal we can expand it into a sum of scaling and wavelet functions, and this process is called wavelet transform (WT). Similarly to the Fourier transform, wavelet transform also has a discrete analogue called discrete wavelet transform (DWT). The discrete wavelet expansion of any signal $f(t) \in L^2(R)$ is given by

$$f(t)=\sum_{k=-\infty}^{\infty} c_{j_0}(k)\varphi_{j_0,k}(t)+\sum_{k=-\infty}^{\infty}\sum_{j=j_0}^{\infty} d_j(k)\psi_{j,k}(t) \tag{4.27}$$

for $j,k\in Z$. Z is the set of all integers, $L^2(R)$ is the vector space of square integrable function, and j_0 is an arbitrary integer. It can be seen that j and k provide the frequency (or scale) and time localization. $c_j(k)$ also known as detail coefficient, and $d_j(k)$ also known as approximation coefficient in the wavelet expansion (forward DWT of signal $f(t)$), which can be obtained from the following inner products

$$c_j(k)=\left\langle f(t),\varphi_{j,k}(t)\right\rangle=\int_{-\infty}^{\infty} f(t)\varphi_{j,k}(t)dt \tag{4.28}$$

$$d_j(k)=\left\langle f(t),\psi_{j,k}(t)\right\rangle=\int_{-\infty}^{\infty} f(t)\psi_{j,k}(t)dt \tag{4.29}$$

Combine Eqs. (4.14) and (4.28), (4.19) and (4.29), following relationship can be deduced [85]

$$c_j(k)=\sum_{m=-\infty}^{\infty} h(m-2k)c_{j+1}(m) \tag{4.30}$$

$$d_j(k)=\sum_{m=-\infty}^{\infty} g(m-2k)c_{j+1}(m) \tag{4.31}$$

Using Eq. (4.30) and (4.31), the DWT of a signal $f(t)$ can be efficiently computed using discrete-time filter banks that are either infinite-time response (IIR) or finite time response (FIR) filters *g* and *h* [81-89]. In practical applications and for computational efficiency, one prefers a wavelet with compact support where the scaling function $\varphi(t)$ and wavelet function $\psi(t)$ can be considered finite in length. Detailed filter bank implementation of the DWT algorithm is as follows: To start the DWT, one needs to get the detail coefficients $c_j(k)$ at high resolution and for high enough scale the scaling function, $\varphi_j(t)$ acts as delta function with the inner product as a sampling of $f(t)$ according to Eq. (4.28). Therefore the samples of $f(t)$ are passed through a low-pass filter (scaling filter) *g* and high-pass filter (wavelet filter) *h* simultaneously, resulting in a convolution of the two. The two filters are related to each other and they are known as a quadrature mirror filter (QMF); the filter outputs

are then down-sampled by 2 since half the frequencies of the signal have been removed, half of the samples can be discarded according to Nyquist's theory; the outputs will give the detail coefficients $c_j(k)$ (from the high-pass filter h) and approximation coefficients $d_j(k)$ (from the low-pass filter g) as we show from Eqs. (4.30) and (4.31); this decomposition process can be repeated to further increase the frequency resolution, but only the approximation coefficients are decomposed. The above implementation of algorithm can be represented as a lower-half binary tree structure as shown in Fig.4.3. It is important to notice that for a 2^n-point DFT, the bandwidth is uniformly divided; however for an n-level DWT, the bandwidth is logarithmically divided since only half of the spectrum - the low pass filter outputs are decomposed at each level. An explicit comparison of the bandwidth division feature between DFT and DWT is shown in Fig.4.4.

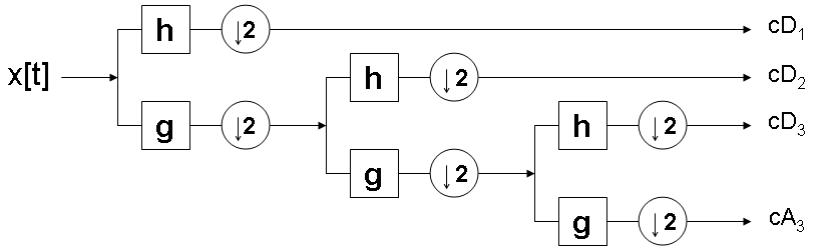

Fig.4.3 Block diagram of a discrete wavelet transform (DWT) with 3 level filter banks.↓2 stands for two times down-sampling. f(ti) at the input is the sampled input signal f(t).

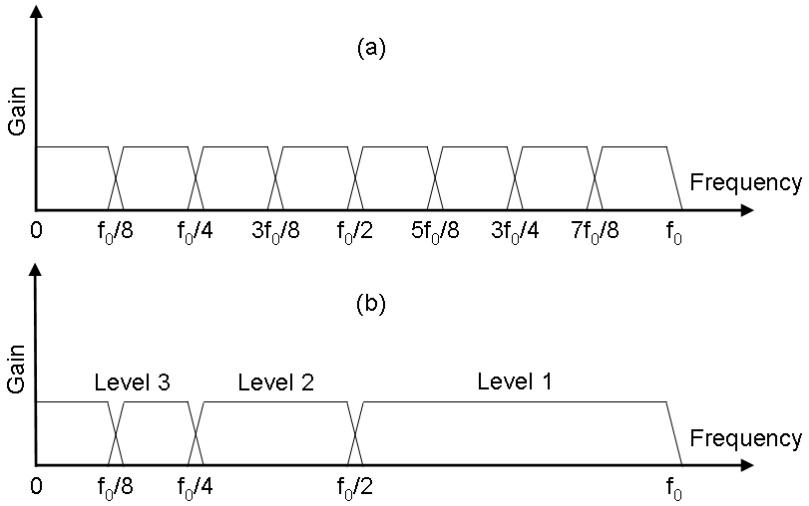

Fig.4.4 Frequency domain responses of Discrete Fourier transform(DFT) and discrete wavelet transform(DWT) (a) DFT with uniform division of bandwidth. (b) DWT with dyadic division of bandwidth.

4.2.2 Wavelet packet transform (WPT)

The logarithmic division of the bandwidth in the wavelet transform is not well suited for multicarrier communication such as OFDM systems [90]. Wavelet packet transforms are generalization of wavelet transforms where the orthogonal basis functions are 'wavelet packets' [80-81]. As we have previously discussed, in DWT process, each level is calculated by passing only the previous approximation coefficients $d_j(k)$ through high and low pass filters. A discrete wavelet packet transform (DWPT), also called wavelet packet decomposition (WPD), on the other hand, decompose both the detail and approximation coefficients at each level. Therefore DWPTs have more flexibility in tree structure where the bandwidth can be arbitrarily (or uniformly, which is more commonly used) divided according to tree pruning [80-81]. In order to explain the concept DWPT, first we define a set of wavelet packet functions $\zeta_{j,k}^n(t)$ as [92]

$$\zeta_{j,k}^n(t) = 2^{j/2}\zeta^n(2^j t - k) \quad j,k \in Z \tag{4.32}$$

where ζ^n (no subscripts) is to have $j = k = 0$. The extra index $n = 0,1,...$ is called the modulation parameter or oscillation parameter. The first two wavelet packet functions are known as the usual scaling function and wavelet function

$$\zeta^0(t) = \varphi(t), \quad \zeta^1(t) = \psi(t) \tag{4.33}$$

Wavelet packet functions $\zeta^n(t)$ for $n = 2,\ 3,\ ...$ are defined via the recursive relationships

$$\zeta^{2n}(t) = \sum_{k=-\infty}^{\infty} h(k)\sqrt{2}\zeta^n(2t - k) \tag{4.34}$$

and

$$\zeta^{2n+1}(t) = \sum_{k=-\infty}^{\infty} g(k)\sqrt{2}\zeta^n(2t - k) \tag{4.35}$$

We show in Section 4.2.1 that $v_j = \overline{\underset{k}{Span}\{\varphi_{j,k}(t)\}}$. Another possible orthonomal basis for v_j is the set of wavelet packet functions

$$v_j = \overline{\underset{k}{Span}\{\zeta_{0,k}^n(t)\}}, \quad 0 \le n < 2^j, \quad k \in Z \tag{4.36}$$

If we also require w_j as the orthogonal complement of v_j in v_{j+1}, as in Eq. (4.15), that is $v_{j+1} = v_j \oplus w_j$, $j \in Z$, it can be seen that an orthonomal basis for the complementary space w_j is

$$w_j = \overline{\underset{k}{Span}\{\zeta_{0,k}^n(t)\}}, \quad 2^j \le n < 2^{j+1}, \quad k \in Z \tag{4.37}$$

The orthonormal bases $\{\varphi_{j,k}(t), \quad k \in Z\}$ and $\{\psi_{j,k}(t), \quad k \in Z\}$ in DWT we already familiar with can be re-written in terms of this new notion as $\{\zeta_{j,k}^0(t), \quad k \in Z\}$ for v_j and $\{\zeta_{j,k}^1(t), \quad k \in Z\}$ for w_j.

There are many other bases that can be used resulted from the appropriate selection of combination of the indices of n, j. Precisely speaking, a basis for $L^2(R)$, $\zeta_{j_i,k}^{n_i}(t)$ can be formed by allowing k to range over Z, and choosing an index set $I = \{(n_0, j_0), (n_1, j_1)..., (n_i, j_i), ...\}$ so that the intervals $[2^{j_i} n_i, 2^{j_i}(n_i + 1)]$ are disjoint and cover the entire interval $[0, \infty)$, which means

$$\bigcup_{i=0}^{\infty} [2^{j_i} n_i, 2^{j_i}(n_i + 1)] = [0, \infty) \tag{4.38}$$

This equation can be thought as equivalent to covering the entire time-frequency plane with windows of various shapes. It can be easily seen that wavelet basis forms such a cover. However, for wavelet packet, the collection of all wavelet packet functions $\{\zeta_{j,k}^n, \quad j,k \in Z, n = 0,1,...\}$ contains too many elements to form an orthonormal basis. We need to carefully choose a subset of this collection in order to obtain a proper basis. Assuming there is a suitably chosen set of indices denote by I, we can decompose any signal $f(t) \in L^2(R)$ into its wavelet packet components by [92]

$$f(t) = \sum_{(n,j) \in I} \sum_{k \in Z} c_j^n(k) \zeta_{j,k}^n(t) \tag{4.39}$$

the coefficients can be computed via

$$c_j^n(k) = \int_{-\infty}^{\infty} f(t) \omega_{j,k}^n(t) dt \tag{4.40}$$

Combining with Eqs. (4.30) and (4.31), we can obtain the following relationship

$$c_j^{2n}(k) = \sum_{m=-\infty}^{\infty} h(m-2k)c_{j+1}^n(m) \tag{4.41}$$

$$c_j^{2n+1}(k) = \sum_{m=-\infty}^{\infty} g(m-2k)c_{j+1}^n(m) \tag{4.42}$$

and this is equivalent to a *j*-level full wavelet packet decomposition (full binary tree structure).

For OFDM systems that require uniformly division of bandwidth, a WPT with a full binary tree structure is utilized (see Fig.4.5). Detailed implementation of the DWPT algorithm is given as follows: the *n*-level DWPT process has a binary tree structure consisting of 2^m 'high' and 'low' FIR filters (*h* and *g*) at level m. Similar to DWT, the 'root' furthest to the left is the sampled time-domain signal. It is first split into two equal sequences, then convoluted with the decomposition high-pass filter *h* (or low pass filter *g*), followed by 2 times down-sampling. The high- and low-pass branches are the new inputs for the next level. After n levels of such iterative processes, the 'leaves' furthest to the right are the decomposed wavelet packet coefficients.

The inverse discrete wavelet packet transform (IDWPT), also called the wavelet packet reconstruction (WPR), has a ‘mirror image’ process of the DWPT with a similar tree structure, where the dataflow are from 'leaves' to the 'root', as shown in Fig.4.6. The 'leaves' furthest to the left are the packet coefficients, followed by convolution with reconstruction high-pass filter *h′* (or low-pass filter *g′*). The high- and low-pass branches are then summed up generating a new sequence. After n levels of such iterative processes, the 'root' furthest to the right gives the time-domain transformed data. For data transmission, DWPT and IDWPT must be used as a pair with the reconstruction and decomposition filters having the following relationship [82]

$$h'(n) = h(N-1-n) \tag{4.43}$$

$$g'(n) = g(N-1-n) \tag{4.44}$$

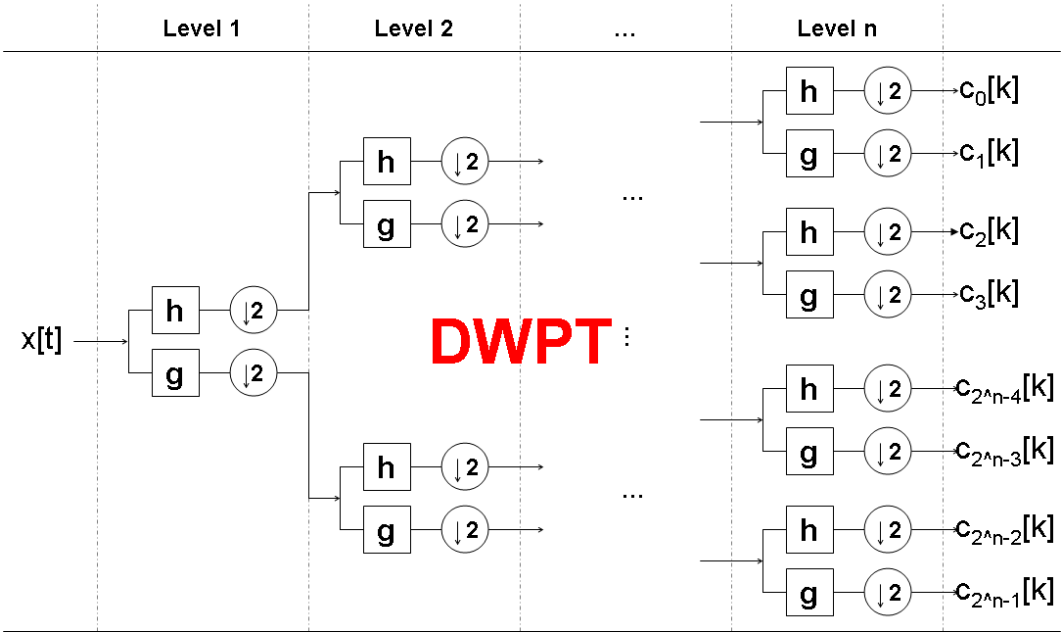

Fig.4.5 Implementation of discrete wavelet packet transform (DWPT). ↓2 stands for 2 times down-sampling.

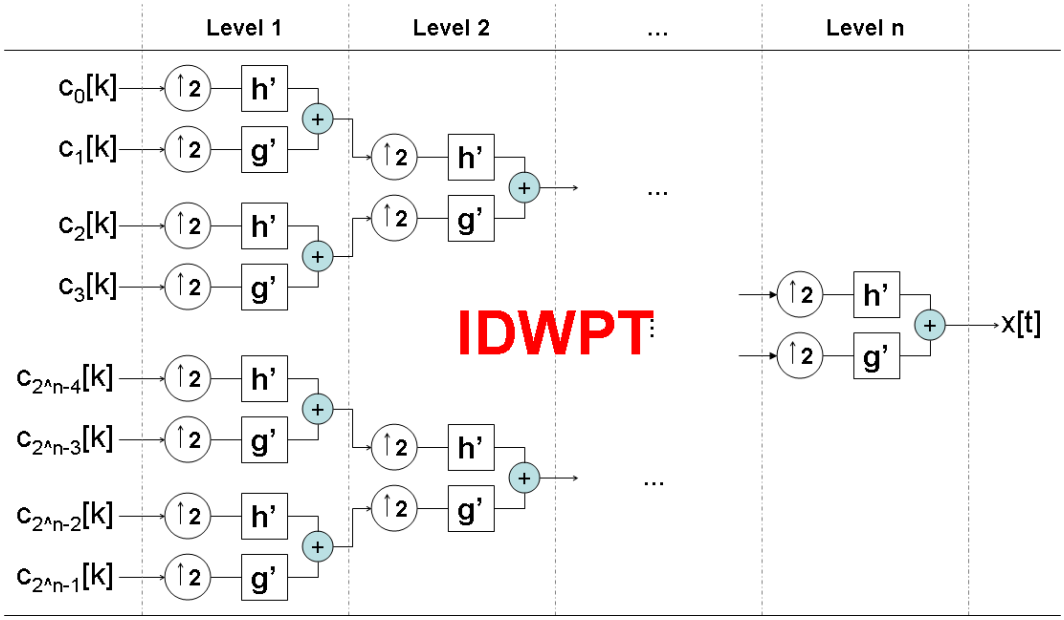

Fig.4.6 Implementation of inverse discrete wavelet packet transform (IDWPT). ↑2 stands for 2 times up-sampling.

Different from Fourier transform, the basic functions of wavelet or wavelet packet transform are not unique. There exist many different types of wavelet families, such as Haar, Daubechies, Coieflet and Johnston wavelet [87-89], etc. Besides, new wavelets can as well be designed according to specific requirements.

4.2.3 Commonly used wavelets

Haar wavelet, the first known wavelet is proposed in 1909 by Alfred Haar [87]. It is also the simplest possible wavelet. The Haar wavelet's mother wavelet function $\psi(t)$ is

$$\psi(t)=\begin{cases}1 & 0\le t<1/2,\\ -1 & 1/2\le t<1,\\ 0 & otherwise.\end{cases} \tag{4.45}$$

and its scaling function $\varphi(t)$ is

$$\phi(t)=\begin{cases}1 & 0\le t<1,\\ 0 & otherwise.\end{cases} \tag{4.46}$$

For a PR-QMF filter bank implementation, Haar wavelet can be computed by making the decomposition high- and low-pass filter coefficients to be

$$h(n)=\frac{1}{\sqrt{2}}[-1 \quad 1] \quad , \quad g(n)=\frac{1}{\sqrt{2}}[1 \quad 1] \tag{4.47}$$

Fig.4.7 shows the coefficients of a Haar wavelet.

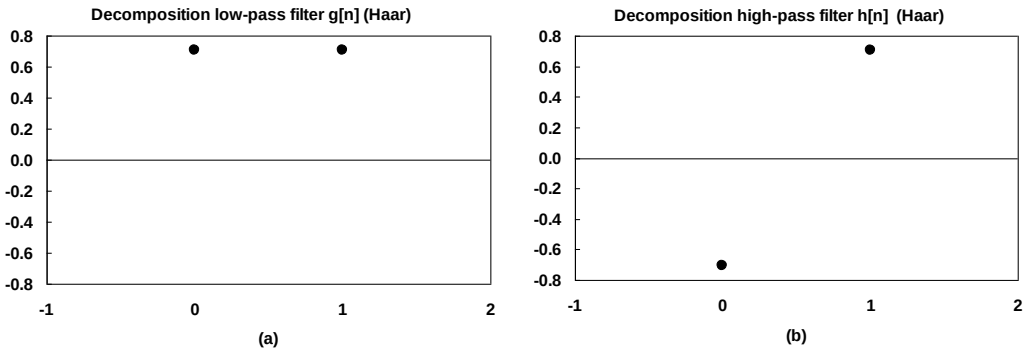

Fig.4.7 Filter coefficients of Haar wavelet (a) low-pass filter (b) high-pass filter.

Ingrid Daubechies has invented a kind of so called compactly supported orthonormal wavelets - the Daubechies family [88]. The names of the Daubechies family wavelets are usually written as dbN, where N is the order that refers to the number of vanishing moments, and db the 'surname' of the wavelet. The db1 wavelet is the same as Haar wavelet. Fig.4.8 shows the coefficients of a db10 wavelet.

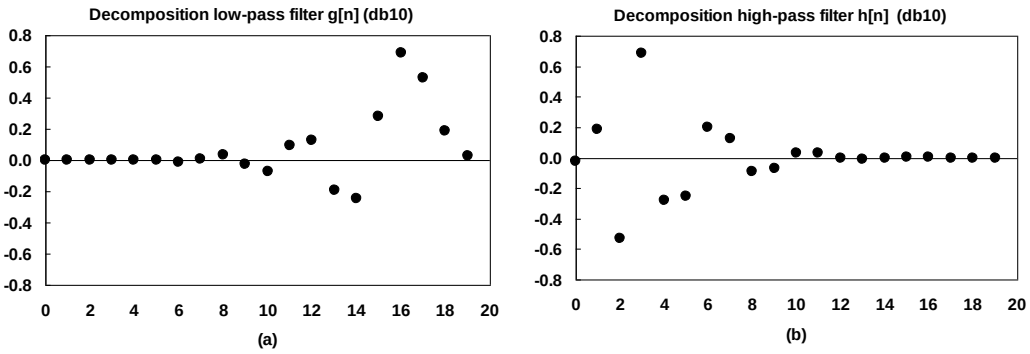

Fig.4.8 Filter coefficients of db10 wavelet (a) low-pass filter (b) high-pass filter.

Coiflets were built by I. Daubechies at the request of R. Coifman [88]. The names of the Coiflet family wavelets are usually written as coifN, where similar as the Daubechies family dbN, N is the number of vanishing moments for both the wavelet and scaling functions of the coifN wavelet. The coifN's mother wavelet function ψ and scaling function ϕ are much more symmetrical than the dbNs. Fig.4.9 shows the coefficients of a typical coif5 wavelet vs. the order of taps.

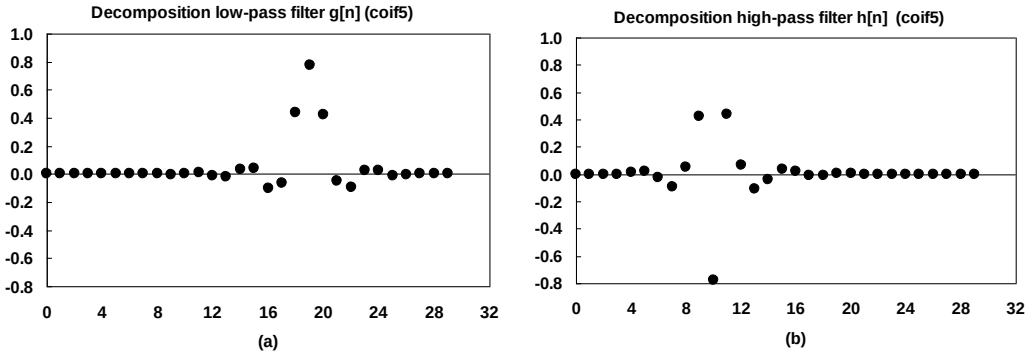

Fig.4.9 Filter coefficients of coif5 wavelet (a) low-pass filter (b) high-pass filter.

Johnston Wavelets were proposed in 1980 by J. D. Johnston on his paper "A Filter Family Designed for Use in Quadrature Mirror Filter Banks". These filters were designed using a Hooke and Jeaves optimization routine with a Hanning window prototype. Using the discussed procedure, one can obtain QMF banks with as little as ±0.0015 dB ripple in their frequency response. Different from the above three wavelet families, Johnston wavelet with same number of taps can have different variations. For easy understanding, Johnston wavelet is indentified by johN(V) where N denote the order that equals to the length of the associated QMF. V denote the constraint group used in the design, exactly the same as in Johnston's paper [89]. Fig.4.10 shows the coefficients of joh64(E) wavelet vs. the order of taps.

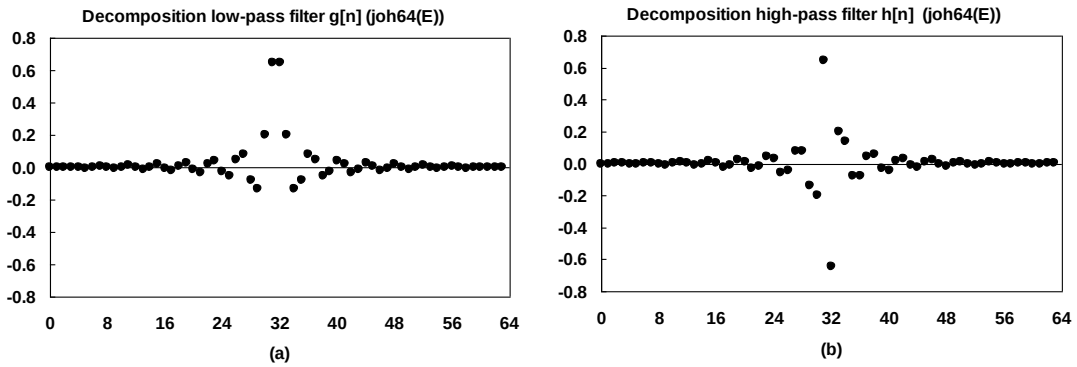

Fig.4.10 Filter coefficients of joh64(E) wavelet (a) low-pass filter (b) high-pass filter.

4.2.4 System configuration of WPT-OFDM

In order to best understand the principle of WPT-OFDM, we first recall the principle of conventional FT-OFDM. In a FT-OFDM system with coherent detection (CO-OFDM) [18], at the transmitter, block based sampled data are mapped onto complex domain through quadrature phase shift keying (QPSK) or QAM modulation, each corresponding to the orthogonal frequency domain subcarriers and transformed into time domain RF signal though IDFT, then up-converted to optical domain for fibre transmission. At the receiver, the coherent received optical signal is down-converted to RF domain, then transformed back to block data through DFT and ready for equalization and decision. As we have previously discussed, wavelet packet transform has similar time-frequency representation that can also provide orthogonality between OFDM subcarriers as Fourier transform, therefore a simple idea is to use DWPT to replace DFT in the system setup and we will get WP(F)T-OFDM. A conceptual block diagram of WPT-OFDM is given in Fig.4.11. Similarly to the FT-OFDM, in WPT-OFDM, IDWPT are used at the transmitter that reconstructs the time domain signal from the one-on-one mapped OFDM packets (subcarriers for Fourier transform). DWPT are used at the receiver to decompose the time domain signal into different wavelet packets by means of successive low-pass and high-pass filtering in the time domain. The prominent difference between IDWPT and IDFT is that IDWPT is not block based. For FT-OFDM, sinusoids are infinitely long in time domain, so in order to adapt compact support a windowing has to be applied, which will lead to out-of-band radiation and performance degradation because of inter-symbol interference (ISI). An efficient technique to mitigate this degradation is to introduce CP - a partition duplicate of previous signal which can be appended to each OFDM block. Properly designed CP will significantly increase the tolerance to CD. However for

WPT-OFDM, its basic function 'wavelets' are finite in time. The inter-symbol orthogonality in wavelet transform is maintained due to the shift orthogonal property of the waveforms. In wavelet transform, symbols are overlapped in time domain. This feature increases the symbol duration which provide CD tolerance, but also prevents the availability of CP.

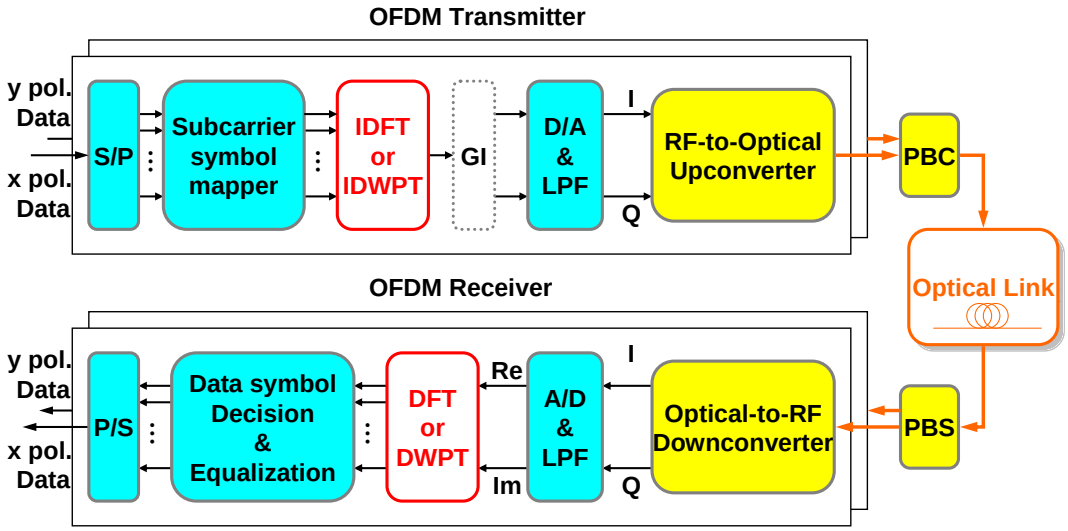

Fig.4.11 Conceptual diagram of WP(F)T-OFDM system setup. For WPT-OFDM, IDWPT and DWPT are used as a pair, and for FT-OFDM, IDFT and DFT are used as a pair. PBC/PBS: Polarization Beam Combiner /Splitter, LPF: Low Pass Filter. GI: Guard Interval, arbitrary length of CP can be inserted for FT-OFDM but not available for WPT-OFDM

Wavelet transform is generally defined in the real domain but can be also defined in the complex domain, solely depending of the scaling and dilatation filter coefficients. Real-valued wavelets are predominantly designed to process real signals such as patterns and images. However for the fibre optic channel, whether the input signal is modulated by real or complex signal, the up-conversion to the optical domain will inevitably generate two spectral sidebands - one positive and the other negative. Fig 4.2 and 4.3 shows the time domain and frequency domain representation of Coiflet5 (coif5) wavelet [88], a typical wavelet with positive and negative sidebands in spectrum.

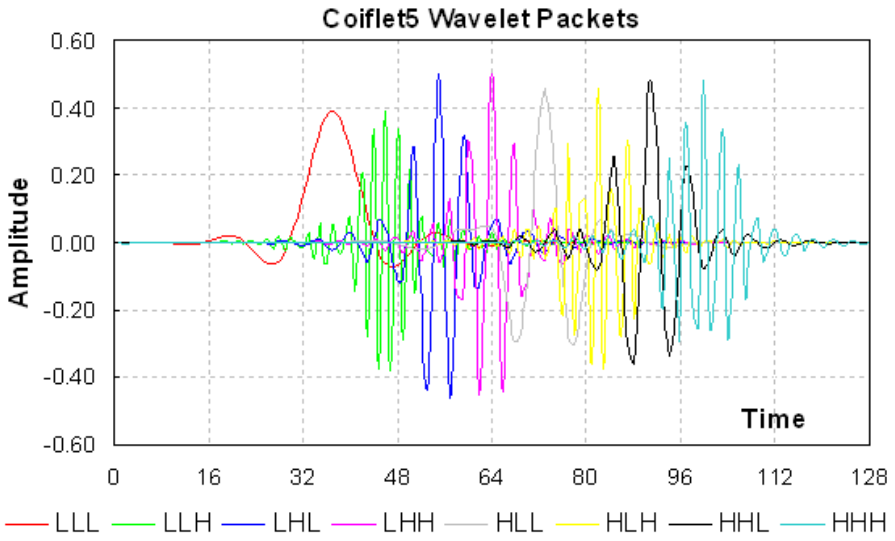

Fig.4.12 Time domain representation of 8 coif5 wavelet packets, constructed using 3-level IDWPT.

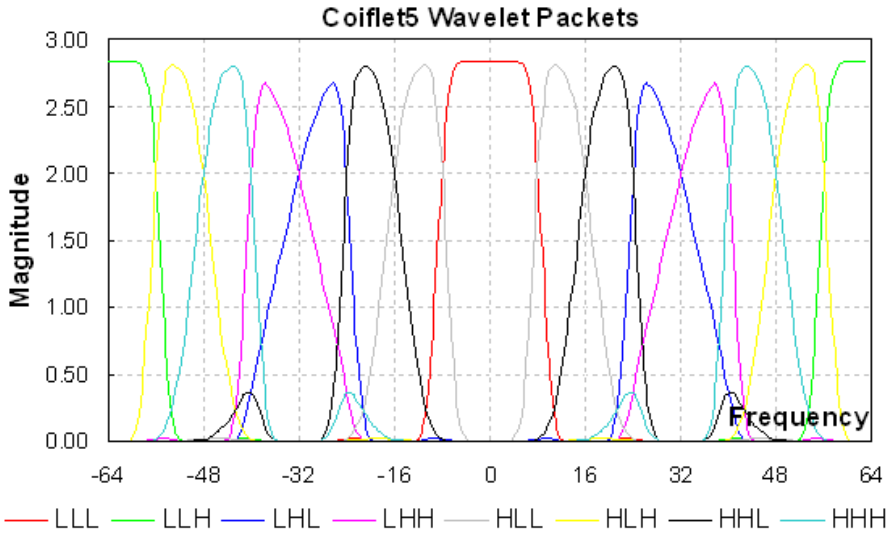

Fig.4.13 Frequency domain representation (Spectrum) of 8 coif5 wavelet packets, constructed using 3-level IDWPT.

In order to evaluate the PMD impact on WPT-OFDM systems and compare with FT-OFDM counterpart, we use the model of CO-OFDM transmission in a 2×2 multiple-input multiple-output (MIMO) representation [39, 58]. The received OFDM symbol in a form of Jones vector for the *i*-th OFDM symbol on the *k*-th subcarrier can be written as [58]

$$\mathbf{r}(k,i) = e^{j\phi_i} e^{j\Phi_D(f_k)} \mathbf{T}(k)\mathbf{c}(k,i) + \mathbf{n}(k,i) \tag{4.48}$$

where $\mathbf{c}(k,i)$ is the transmitted symbol as a Jones vector and $\mathbf{n}(k,i)$ is the corresponding received noise vector. ϕ_i is the OFDM symbol dependent phase noise. Phase dispersion due to fibre chromatic dispersion is given by

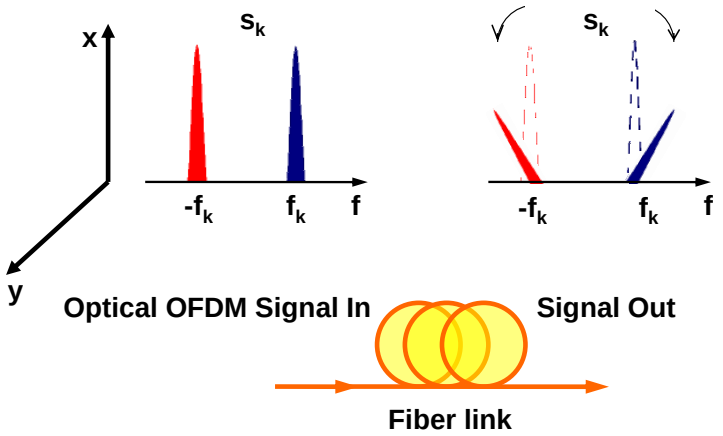

Fig.4.14 A conceptual illustration of the PMD impact on *k*-th wavelet packet in WPT-OFDM systems for x polarization component.

$$\Phi_D(f_k) = \pi c D f_k^2 / f_{LD}^2 \tag{4.49}$$

For simplicity, we use the commonly-used first-order PMD approach for which the Jones matrix for the fibre link on the *k*-th subcarrier can be modelled as

$$T(k) = M^{-1}\begin{bmatrix} e^{-j\pi f_k \tau} & 0 \\ 0 & e^{j\pi f_k \tau} \end{bmatrix} M \tag{4.50}$$

$$M = \begin{bmatrix} \cos(\theta/2)e^{-j\psi/2} & -\sin(\theta/2)e^{-j\psi/2} \\ \sin(\theta/2)e^{j\psi/2} & \cos(\theta/2)e^{j\psi/2} \end{bmatrix} \tag{4.51}$$

where τ is the DGD of the link, θ and ψ are the polar and azimuth angle of the principle state of polarization (PSP) respectively, and f_k is the subcarrier frequency. In FT-OFDM systems, the individual subcarrier, as the orthogonal basis of the Fourier transform is single-sideband by nature, $\Phi_D(f_k)$ in Eq. (4.49) and $T(k)$ in Eq. (4.50) can be conveniently estimated and compensated. In contrast, in WPT-OFDM systems, the modulated signals are double-sideband by nature (see Fig.4.13). By applying theory similar to Eq. (4.48)-(4.51), chromatic dispersion influence on WT-OFDM is benign because the two sidebands experience equal phase dispersion $\Phi_D(f_k) = \Phi_D(-f_k)$. However PMD does not hold such phase symmetry. The Jones matrixes for the positive and negative sidebands do not equal, i.e., $T(k) \neq T(-k)$.

Upon reception where the two sidebands need to be recombined and projected onto real wavelet basis, the two sidebands experience two different dispersions, and the addition of the two does not reproduce the real-wavelet basis, resulting in violation of the orthogonality and therefore inter-packet-interference. This is illustrated in Fig.4.14 where the conceptual figure of PMD impact on OFDM subcarriers in one polarization launch is shown. We conclude that WPT-OFDM will be more susceptible to PMD than conventional FT-OFDM.

A similar one-tap equalizer [39, 58， 132-134] is utilized to equalize both CD and PMD impact in WPT-OFDM. The channel matrix H is estimated by sending OFDM symbols using alternative polarization launch. Mathematically, the transmitter information symbol of the two polarizations and fibre response in the forms of Jones vector are given by

$$c = \begin{pmatrix} c_1 \\ c_2 \end{pmatrix}, \quad H = \begin{pmatrix} h_{11} & h_{12} \\ h_{21} & h_{22} \end{pmatrix} \tag{4.52}$$

The received symbol is given by

$$c' = \begin{pmatrix} c_1 \\ c_2 \end{pmatrix} = H \cdot c \tag{4.53}$$

Using odd training symbols, the associated channel estimation can be expressed as

$$\begin{bmatrix} c_1 \\ c_2 \end{bmatrix} = \begin{bmatrix} h_{11} & h_{12} \\ h_{21} & h_{22} \end{bmatrix} = \begin{bmatrix} c_1 \\ 0 \end{bmatrix} \Rightarrow \begin{cases} h_{11} = c_1' / c_1 \\ h_{21} = c_2' / c_1 \end{cases} \tag{4.54}$$

And using even symbols,

$$\begin{bmatrix} c_1 \\ c_2 \end{bmatrix} = \begin{bmatrix} h_{11} & h_{12} \\ h_{21} & h_{22} \end{bmatrix} = \begin{bmatrix} 0 \\ c_2 \end{bmatrix} \Rightarrow \begin{cases} h_{12} = c_1' / c_2 \\ h_{22} = c_2' / c_2 \end{cases} \tag{4.55}$$

4.2.5 Simulation and results

We have carried out numerical simulation to compare the transmission performance of dual-polarization WPT-OFDM systems with FT-OFDM systems. The simulation parameters are shown in Table 4.1: Dual-polarization OFDM data rate at 112 Gb/s, the number of subcarriers varying from 64 to 256. The number of symbols in FT-OFDM is 256 and for WPT-OFDM we maintain the same total length as in FT-OFDM. We have three choices of oversampling, no oversampling, oversampled by

factor of 2, or oversampled by factor of 8. CP is not applied for WPT-OFDM, but for FT-OFDM we have two choices, no CP or 1/8 CP. Wavelets from Haar, Daubechies, Coiflet and Johnston family [87-89] as discussed in Section 4.2.3 are chosen for wavelet transform and compared with Fourier transform.

Table 4.1 Simulation Parameters

Parameters	WPT-OFDM	FT-OFDM	Unit
Bit Rate	112	112	Gbit/s
Bandwidth	28	28 or 31.5	GHz
No. of subcarriers	64~256	64~256	
No. of symbols	Same length as FT-OFDM	256	
Oversampling factor	1, 2 or 8	1, 2 or 8	
CP	0	0 or 1/8	
No. of polarization	2	2	
No. of training symbols	5	5	per pol
OSNR	5~20	5~20	dB
BER threshold	1×10^{-3}	1×10^{-3}	
Fibre length L	0~500	0~500	km
Chromatic dispersion	17	17	ps/nm/km
PMD	0.1 or 1	0.1 or 1	
Wavelet families	Haar, coif1, coif5, db32 and Joh64(E)	N/A	

The signal flow of a typical WPT-OFDM system used in simulation is as shown in Fig.4.11. At the transmitter, the serial PRBS at 56 Gb/s is converted into 64 parallel data pipes, mapped onto the complex plane in QPSK modulation, each corresponding to the wavelet packet coefficient in frequency domain. The wavelet coefficients are converted into serial time-domain wavelet signal IDWPT. The wavelet signal is then up-converted onto an optical carrier with central frequency at 193.1 THz using an ideal optical I/Q modulator. The two 56-Gb/s optical signals are polarization combined into a 112-Gb/s WPT-OFDM signal and launched into the optical fibre.

Fig.4.15 shows the electrical spectrum of WPT-OFDM signal with a bandwidth of 28 GHz. The WPT-OFDM signal is then passed through a fibre with chromatic dispersion and PMD. At the receiver, the WPT-OFDM signal is coherently down-converted to the RF domain, sampled and transformed back from time to frequency domain through DWPT, followed by the channel equalization, symbol decision, and bit-error-ratio (BER) computation. 10 training symbols with alternative polarization launch is sent for channel estimation. A one-tap equalizer is introduced for equalization of CD and PMD at the receiver as described in Section 4.2.4. In all simulation and analysis for the PMD impact, we have assumed that the signal on each polarization is launched 45^{o} with respect to the PSP of the PMD for which we find the worst penalty takes place.

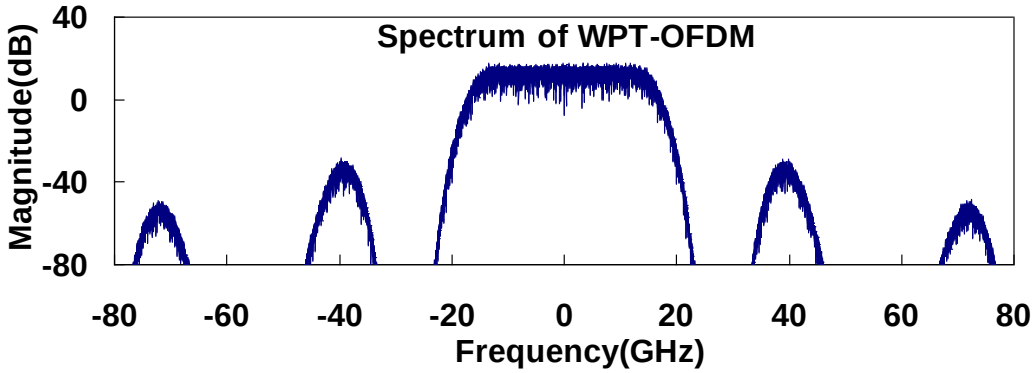

Fig.4.15 Electrical spectrum of simulated 112 Gb/s dual-polarization WPT-OFDM system using db32 wavelet.

Fig.4.16 shows the simulated BER of WPT-OFDM using different wavelets as well as FT-OFDM. For FEC limit at BER of 1×10^{-3} and optical signal-to-noise ratio (OSNR) of 20 dB, Johnston64 (E) wavelet has the longest reach, indicating a remarkable over 5,600ps/nm CD tolerance(~330 km for SSMF with $CD=17\,ps/nm/km$). The naming convention of the wavelet is its family name followed by the order. Fig.4.17 shows the BER performance versus OSNR at 0 and 10 ps of DGD with different wavelets for a 112-Gb/s WPT-OFDM signal. The required OSNR at FEC threshold as a function of DGD for the same set of wavelets are analysed and the results are shown in Fig.4.18. For 1-dB OSNR penalty, the DGD tolerance is about 11, 6, 6, and 5 ps for Haar, Coifilet5, Daubechies32, and Johnston64(E) wavelets, respectively. The performance of OSNR penalty versus DGD for FT-OFDM systems is shown in Fig.4.19, indicating 132 and 80 ps DGD can be tolerated with and without CP respectively. Consequently, the PMD tolerance of

FT-OFDM is more than seven times higher than that of WPT-OFDM. By using sufficiently long CP, the PMD penalty can be greatly alleviated or even eliminated in FT-OFDM systems [39, 58]. We also perform the simulation to study the PMD tolerance dependence on the number of subcarriers for WPT-OFDM and result is presented in Fig.4.20. It can be seen that for WPT-OFDM systems, almost no improvement can be gained by increasing the number of subcarriers. This is because that the double-sideband characteristics of WPT-OFDM spectrum will always adversely affect the PMD performance, irrespective of how finely each wavelet is being partitioned.

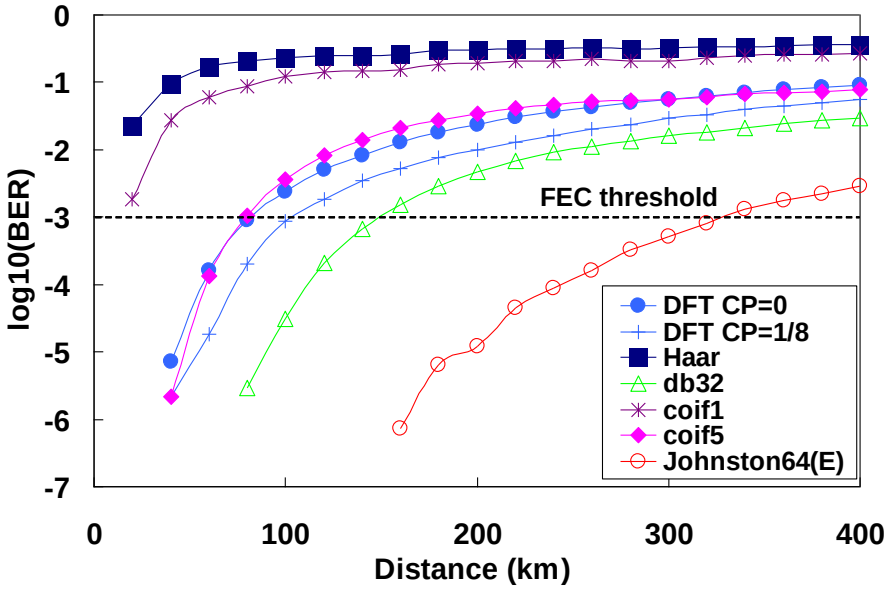

Fig.4.16 BER vs. transmission distance for WPT-OFDM and FT-OFDM. *CD = 17 ps/nm/km*. Wavelets are Haar, Coiflet, Daubechies [88] and Johnston [89] family. Number of subcarriers *Nsc = 64*.

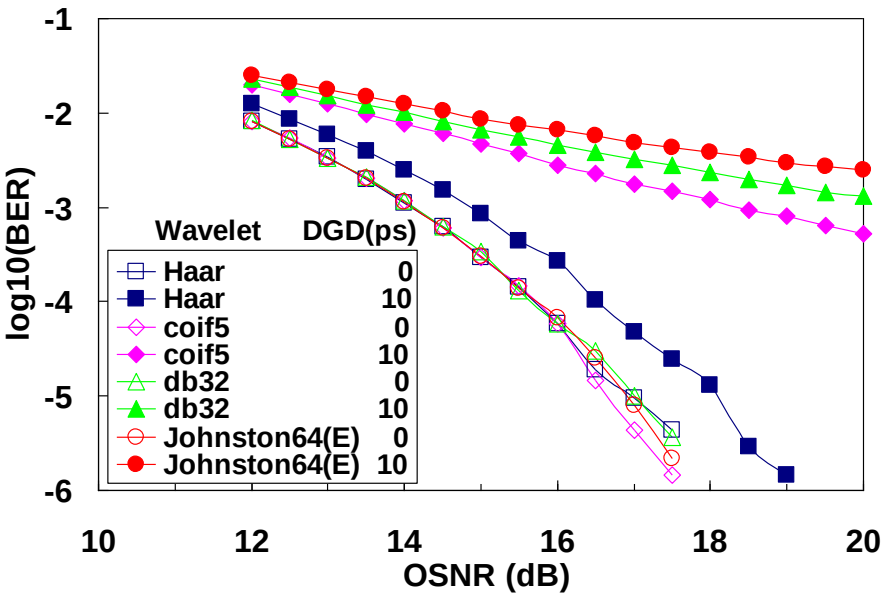

Fig.4.17 BER vs. OSNR for WPT-OFDM without DGD (0ps) and with DGD (10ps). *Nsc = 64*.

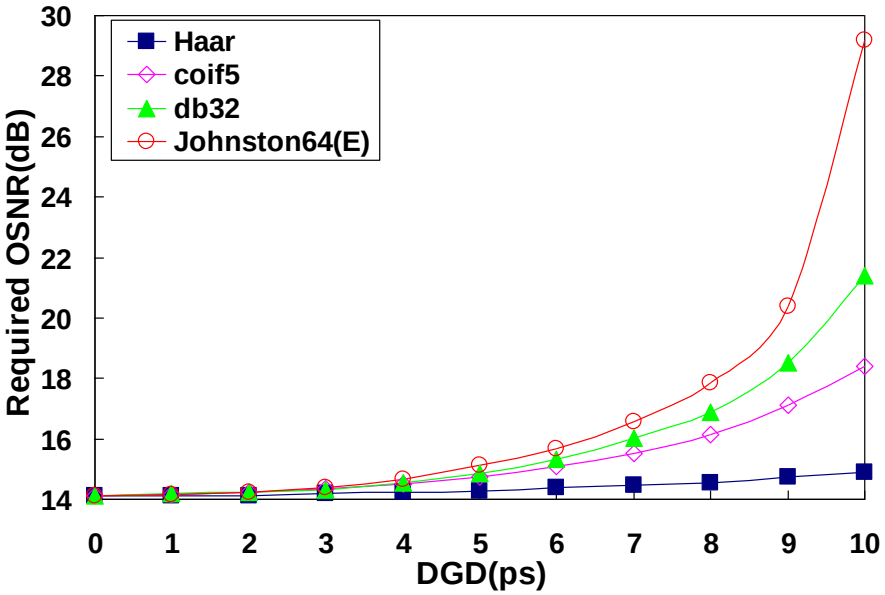

Fig.4.18 Required OSNR at BER=1×10^{-3} vs. DGD for WPT-OFDM. *Nsc = 64*.

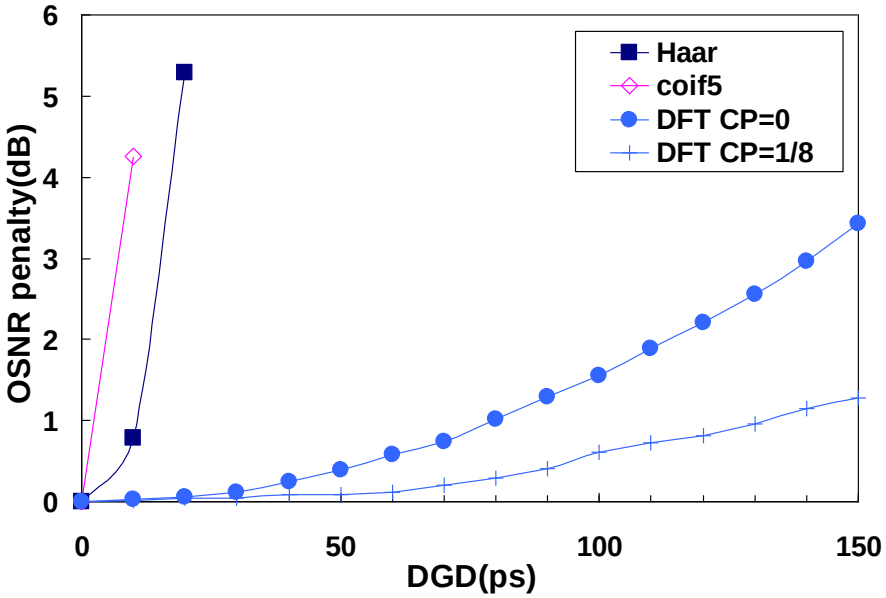

Fig.4.19 OSNR penalty vs. DGD for FT-OFDM without CP and with CP of 1/8.

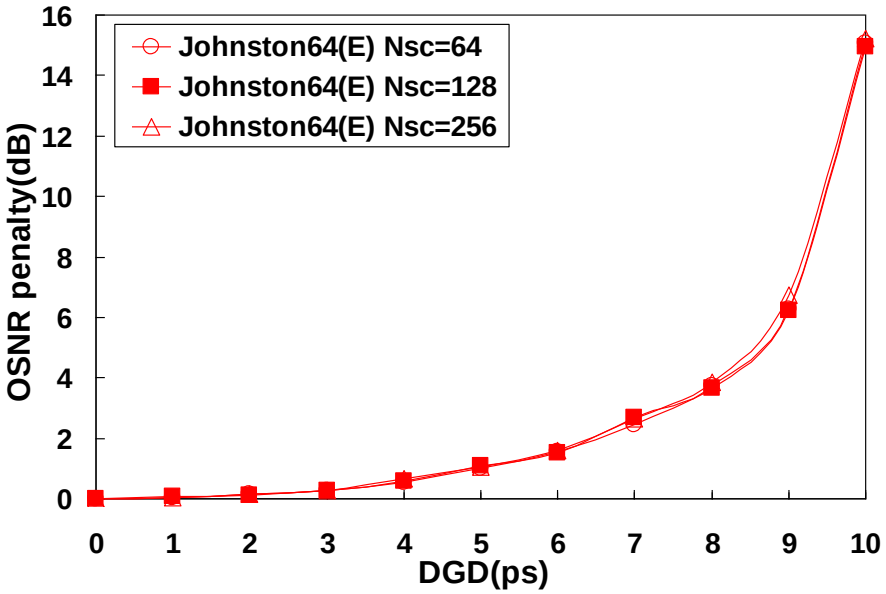

Fig.4.20 OSNR penalty vs. DGD for WPT-OFDM using Johnston wavelet with *Nsc = 64, 128, 256*.

In OFDM systems, nonlinearity performance is correlated to the peak-to-average power ratio (PAPR) of the transmitted RF domain OFDM signal. The complementary cumulative distribution function (CCDF) distributions of PAPR are plotted in Fig.4.21 and Fig.4.22, for the non-oversampled and oversampled scheme. We find out that without oversampling, the differences between WPT-OFDM and FT-OFDM are minimal. Oversampling is usually applied in real OFDM system to avoid aliasing noise. When 8-times oversampling is applied we see that Haar wavelet has the lowest

PAPR. The nonlinearity performance is analysed by the BER at the receiver vs. launch power into the fibre, as shown in Fig.4.23 and Fig.4.24. In this simulation we only focus on the relationship between PAPR and nonlinearity performance, PMD impact on nonlinear transmission performance is ignored (for PMD impact we are more concern about the linear compensation). For a fair comparison we use two different dispersion configurations, one is 100% dispersion compensated and the other 95% compensated. The optical link consists of two spans. In each span we have one 100 km SSMF with *CD = 17ps/nm/km* followed by a 14.94 km (100% comp.) or 14.2 km (95% comp.) DCF with *CD = -113.7778 ps/nm/km*. Power loss due to SSMF and DCF are fully compensated by two EDFAs with noise figure at 6 dB. The launch power into SMF is swept from 4 dBm to 10 dBm to show the performance and nonlinearity limit. We find out that Haar wavelet has the best nonlinearity performance in the full dispersion compensation setup. The nonlinear limit of launch power for a BER of 1×10^{-3} has been increased by ~1.7 dB compared with FT-OFDM (*CP = 0*), and 0.9 dB (*CP = 1/8*).

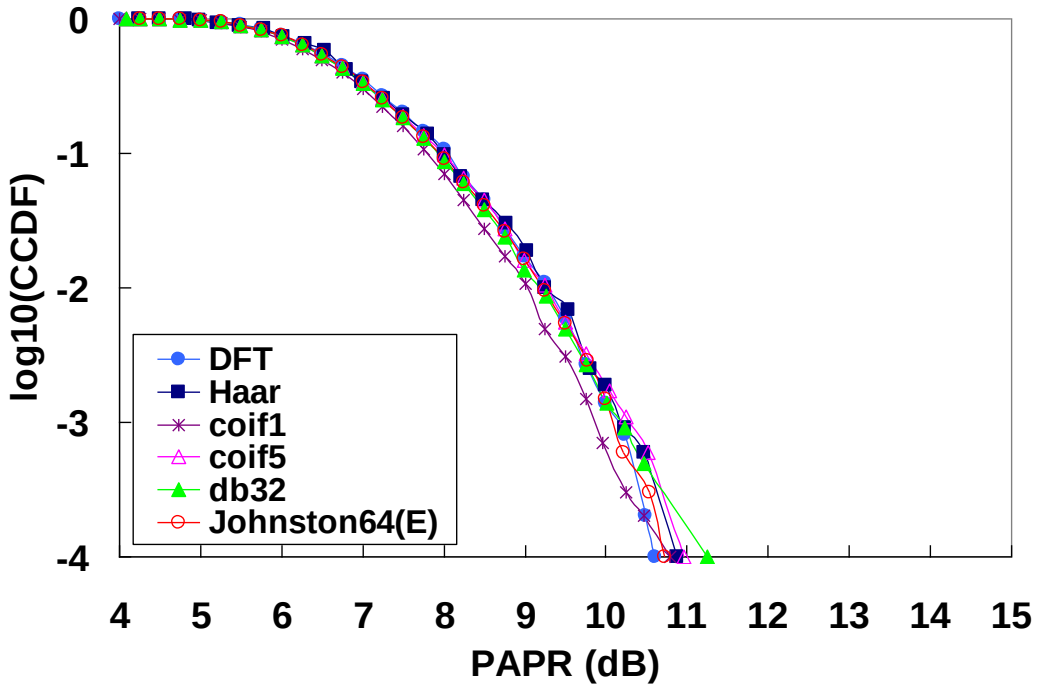

Fig.4.21 CCDF of PAPR for WPT-OFDM and FT-OFDM. *Nsc = 64*, oversampling factor *No = 1*.

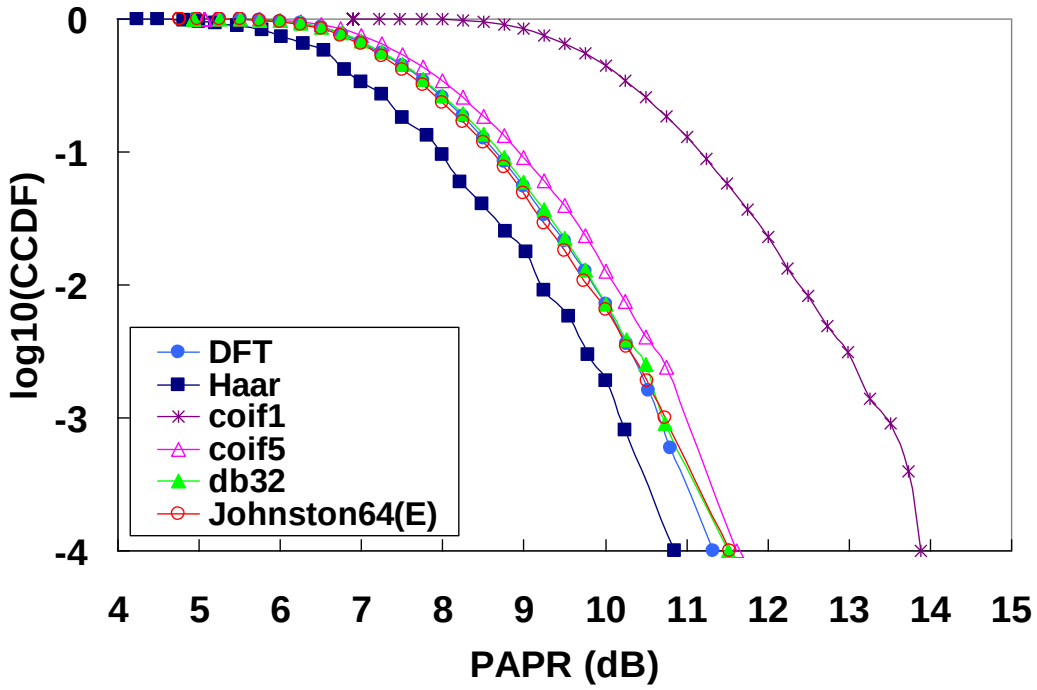

Fig.4.22 CCDF of PAPR for WPT-OFDM and FT-OFDM. *Nsc = 64*, *No = 8*.

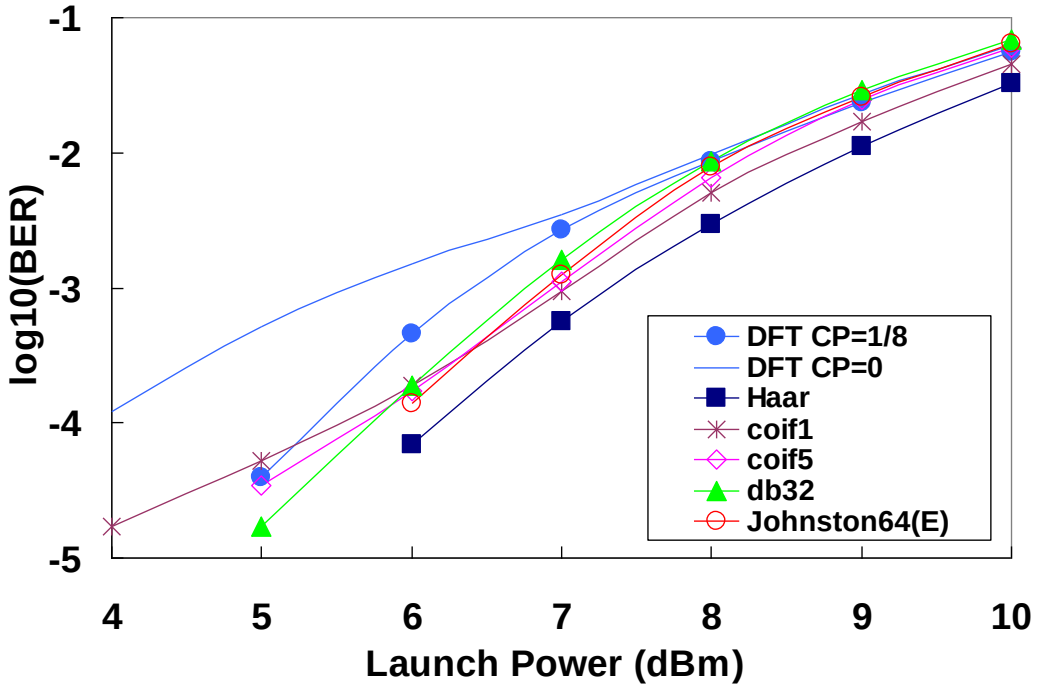

Fig.4.23 BER vs. launch power after 2×100 km transmission. CD in each span is fully compensated by DCF. *Nsc = 64*, *No = 8*.

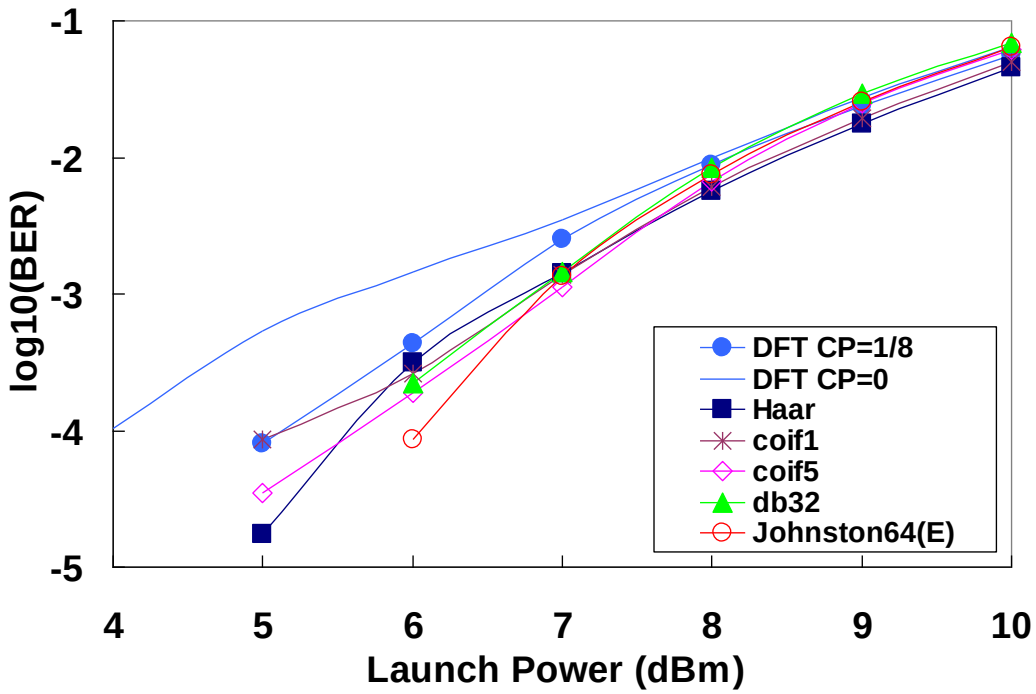

Fig.4.24 BER vs. launch power after 2×100 km transmission. CD in each span is 95% compensated by DCF.

Although Haar wavelet has the lowest sensitivity to PMD and the best nonlinearity tolerance among all wavelets, its application is limited due to very low CD tolerance (see Fig.4.16). For wavelets with high CD tolerance such as Johnston wavelet, PMD sensitivity becomes a major drawback. In order to solve this problem of PMD sensitivity, one natural way is to generate single-sideband wavelets in frequency domain. Similar to the Fourier transform that is based on complex-valued oscillating sinusoids, specifically designed complex wavelets with complex-valued scaling function and wavelet function $\psi_c(t) = \psi_r(t) + j\psi_i(t)$ can also have the same characteristics if $\psi_r(t)$ and $\psi_i(t)$ form a Hilbert transform pair [135-138]. This 'simple' solution leads us to a path searching for a complex wavelet suitable for use for optical fibre channel. Unfortunately, complex wavelet by itself is a relatively new field [135-144] The analytical solution of the complex wavelet - which needs to be realizable by FIR filters from a practical point of view - is rarely found, or perhaps impossible. Dual-tree structure can give some kind of approximately single-side band characteristics, but will lead to additional redundancy [138]. So the solution in terms of Hilbert pair complex wavelet, or approximate Hilbert pair, is still an active research topic in the field of mathematics, and its adaptation into optical communications remains an open question, which we will explore in our future work.

4.3 Discrete Fourier transform spread OFDM system (DFTS-OFDM)

Optical communication has rapidly advanced toward 1-Terabit per second (Tb/s) and beyond transport. As the available bandwidth of standard single-mode fibre (SSMF) is limited, high spectral efficiency (SE) becomes an important issue. Coherent optical OFDM (CO-OFDM) has become one of the promising candidates due to its high SE and resilience to linear channel impairments such as chromatic dispersion (CD). Experimental demonstration at data rate of 1-Tb/s [40-43] and beyond [44-51] has been achieved using either single carrier (SC) system or CO-OFDM. Despite many promising features, CO-OFDM system also suffers from high peak-to-average power ratio (PAPR) which leads to inferior tolerance to fibre nonlinearity compared with SC system, and has become an obstacle to its practical implementation in long haul transmission systems. Although specialty fibres such as ultra-large area fibre (ULAF) [41,47-48,93] or low-loss low-nonlinearity pure silica core fibre (PSCF) [94] with Raman amplification has been suggested to further extend the reach of transmission systems, it could be either more expensive than or not compatible with the deployed links. To solve the nonlinear tolerance problem, discrete-Fourier-transform spread OFDM (DFTS-OFDM) has recently been proposed with an attractive feature of much reduced PAPR [26]. DFTS-OFDM is called single-carrier frequency-division multiplexing (SC-FDM) that has been incorporated into the 3GPP-LTE standard in uplink for the next generation mobile system with many interesting features [27]. Furthermore, benefited from the sub-band or sub-wavelength accessibility of CO-OFDM, properly designed multiband DFTS-OFDM (MB-DFTS-OFDM) can potentially have better nonlinearity tolerance over either conventional CO-OFDM or SC system for ultra-high speed transmission [95]. The nonlinearity advantage of MB-DFTS-OFDM has been verified through simulation in [95-96]. In addition, optical transmission experiments utilizing the DFTS-OFDM or SC-FDM have been demonstrated very recently by several groups [94,97-101], which shows a potential advantage of better nonlinear tolerance and high SE. The ROADM functionally has also been demonstrated on SC-FDM superchannel [100].

In this section, we introduce and implement a novel variant of DFTS-OFDM with unique words embedded at both ends of OFDM symbols to facilitate the estimation and compensation of linear and nonlinear phase noise, which we called unique-word assisted DFTS-OFDM (UW-DFTS-OFDM).

4.3.1 System configuration of DFTS-OFDM

The digital signal processing at transmitter and receiver of a DFTS-OFDM system is shown in Fig.4.25. For comparison, the signal processing of conventional OFDM is also illustrated.

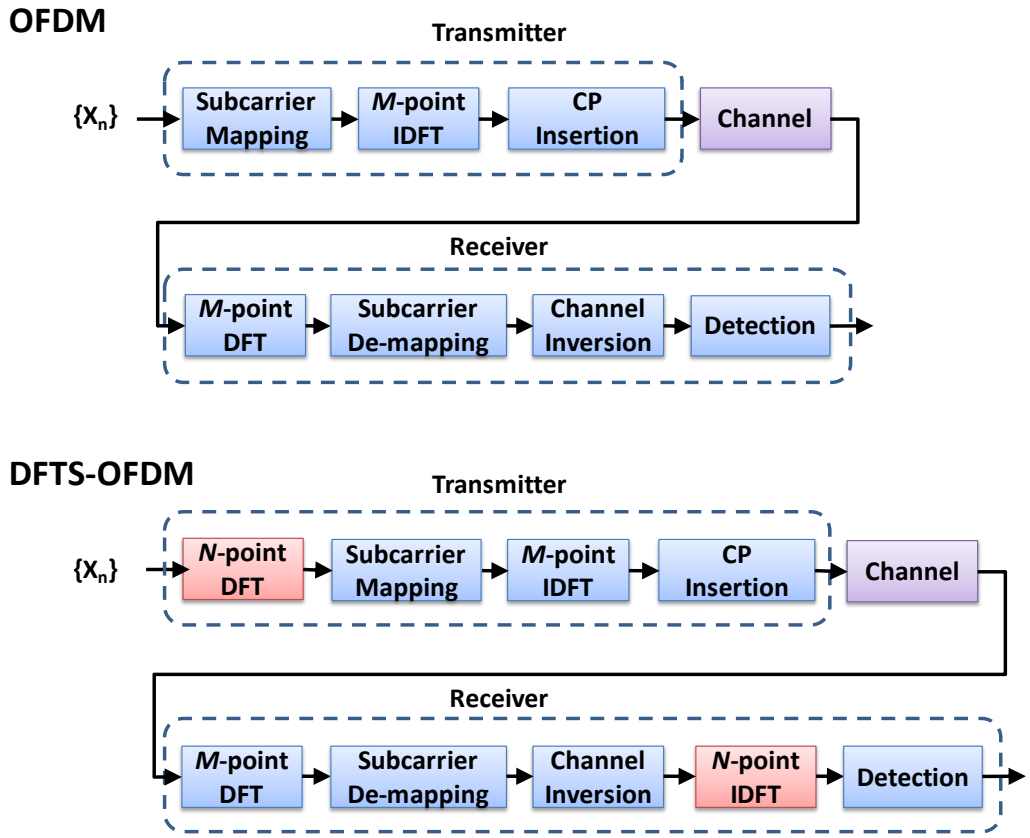

Fig.4.25 Signal processing of conventional OFDM and DFTS-OFDM. The pink blocks show the additional pair of DFT/IDFT in DFTS-OFDM.

Same as in conventional OFDM, signal processing in DFTS-OFDM is repetitive in a few different time intervals called blocks. At the input to the transmitter, a baseband modulator transforms the binary serial input data to a multilevel modulation formats such as M-ary phase shift keying (M-PSK) or M-ary quadrature amplitude modulation (M-QAM). The most commonly used modulation formats in OFDM system include binary phase shift keying (BPSK), QPSK, 16-QAM and 64-QAM. The modulation format can be made adaptive by the system to match the current channel conditions, and thereby the transmission data rate. The transmitter next group the modulation symbols xn into many OFDM blocks (serial to parallel), each containing N symbols. After that, the first unique step in DFTS-OFDM is an N-point DFT before the subcarrier mapping operation to produce a frequency domain representation X_k of

the input symbols. Then each of the N-point DFT outputs is mapped to one of the *M* (> *N*) subcarriers in a conventional OFDM that can be transmitted. As in conventional OFDM, the typical value of M must be a power of 2 (e.g., 64, 128 or 256). The choice of N in DFTS-OFDM must follow the relationship $N = M/Q$, which means N must be an integer submultiple of M. Q is called bandwidth expansion factor of the symbol sequence. DFTS-OFDM can handle Q simultaneous transmissions without co-channel interference (CCI) when each terminal is allocated N symbol per block. The result of the subcarrier mapping is the set $\tilde{X}_l$ ($l = 0, 1, 2, \ldots, M-1$) of complex subcarrier amplitudes, where N of the amplitudes are non-zero. As in conventional OFDM, an M-point inverse DFT (IDFT) transforms the subcarrier amplitudes to a complex time domain signal $\tilde{X}_m$. Each $\tilde{X}_m$ then modulates a single frequency carrier and all the modulated symbols are transmitted sequentially. The transmitter then inserts CP in order to provide a guard time to prevent inter-symbol interference (ISI). The modulated DFTS-OFDM signal is then launched into a wireless or fibre-optic channel for transmission.

After transmission, the receiver first transforms the time domain received signal into the frequency domain via DFT, de-maps the subcarriers, and then performs frequency domain equalization to remove the channel distortion. Minimum mean square error (MMSE) frequency domain equalization method is generally preferred over zero forcing (ZF) due to the robustness against noise. Subsequently the equalized symbols are transformed back from frequency- to time-domain via IDFT, and finally the detection and decoding is performed.

In DFTS-OFDM, since the DFT size $M > N$, several approaches have been proposed to the mapping of transmission symbols X_k to DFTS-OFDM subcarriers. These approaches can be divided into two categories; distributed and localized. Distributed subcarrier mapping means the DFT outputs of the input data are allocated over the entire bandwidth with the unused subcarriers filled with zeros, resulting in a non-continuous comb-shaped spectrum. The well-known interleaved DFTS-OFDM (IDFTS-OFDM), or so-called interleaved SC-FDMA (IFDMA) [145] is at special case of distributed DFTS-OFDM [27-28]. On the contrary, localized subcarrier mapping means consecutive subcarriers are occupied by the DFT outputs of the input data, resulting in a continuous spectrum that occupies a fraction of the total available

bandwidth. For IDFTS-OFDM, time symbols are simply a repetition of the original input symbols with a systematic phase rotation applied to each symbol in the time domain [145]. Therefore, the PAPR of IDFTS-OFDM signal is the same as in the case of a conventional single carrier signal. In the case of localized DFTS-OFDM (LDFTS-OFDM), or so-called localized SC-FDMA (LFDMA), the time signal has exact copies of input time symbols in N sample positions. The other M-N time samples are weighted sums of all the symbols in the input block [146]. As we can see from Fig.4.25, the first and obvious difference between conventional OFDM and DFTS-OFDM is the additional pair of N-point DFT/IDFT (pink blocks in Fig.4.25) in the DFTS-OFDM, with DFT in the transmitter and IDFT in the receiver. The second fundamental difference between DFTS-OFDM and conventional OFDM is in the receiver equalization and detection processes [28]. In conventional OFDM, since the data symbol is carried by individual subcarriers, channel equalization, channel inversion and data detection is performed individually on each subcarrier [16]. Channel coding or power/rate adaptation is required for OFDM to protect individual subcarriers if there are nulls in the channel spectrum, which would severely degrade the system performance since there is essentially no way to recover the data affected by the null. In the case of DFTS-OFDM, channel equalization and inversion is done similarly in the frequency domain but data detection is performed after the frequency domain equalized data is reverted back to time domain by IDFT [28]. Hence, it is more robust to spectral nulls compared to conventional OFDM since the noise is averaged out over the entire bandwidth. Additional advantages of DFTS-OFDM are the less sensitivity to carrier frequency offset (CFO) and less nonlinear distortion due to the much reduced PAPR [26], whilst conventional OFDM suffers due to the multicarrier nature of OFDM [147].

4.3.2 Principle of unique word DFTS-OFDM (UW-DFTS-OFDM)

Unique-word (UW) was first proposed for single carrier frequency domain equalization (SC-FDE) systems and has been extensively studied in wireless communications [145-150]. The data pattern structure of UW-DFTS-OFDM for two polarizations is illustrated in Fig.4.26. The unique-words (UWs), normally comprising of a Zadoff-Chu (ZC) sequence [151] and an optional guard interval (GI) are inserted periodically at the both ends of payload. The Zadoff-Chu sequence is generated with the following equation

$$x_u(n)=\begin{cases} e^{-j\frac{\pi un(n+1)}{N_{ZC}}} & if \quad N_{ZC} \quad is \quad odd \\ e^{-j\frac{\pi un^2}{N_{ZC}}} & if \quad N_{ZC} \quad is \quad even \end{cases} \quad (0 \le n \le N_{ZC}-1) \tag{4.56}$$

where$\mathbf{x_u(n)}$ $x_u(n)$ is the Zadoff-Chu sequence, N_{zc} is sequence length, u is an integer relatively prime of N_{zc}. A similar OFDM symbol structure can be drawn for the second polarization by using different UWs. The reason to use two UWs within one OFDM symbol is compatibility with polarization diversity where the first and second UWs are orthogonal to each other when combining the two OFDM symbols for two polarizations in a Jones vector form. The two UWs for the two polarizations (see Fig.4.26), $\begin{pmatrix} UW_{x1} \\ UW_{y1} \end{pmatrix}$ and $\begin{pmatrix} UW_{x2} \\ UW_{y2} \end{pmatrix}$ are given by

$$\begin{pmatrix} UW_{x1} & UW_{x2} \\ UW_{y1} & UW_{y2} \end{pmatrix} = \begin{pmatrix} UW & -cshift(UW)^* \\ cshift(UW) & UW^* \end{pmatrix} \tag{4.57}$$

where cshift(.) denotes a circular shift of the sequence by half of the sequence length and '*' denotes complex conjugate. The circular shift ensures that UWs for two polarizations, e.g., UW_{x1} and UW_{y1} are uncorrelated so long as the channel length is shorter than half of the unique word length. The short UWs in each OFDM symbol can be used for multiple purposes: timing synchronization, channel estimation, and phase estimation, etc. Phase estimation has been applied in our experimental demonstration and will be discussed in Section 4.3.4.

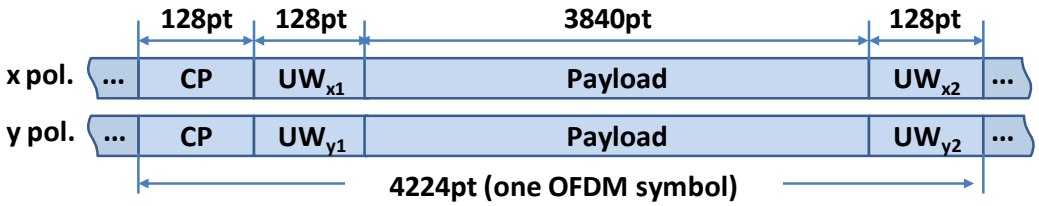

Fig.4.26 Structure of UW-DFTS-OFDM data symbol. UW: Unique Word; CP: Cyclic Prefix.

The nonlinear advantage of multi-band DFTS-OFDM has been theoretically analysed in [95]. In multi-band DFTS-OFDM systems, each subband is essentially filled with a digitally-generated single-carrier signal [95-96]. It has been numerically studied that DFTS-OFDM signal processes lower PAPR compare with conventional OFDM signal. For instance, the PAPR value of 7.5 dB occupies the probability higher than 99.9%, and this PAPR is 3.2 dB lower than the value in conventional OFDM

with the same probability [152]. Furthermore, one of the important findings of DFTS-OFDM for optical transmission is that there exists an optimal bandwidth within which the subbands should be partitioned. The insertion of UWs and the partitioned subcarrier mapping can slightly vary the performance of the DFTS-OFDM, but nevertheless the advantage of reduced PAPR remains significant.

4.3.3 Simulation and Results

We first perform numerical simulation to analyse the performance of the proposed UW-DFTS-OFDM system. We choose the same parameters as will be used in following experiments, and without loss of generality, we simulate transmission distance up to 960 km. The loop parameter is 12 spans of 80 km without inline dispersion compensation. The noise figure of EDFAs is set at 6 dB. The parameters for SSMF are as follows, nonlinearity coefficient $\gamma = 1.3\ W^{-1} * km^{-1}$, chromatic dispersion $D = 17\ ps/nm/km$, loss $\alpha = 0.2\ dB/km$. Totally 48 bands are generated with random (call random filling) or identical data pattern (called uniform filling).

The parameters of DFTS-OFDM and conventional OFDM are chosen in the way so that they can be fairly compared: Two types of modulation formats are simulated, QPSK and 16QAM. For PDM-QPSK UW-DFTS-OFDM the parameters are as follows, total number of subcarriers is 4096, middle 2625/4096 subcarriers are filled with data whilst the centre 65 subcarriers around DC are nullified to avoid performance degradation due to DC leakage. The 2560 data subcarriers are mapped from DFT-spreaded UW assisted data pattern as discussed in the previous Section 4.3.2. For PDM-QPSK conventional OFDM the parameters are as follows, total number of subcarrier is 128, the middle 83/128 subcarriers are filled with data whilst 3 subcarriers around DC are nullified, occupying a bandwidth of 6.484 GHz. 80 data subcarriers are modulated and mapped from 16QAM data pattern. For both systems, after IFFT to convert data from frequency- to time-domain, a 128-point cyclic prefix (CP) is appended before each symbol. For PDM-16QAM UW-DFTS-OFDM the parameters are similar to the PDM-QPSK UW-DFTS-OFDM except that the middle 2113/4096 subcarriers are filled with data whilst 65 subcarriers around DC are nullified. The 2048 data subcarriers are mapped from DFT-spreaded UW assisted data pattern. For PDM-16QAM conventional OFDM the parameters are also similar to the PDM-QPSK conventional OFDM except that the middle 67/128 subcarriers are filled

with data whilst 3 subcarriers around DC are nullified. 64 data subcarriers are mapped from 16QAM data pattern.

In order to facilitate a stable comparison, time-domain signals of DFT-S OFDM and conventional OFDM are cascaded digitally in MATLAB before loading onto the AWGs. Fig.4.27 and Fig.4.28 shows the Q-factor of the system against launch power for the two modulation scenarios. We find out that the performance of DFTS-OFDM outperforms conventional OFDM in both random filling and uniform filling schemes. For QPSK modulation, the optimum launch power for DFTS-OFDM is 8(6) dBm for random (uniform) filling, and optimum launch power for conventional OFDM is 7(4) dBm for random (uniform) filling. An improvement in launch power of 1 dB and Q of 1 dB is confirmed for DFTS-OFDM compared with conventional OFDM with random filling. For 16QAM modulation, the optimum launch power for DFTS-OFDM is 9(8) dBm for random (uniform) filling, and optimum launch power for conventional OFDM is 8(6) dBm for random (uniform) filling. A 0.7 dB improvement in Q factor is confirmed for DFTS-OFDM compared with conventional OFDM with random filling.

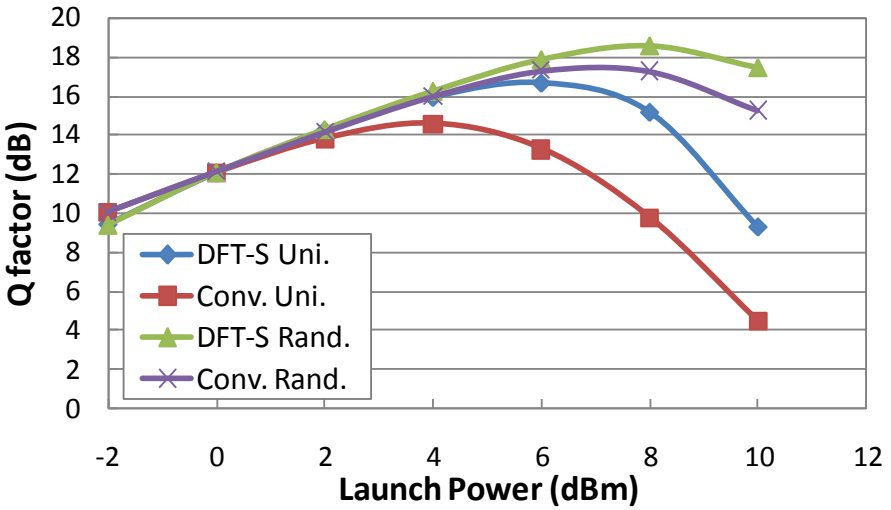

Fig.4.27 Simulated Q factor as a function of launch power at transmission distance of 960-km for 1-Tb/s PDM-QPSK UW-DFTS-OFDM and conventional OFDM. DFTS: DFTS-OFDM, Conv.: Conventional OFDM, Uni.: uniform filling, Rand.: random filling.

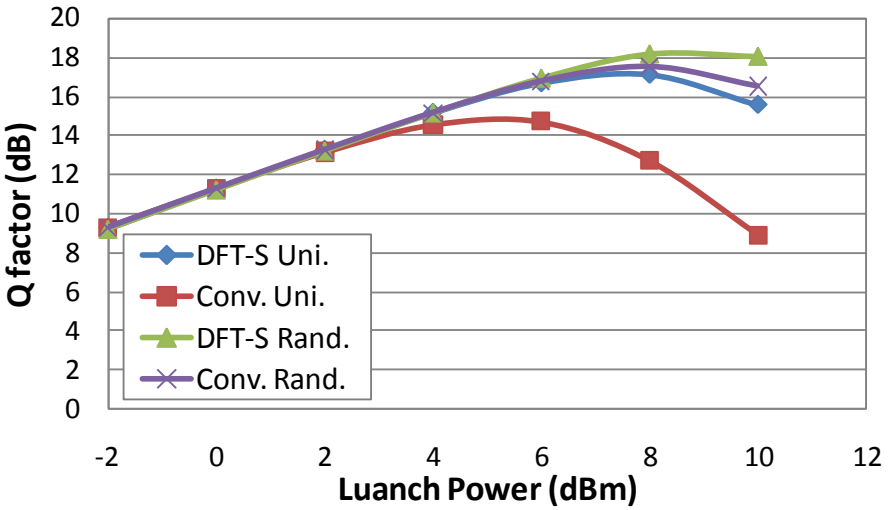

Fig.4.28 Simulated Q factor as a function of launch power at transmission distance of 960-km for 1.63-Tb/s PDM-16QAM UW-DFTS-OFDM and conventional OFDM. DFTS: DFTS-OFDM, Conv.: Conventional OFDM, Uni.: uniform filling, Rand.: random filling.

4.3.4 Experimental demonstration of 1-Tb/s PDM-QPSK UW-DFTS-OFDM superchannel transmission

In this section, we show experimental demonstration of 1-Tb/s PDM-QPSK UW-DFTS-OFDM transmission over 80-km span engineering SSMF and EDFA-only amplification that compatible with most of the deployed links. We have successfully achieved transmission of 1-Tb/s PDM-QPSK UW-DFTS-OFDM over 8,000-km SSMF, with BER of all bands below 7% FEC threshold (@BER=4.6×10^{-3}) [153]. The reach can be further extended to beyond 10,000-km if a 20% FEC is used (@BER=2×10^{-2}) [154]. To the best of our knowledge, we have obtained a record spectral efficiency and reach product of 24,800 bit/s/Hz*km for a 1-Tb/s superchannel at SE of 3.1 bit/s/Hz, with 80-km span engineering and EDFA-only amplification that compatible with most of the deployed links. Compare with our former 440.8 Gb/s experiment in [97], we have extended our performance comparison between UW-DFTS-OFDM and conventional OFDM from 1,000 km to 10,000 km.

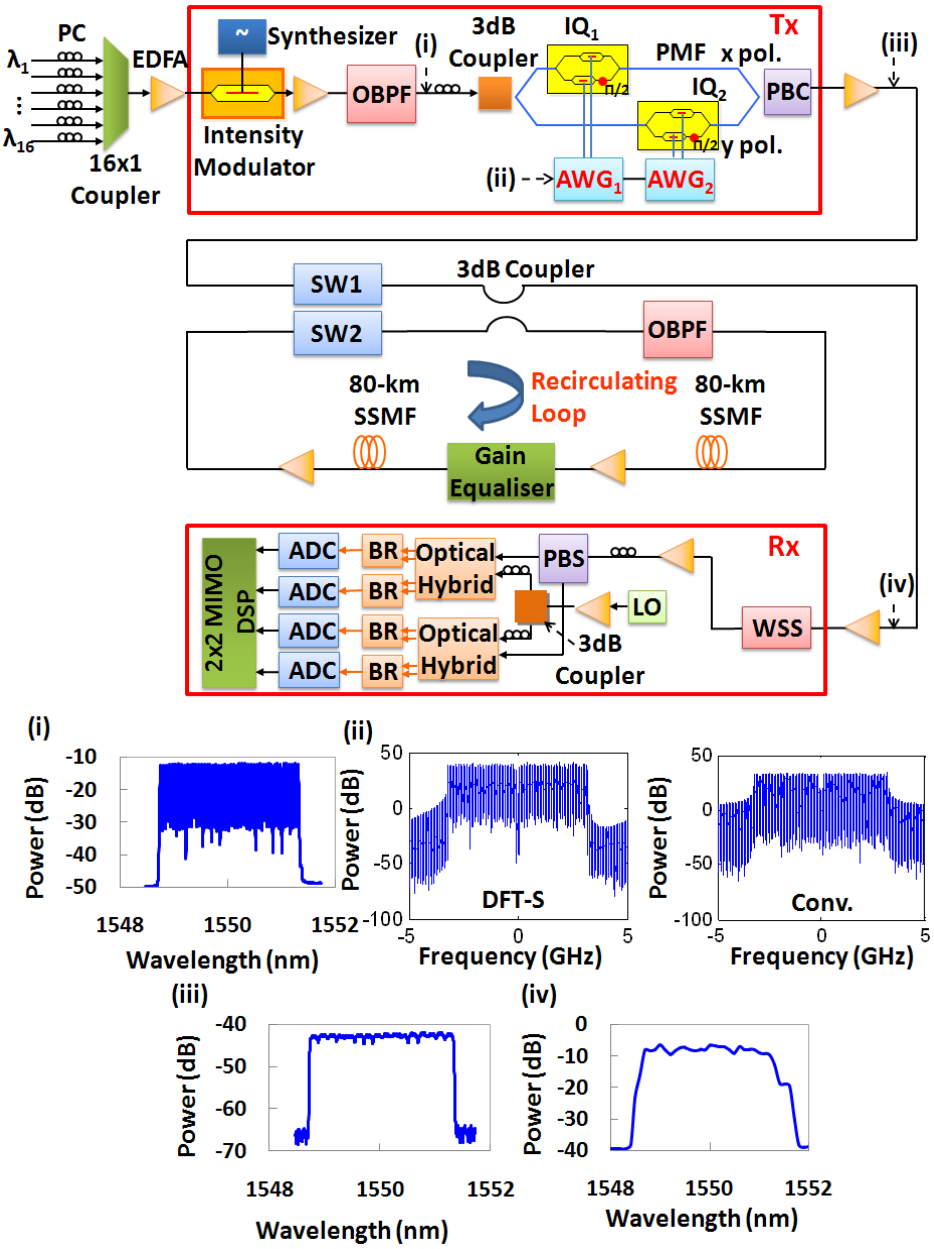

Fig.4.29 Experimental setup of 1-Tb/s UW-DFTS-OFDM system. OBPF: optical band-pass filter; AWG: arbitrary waveform generator; PMF: polarization maintaining fibre; PBC/PBS: polarization beam combiner/splitter; SSMF: standard single mode fibre; SW: (optical) switch; WSS: wavelength selective switch; LO: local oscillator; BR: balanced receiver; ADC: analogue-to-digital converter. Insets: measured optical and electrical spectra of (i) 48-tone source; (ii) data pattern loaded onto AWG; (iii) transmitted OFDM signal; (iv) received OFDM signal.

The experimental setup of 1-Tb/s UW-DFTS-OFDM system is shown in Fig.4.29. Our laser source are 16 external-cavity lasers with low laser linewidth (<100 kHz) combined together and fed into an optical intensity modulator to impress three tones on each wavelength. The tone spacing is set at 6.5625 GHz driven by a synthesizer.

The wavelength spacing of all the external-cavity lasers (ECL) is carefully controlled and stabilized at ~20.1875 GHz (1.615nm). Inset (i) of Fig.4.29 shows the generated densely-spaced 48 tones monitored at point (i) using a high resolution (0.01nm) optical spectrum analyser (OSA). After tone generation, the optical carrier is split into two equal branches by a 3-dB PM coupler and two AWGs are used to drive two IQ modulators to modulate different data pattern on the two polarizations. The baseband spectra for the data pattern are shown in the inset (ii) of Fig.4.29. After IQ modulation, the optical outputs on the two polarizations are multiplexed with a polarization beam combiner. The optical spectrum of generated 16-channel PDM-OFDM signal occupying a bandwidth of 323 GHz is monitored at point (iii), shown as inset (iii) of Fig.4.29. The 16-channel OFDM signal is then launched into a recirculating loop which consists of two spans of 80-km SSMF with loss compensated by EDFAs. The received OFDM signal after transmission is shown in inset (iv) of Fig.4.29. At the receiver, a 10-GHz optical filter is used to filter out one band each time, and the optical signal is converted to the electrical domain by an optical coherent receiver. The baseband signal is then received by a 4-channel Tektronix oscilloscope at 50-GSa/s sampling rate. The digital signal processing at the transmitter and receiver is shown in Fig.4.30.

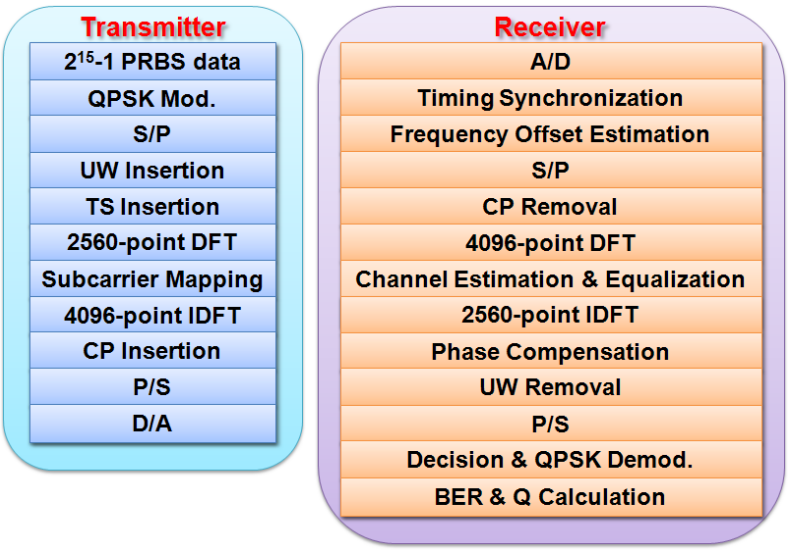

Fig.4.30 Digital signal processing at the transmitter and receiver of DFTS-OFDM. Pilot symbols of the same pattern are inserted for timing synchronization and frequency offset estimation using Schmidl-Cox's method [155]. For channel estimation, a novel algorithm with hybrid short- and long- training sequences is used. For phase noise compensation, a joint 'phase propagation' method that combines DAML [156-157] and block-based DFML method [158] is used.

The transmitted data pattern is generated following the procedure as shown in the 'transmitter' block of Fig.4.30. In order to facilitate a stable comparison, time-domain signals of DFTS-OFDM and conventional OFDM are cascaded digitally in MATLAB before loading onto the AWGs. The parameters of DFTS-OFDM and conventional OFDM are same as we use for simulation in Section 4.3.3 and reemphasized below: For DFTS, middle 2625/4096 subcarriers are filled with data whilst the centre 65 subcarriers around DC are nullified to avoid performance degradation due to DC leakage, occupying a bandwidth of 6.409 GHz/band. For conventional OFDM the middle 83/128 subcarriers are filled with data whilst 3 subcarriers around DC are nullified, occupying a bandwidth of 6.484 GHz/band. The difference between UW-DFTS-OFDM and conventional OFDM is that the 2560 data subcarriers in UW-DFTS-OFDM are mapped from DFT pre-coded UW assisted data pattern which will be described later, while in conventional OFDM the 80 data subcarriers are directly mapped with QPSK data pattern. After IFFT to convert data from frequency- to time-domain, a 128-point cyclic prefix (CP) is appended before each symbol. The dissimilar number of subcarriers used in conventional OFDM and UW-DFTS-OFDM is because that conventional OFDM can only compensate common phase error (CPE) within one OFDM symbol thus imposes a constraint to the use of long symbol unless other complicated phase noise compensation method is used such as RF-pilot tone [60]. However for ultra-long-haul transmission a large CP length is needed, therefore a large number of subcarriers are preferred or else the overhead too much (in conventional OFDM the overhead of CP is more than 50%, whilst in DFTS-OFDM the overhead of CP is only 3%).

At receiver, the received four data streams I_x, Q_x, I_y, Q_y, are first converted from analogue to digital by ADCs, then combined to complex signal and timing synchronized using pilot symbols [155]. The frequency offset is then estimated and compensated, also using the pilot symbols [155]. The time domain signal is then converted from serial to parallel followed by the removal of CP. Subsequently the data is transformed from time to frequency domain by a 4096 point DFT. Channel estimation and equalization is first performed with the assistance of short- and long-UW pattern training sequence. After that phase noise compensation is realized with the assistance of short UWs in each OFDM symbol using a novel channel estimation and phase estimation method which will be discussed later. The UWs are then

removed followed by the payload data decision, QPSK demodulation and finally BER calculation for the performance evaluation.

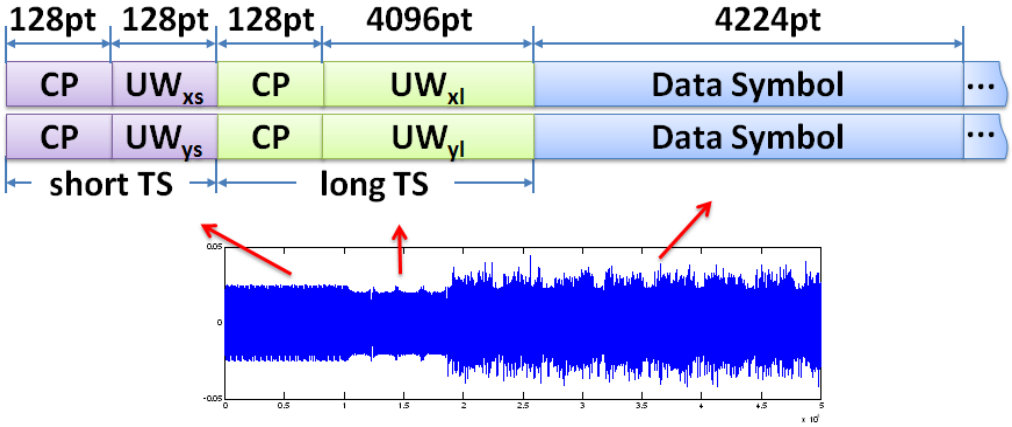

Fig.4.31 Structure of UW-DFTS-OFDM consisting of training and data symbol. UW: Unique Word; CP: Cyclic Prefix. The bottom figure shows a realistic data pattern generated and loaded onto the AWG in experiment.

Because of constant amplitude feature of Zadoff-Chu sequence in both frequency- and time-domain, we insert Zadoff-Chu sequences as training sequences (TSs) at the beginning for initial channel estimation as shown in Fig.4.31. To assist channel estimation of long symbol DFTS-OFDM system, a hybrid TS of 20 short (256-pt) and 2 long (4224-pt) symbols are used to mitigate phase noise during channel estimation. The channel estimation algorithm based on received TS symbols is shown in Fig.4.32 and explained as follows: Short training symbols are first used to carry out channel estimation; then we interpolate this 80-tap channel response to 2560-tap one by polynomial curve fitting; after that we equalize long training symbols with the 2560-tap channel response, and compare with transmitted data for phase estimation; The phase compensated long symbols are used to obtain a new channel response. The process can be iterated until an accurate channel response is obtained. This new algorithm enables the use of long OFDM symbol without being constrained by the laser phase noise. The effectiveness of this new algorithm has been confirmed in both simulation (Fig.4.27) and experiment, which shows almost no penalty compared to the conventional channel equalization method in [158] as we used for conventional OFDM. It proves that the channel response of optical fibre is smooth, slow time varying, and dominated by the chromatic dispersion. Compare with the conventional OFDM channel estimation and phase noise compensation method [39], the proposed channel estimation method - in combination with the new phase noise compensation

method that will be discussed later - could solve the laser phase noise problem in long training symbols thus provide the detailed information of elaborate channel response. It therefore has better performance in experiment than solely use short training symbols for long data symbols. Compare with RF-pilot method proposed in [60] which can also solve the phase noise problem in long OFDM symbol, the proposed method does neither consume additional power at transmitter for the pilot subcarrier, nor require any additional components at receiver such as low-pass filter and large memory, which greatly reduces the system complexity.

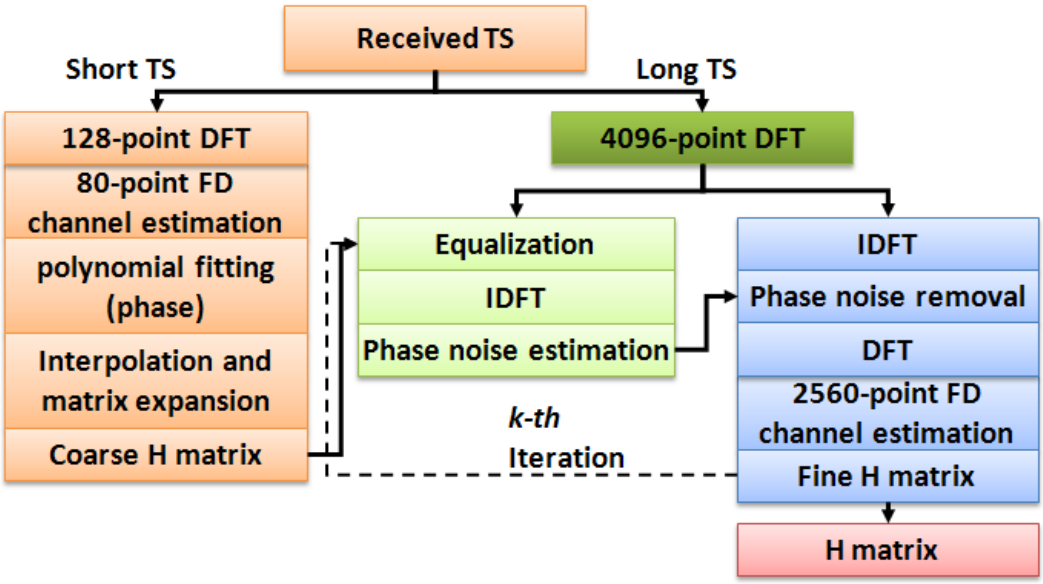

Fig.4.32 Flow chart of channel estimation algorithm using hybrid short- and long- training symbols.

For the received data symbols, the short UWs inserted at the both ends of the OFDM symbols can be used for phase estimation. Here we apply a joint 'phase propagation' method that combines data-aided maximum-likelihood (DAML) phase estimation method [156-157] and block-based decision feedback maximum-likelihood (DFML) method [158] with the same step size and block size of *L*. The joint phase estimation algorithm is implemented as follows: The entire OFDM symbol is partitioned into blocks of size *L*. To estimate carrier phase in the *j*-th block, we assume that the carrier phase in preceding block *j-1* has been either estimated or is known. In the first step, we estimate the phase of the *k*-th information symbol in the *j*-th block using the carrier phase information of preceding *L* symbols. We first calculate a complex reference quality V_k given by

$$V_k \equiv \sum_{l=k-L}^{k-1} r_l \hat{m}_l^* \tag{4.58}$$

where r_l denotes the received complex signal and $\hat{m}_l$ denotes the receiver's decision on the *l*-th symbol, '*' denotes complex conjugation. Subsequently we de-rotate the constellation of the *k*-th symbol by

$$r_k' = r_k V_k^* \tag{4.59}$$

For a M-ary PSK constellation, we use the decision criterion given by

$$q_{ik} = \arg\max_i \mathrm{Re}[r_k' C_i^*] \tag{4.60}$$

where C_i is the possible symbol in the M-ary PSK constellation. The receiver calculates q_{ik} for each possible value Q_i of data symbol m_k and decides $\hat{m}_k = Q_i$ if $\mathrm{Re}[r_k' C_i^*]$ is maximized. Then we continue to the next (*k+1)*-th symbol. After all the symbols in the *j*-th block has been decided, in the second step, we estimate the phase of the *k*-th symbol using the phase information of the *L* symbols in the same block *j* by

$$\hat{\phi}_j = angle\left(\sum_{l=1}^{L} (r_{jl}' \hat{m}_{jl}^*) \right) \tag{4.61}$$

where 'angle' denotes the angle of an quality, $\hat{\phi}_j$ denotes the carrier phase estimated for the *j*-th block, r_{jl}' and $\hat{m}_{jl}$ denote the de-rotated and sliced *l*-th symbol in the *j*-th block obtained in the first step. The constellation of the *j*-th block is then de-rotated again using the phase ϕ_j by

$$r_{jl}'' = r_{jl}' \, \mathrm{e}^{-i\langle \phi_j^* \rangle} \tag{4.62}$$

The new symbol r_{jl}'' is then decided again using Eq.(4.60). After the above two steps, the carrier phase information can be passed to the following block with another iteration of the above-mentioned two steps. The first and last blocks are pilot blocks from the UWs whose values are known. Therefore either forward or backward propagation can be applied from one end to the other, or simultaneously from both ends towards centre. In our experiment, we choose to propagate from both ends of the payload to the centre as shown in Fig.4.33. We found that L of 32 is optimum for our transmission experiment.

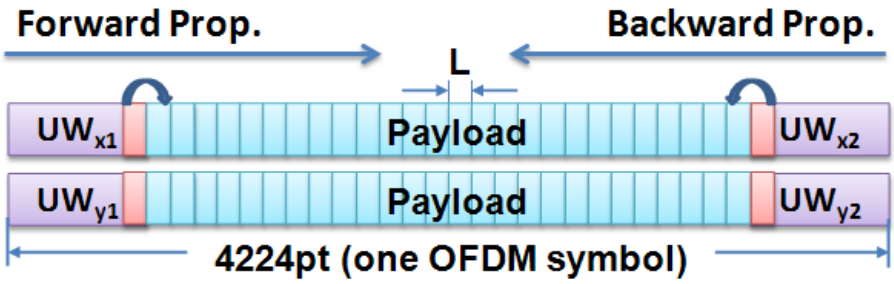

Fig.4.33 Conceptual diagram of the proposed phase propagation method. The joint method combines DAML method for the inter-block phase estimation and block-based DFML method for the intra-block phase estimation with a block size *L*. with a block size *L*.

The raw data rate of our UW-DFTS-OFDM signal is 1.2-Tb/s (6.25 GHz × 48 band × 2 bit/s × 2 pol) and the net data rate is 1.0-Tb/s after excluding all the overheads. The net spectral efficiency is 3.1 bit/s/Hz. Fig.4.34 shows the BER sensitivity for optical back-to-back of 1-band (with 1 laser), 3-band (with 1 laser), and 48-band (with 16 lasers) PDM-QPSK UW-DFTS-OFDM system corresponding to a raw data rate of 25-Gb/s, 75-Gb/s and 1.2 Tb/s. The required OSNR for DFTS-OFDM system is similar to conventional OFDM system measured at 22.9 dB for a BER of 4.6×10^{-3} (7% FEC). This is 17 dB more than that of a single-band system and only 0.9 dB away from the theoretical value. Fig.4.35 shows the Q factor performance against launch power. The optimum launch power is 8 dBm for conventional OFDM and 9 dBm for DFTS-OFDM which agrees well with our simulated value. A noticeable 0.6 dB improvement in Q factor is observed for DFTS OFDM compared with conventional OFDM. Fig.4.36 shows the measured BER against the transmission distance for DFTS-OFDM and conventional OFDM at launch powers of 8 and 9 dBm. It can be seen that the maximum possible transmission distance at a BER of 4.6×10^{-3} (7% FEC) [153] is 8,300 km and 7,300 km for DFTS-OFDM and conventional OFDM, respectively, which shows a 20% increase in reach for DFTS-OFDM. If BER of 2×10^{-2} (20% FEC) [154] is used, the reach of DFTS-OFDM can be extended to more than 10,000 km. Finally, the BER performance of all 48 bands is measured at the launch power of 9 dBm and transmission distance of 8,000km (80 km × 100) as shown in Fig.4.37. The BERs of all bands in DFTS-OFDM are below the 7% FEC threshold, whereas for conventional OFDM all bands have crossed the BER limit.

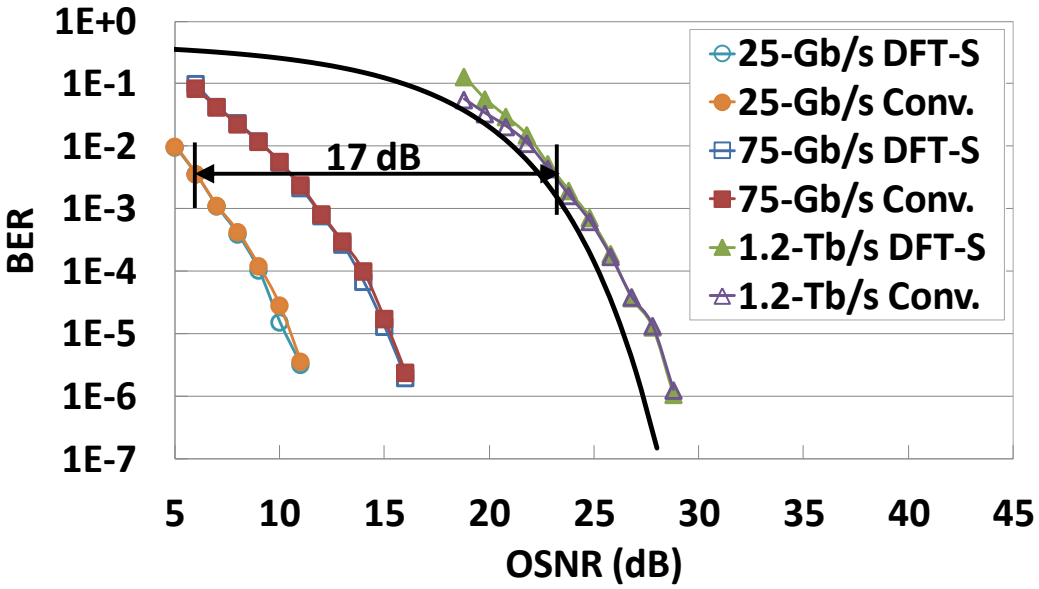

Fig.4.34 Measured optical back-to-back BER performance. The data rates shown are raw data rates. DFTS: DFTS-OFDM; Conv.: conventional OFDM.

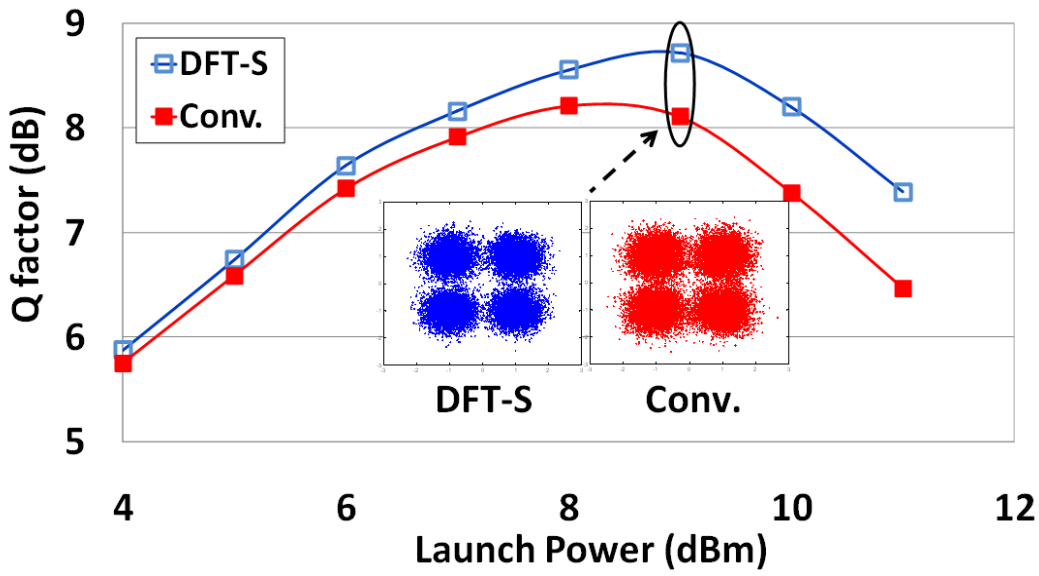

Fig.4.35 Measured Q-factor vs. launch power after 8000-km transmission. Inset: recovered constellations at the launch power of 9 dBm.

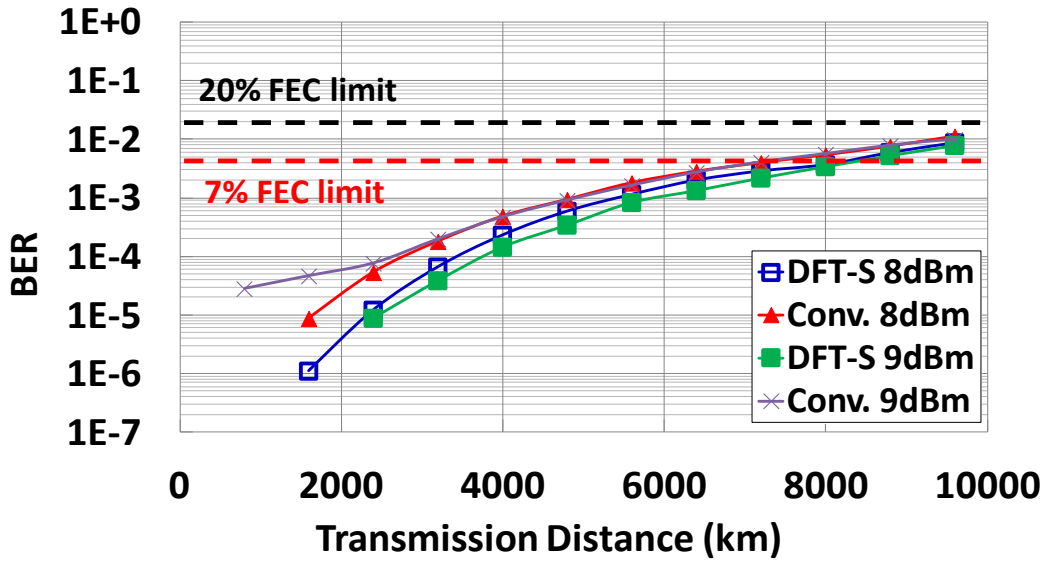

Fig.4.36 Measured BER performance of 1.0-Tb/s UW-DFTS-OFDM system at different transmission distances.

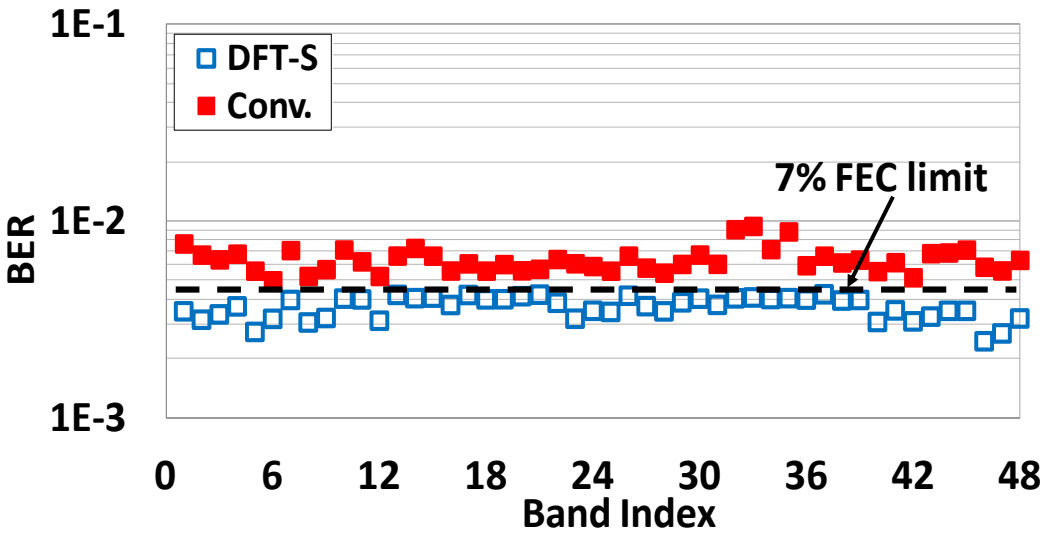

Fig.4.37 Measured BER performance for all 48 bands for 8,000-km transmission at a launch power of 9 dBm.

4.3.5 Experimental demonstration of 1.63-Tb/s PDM-16QAM UW-DFTS-OFDM superchannel Transmission

In previous section 4.3.4 we have demonstrated successful transmission of 1Tb/s PDM-QPSK UW-DFTS-OFDM transmission over 8,000-km EDFA-only SSMF link at a SE of 3.1 bit/s/Hz. For future high speed optical transports, higher data rate and higher SE are unavoidable trends. To further increase SE, higher order modulation format such as 16QAM turns out to be a promising solution while maintaining low system complexity. In this section, we show an experimental demonstration of 1.63-Tb/s PDM-16QAM UW-DFTS-OFDM transmission over 1,010-km SSMF with 80-

km span engineering and EDFA-only amplification, with BER of all bands below the 7% FEC threshold ($@BER = 4.6\times10^{-3}$) [153]. The reach can be further extended to 2,610-km ($@BER = 2\times10^{-2}$) if a 20% FEC is used [154]. Although there have been prior demonstration using ULAF [41,47-48,93] or low-loss low-nonlinearity PSCF [94] and Raman amplifier, to the best of our knowledge, we have shown the record reach of 1,010-km (960-km excluding leading fibre) for a Tb/s superchannel at the spectral efficiency of 6.2 bit/s/Hz and 2,500-km at the spectral efficiency of 5.5 bit/s/Hz, with a span engineering of 80-km span without Raman amplification compatible with most deployable links.

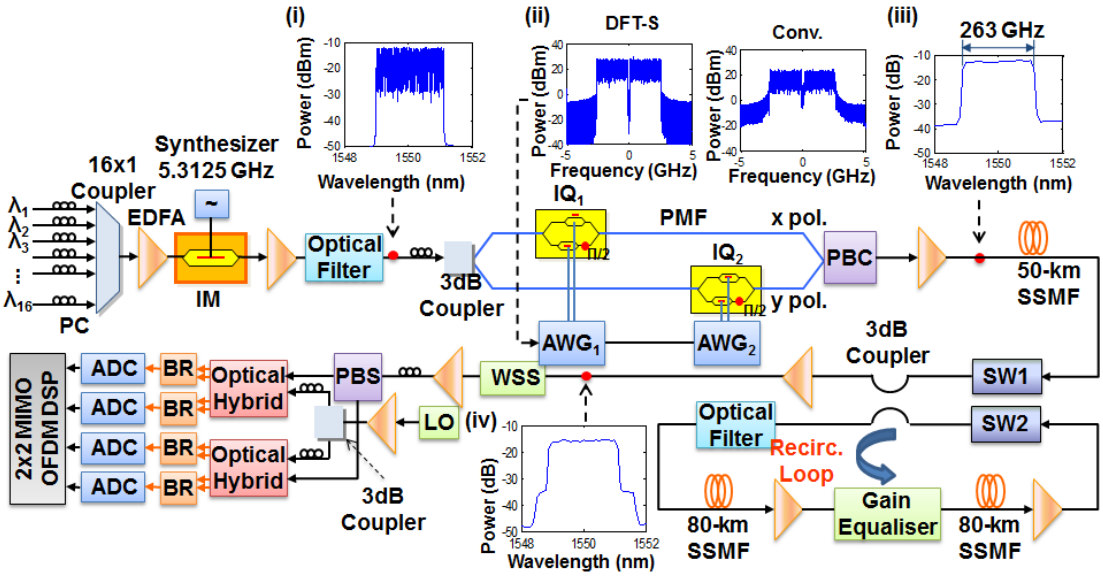

Fig.4.38 Experimental setup of 1.63-Tb/s PDM-16QAM UW-DFT-S-OFDM system. PC: polarization controller; AWG: arbitrary waveform generator; PMF: polarization maintaining fibre; PBC(S): polarization beam combiner(splitter); SW: optical switch; WSS: wavelength selective switch; LO: local oscillator; BR: balanced receiver. DFT-S: DFT-S-OFDM; Conv.: conventional OFDM. Insets: measured optical and electrical spectra of (i) 48-tone source; (ii) Frequency domain data pattern loaded onto AWG; (iii) transmitted OFDM signal; (iv) received OFDM signal.

Fig.4.38 shows the schematic diagram of the experimental setup of 1.63-Tb/s PDM-16QAM UW-DFT-S-OFDM systems. At the transmitter, 16 external-cavity lasers are combined by a 16x1 coupler and fed into an optical intensity modulator. The spacing between the 16 lasers is tuned at around 16.4375GHz which indicates a ~500 MHz gap between side bands of nearby lasers. Three bands are generated on each laser with a tone spacing of 5.3125 GHz driven by a synthesizer. The optical

spectrum of generated densely-spaced 48 bands is monitored by a high-resolution OSA shown as the inset (i) of Fig.4.38. After tone generation, the optical carrier is split into two equal branches. Two synchronized AWGs are used to drive two IQ modulators with independent data patterns, which enable the UWs in both TS and data.

The parameters of DFTS OFDM and conventional OFDM are same as used for simulation in Section 4.3.3 and reemphasized as below: total number of subcarriers is 4096, out of which the middle 2113/4096 subcarriers are filled with data whilst 65 subcarriers around DC are nullified to avoid degradation due to DC leakage, occupying a bandwidth of 5.159 GHz/band. The 2048 data subcarriers are mapped from DFT-spreaded UW assisted data pattern. Similar as we did in PDM-QPSK UW-DFTS-OFDM, a hybrid training sequence of 20 short (144-pt) and 2 long (4112-pt) symbols is also used to mitigate phase noise during channel estimation. For conventional OFDM, total number of subcarrier is 128, out of which the middle 67/128 subcarriers are filled with data whilst 3 subcarriers around DC are nullified, occupying a bandwidth of 5.234GHz/band. The 64 data subcarriers are also modulated and mapped with 16QAM data pattern. In order to facilitate a stable comparison, time-domain signals of DFT-S OFDM and conventional OFDM are cascaded digitally in MATLAB before loading onto the AWGs. The baseband spectra for the data pattern are shown in the inset (ii) of Fig.4.38.

After IQ modulation, the optical outputs on the two polarizations are multiplexed by a polarization beam combiner. The optical spectrum of a 16-channel PDM-OFDM signal occupying a bandwidth of 263 GHz is monitored and shown as inset (iii) of Fig.4.38. The 16-channel OFDM signal first passes through a 50-km SSMF fibre with low optical power (2 dBm) to de-correlate the signals in all bands, and is then launched into a recirculation loop which consists of two spans of 80-km SSMF loss-compensated by EDFAs. At the receiver, a 10-GHz optical filter is used to filter out one band each time, and the optical signal is converted to the electrical domain by an optical coherent receiver. The baseband signal is then received by a 4-channel Tektronix oscilloscope at 50GSa/s sampling rate. The timing synchronization and frequency offset is done using UWs. After serial-to-parallel conversion and CP removal, the time-domain signal is transformed into the frequency domain using a 4096-pt DFT. With the knowledge of estimated channel matrix *H*, the data symbol

can be equalized with a one-tap equalizer. Following this we use a 2048-pt IDFT to obtain time-domain data, and use the phase estimation method proposed in Section 4.3.4 to compensate linear and nonlinear phase noise. Finally the symbol decision is made based on the phase compensated data information. The net data rate is 1.63 Tb/s after counting all the overheads and the net spectral efficiency is 6.2 bit/s/Hz.

We first measure the BER performance for optical back-to-back of the 1.63-Tb/s PDM-16QAM system and the result is shown in Fig.4.39. The required OSNR for DFT-S system at 7% FEC [153] is 29.2 dB, which is only 0.4 dB away from the theoretical value, and is 0.8 dB lower than the conventional OFDM. This result indicates that DFT-S OFDM has less nonlinear distortion in optical IQ modulator and better compensated phase noise using proposed intra-symbol phase estimation method. Fig.4.40 shows the Q factor performance against launch power. The optimum launch power is 8 dBm and a noticeable 0.5-dB improvement in Q factor for DFT-S OFDM is observed compared with conventional OFDM. The advantage of DFT-S over conventional OFDM is reduced in 16QAM modulation compared to that of QPSK because the PAPR reduction due to DFT spreading is partially offset by the amplitude variation. Fig.4.41 shows the measured Q factor of the worst band at different transmission distance for DFT-S OFDM and conventional OFDM at launch power of 8 and 9 dBm. It can be seen that the maximum possible transmission distance at 7% FEC [153] is 1,400 km and 1,150 km for DFT-S OFDM and conventional OFDM, respectively, which shows a 20% increase in reach for DFT-S OFDM. If 20% FEC [154] is used, the reach of DFT-S OFDM can be extended to more than 2,500 km. Finally, the BER performance of all 48 bands is measured at the launch power of 8 dBm and transmission distance of 1,010 km ($(50+6\times160)\ km$), as shown in Fig.4.42. The BER of all bands in DFT-S OFDM are well below the 7% FEC threshold, whereas for conventional OFDM some bands have already crossed the BER limit.

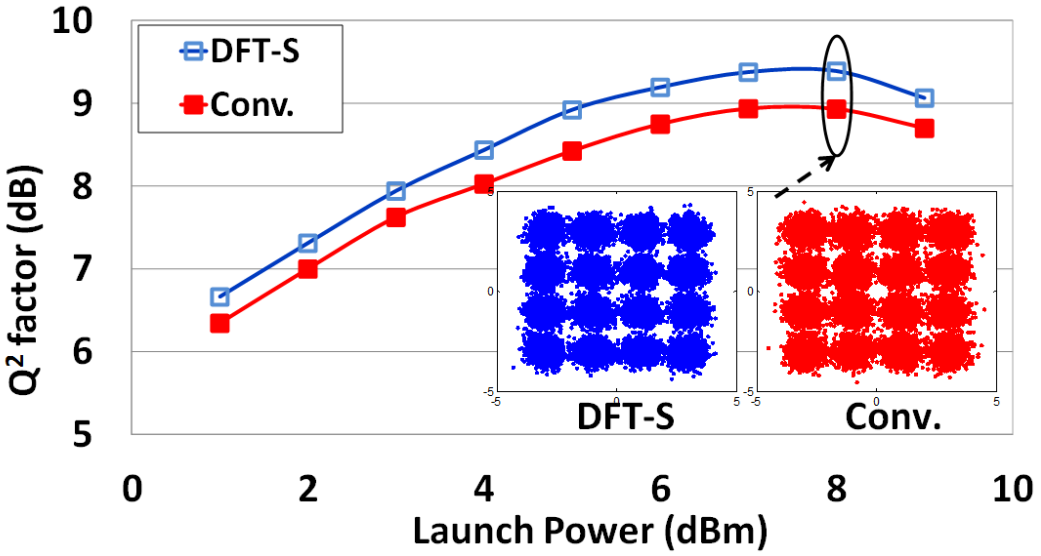

Fig.4.39 Measured optical back-to-back BER performance of the center band. The inset shows the recovered constellations at *OSNR = 41 dB*. DFT-S: DFT-S-OFDM; Conv.: conventional OFDM.

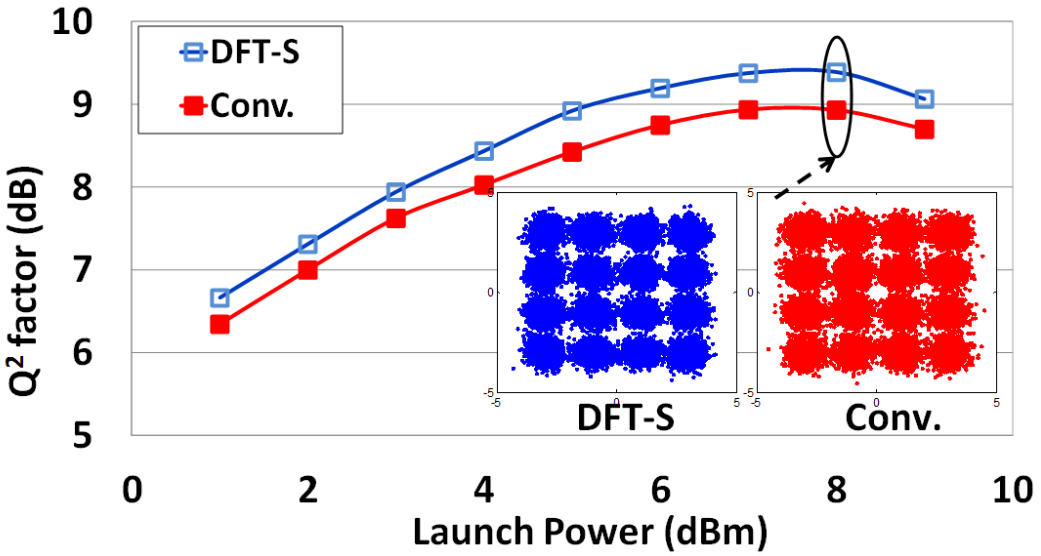

Fig.4.40 Measured Q-factor vs. launch power. Inset: recovered constellations at the launch power of 8 dBm.

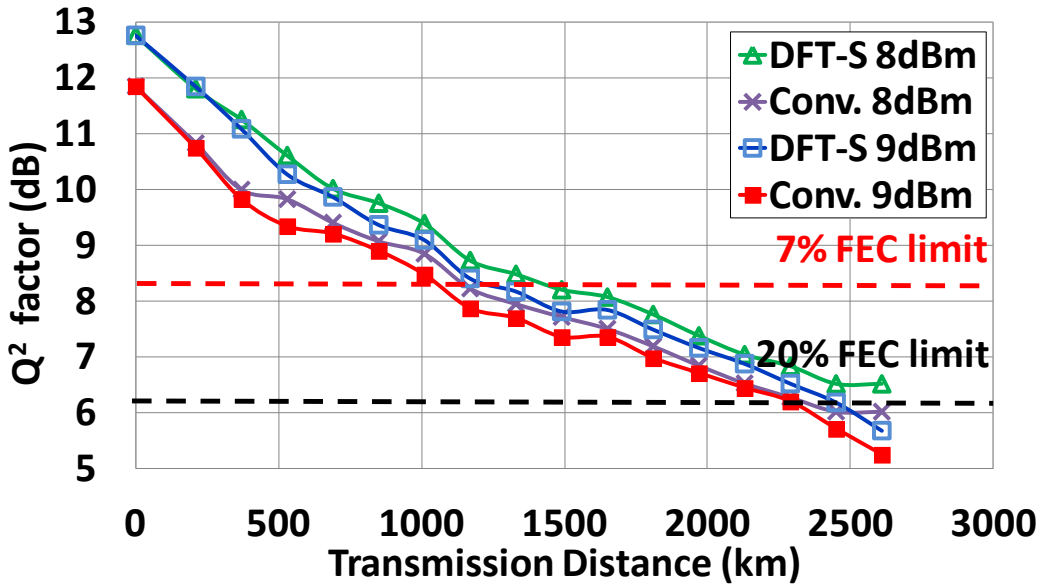

Fig.4.41 Measured Q-factor for the worst band of 1.6Tb/s PDM-16QAM-OFDM system at different transmission distances.

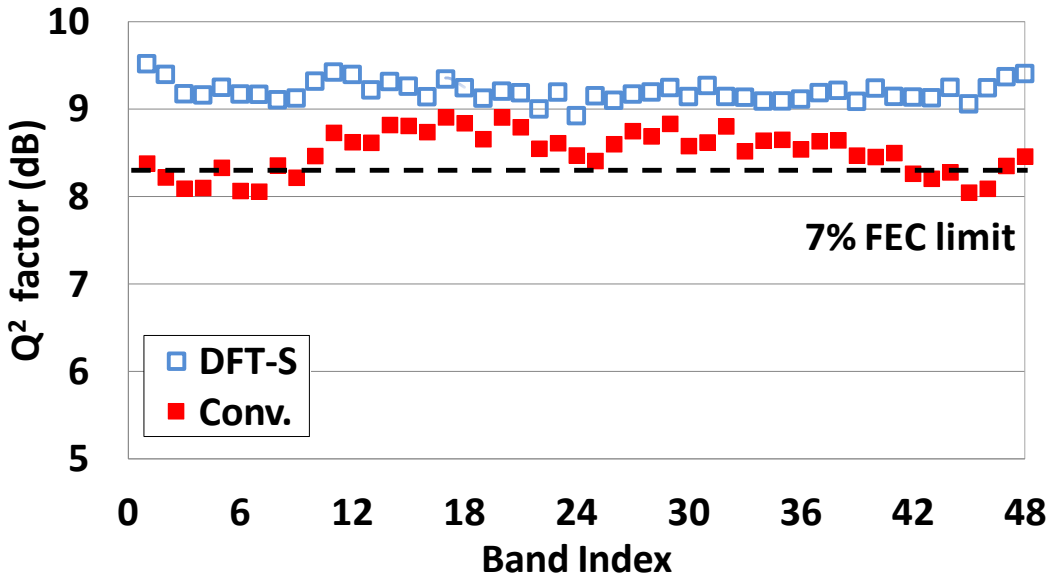

Fig.4.42 Measured Q-factor for all 48 bands at the launch power of 8 dBm after 1,010-km transmission.

4.4 Conclusion

In this section we have proposed two new variants of CO-OFDM system, the WPT-OFDM and DFTS-OFDM. We first investigate the performance and limitation of real WPT-OFDM systems. Its double-sideband characteristic makes it sensitive to spectrally non-symmetric dispersion such as polarization-mode dispersion (PMD). Simulations of dual-polarization WPT-OFDM transmission are carried out in the presence of PMD, and compared with conventional Fourier transform-based optical

OFDM (FT-OFDM). The results show that WPT-OFDM is very sensitive to PMD, incurring 1-dB penalty at 5~11 ps DGD for 112-Gb/s dual-polarization transmission. PAPR and nonlinearity performance of WPT-OFDM are also analysed in this work. We show that the Haar wavelet has 0.9-dB improvement in nonlinear launch power limit compared with FT-OFDM (CP=1/8) in a conventional transmission dispersion configuration where inline dispersion is fully compensated by DCF. Then we look at the other variant DFTS-OFDM system. We first introduced the concept of DFTS-OFDM and unique word (UW). Then we proposed a novel system called UW-DFTS-OFDM. The performance of UW-DFTS-OFDM has been analysed through simulation. Two experimental demonstrations of UW-DFTS-OFDM superchannel transmission has been achieved, (1) 1-Tb/s PDM-QPSK UW-DFTS-OFDM superchannel transmission over 8,000-km SSMF, and (2) 1.63-Tb/s PDM-16QAM UW-DFTS-OFDM superchannel transmission over 1,010-km SSMF, with 80-km span engineering and EDFA-amplification compatible with most of the deployed links. In the first demonstration we show record spectral efficiency and reach product of 24,800 bit/s/Hz*km for a 1-Tb/s superchannel at SE of 3.1 bit/s/Hz, and in the second we show record reach of 1,010-km (960-km excluding leading fibre) for a Tb/s superchannel at the spectral efficiency of 6.2 bit/s/Hz and 2,500-km at the spectral efficiency of 5.5 bit/s/Hz.

5 Few-Mode and Two-Mode Fibre

The highest reported single optical fibre data transmission speed has reached over 100-Tb/s [14-15]. However, there is a need to continue enhancing the total data transmission capacity while keeping the signals within the available optical spectrum of the conventional Erbium doped fibre amplifier (EDFA), which translates into the requirement for increased spectral efficiency (SE, expressed in b/s/Hz). Although Shannon's theory predicts SE to increase with higher received SNR as a result of increased transmission power, fibre nonlinearity imposes a hard constraint on the channel capacity [24]. It is foreseen that the saturation of the fibre capacity for on the SSMFs that we use today is fast coming. Information theory reveals that by adding another degree of freedom, namely the spatial mode, the fibre capacity of MMF or FMF can be increased. Therefore it is of great interest to know whether the few-mode fibre (FMF) such as two-mode fibre (TMF) can offer capacity beyond that of SSMF in a cost effective manner. In this chapter, we show the design of a practical TMF. We first review fundamentals of optical fibre and fibre modes. Then we discuss the parameters and process to fabricate a practical FMF for future space division multiplexing (SDM) based high speed optical networks. At last we show characterization of our custom-designed TMF.

5.1 Overview of optical fibres

As was elucidated in Section 1.1.1, an optical fibre normally consists of a core surrounded by a cladding layer whose refractive index n_2 is slightly lower than the core index n_1. If the refractive index of the core n_1 is uniform in the core region, it is called step-index fibre. In contrast, if the refractive index of the core n_1 decreases gradually from centre to core boundary [159-161] it is called a graded-index fibre. There are two important parameters that characterize an optical fibre: the relative core-cladding index difference

$$\Delta = \frac{n_1 - n_2}{n_1} \tag{5.1}$$

and the normalized frequency (also called *V*-number) parameter defined as

$$V = k_0 a \sqrt{n_1^2 - n_1^2} \tag{5.2}$$

where $k_0 = 2\pi / \lambda$ is the wavenumber, λ is the wavelength of light, and a is the radius of core The V number determines how many modes can be supported by the fibre. The fibre modes denoted here refer to transverse modes and will be discussed in Section 5.2. It is shown that a step-index fibre supports a single mode if V < 2.405 [76, -163], which is also called the single mode condition. Optical fibres that support a single mode are called single-mode fibres (SMF), and can be easily fabricated by satisfying the single mode condition. On the contrary, optical fibres that support many modes are called multimode fibres (MMF). The main difference between SMF and MMF is the core size. The core diameter is typically < 10 μm for SMF, e.g., Corning® SMF28e®fibre [164] (a typical SMF and ITU-T G.652.D [165] compliant) the core diameter is 8.2 μm. For MMF, The recommended core diameter is typically 50 or 62.5 μm, e.g., Corning® ClearCurve® fibre (a typical MMF and ITU-T G.651.1 [166] compliant) the core diameter is 50 μm, and Corning® InfiniCor® fibre has a core diameter of 62.5 μm. The value of the cladding radius b is less critical as long as it is large enough to confine the fibre modes, however, a standard value of $b = 62.5\mu m$ is recommended for both SMF and MMF in standards ITU-T G.651 and G.652.

Although there are other types of fibre such as plastic optical fibre which uses plastic, the commonly used low-loss telecommunication fibre is silica fibre whose basic material (substrate) is pure silica glass synthesized by fused silica (SiO_2). The core and cladding can be doped during the fabrication process to achieve higher or lower refractive index than fused silica (≈ 1.44402@1550 nm). Dopants such as GeO_2 and P_2O_5 can increase the refractive index of fused silica, therefore very suitable for core, whilst dopants such as boron and fluorine can decrease the refractive index of fused silica, therefore very suitable for cladding. The widely used core-cladding fibre type can be divided into three categories, (1) doped core with undoped cladding, (2) undoped core with doped cladding, and (3) doped core with doped cladding. The first two types are predominant in modern fibre-optic communications, e.g., commercial available Corning® SMF28e® fibre has a GeO_2 doped core with pure silica cladding. The second type is usually referred as pure-silica core fibre (PSCF) [94, 167-169], which has a pure-silica core and fluorine doped cladding. Other dopants are also used for specific applications, e.g., in fibre amplifiers and lasers the core is codoped with rare-earth ions such as $ErCl_3$ and Nd_2O_3.

There are typically two stages for the fabrication of optical fibres [170]. The first stage is to make a cylindrical fibre preform, normally using a vapour-deposition method such as vapour axial deposition (VAD), outside vapour deposition (OVD), advanced plasma vapour deposition (APVD),modified chemical vapour deposition (MCVD), furnace chemical vapour deposition (FCVD) and plasma activated chemical vapour deposition (PCVD). The latter three methods are very similar. A typical preform is 1-m long with 2-cm diameter. The second stage is to draw the preform into a fibre using a precision-feed mechanism and fed into a furnace. The ratio of core-cladding dimension is preserved during the drawing process. Sophisticated technology is involved in both stages to guarantee the uniformity of the core size, index profile, core-clad concentricity, and cladding circularity [170-172].

5.2 Fundamentals of fibre modes

In an optical fibre, the supported fibre modes can be divided into two categories - guided and unguided modes. Optical fibre can support finite number of guided modes which are well-confined in the core with low loss. For guided modes, the spatial distribution $\mathbf{E}(\mathbf{r},\omega)$ must be a solution of the wave equation [162]

$$\nabla^2\tilde{\mathbf{E}} + n^2(\omega)\frac{\omega^2}{c^2}\tilde{\mathbf{E}} = 0 \tag{5.3}$$

where ω is the frequency. $\tilde{\mathbf{E}}$ is the Fourier transform of the electric field $\mathbf{E}$, i.e.,

$$\mathbf{E}(r,t) = \frac{1}{2\pi}\int_{+\infty}^{\infty}\tilde{\mathbf{E}}(r,\omega)\exp(-i\omega t)d\omega \tag{5.4}$$

Also they must satisfy appropriate boundary conditions. Optical fibre can also support a continuum of unguided radiation modes, which usually lead to power leakage (high loss). Consider the cylindrical symmetry of fibres, Eq. (5.3) can be rewritten with cylindrical coordinates ρ, ϕ and z as

$$\frac{\partial^2\tilde{\mathbf{E}}}{\partial\rho^2} + \frac{1}{\rho}\frac{\partial\tilde{\mathbf{E}}}{\partial\rho} + \frac{1}{\rho^2}\frac{\partial^2\tilde{\mathbf{E}}}{\partial\phi^2} + \frac{\partial^2\tilde{\mathbf{E}}}{\partial z^2} + n^2k_0^2\tilde{\mathbf{E}} = 0 \tag{5.5}$$

where $k_0 = \frac{\omega}{c} = \frac{2\pi}{\lambda}$ is the wavenumber. The wave equation for $\tilde{\mathbf{E}}(r,\omega)$ can be written in a general form as

$$\tilde{\mathbf{E}}_z(r,\omega) = A(\omega)F(\rho)\exp(\pm im\phi)\exp(i\beta z) \tag{5.6}$$

where A is a normalization constant, β is the propagation constant, m is an integer and $F(\rho)$ is the solution of differential equation

$$\frac{d^2F}{d\rho^2}+\frac{1}{\rho}\frac{dF}{d\rho}+\left(n^2k_0^2-\beta^2-\frac{m^2}{\rho^2}\right)F=0 \tag{5.7}$$

The solution of Eq. (5.7) is the well-known Bessel function. The general solution in the core region ($\rho \le a$) can be written as

$$F(\rho)=C_1J_m(\kappa\rho)+C_2N_m(\kappa\rho) \tag{5.8}$$

where J_m is the Bessel function, N_m is the Neumann function, and $\kappa=\sqrt{n_1^2k_0^2-\beta^2}$. C_1 and C_2 are constants determined by the boundary conditions. C_1 can be absorbed into A in Eq. (5.6), therefore

$$F(\rho)=J_m(\kappa\rho), \quad \rho \le a \tag{5.9}$$

In the cladding region ($\rho \ge a$), the solution is the modified Bessel function that decays exponentially for large ρ . Therefore

$$F(\rho)=K_m(\gamma\rho), \quad \rho \ge a \tag{5.10}$$

where $\gamma=\sqrt{\beta^2-n_2^2k_0^2}$. The magnetic field component $\tilde{H}_z$ can be obtained follow the same procedure, and the boundary condition requires $\tilde{E}_z=\tilde{H}_z=\tilde{E}_\phi=\tilde{H}_\phi$ when $\rho=a$ is approached from inside or outside the core. This leads to an eigenvalue equation that determines the propagation constant β for the fibre modes. The eigenvalue equation can be written as [162]

$$\left[\frac{J_m'(\kappa a)}{\kappa J_m(\kappa a)}+\frac{K_m'(\kappa a)}{\gamma K_m(\kappa a)}\right]\left[\frac{J_m'(\kappa a)}{\kappa J_m(\kappa a)}+\frac{n_2^2}{n_1^2}\frac{K_m'(\kappa a)}{\gamma K_m(\kappa a)}\right]=\left(\frac{m\beta k_0(n_1^2-n_2^2)}{an_1\kappa^2\gamma^2}\right)^2 \tag{5.11}$$

where prime denotes differentiation, and from the definition of κ and γ we have the following relation

$$\kappa^2+\gamma^2=(n_1^2-n_2^2)k_0^2 \tag{5.12}$$

The eigenvalue equation Eq. (5.12) usually has more than one solution of β for each integer value of m . Therefore β is rewritten as β_{mn} where m and n are integer

values, and each eigenvalue correspond to a specific mode, HE_{mn} or EH_{mn} [191,173-174]. When $m=0$, these modes are analogous to the transverse electric (TE) and transverse magnetic (TM) modes of a planar waveguide, where the magnetic field are zero. For $m>0$, hybrid modes exist, i.e., all six components of electromagnetic fields $\tilde{E}_\rho, \tilde{H}_\rho, \tilde{E}_\phi, \tilde{H}_\phi, \tilde{E}_z,$ and $\tilde{H}_z$ are nonzero.

5.3 Few-mode fibre for terabit and beyond optical networks

Few-mode fibre (FMF) has been proposed to significantly reduce the system complexity to a manageable level which supports very a small number of modes (e.g., 3 or 5 modes). It has the advantage of better mode selectivity and easier management of the mode impairments. By utilizing mode-division multiplexing (MDM) and multiple-input multiple-output (MIMO) digital signal processing (DSP) technique, it is expected that *N* spatial modes in a FMF can support *N* times the capacity of a SSMF. A typical FMF, such as two-mode fibre (TMF), has a core-size and refractive index slightly larger than single-mode fibre [103]. A TMF in fact supports three spatial modes, LP_{01} and two orthogonal LP_{11} modes. LP_{11} mode is spatially asymmetric and has two degenerated modes, LP_{11a} and LP_{11b} [163,175-178], each support two polarization modes. It is well known that the LP modes are not the strict modes, they are approximate modes classified by the eigenvalues. Conventional modes (TE, TM and HE) can be used for a more rigorous analysis. The relationship between LP mode and conventional mode in a TMF is as follows, LP_{01} (HE_{11}) and LP_{11} (TE_{01}, TM_{01}, HE_{21}). The two-mode condition we found is that the *V* number must be above the single-mode condition ($V > 2.4$) and also below the triple-mode condition ($V < 3.8$).

5.4 Two-mode fibre design

A simple yet practical approach to make a TMF is to design a step-index profile with normalized frequency $2.4 < V < 3.8$, as we have discussed earlier. The TMF we design and fabricated [103] is a customized Ge-doped step-index fibre with a core diameter of 11.9 μm, nominal refractive index step (Δn) of 5.4×10^{-3}, LP_{11} mode cutoff wavelength of 2323 nm and loss of 0.26 dB/km. It has a normalized frequency of V = 3.62. Fig.5.1 shows the simulated modal index vs. wavelength profile based on the parameters of the TMF we designed. The three images to the bottom of Fig.5.1 are measured modal profiles for LP_{01} mode and two degenerate LP_{11} modes. It can be

seen that TMF fibre in fact supports three spatial modes: one LP_{01} mode and two degenerate LP_{11} modes. The parameters of this custom-designed TMF are summarized in Table 5.1. The main feature of our designed TMF is that it has very small coupling and high DMD. The loss parameter α = 0.26 dB/km is also a little bit higher than a typical SSMF due to non-optimized fabrication.

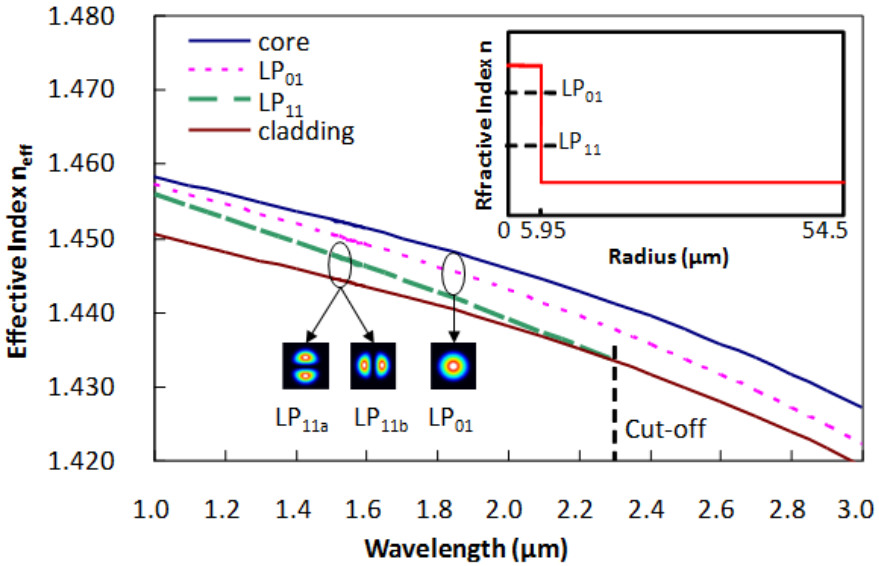

Fig.5.1 Effective modal indices for the LP_{01} and LP_{11} modes of the custom-designed TMF. The inset at the top right shows the step-index profile of the TMF [103].

TABLE 5.1. CUSTOM-DESIGNED STEP-INDEX TWO-MODE FIBRE[103-107]

Parameter	Unit	Value
Spool length	m	4500 and 30000
Core diameter	μm	11.9
Cladding diameter	μm	109
Dispersion LP_{01}	ps/(nm*km)	22.1
Effective area LP_{01}	μm^2	94.7
Dispersion LP_{11}	ps/(nm*km)	17
Effective area LP_{11}	μm^2	99.9
DMD LP_{01}-LP_{11}	ps/m	3.0
LP_{01} Cut-off Wavelength	nm	2323
Fibre Loss(LP_{01},LP_{11})	dB/km	0.26

Many other types of FMF fibres have also been developed by several groups at almost the same time [104-115]. It is worth noting that very recently *OFS* has designed a low-DMD, low-mode coupling and low-loss TMF with graded-index profile and double cladding structure [115]. The parameters of this fibre are also shown in Table

5.2 for comparison. The graded-index core design helps reducing the DMD, and the double cladding structure facilitate low loss for LP_{11} modes, which has become a tendency for FMF design that will be used in future space-division multiplexing (SDM) based high speed optical networks.

TABLE 5.2. *OFS*-DESIGNED GRADED-INDEX TWO-MODE FIBRE[115]. *RED ITALIC VALUES* ARE CALCULATED FROM INDEX PROFILE. BLACK NON-ITALIC VALUES ARE MEASUREMENTS.

Parameter	Unit	Value
Spool length	m	30000
Distributed mode coupling	dB	-25
Dispersion LP_{01}	ps/(nm*km)	20.0/*19.8*
Dispersion slope LP_{01}	ps/(nm^2*km)	0.065/*0.067*
Effective area LP_{01}	μm^2	97/*95*
Dispersion LP_{11}	ps/(nm*km)	*20.0*
Dispersion slope LP_{11}	ps/(nm^2*km)	*0.065*
Effective area LP_{11}	μm^2	*96*
DMD LP_{01}-LP_{11}	ps/m	-0.076/ *-0.081*
Fibre Loss LP_{01}	dB/km	0.198
Fibre Loss LP_{11}	dB/km	0.191
PMD LP_{01}	ps/√km	0.022

5.5 Fibre characterization

5.5.1 Physical properties

The parameters of our custom-designed TMF have been characterized using available testing equipment. The refractive index profile of our designed TMF is first measured, as shown in Fig.5.2. A reflective surface scanning method is used and the wavelength of scanning laser beam is at 670 nm.

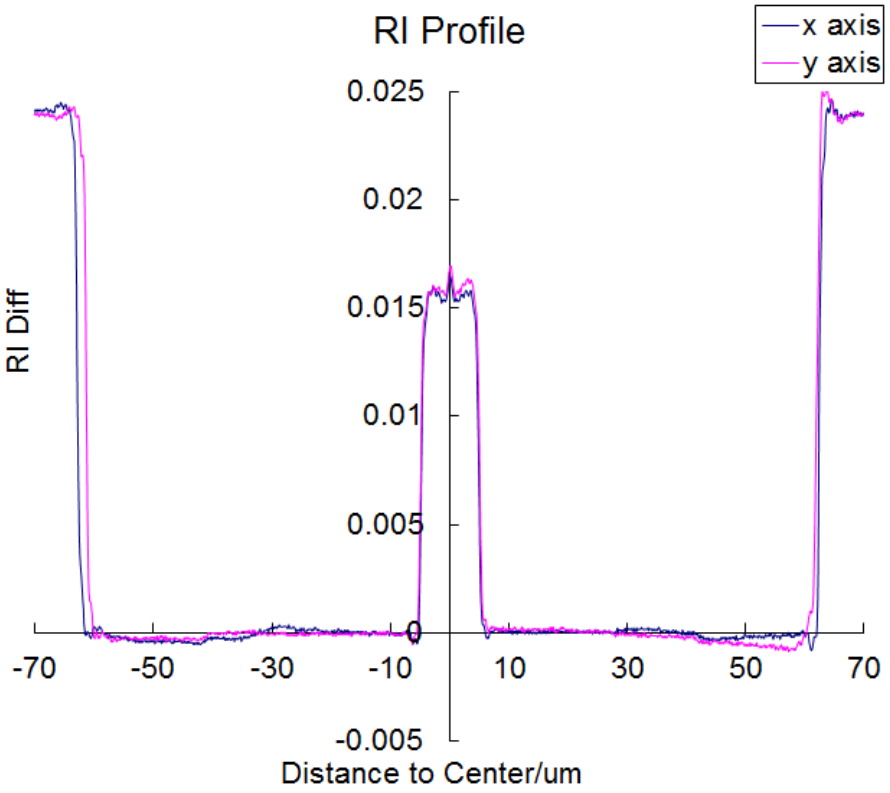

Fig.5.2 Measured refractive index profile of the custom-designed two-mode fibre [103].

Then we measure the mode profile of TMF. We use centre launch technique to generate LP_{01} mode. Then we use mode converter to generate pure LP_{11} mode source. The far field mode pattern is observed at the end facet of a 1-m TMF with an image system and an infrared camera, as shown in Fig.5.3.

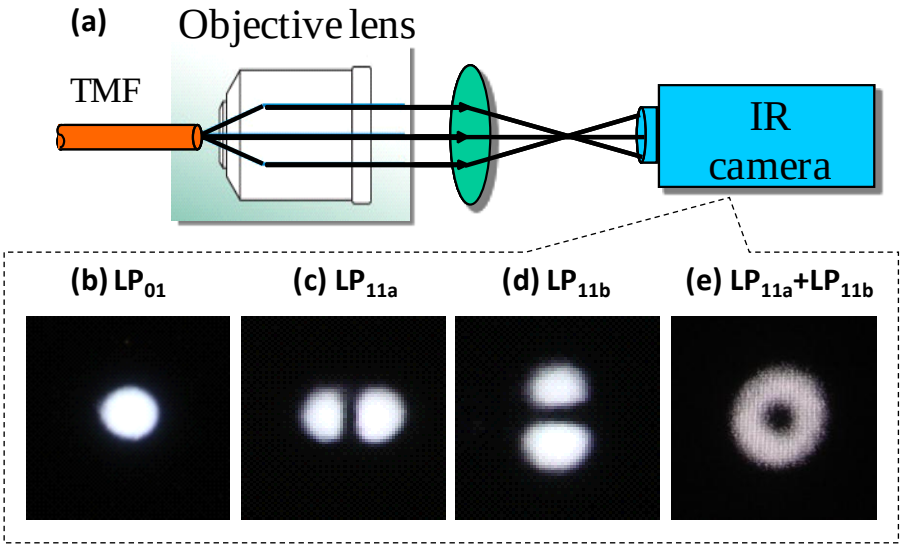

Fig.5.3 (a) Experimental setup for the measurement of mode profile. (b)-(e): Measured mode profile of the custom-designed two-mode fibre [103]. (b) LP_{01} mode, (c) LP_{11a} mode, (d) LP_{11b} mode and (e) LP_{11a}+LP_{11b} mode.

5.5.2 Characterization of linear impairments

We first measure the loss of fibre. The loss can be estimated by the equation

$$\alpha = \left(P_{in} - P_{out}\right) / L \tag{5.13}$$

where in the case of TMF, there are two loss parameters for the two eigen modes - LP_{01} and LP_{11}. We first launch pure LP_{01} mode into a 4.5km TMF-span through centre launch technique and measure the loss using an Optical Time Domain Reflectometer (OTDR), which gives us a value of around 0.26 dB/km. Then we launch pure LP_{11} mode into the same 4.5 km TMF-span with a mode converter (MC) which will be discussed later in Section 6.2.2. The loss value we found for LP_{11}mode is almost the same as in LP_{01} mode scenario, which confirms good design of our TMF.

Then we estimate the chromatic dispersion (CD) parameter for LP_{11} mode. Since CO-OFDM is a powerful tool for the performance monitoring of channel impairments in a transmission link, and we have 4×4 MIMO CO-OFDM setup with signal processing, readily available we choose to launch dual-LP_{11} mode to demonstrate MDM transmission over 4.5 km TMF, while we have also estimated the chromatic dispersion parameter from channel matrix during channel estimation [104], as will be discussed later in Section 7.2. Using polynomial curve fit of the phase angle of the diagonal components (H_{11}, H_{22}, H_{33} *and* H_{44}), the second order coefficient p_2 is calculated to be 2×10^{-5} which corresponds to the accumulated CD of 28.9 *ps/nm/km*.

The differential-modal-delay (DMD) between the LP_{01} and LP_{11} modes is estimated by inserting a broadband light source (black line in Fig.5.4(b)) into a 1-m-long TMF with core-position offset such that both modes are excited, and then measuring the coherent mode beating period from output of the TMF (green line in Fig.5.4(b)) [179]. The beating period of 2.7 nm observed on the OSA is inversely proportional to the modal delay, which is 3.0 ps in this case. This measured modal dispersion (3.0 ps/m) of the TMF corresponds to a group index difference of 8.8×10^{-4}.

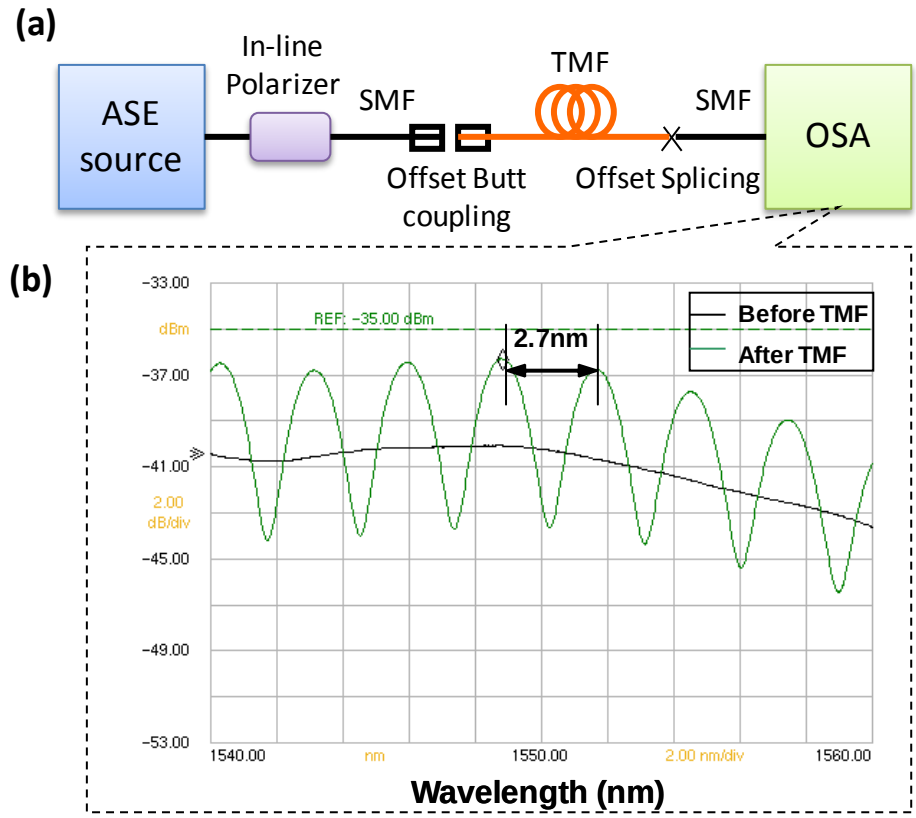

Fig.5.4 (a) Experimental setup for the measurement of DMD between LP_{01} and LP_{11} modes through coherent beating. (b) Optical spectrum before (black line) and after (green line) a 1-m-long TMF fibre measured with an OSA. The spectral power before TMF was scaled to be in the same region as after TMF and does not reflect the real power level.

In addition, we have also estimated the mode beat length of our TMF. The LP_{01}/LP_{11} mode beat length is given by [176-178]

$$L_B = 2\pi / (\beta_0 - \beta_1) \tag{5.14}$$

The value of L_B is first theoretically calculated using the refractive index profile of our TMF and the result is 526 μm. Then we fabricate metal gratings which different pitch size from 500~520 μm to make mode converters as will be discussed in Section 6.2.2. Maximum extinction ratio(ER) can be achieved when the grating pitch exactly matches the beat length $L_{B,}$ which can be used as an indication of the real L_B value. It is found that L_B is in the range of 510~520 μm at the wavelength of 1.55 μm. The corresponding effective modal index difference Δn_{eff} is 2.98×10^{-3}, which agrees with the calculation in Fig.5.1.

5.6 Conclusion

In this chapter, we show the design of the most basic but critical element in a space-division multiplexing (SDM) system – few-mode fibre. First we have reviewed the history and fundamentals of optical fibre and fibre modes. Then we show the parameters of our custom-designed TMF. Finally the characterization of TMF is given including physical properties and linear parameters. Our designed TMF has been used in several proof-of-principle mode-division multiplexing (MDM) experiments (Chapter 7), which shows the successful design and good quality.

6 Fundamentals of Space-Division Multiplexing and Design of Few-Mode Components

In optical communication scenario, space-division multiplexing (SDM) can be realized either on a multi-core fibre (MCF) with many fibre cores where each core acts like a single mode fibre, or on a multimode fibre (MMF) where a number of transverse modes are propagated simultaneously.

6.1 Architecture of SDM based high speed superchannel system

The concept of a SDM based superchannel system is that the wavelength channels containing all the modes are routed as one entity which is subsequently optically added/dropped [107] and amplified without mode-multiplexing/de-multiplexing (MMUX/MDEMUX) during transmission, as shown in Fig.6.1.The analogy can be drawn between such a SDM fibre-based system and polarization division-multiplexed (PDM) system where the two polarizations are not separately processed during the transmission, which greatly simplifies the system design while doubling the system capacity. The advantage of SDM based superchannel transmission is that it utilizes all the dimensions of the optical light so that the system capacity is greatly increased, while the wavelength, polarization and spatial mode are treated as an entity so that the system complexity is maintained at very low level. The SDM fibre compatible ROADM is a key enabling component towards the realization of SDM based superchannel system, and the first step of such a FMF-compatible OADM has been demonstrated recently in [107].

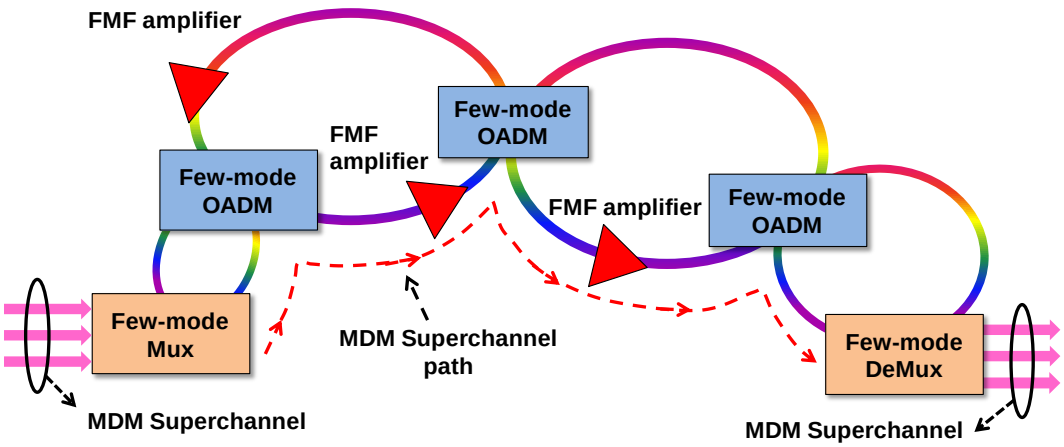

Fig.6.1 Conceptual diagram of FMF based SDM superchannel transmission utilizing few-mode compatible ROADM.

The architecture of $N \times N$ SDM based superchannel system is further illustrated in Fig.6.2. The signals are first generated by N transmitters. Mode multiplexing of the N signals is achieved using the MMUX. The signals carried by different spatial modes are then launched into the SDM fibre. After SDM fibre transmission, the received signals are then mode de-multiplexed by a MDEMUX. The de-multiplexed signals are then detected by N coherent receivers. The signals are converted from optical-to - electrical domain, sampled by a digital oscilloscope or high speed ADCs, and finally processed using a DSP module. MIMO algorithm is used for compensating the mode coupling and/or crosstalk in the channel that may be introduced in MMUX/MDEMUX or SDM fibre. It is expected that if the MMUX/MDEMUX has a unitary transfer function with a freedom of N equals to the number of modes supported in a SDM fibre, the channel capacity can be increased by a factor of N times that of single mode system [180].

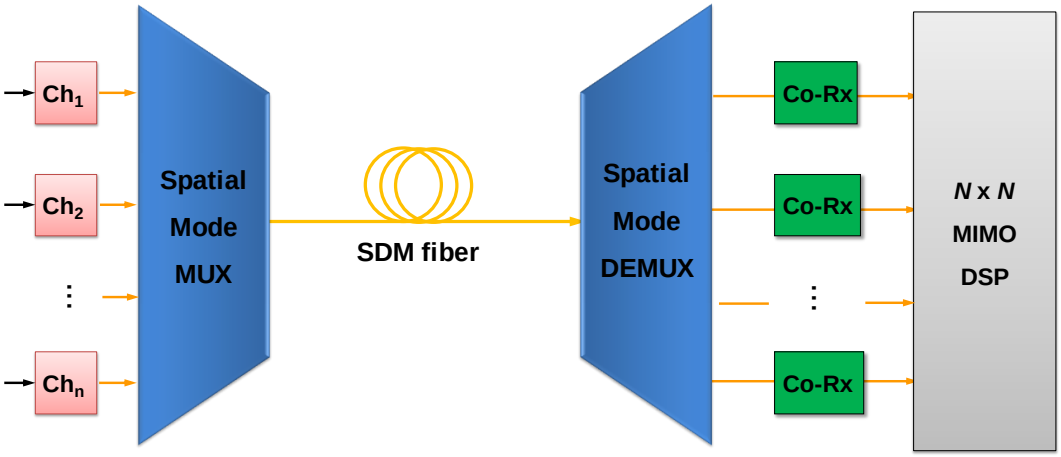

Fig.6.2 Architecture of $N \times N$ SDM based superchannel transmission utilizing coherent MIMO digital signal processing. MUX/DEMUX: multiplexer/demultiplexer, Co-Rx: coherent receiver.

6.2 Few-mode components

6.2.1 Mode stripper

The mechanism of MS is by using macro-bending to strip out higher order modes. The macro-bending loss model is given by [181]. For our experiments, the MS is made by wrapping 20 turns of the bare TMF or 0.9-mm jacketed TMF around a 9-mm diameter post. The excess loss of the MSs are measured to be within 0.2~0.4 dB. The attenuation for LP_{11} mode in a MS can be as high as 1,500~2,200 dB theoretically

over the whole C-band. The rejection ratio we measured in experiment is ≥30 dB which is a very conservative result due to the limitation of devices.

6.2.2 Mode converter

The main purpose of the MC is to convert optical signals from LP_{01} to LP_{11} mode, or vice versa. There are various methods that can realize LP_{01}/LP_{11} mode conversion such as microbending [176, 182], periodic mechanical pressure [183 - 184], and refractive index modulation induced by lasers [185] on a FMF or TMF fibre. The resonant coupling happens when the grating pitch Λ equals to the beat length $L_B = 2\pi/(\beta_{01} - \beta_{11})$, where β_{01} and β_{11} are the propagation constants of the LP_{01} and LP_{11} modes [176-178]. Fig.6.3 shows the physical design of the MC. The TMF we use is a 4.5-km Ge-doped step-index fibre with a core diameter of 11.9 μm and nominal refractive index step (Δn) of 5.4×10^{-3}, LP_{11} mode cut-off wavelength is 2323 nm and loss of 0.26 dB/km. The measured differential-modal delay (DMD) is 3.0 ns/km and mode beat length L_B is around 524 μm. The large DMD results in very small modal mixing in our TMF due to large mismatch of modal effective indices [178]. To simplify the analysis here we only consider the deformation effect formed in a mode converter. The simulation is based on beam propagation method [186] and the core deformation is assumed to be an s-bend arc shape as shown in Fig.6.3. The coupling efficiency depends on the coupling length with various core deformation defined by the radius of the s-bend arc (r = 0.08, 0.1 and 0.2 μm) is shown in Fig.6.4. We find out that the optimum coupling length is inversely proportional to the core deformation radius r, and for a 0.2 μm deformation the optimum coupling length is 8.1 mm, which assures that our MC can be very compact. Fig.6.5 shows the wavelength dependence of coupling efficiency at a coupling length of 8.1 mm (~15.5 ridges) and core deformation of 0.2 μm. Fig.6.6 shows the extinction ration (ER) vs. wavelength under the same coupling length and core deformation. The extinction ratio is defined as the power ratio between LP_{11} mode and LP_{01} mode after mode conversion. It can be seen that theoretically the ER can be very high around 1550 nm and maintain above 20 dB for more than 10-nm wavelength range. In light of the simulation result, we fabricated 4 metal gratings with 20 evenly-spaced grooves on one polished surface. The groove pitch is controlled to be $\Lambda_0 = 510 \pm 5\mu m$. All four MCs are made as follows: first we place a 0.9-mm jacketed TMF onto an aluminium

slab with tape. The TMF and grating are then mounted between a 3-axis stage and L-shape steel. The angle between grating and fibre and applied pressure can be controlled by the stage and the position of fibre. The angle between grating and fibre determines the effective pitch $\Lambda = \Lambda_0 / \sin\theta$ where Λ_0 is the original pitch size of the grating and θ is the angle. After appropriate adjustment of the stage and position of the fibre, maximum coupling ratio and ER for all MCs occur at around 1550 nm. The measured ERs are also shown in Fig.6.6, and it is confirmed that ER can be maintained beyond 20 dB for a 13-nm wavelength range. The best ERs of 26.8, 22.8, 24.6, and 24.3 dB for MCs 1-4 occur at 1551 nm. One of our fabricated MCs is demonstrated in Fig.6.7.

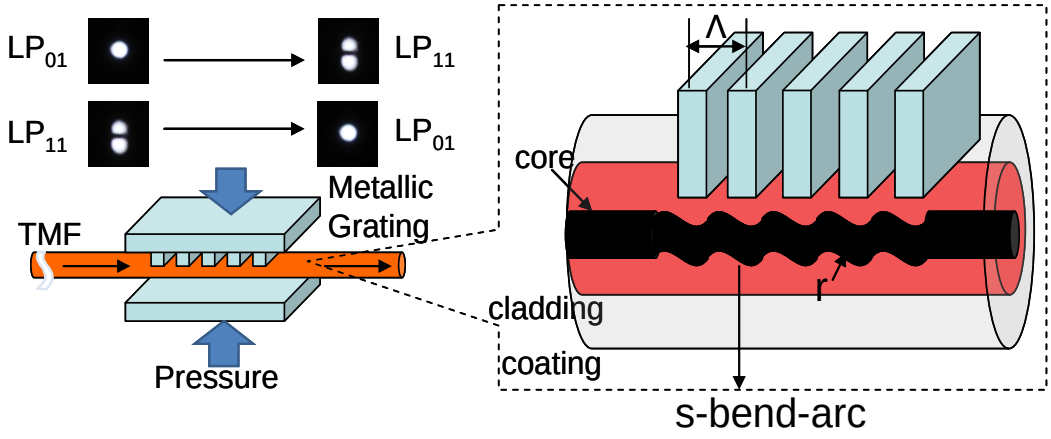

Fig.6.3 Schematic diagram of a LPFG based LP_{01}/LP_{11} mode converter. The groove pitch Λ and pressure can be adjusted for optimization for certain wavelength or conversion ratio. The deformation of fibre core is assumed to be s-bend arc shape with radius r.

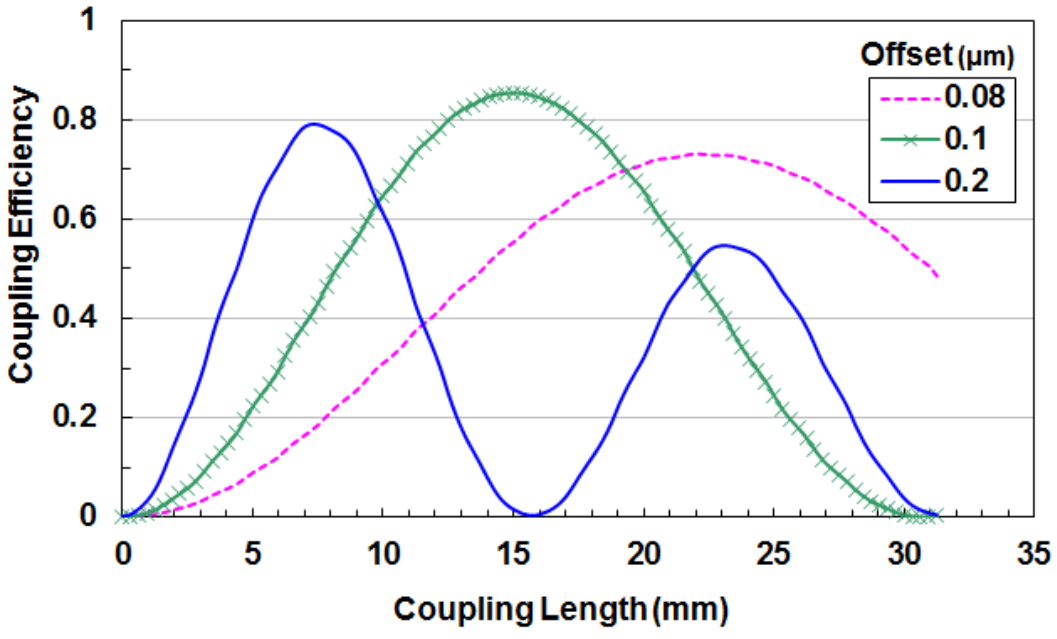

Fig.6.4 Simulated coupling efficiency (LP_{01} to LP_{11}) versus effective coupling length for a LPFG-based mode converter under the grating pitch $\Lambda = 524\ \mu m$, at wavelength of $\lambda = 1550\ nm$. The three curves correspond to the core deformation radius of $r = 0.08,\ 0.1$ and $0.2\ \mu m$, respectively.

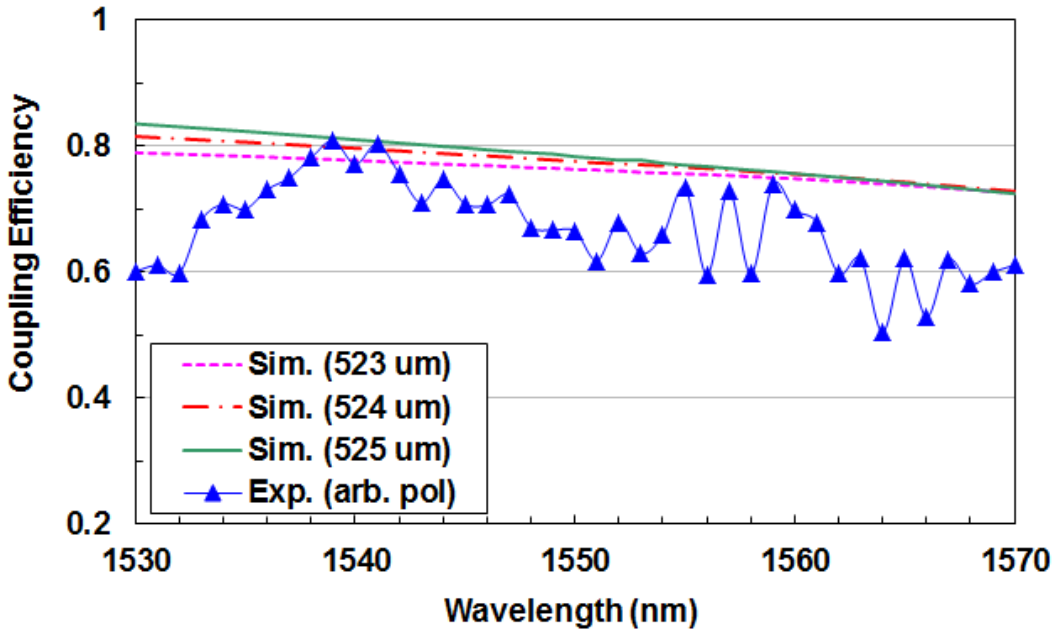

Fig.6.5 Coupling efficiency (LP_{01} to LP_{11}) versus wavelength for a LPFG-based mode converter with core deformation $r = 0.2\ \mu m$. Sim.: Simulation; Exp.: Experiment.

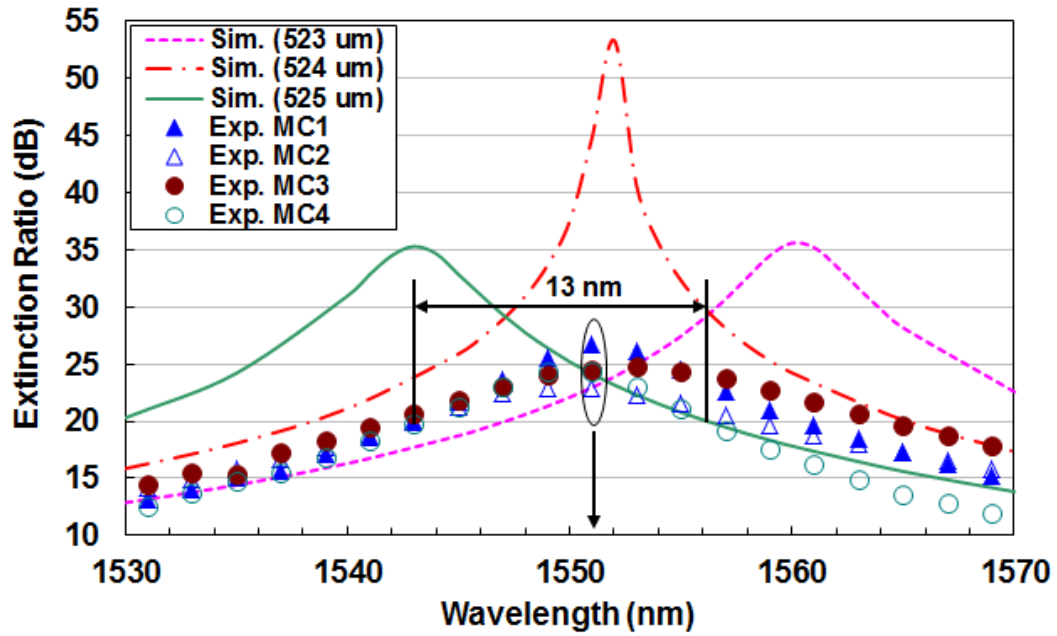

Fig.6.6 Extinction ratio versus wavelength for a LPFG-based mode converter with core deformation $r = 0.2\ \mu m$. Sim.: Simulation; Exp.: Experiment.

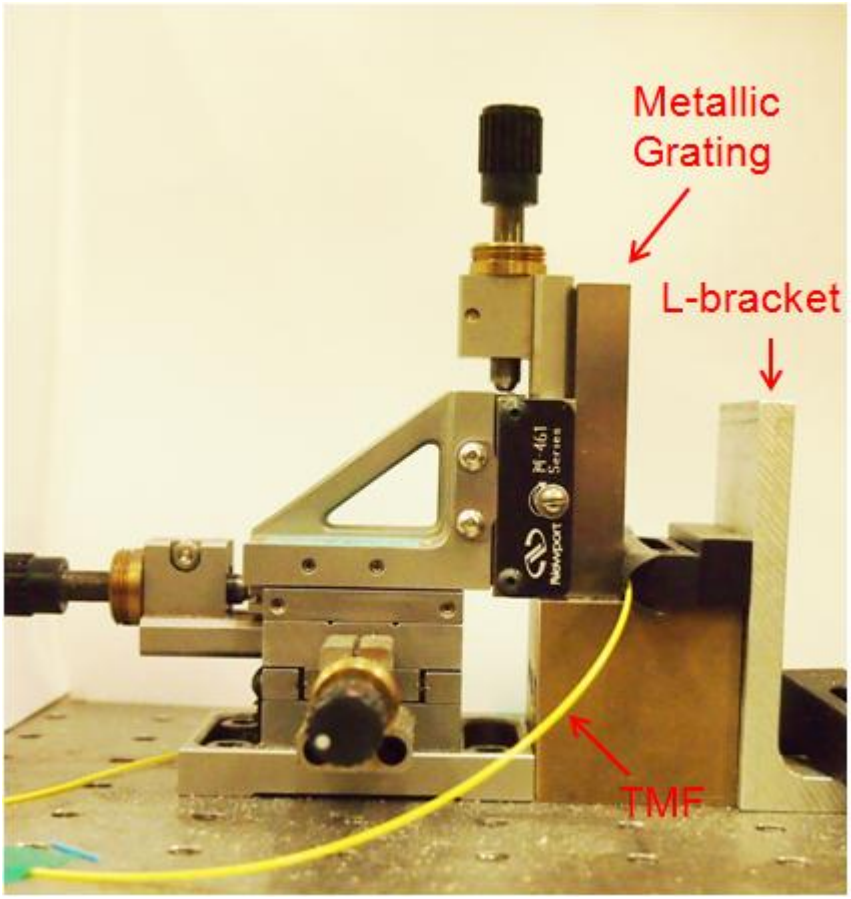

Fig.6.7 Lab demonstration (side view) of a LPFG based LP_{01}/LP_{11} mode converter.

6.2.3 Mode combiner

In order to appropriately design a spatial mode combiner (SMC), we first examine the application of SMC from system point of view. Fig.6.8 shows conceptual diagram of coherent MIMO transmission systems (e.g., OFDM system [17-18]) based on TMFs. The input data are first carried over six coherent transmitters, modulated and up-converted to optical domain, and then polarization multiplexed (Pol-Muxed) through polarization-beam combiners (PBCs) to a SSMF fibre. The three SMFs with Pol-Muxed signal are fed into a SMC. At the output of the SMC, the input signals are already coupled into LP_{01}, even LP_{11} (LP_{11a}) and odd LP_{11} (LP_{11b}) modes in the TMF. Similarly, at the receive side, the three spatial modes in TMF are first split and coupled into three SSMF fibres through a spatial mode splitter (SMS), subsequently polarization de-multiplexed and received by six coherent receivers, and finally down-converted and de-modulated to electrical domain and processed with electronic DSP using MIMO signal processing.

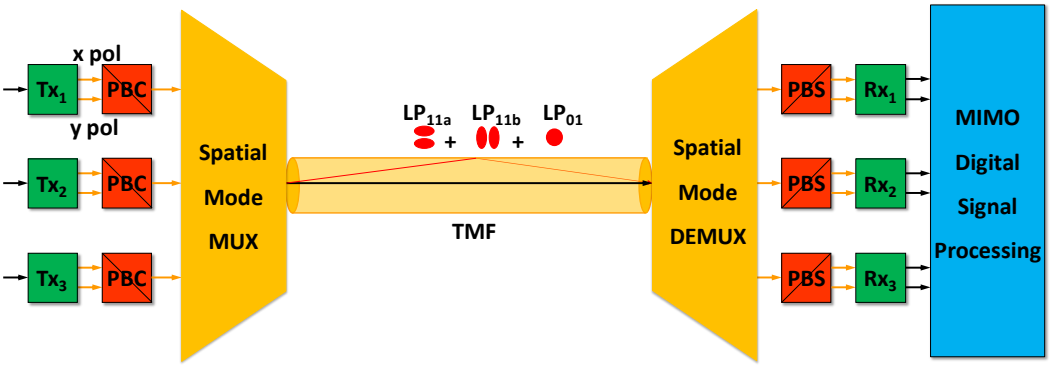

Fig.6.8 Block diagram of a coherent MIMO system over a two-mode fibre (TMF). Middle inset shows three possible spatial orientations: LP_{01}, LP_{11a} and LP_{11b}. PBC/PBS: polarization beam combiner/splitter. MUX/DEMUX: multiplexer/de-multiplexer.

The main function of SMC/SMS is to couple optical signals of LP_{01} mode of three SMFs at the input into LP_{01}, LP_{11a} and LP_{11b} modes of the TMF at the output, or other way around.

6.2.3.1 Free Space Mode Combiner

The mode combiner/splitter is comprised of two 2-axis precision stages, one beamsplitter (BS) and three collimating lenses as shown in Fig.6.9. The signal is polarization multiplexed and mode converted before entering into the mode combiner. The two input TMFs that carry either LP_{11a} or LP_{11b} modes generated by MCs are connected with the two input ports of the mode combiner, whose position can be manually aligned by the precision stages. Output port of the mode combiner is fixed using a fibre collimator and connected with the 4.5-km transmission fibre. The input signal is first collimated to a spot size of diameter of 2 mm by one of the movable collimating lens with numerical aperture NA = 0.25 and effective focal length f = 11.0 mm. The collimated beam is subsequently passing through the BS in either transmission or reflection direction, and finally focused onto the core of the output fibre by another lens inside the packaged collimator. The BS is polarization insensitive with less than 5% difference in transmission for s- and p-polarization at 1550 nm. The input and output of TMFs are connectorized before mounted onto the stage with a FC-type adapter. The connectors are specially designed with an adjustable key so that the fibre can be axially rotated. By adjusting the key of the connectors, the orientation of the two LP_{11} modes can be manipulated to be orthogonal (90^o) to each other. An IR camera is placed in the unused path of the BS to monitor the orientation and orthogonality of the two LP_{11} modes, as shown in Fig.6.9.

Fig.6.10 is the lab demonstration of our assembled free-space mode combiner. The loss in the reflection / transmission path of the BS is estimated to be about 3.5 / 4.5 dB, and the loss of the focusing system due to misalignment and Fresnel reflection is around 1 dB. The 1-dB power difference of the two paths is balanced using SMF attenuator before mode conversion. It is also possible to upgrade to a 3×1 mode combiner by introducing another set of precision stage and collimating lens together with one more BS, which we will apply in the future for triple-mode transmission experiment (LP_{01} + LP_{11a} + LP_{11b}). The mode splitter has the same structure as the combiner except that it is operated in opposite direction.

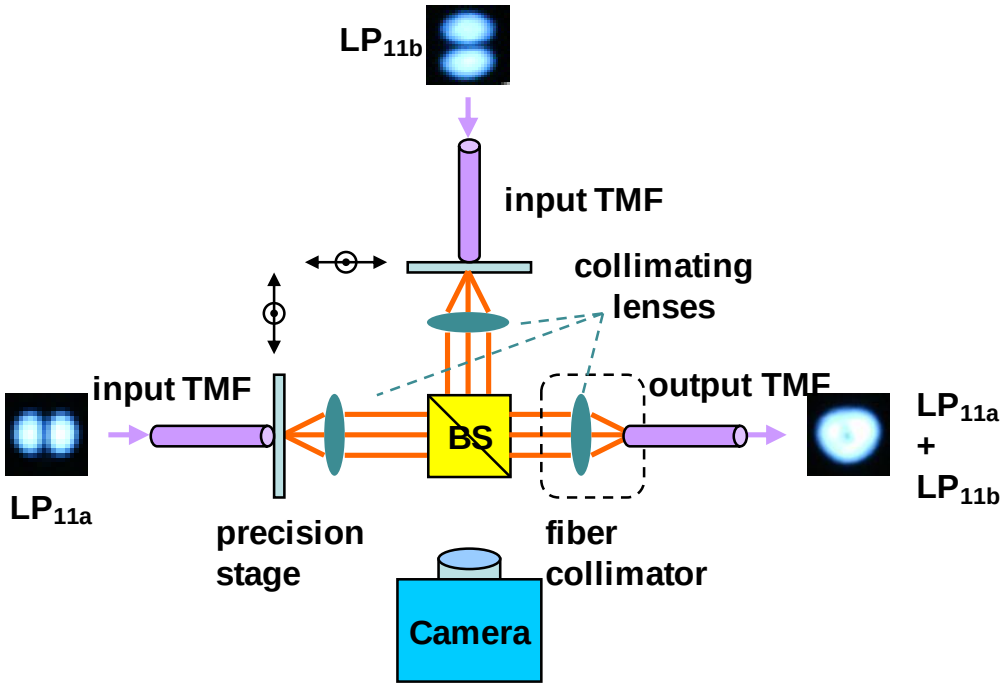

Fig.6.9 Schematic diagram of a free-space mode combiner. BS: beamsplitter. The precision stages have freedom of two-axes (X and Y. Z is the light propagation axis). The beams are collimated before entering the BS to minimize the divergence and distortion.

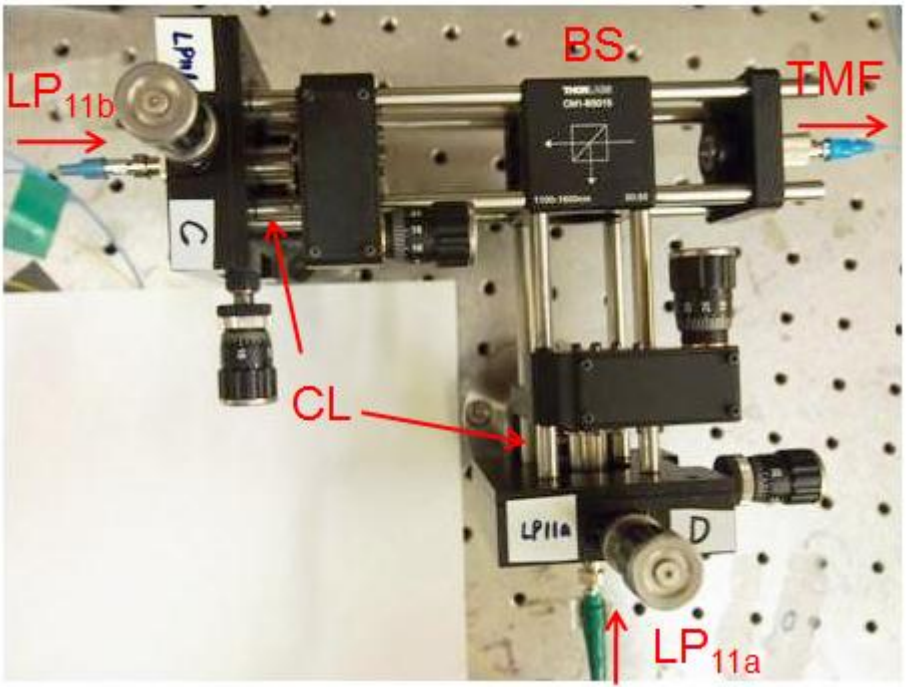

Fig.6.10 Lab demonstration (top view) of a free-space mode combiner.

6.2.3.2 Fused Fibre Mode Combiner

The disadvantage of using free-space SMC/SMS is that it is bulky and high loss due to the BS. To overcome this problem, recently we have proposed a fused-fibre based mode coupler [187]. A similar type of mode selective coupler (MSC) has been proposed as a mode multiplexing component to combine or split LP_{01} and LP_{11} modes in [188] about ten years ago. However, the coupler was based on highly elliptical core fibres, where the odd LP_{11} mode (along minor axis) was intentionally cut off to avoid interference to the even (along major axis) LP_{11} modes, and therefore combing two spatial LP_{11} modes is not being considered. In our work, we propose a MSC design supporting both LP_{11} spatial modes. There are two motivations to support both LP_{11} spatial modes from transmission point of view. First, accommodating one more LP_{11} mode can increase the capacity to triple instead of double of that of SSMF. Second, two degenerate LP_{11} modes actually have much less mode dispersion than that between LP_{01} and LP_{11} modes, and perhaps it is quite plausible to support transmission using only these two degenerated spatial modes. To enable the transmission of two LP_{11} modes, the LP_{11} spatial mode combiner and splitter are critical to selectively couple into the two lode orientations of LP_{11} mode with low interference.

Fig.6.11(a) shows one design of the SMC/SMS consisted of cascaded LP_{11} mode combiner: coupler-1 and -2, shown in Fig.6.11(b) an (c) respectively. It is well known that a mode selective coupler can be made by satisfying the phase-matching condition [189-193].According to the coupled-mode theory the power coupled between any two modes is given by [189-193]

$$P_c = P_0 \frac{\sin^2[\sqrt{\kappa^2 + (\Delta\beta/2)^2}L]}{1+(\Delta\beta/2\kappa)^2} \tag{6.1}$$

where P_c is the coupled power, P_0 is the initial power in the input mode, κ is the coupling coefficient per unit length, $\Delta\beta$ is the phase mismatch between the two modes $\Delta\beta = \Delta n_{eff} 2\pi/\lambda$, Δn_{eff} is the effective refractive index (also called modal index) difference between the two modes, and L is the coupling length. This formula might not be strictly valid if there exist more than two modes, but we can use Eq. (6.1) as a rough estimation of the coupling performance for our mode combiner. From Eq. (6.1) we can see that when the phase mismatch between the two modes is very small ($\Delta\beta \approx 0$) the coupled power becomes $P_c = P_0 \sin^2(\kappa L)$. Obviously, if the coupling coefficient κ is constant, we can obtain almost 100% power coupling to the target mode if the phase mismatch between the initial mode and target mode is very small whereas phase mismatch to other modes is large. In a circular-core TMF(c-TMF), the two eigen spatial orientations of LP_{11} mode, LP_{11a} and LP_{11b}, have similar modal indices, and therefore the two modes are coupled to each other as they propagate along the fibre and the intensity distribution is not maintained [176]. However, in an e-TMF, the two LP_{11} modes split and their spatial orientations can be maintained for a long distance with one mode along the major axis(LP_{11a}) and the other minor axis (LP_{11b}) [175-177]. We therefore design an e-TMF such that the modal indices of the two spatial modes are well separated but not being cut-off. The e-TMF has a core radius of 6.5 × 4.5 μm, and the cladding diameter is standard 125 μm. It has a step index profile with a fractional index difference $\Delta = 0.47\%$ at 1550 nm. We use alternating direction implicit (ADI) method and six eigen modes (three spatial orientations, each can have two polarizations) were found with three x-polarization modes and three y-polarization modes, as shown in Fig.6.12. Here we denote the major axis of core as x and the minor axis as y. Fig.6.13 shows the modal indices of the three TE modes of the e-TMF with respect to the wavelength. For TM modes the

modal indices are almost the same as their TE counterpart. The modal indices of the two LP_{11} mode spatial orientations are well separated. With the knowledge of modal indices of the two spatial orientations, we can readily design the two SMFs to match the phase velocities of LP_{11a} and LP_{11b}. We choose two Corning's SMF-28e fibre ($r = 4.1\mu m$ and $\Delta = 0.36\%$) and reduce their core diameters to 89.2% (SMF_a) and 62.9% (SMF_b) of their original size by pre-pulling. The modal index mismatch between LP_{01} of SMF_a ($LP_{01(a)}$) and LP_{11a} of e-TMF, or LP_{01} of SMF_b ($LP_{01(b)}$) and LP_{11b} of e-TMF, is estimated to be both less than 10^{-5}. In addition to the phase-matching condition, because LP_{11} mode is spatially asymmetric, the coupling is also sensitive to the position where we place the single-mode fibre. Ideally for LP_{11a} mode we align SMF_a along the x-axis, and for LP_{11b} mode we align SMF_b along the y-axis, where we obtain best coupling performance and discrimination against the other mode.

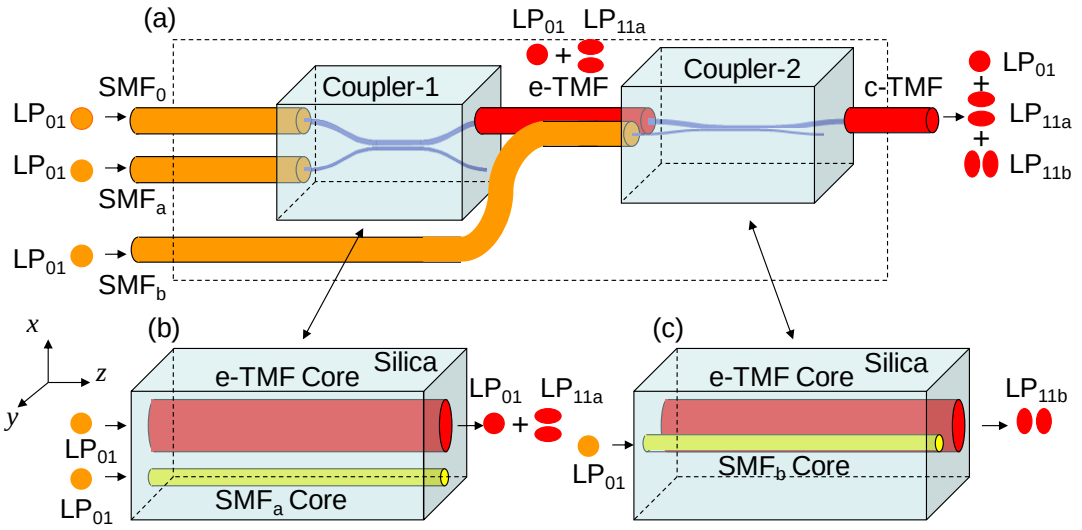

Fig.6.11 (a) Mode selective combiner consisting of cascaded LP_{11} mode combiners. c(e)-TMF: circular(elliptical)-core TMF. (b) coupler-1, couples LP_{01} mode of SMF_a to LP_{11a} mode of e-TMF; (c) coupler-2, couples LP_{01} mode of SMF_b into LP_{11b} mode of e-TMF.

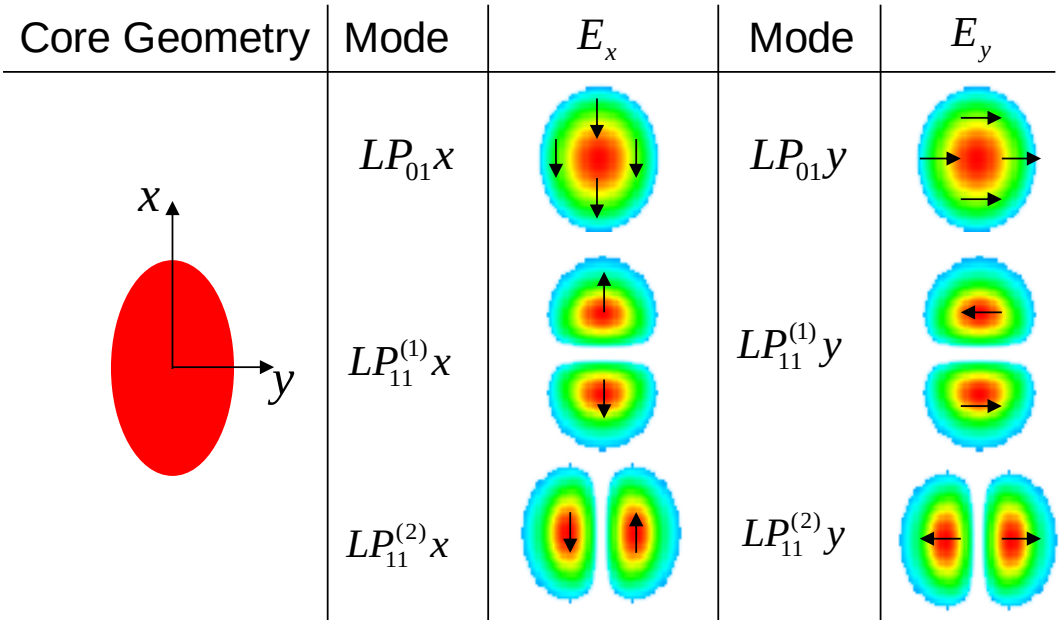

Fig.6.12 Fibre core geometry and eigen modes in an e-TMF.

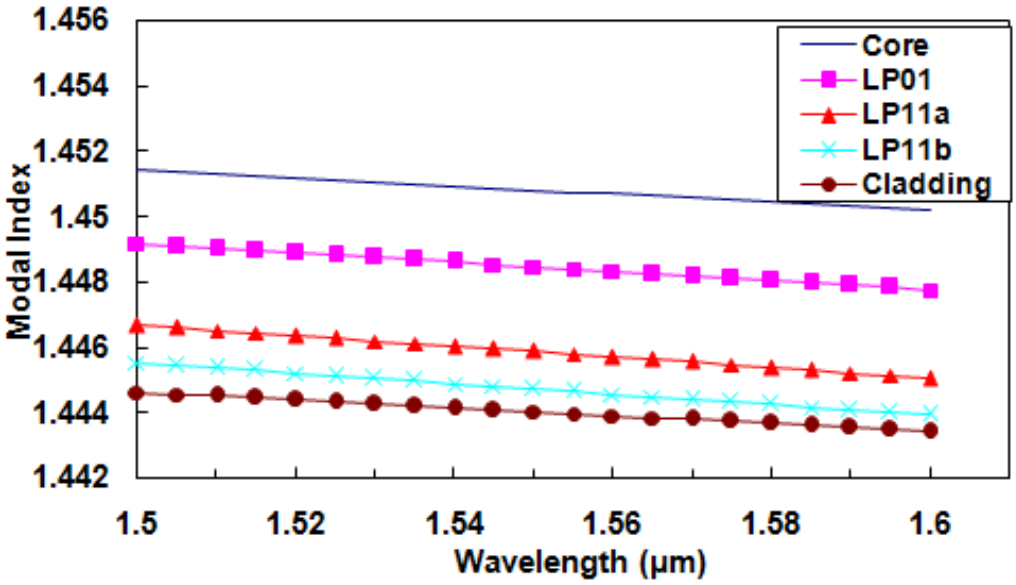

Fig.6.13 Modal index as a function of wavelength for TE modes in an e-TMF.

We first analyse the coupling efficiency and extinction ratio with a simple parallel line setup, as shown in Fig.6.11(b) and (c). The space between two fibre cores is first set constant at 15 μm that is feasible to achieve with most standard fused biconic tapering (FBT) stations [102]. The parameters we used for simulation are as follows: designed waveguide is made of pure silica with a wafer length of 30 mm and a width of 125 μm. At the output port of SMC the e-TMF is connected to a circular core two-mode fibre ($r = 6.2\ \mu m$), which will be used for transmission. The simulation mode was set to 401 × 401 points in mesh, and propagation step is 10μm. We assume an

initial $LP_{01}x$ mode launched into the SMF, and the coupling efficiency dependence on the coupling length is shown in Fig.6.14 and Fig.6.15 at wavelengths of 1.505, 1.55 and 1.6 μm. It can be seen that almost 100% power has been coupled into only one ($LP_{11a}x$) mode, who has phase constant, polarization same as the launched mode $LP_{01}x$, and spatial orientation with the same axis as two fibre cores are aligned (axis x for coupler 1 as shown in Fig.6.11(b)). The result can be explained by Eq. (6.1) and the nature that if the TMF fibre core is intentionally designed to have high ellipticity, it will become a mode- maintaining fibre due to the high birefringence. The axis that two fibre cores are aligned would dominate mode orientation that has the highest coupling efficiency. The result for coupler 2 is also given in Fig.6.16 and Fig.6.17. From Fig.6.14 and Fig.6.16, an optimal coupling length can be chosen and the coupling efficiency at various wavelengths can be studied at the optimal coupling length. In addition to the coupling power, we are also interested in the inter-channel interference (ICI) in the coupler which is characterized by extinction ratio (ER). The extinction ratio is defined as $ER = P_1/P_2$, where $P_1$is the power coupled to specific mode with specific polarization, P_2 is the power coupled to all other modes and/or polarization. The wavelength dependence of ER is shown in Fig.6.18 and Fig.6.19. We find out that the achievable ER at the first maximum ($L = 3\ mm$) is above 20 dB and 19 dB for coupler-1 and -2, respectively. This result confirms that although the coupling performance depend strongly on the working wavelength and coupling length, by appropriate design the ER can maintain at very high value. Therefore we conclude that our designed MSC could have potential applications in two-mode fibre based optical transmission system [102-113].

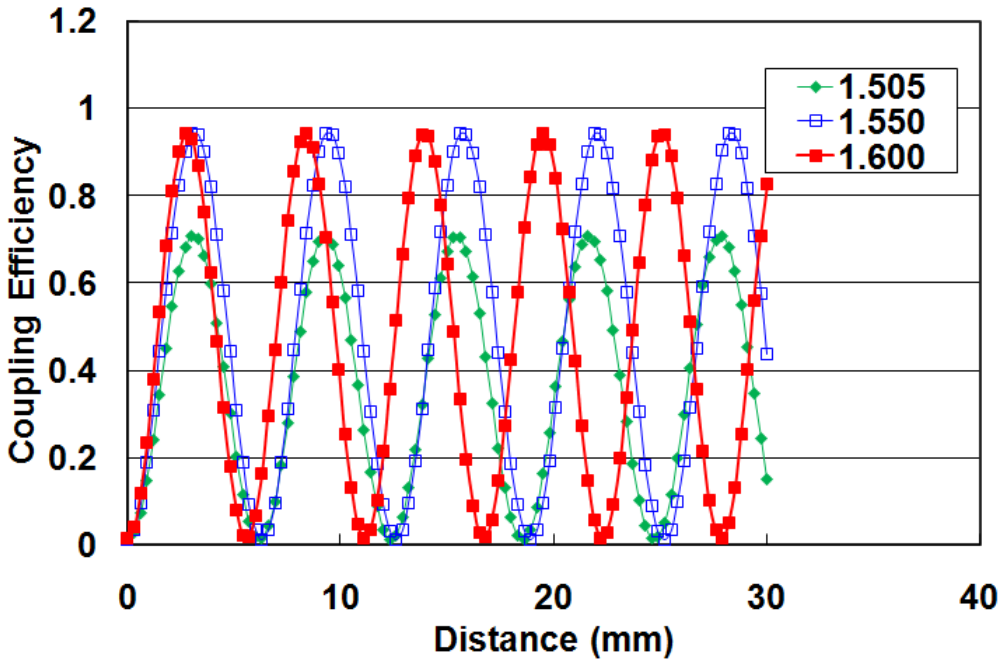

Fig.6.14 Normalized power coupled into $LP_{11a}x$ mode (target mode) as a function of coupling length for coupler-1.

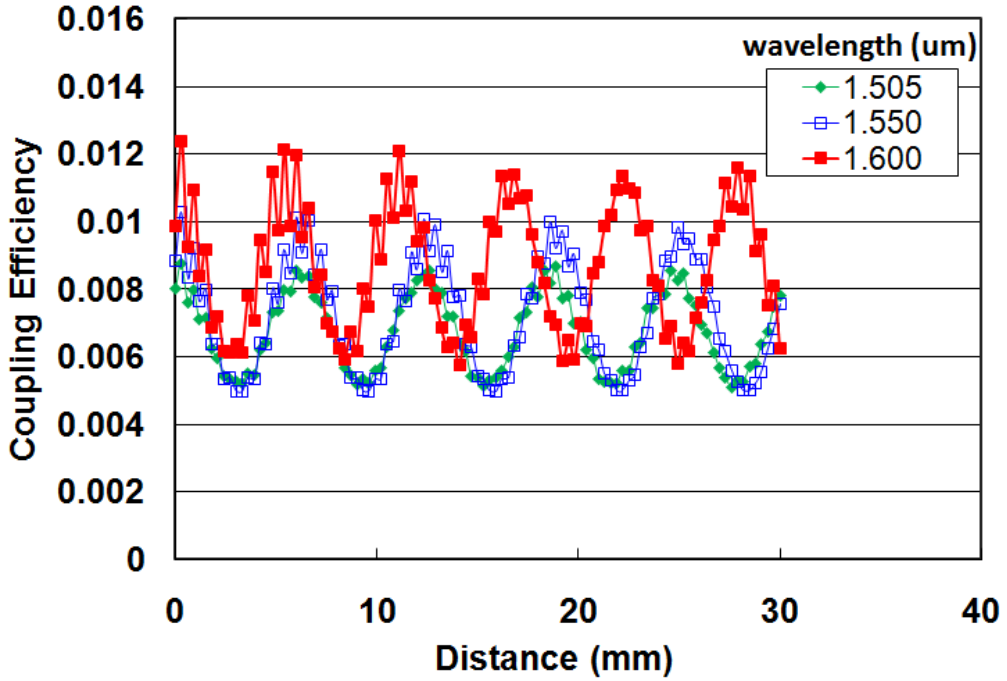

Fig.6.15 Total power coupled into other modes: $LP_{01}x$, $LP_{01}y$, $LP_{11a}y$, $LP_{11b}x$, and $LP_{11b}y$ as a function of coupling length for coupler-1.

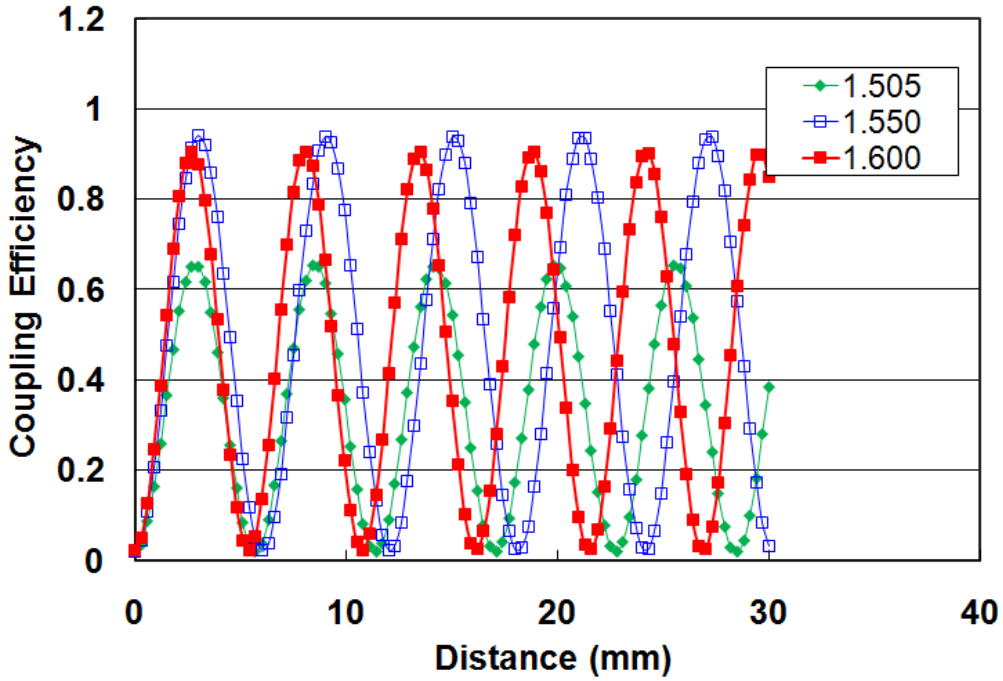

Fig.6.16 Normalized power coupled into $LP_{11a}y$ mode as a function of coupling length for coupler-2.

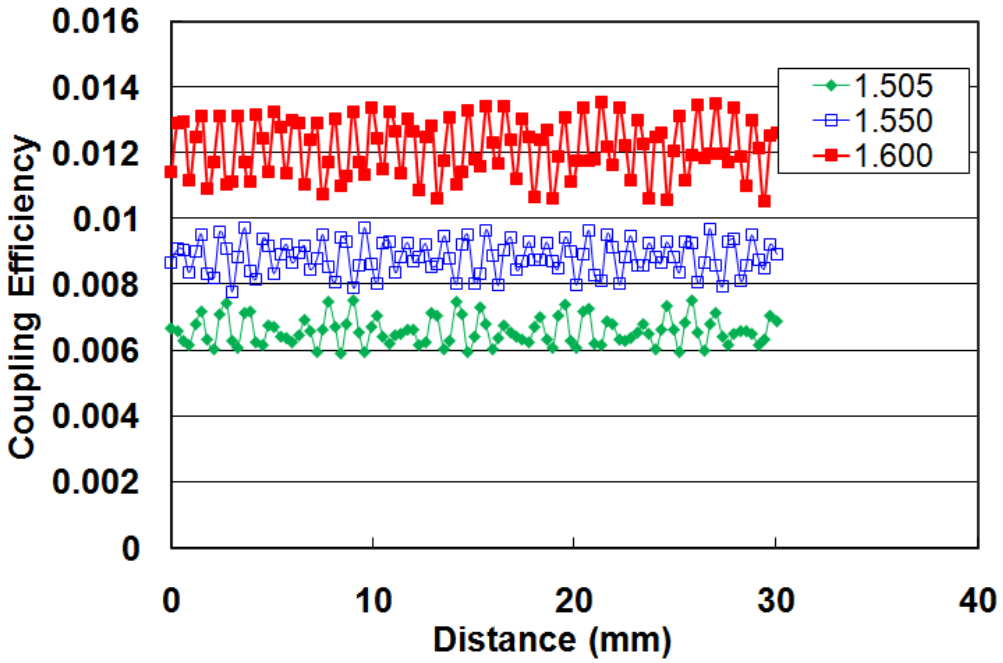

Fig.6.17 Total power coupled into other modes: $LP_{01}x$, $LP_{01}y$, $LP_{11a}x$, $LP_{11a}y$, and $LP_{11b}x$ as a function of coupling length for coupler-2.

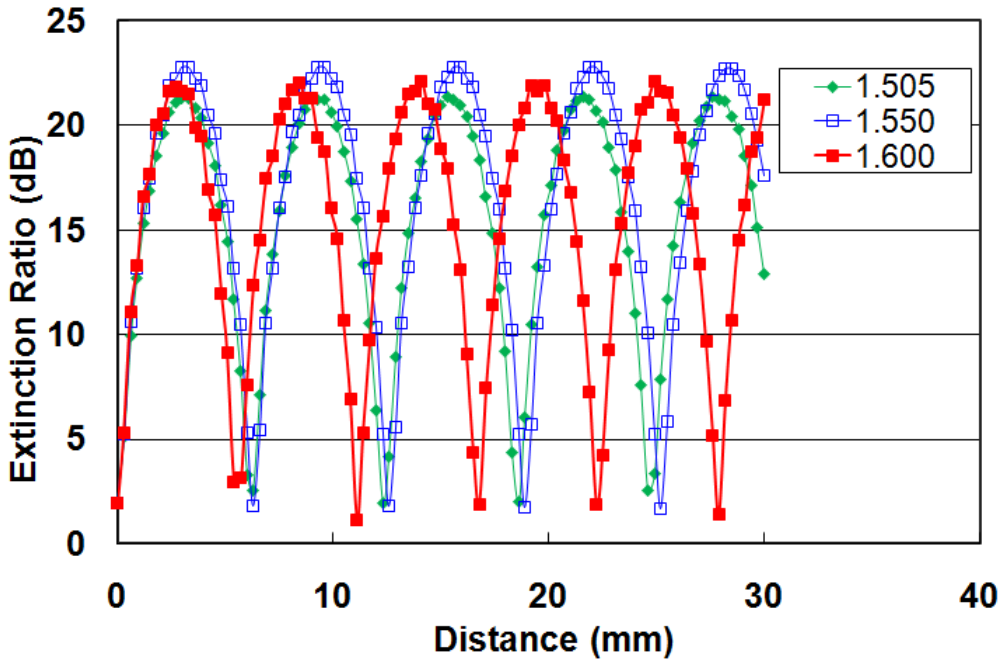

Fig.6.18 Extinction Ratio of power coupled to $LP_{11a}x$ mode as function of coupling length for coupler-1. At the first maximum ($L = 3\ mm$) the extinction ratio is above 21dB.

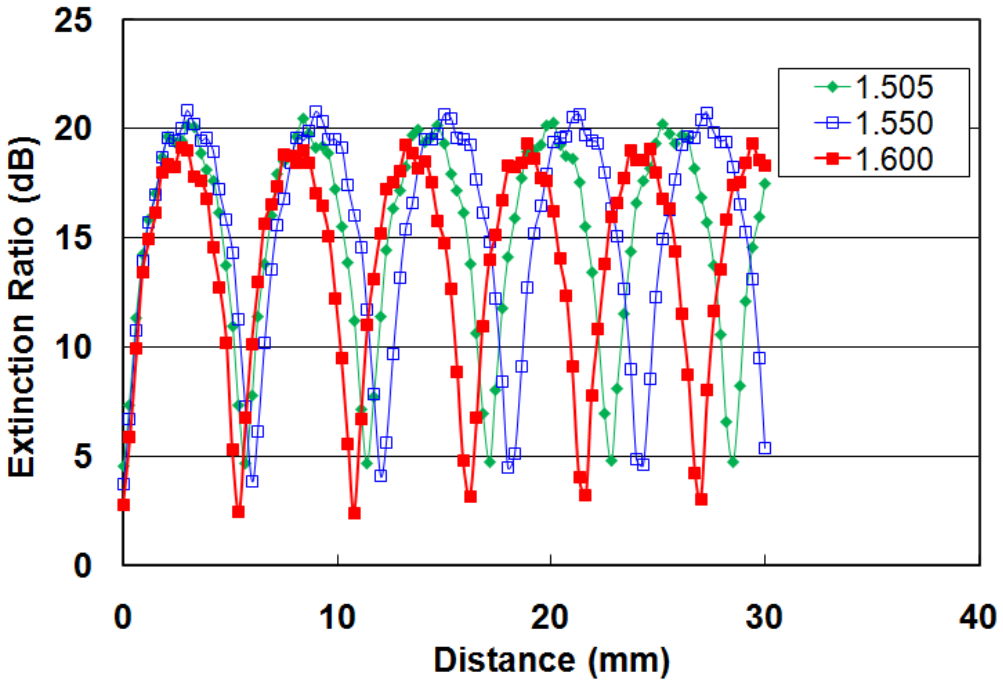

Fig.6.19 Extinction Ratio of power coupled to $LP_{11b}x$ mode as function of coupling length for coupler-2. At the first maximum ($L = 3\ mm$) the extinction ratio is above 20 dB.

Fig.6.20 shows the coupling efficiency wavelength dependence at two possible coupling lengths: 3 mm (first maxima) and 9 mm (second maxima), for both couplers. From Fig.6.14 it's observed that the maxima of coupling efficiency could vary with wavelength, and the separation of maxima under different wavelengths will increase

as the coupling length increases. Therefore it is preferable to use the first coupling maximum to minimize the coupling efficiency variance for different wavelengths when making the combiner. The coupling efficiencies are scanned over the wavelength range from 1.505 to 1.6 μm and estimated to be about 70~97.5% for LP_{11a} mode in coupler-1 and 65~96.5% for LP_{11b} mode in coupler-2 at $L = 3\ mm$. The wavelength dependence of ER is shown in Fig.6.21. It can be seen that the ER can be maintained above 19 dB within wavelength range at $L = 3\ mm$. We also perform the simulation for TM excitation and find both coupling efficiency and extinction ratio has similar performance to that of TE excitation as shown in Fig.6.14 ~ Fig.6.18. This indicates good polarization insensitivity of our proposed SMC design.

Because the separation between two fibre cores in a real selective mode coupler will highly depend on the HF etching process and the subsequent fusion tapering process on the FBT station, it is somehow not always easy to achieve very small gap. Although in a single mode coupler tapering is usually used to reduce the gap region and reduce core size to expand the mode field so as to strengthen the resonant coupling, in a TMF based SMC the tapering technique is limited to a very small extent, or else the mode characteristics would change significantly or even become single mode. Therefore it imposes a much higher requirement on the etching process as well as handling of very thin etched fibre. The feasible etched fibre is usually around 20-30 μm, therefore we analysed the coupling efficiency as function of coupling length for various core separation distances from 12 to 30 μm. The coupling efficiency of coupler-1 under three typical separation distances of 12μm, 15μm and 18μm are shown in Fig.6.22 with respect to the coupling length, where we see that as the separation becomes larger, the required coupling length to achieve first maximum also increases. This result agrees well with the coupled-mode theory [190-191]. Fig.6.23 shows the maximum achievable coupling efficiencies as function of the core separation for the two couplers. It is observed that the coupling ratio can be very high as above 0.9 for a core separation distance ≤18 μm, whilst it will drop as the core separation goes beyond. The oscillation could be attributed to the change of mode overlap integral and propagation constant variation.

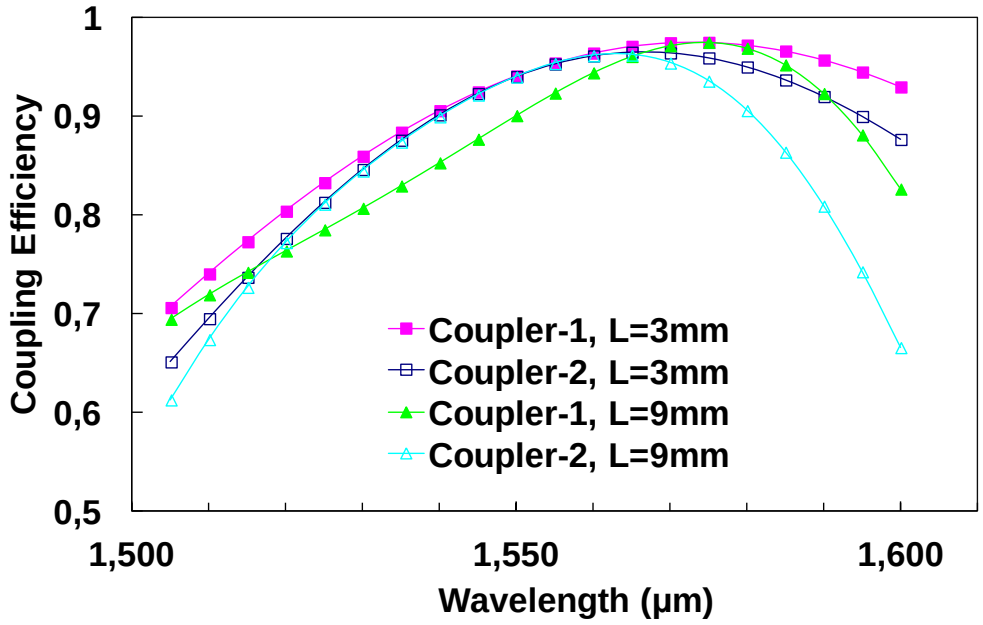

Fig.6.20 Coupling efficiency versus wavelength for both coupler-1 and -2, at coupling lengths of 3 and 9 mm.

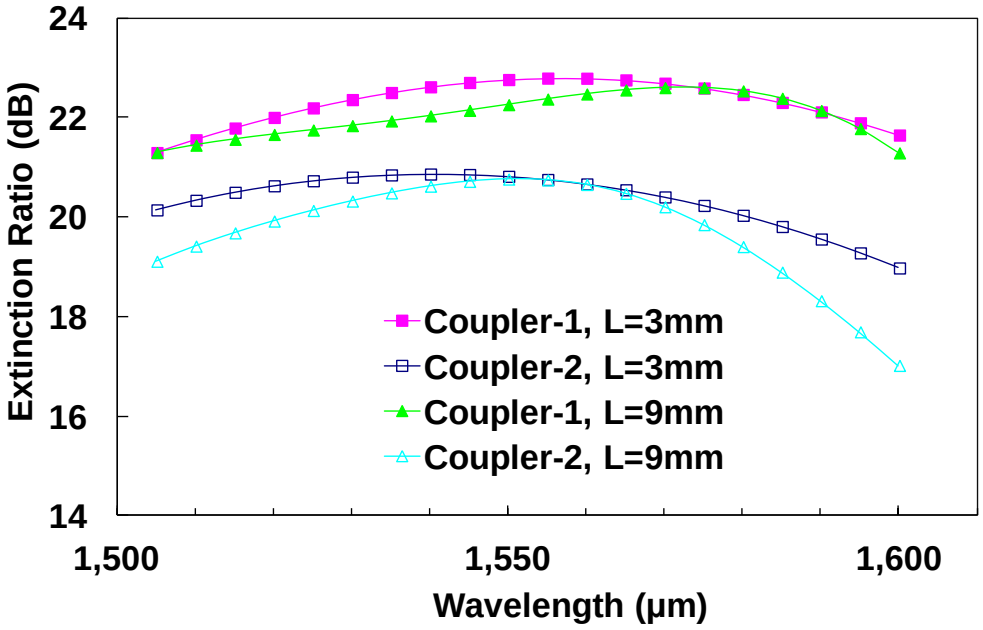

Fig.6.21 Extinction ratio versus wavelength for both coupler-1 and -2, at coupling lengths of 3 and 9 mm.

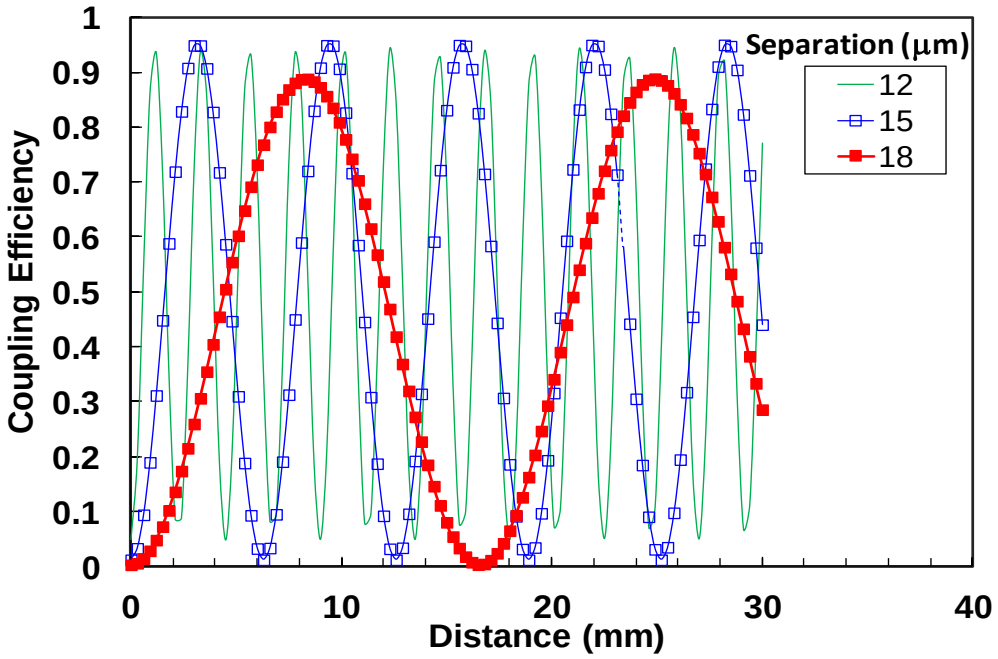

Fig.6.22 Coupling efficiency as function of coupling length for various core separation distances of 12, 15 and 18 μm.

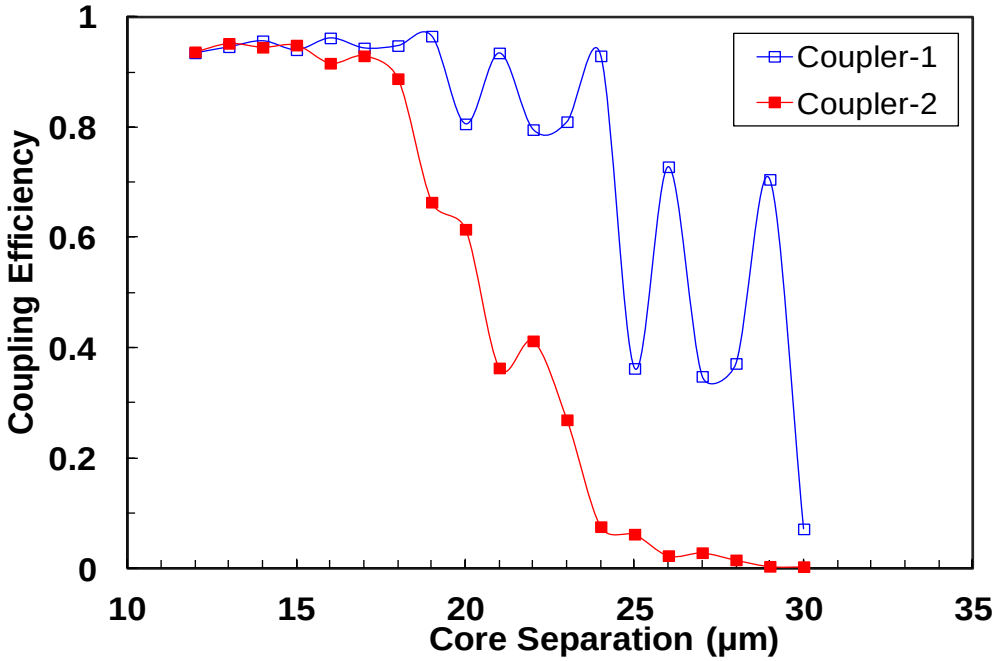

Fig.6.23 Maximum coupling efficiency as function of core separation for both couplers.

We then added two s-bends with 3 mm long and maximum 125 μm apart on both input and output ports and for both coupler-1 and -2, to facilitate connection to standard fibres, as shown in Fig.6.11(a). The waist length (coupling region) is thus shortened to $L_w = 2.45\ mm$ due to partial coupling in the s-bend region. The connection of input ports to SSMF fibres and the output port to a c-TMF fibre (see Fig.

2a) can be easily achieved by centre splicing. The loss due to the splicing is estimated to be less than 0.18 dB for the LP_{01} mode at the input port, and 0.25 dB/0.26 dB/ 0.15 dB for LP_{11a} / LP_{11b} /LP_{01} modes at the output port, if the misalignment between two fibre cores is within 1 μm.

In summary, a high-performance LP_{11} spatial mode combiner using elliptical-core two-mode fibres (e-TMFs) has been designed. LP_{01} modes in two pre-pulled SMF-28e fibres are selectively coupled into the LP_{11a} or LP_{11b} mode of the TMF. The mode coupling efficiency, extinction ratio is analysed under different conditions of wavelength and coupling length. The proposed SMC can achieve >65% coupling efficiency and > 19 dB extinction ratio within a broad wavelength-range of 1505~1600 nm [187].

6.2.4 Few-mode fibre amplifier (EDFA, Raman)

Few-mode amplifier is another critical component when the accumulated power loss is significant, e.g., in long-haul multi-span FMF transmissions. Currently there are two methods to achieve few-mode amplification, multimode erbium-doped fibre amplifier (MM-EDFA) [117-119] and Raman amplifier [120]. The setup of a feasible inline MM-EDFA is depicted in Fig.6.24.

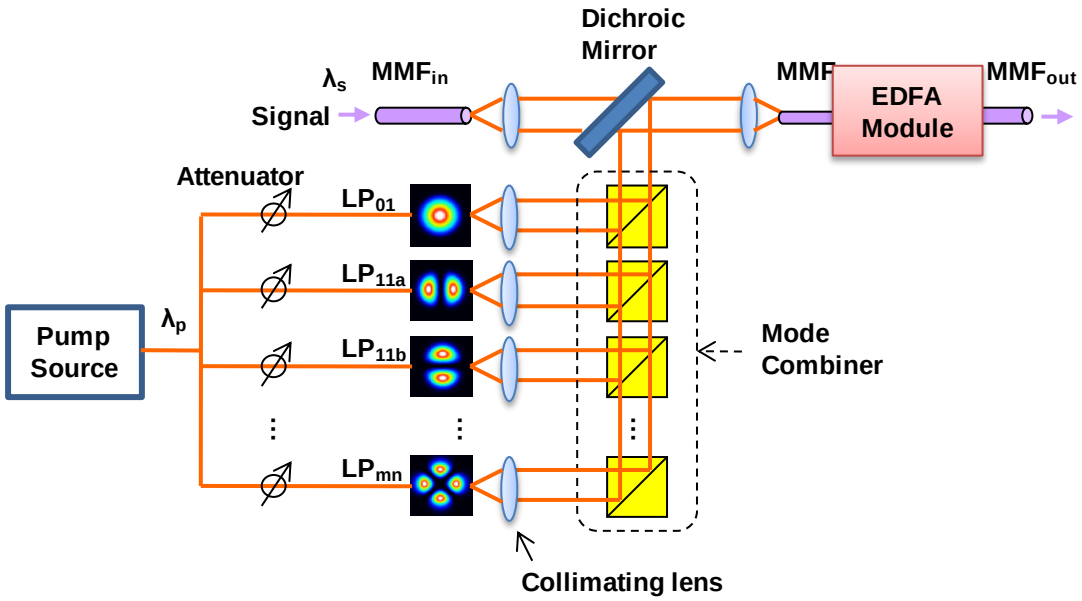

Fig.6.24 Schematic diagram of a MM-EDFA [111].

In order to generate the desired pump intensity profile, the pump source is first split into *N* paths, and use LPFG-based MCs as proposed in Section 6.2.2 or phase plate based MCs proposed in [108] or [109] to convert the spatial mode of the pump

source into the *N* spatial modes of the FMF. The variable attenuators on each path could control the power distribution of pump on modes, and therefore the mode-dependant gain (MDG) of the MM-EDFA. The pump modes are then collimated, spatially combined with the signal using free-space mode combiner similar to the one we proposed in Section 6.2.3.1 with an additional dichroic mirror, which are then focused into a FMF and injected into the erbium-doped MMF. Following this concept, recently a reconfigurable multimode pump has been proposed to excite a MM-EDFA so that by varying the mode content of the pump the MDG can be controlled [119]. The main idea of this reconfigurable multimode pump configuration is by adjusting relative amount of $LP_{01,p}$ and $LP_{21,p}$, the gains of the $LP_{01,s}$ and $LP_{11,s}$ signal modes can be tuned over a wide dynamic range.

6.3 Comparison of SDM techniques

A comparison of SDM techniques is summarized in Table 6.1 based on devices and techniques currently available [29-37, 102-123, 175-189]. We can see that, despite of its disadvantages like high complexity due to the MIMO algorithm, SDM technique based on MMF or FMF has many advantages such as reduced number of devices (amplifier, ROADM), and most importantly, the *N* times channel capacity that can enable future Terabit and beyond optical networks.

TABLE 6.1. COMPARISON OF DIFFERENT SDM APPROACHES (INFORMATION FROM [29-37, 102-123, 175-189])

Parameter	Bundled Fibre (BF)	Multi-core fibre (MCF)	Multi-mode fibre (MMF)
Fibre Loss	Standard	Can be as low as SMF	Can be as low as SMF
Effective Core Area	Standard	Small or standard	**Large**
Intra-Mode Nonlinearity	Standard	Standard or high	**Low**
Inter-Mode Nonlinearity	**No**	Low	Low to medium
Mode Coupling/Crosstalk	**No**	Medium	Low to high, can be optimized
No. of Amplifiers	*N*	*N*	**1**
No. of ROADMs	*N*	*N*	**1**
Fusion Splicing	**Easy,**	Special splicer,	**Easy,**

	low loss	possibly high loss	**low loss**
DSP Complexity	**Low**	Low to medium	Medium to high, MIMO needed
Cost	*N* x SMF	Can be low	**As low as 1 x SMF**

6.4 Conclusion

In this chapter, we have introduced the concept of space division multiplexing and show the system architecture of SDM based high speed superchannel system. The few-mode components including mode stripper, mode converter, mode combiner, OADM and few-mode amplifier are practically designed and implemented in SDM based systems. Finally a brief comparison between different SDM techniques with pros and cons is given based on the current technology, which may serve as a hint for the future SDM based system design.

7 Transmission of Mode-Division-Multiplexed CO-OFDM (MDM-CO-OFDM) Signal over Two-Mode Fibre

7.1 Transmission of LP_{01}/LP_{11} mode MDM-CO-OFDM signal over two-mode fibre

In this experiment we have successfully achieved LP_{01}/LP_{11} dual-mode transmission over 4.5-km TMF [103], using the MSs and MCs as proposed in Section 6.2.1and 6.2.2.

7.1.1 System setup

The transmission experiment setup is as shown in Fig.7.1. Four transmitters are emulated by polarization and mode multiplexing as follows: first, the transmitted signal is generated off-line with MATLAB program. The total number of OFDM subcarriers is 64, and cyclic prefix (CP) is set to be 1/8 of the observation window. The middle 40 subcarriers out of 64 are filled with data mapped from 2^{15}-1 PRBS. 500 OFDM symbols are sent for evaluation, out of which 20 symbols with alternative polarization launch are used for channel estimation. The digital time-domain signal is formed after IFFT operation. The real and imaginary components of the time-domain signal are uploaded onto a Tektronix Arbitrary Waveform Generator (AWG). We generate three optical tones spaced at 6.563GHz by feeding an external cavity laser at 1549.3 nm to two cascaded intensity modulators driven by RF tones at 6.563 GHz. The baseband OFDM signal from AWG is impressed to the three optical tones by a nested Mach-Zehnder modulator. The tone spacing is chosen to be an exact multiple of the OFDM subcarrier spacing to ensure inter-band orthogonality. The orthogonally multiplexed 3-band OFDM signal is then divided and recombined on orthogonal polarizations with one symbol delay to emulate polarization multiplexing. The OFDM symbol length is 7.2 ns. The raw data rate is 150 Gb/s and net data rate after deducting all the overheads is 107 Gb/s for both modes and all 3 bands. The overheads include 7% forward error correction (FEC), 4% training symbol (TS), 12.5% CP and 5 discarded subcarriers around DC. The signal at a power of 5.5 dBm is then coupled into the fibre with mode coupler MC1 to emulate the mode coupler. After a transmission of 4.5-km TMF fibre, the mode delay is 13.5 ns. Since OFDM symbol is 7.2 ns, which is nearly half of the modal delay, the two modes are completely de-correlated at the reception, validating the reception for two independent modes from

the same launch data at the transmitter. At the receiver, the mode demultiplexing is performed as follows: For the LP_{01} mode, an MS is used to remove LP_{11} mode, and the remaining LP_{01} is fed into the coherent optical receiver; for the LP_{11} mode, the second mode converter, MC2 is used to convert the LP_{11} into LP_{01}, and LP_{01} into LP_{11}. The original LP_{01} signal is converted into LP_{11} and is removed by a subsequent MS. The original LP_{11} is converted in LP_{01} and is fed into the coherent receiver. An optical 90 ° hybrid is used for coherent detection of each mode separately, which is then sampled by a 50 GSa/s oscilloscope and processed offline [194]. We use 2 ×2 MIMO-OFDM program to process the received dual-polarization signal. Each mode is processed individually. The signal processing consists of the following five steps: 1) FFT window synchronization; 2) frequency offset compensation; 3) channel estimation; 4) phase estimation and 5) constellation recovery and BER computation [194].

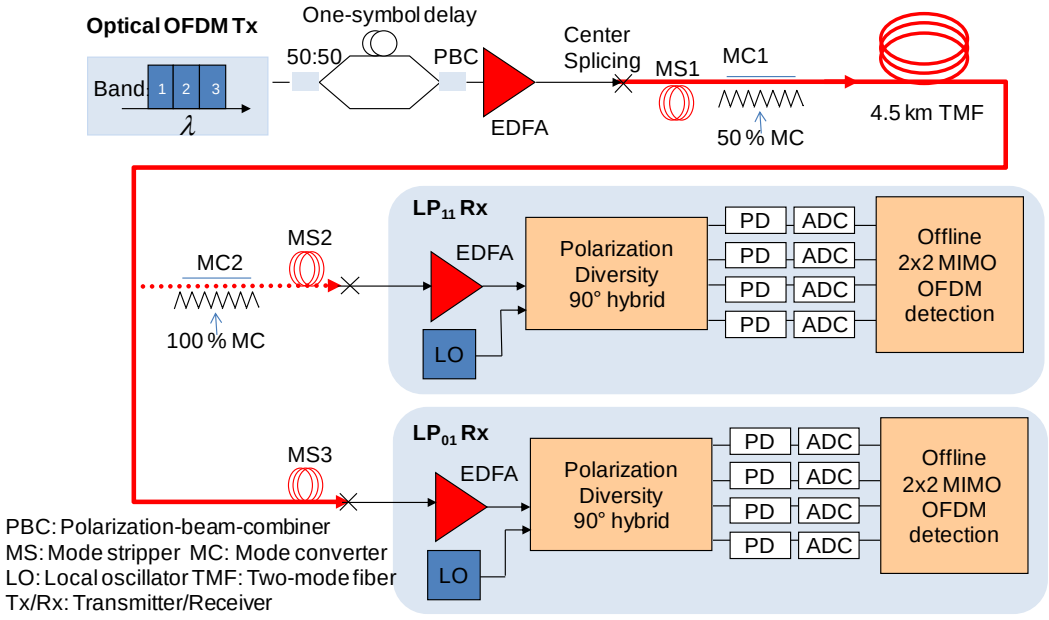

Fig.7.1 Experimental setup for 107-Gb/s dual-mode dual polarization transmission over 4.5-km TMF fibre. 'X' indicates controlled coupling between LP_{01} modes of SMF and TMF by centre splicing. PBC: polarization beam combiner, MS: mode stripper, MC: mode converter, PD: photodiode.

7.1.2 Result and Discussion

With this setup, the received power of LP_{01} mode is -0.5 dBm and of LP_{11} mode is -5.3 dBm. The end-to-end losses for the LP_{01}/LP_{11} mode are measured to be 6 and 10.8 dB, respectively. The higher loss for the LP_{11} mode can be attributed to the fibre

micro-bending loss and polarization/spatial mode dependence of the additional MC2 due to asymmetric deformation [183], combined with the fact that there exists random coupling among the degenerate LP_{11}modes inside the 4.5-km TMF fibre, although initially at MC1 we launch only one of the two orientations. This can be improved with optimization of the MC. Fig.7.2(a) and (b) show respectively the high-resolution (0.01 nm) optical spectra of LP_{01} and LP_{11} modes. It can be seen that the intensity ripple of $LP_{11}$is much more severe than LP_{01} case. These intensity ripples are attributed to the coherent beating between the mode-to-detect and residual unwanted modes, which is related to the rejection ratio of the MC or MS used before receiver as shown in Table 7.1. This explains the reason why in the case of LP_{11} we observe stronger spectral ripple, which is due to the limited ER of the MC2. Nevertheless, despite this level of power variation, we can still receive good constellations in all 3 bands for both LP_{01} and LP_{11} modes as shown in Fig.7.2(c) and (d). Again the constellation of LP_{11} is noisier than LP_{01} due to the limited ER of the MC2, leaving the residual LP_{01} component to act as crosstalk. There are 12 combinations of signal states (3 bands, 2 polarizations and 2 modes). For any given combination, we could not measure any error out of 100,590 bits measured. Overall Q factor for all bands, polarizations and modes are summarized in Table 7.2. The 2-3 dB variation of Q factor for the three bands can be attributed to the varying crosstalk in the case of LP_{11}, as the MC is sensitive to only one of the spatial orientation of LP_{11} modes which is randomly perturbed along the 4.5-km TMF span.

TABLE 7.1. MEASURED PERFORMANCE OF THE MODE DEMULTIPLEXER

Mode	Received power	Rejection Ratio (best/worst polarization)
LP_{01}	-0.5 dBm	≥30 dB / ≥30 dB
LP_{11}	-5.3 dBm	22 dB / 17 dB

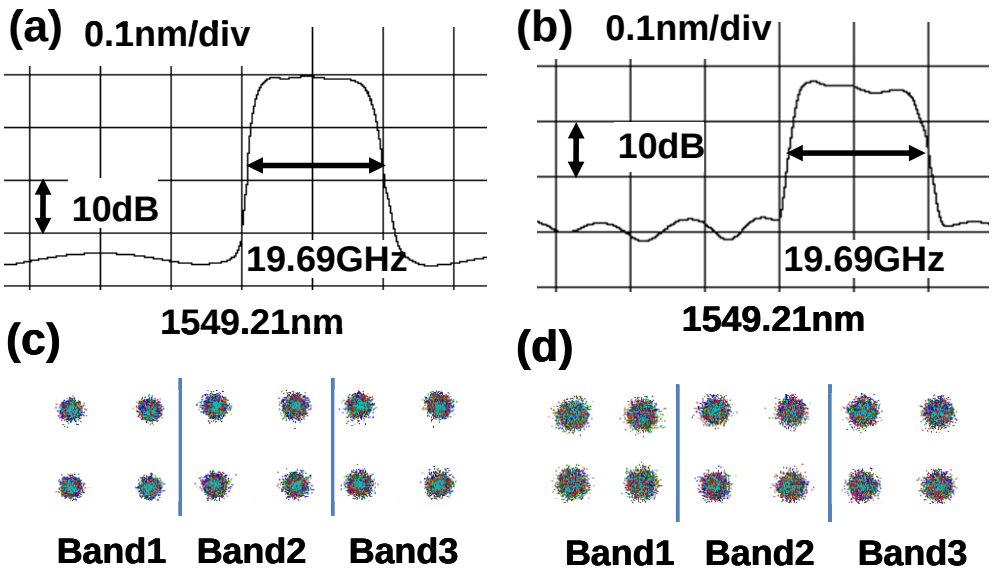

Fig.7.2 (a) Optical spectrum and (c) constellations of LP_{01} mode; (b) optical spectrum, and (d) constellations for LP_{11} mode after 4.5-km transmission in 3 bands.

The results demonstrate the feasibility of use of TMF in dual-mode and dual-polarization transmission to increase the fibre capacity. Considering the OFDM signal spectrum width of 19.7 GHz, the achieved net SE is 5.4 b/s/Hz, which can be further improved by reducing overheads. Even though the fibre available to us is limited to 4.5-km length, transmission to longer distances with the present method is not limited by modal dispersion, rather loss of the end-to-end TMF span. In the absence of practical dual-mode amplification as a repeater, modal splitting followed by single-mode amplification and modal recombining can be a solution, and this can be an interesting topic of future research.

TABLE 7.2. MEASURED Q FACTOR (IN DB) 'POL-X/Y' STANDS FOR X/Y POLARIZATION.

LP_{01}	**Band 1**	**Band 2**	**Band 3**	**Avg.**
Pol-x	19.5	18.4	18.1	18.7
Pol-y	18.5	18.3	17.9	18.3
Avg.	19.0	18.4	18.0	18.5
LP_{11}	**Band 1**	**Band 2**	**Band 3**	**Avg.**
Pol-x	15.2	18.6	16.2	16.9
Pol-y	14.7	17.0	16.5	16.2
Avg.	15.0	17.8	16.4	16.5

7.2 Transmission of dual-LP_{11} mode MDM-CO-OFDM signal over two-mode fibre

In Section 7.1, to detect LP_{11} mode, manual spatial control is used. Similar to polarization-mode division multiplexing, the preferred method of LP_{11} Mode detection is to employ spatial mode diversity. We therefore have also conducted experiment to transmit dual-LP_{11} mode simultaneously over TMF [104-106]. In addition to the MSs and MCs used in Section 7.1, we have also introduced free-space mode combiners proposed in Section 6.2.3 for spatial mode multiplexing and de-multiplexing.

7.2.1 System setup

Fig.7.3 shows the experimental setup of the 4×4 MDM-CO-OFDM system based on TMFs where LP_{11} spatial diversity is employed at both transmitter and receiver. Four transmitters are emulated by polarization and mode multiplexing as follows: first, the transmitted signal is generated off-line with MATLAB program. The total number of OFDM subcarriers is 128, and cyclic prefix (CP) is set to 1/16 of the observation window. Middle 68 subcarriers out of 128 are filled excluding centre 3 subcarriers that are nullified for RF-pilot [60]. 50 OFDM symbols are sent for evaluation, out of which 4 symbols are used for channel estimation. The digital time-domain signal is formed after IFFT operation and uploaded to the AWG. The operating wavelength of ECL is 1550.92 nm. The OFDM symbol length is 13.6 ns in this case. The OFDM signal is then divided and recombined on orthogonal polarizations using polarization beam combiner (PBC) and polarization maintaining fibre (PMF) with one symbol delay to emulate polarization division multiplexing (PDM). After the PDM emulation, the signal is again split with a 3-dB SMF coupler and the two branches are subsequently delayed by two OFDM symbol length (27.2ns), enabling the mode division multiplexing (MDM) emulation. Out of the 4 training symbols, only one symbol is filled whilst all other 3 symbols remain unfilled. After 1 symbol delay for PDM and 2 symbol delay for MDM emulation, TS in all 4 tributaries become orthogonal. These two MDM delayed signals are then converted from fundamental (LP_{01}) mode in SMF to the LP_{11a} and LP_{11b} modes in TMF by utilizing the MC and mode combiner described in Section 6.2.3. After TMF transmission the free-space mode splitter decomposes the signal into two orthogonal LP_{11} modes, each converted back to the fundamental mode in SMFs. Any residual LP_{01} components can be filtered

by mode converting to LP_{11} and then stripped off with the subsequent MSs. In this experiment the MSs are realized by tightly winding the 0.9-mm jacketed TMF fibre over 8-mm posts of about 10 rounds. After this, the two PDM tributaries are further split to orthogonal polarizations by PBS and mixed with 4 LO branches using 3-dB couplers into 4 photodetectors (PDs) with trans-impedance amplifiers. At receiver, we choose heterodyne coherent detection so that only 4 PDs and one digital oscilloscope with 4 channels of ADC are sufficient to realize the 4×4 MIMO reception.

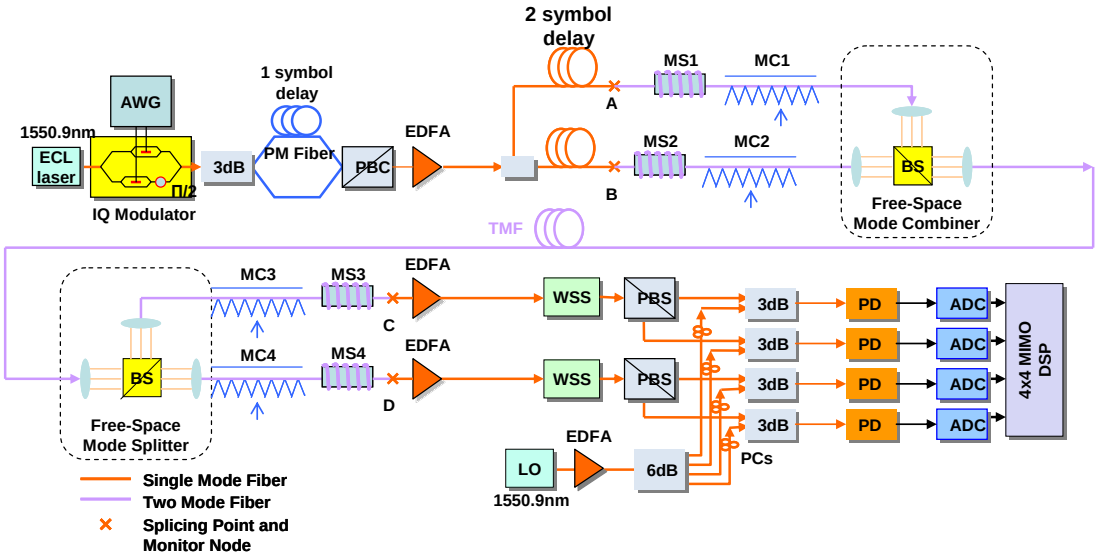

Fig.7.3 Experimental setup of a coherent 4×4-MIMO system over a two-mode fibre (TMF). PBC/PBS: polarization beam combiner /splitter. MC: mode converter, MS: mode stripper. WSS: wavelength selective switch, emulated by a Finisar waveshaper.

7.2.2 Result and Discussion

The optical power in the system is monitored at four nodes (A-D) as depicted in Fig.7.3. The end-to-end loss is estimated for all the possible TX/RX port combinations, as shown in Table 7.3. The relatively high power loss in our system is mainly attributed to the loss of the beamsplitter (3.5-4.5 dB), misalignment/return loss (~1 dB) and mode converter (1.4~2.4 dB). Nevertheless, the received power is well above the sensitivity of PDs. Because of the relatively low differential mode delay (DMD) between the two LP_{11} modes, the modal coupling happens even for a short TMF fibre of 4.5 km due to random perturbation. The 4×4 MDM-CO-OFDM could evaluate the channel matrix in the presence of polarization as well as mode coupling. One of the estimated 4×4 channel matrices for the two LP_{11} modes after 4.5-km TMF transmission is illustrated in Fig.7.4. A smooth channel response for a narrow bandwidth is confirmed which shows slow frequency selectivity. Using polynomial

curve fit of the phase angle of the diagonal components (H_{11}, H_{22}, H_{33} *and* H_{44}), the second order coefficient p_2 is calculated to be 2×10^{-5} which corresponds to the accumulated chromatic dispersion (CD) of 28.9 *ps/nm/km*. The successful reception of all data symbols also confirms the slow time varying of channel within the OFDM symbol length scale. The received spectrum of the signal is shown in Fig.7.5. A 5.3-GHz bandwidth is occupied by the OFDM signal including the RF pilot region. Because of heterodyning detection, signal-to-signal intermixing products is present around LO frequency. To avoid this penalty in the low frequency region, 5-GHz guard band is kept and we also maintain the power ratio of signal-to-LO as high as ≥ 20dB. The net data rate for all polarizations and modes is 58.8 Gb/s (128-point FFT, 68 subcarriers filled, 8QAM) taking into consideration CP and TS overheads. The measured BER versus OSNR for the signal transmission is shown in Fig.7.6. The required OSNR for BER of 1×10^{-3} is found to be 17.9 dB on average for b2b with less than 1-dB discrepancy between the best/worst tributaries, and 18.8 dB after 4.5-km transmission similarly with less than 1-dB variation between tributaries. The discrepancy in polarizations may attribute to the polarization-dependant loss (PDL) of the free-space system as well as possible slightly launch power imbalance in the two polarizations. The discrepancy in modes could be due to the power imbalance and misalignment. The clean constellation in the inset confirms the effectiveness of our MDM-CO-OFDM system. The major limiting factors of the transmission distance of our 4×4 mode multiplexed system are: (i) the crosstalk from residual LP_{01} mode (the ER of MCs and rejection ratio of MSs); (ii) the orthogonality and rejection ratio of the two LP_{11} modes in mode combiner/splitters; (iii) PDL, mode-dependant loss (MDL) and the end-to-end loss; Nevertheless, for a 4.5-km fibre we have sufficient margin as can be seen from Fig.7.6(a). It has been demonstrated in our recent experiment [106] that a 35.3 Gb/s Dual-LP_{11} mode 4×4 MIMO-OFDM transmission was successfully achieved over 26-km TMF using the same setup. Compared with the 107-Gb/s transmission result using LP_{01}/LP_{11} mode in Section 7.1, in this dual LP_{11} mode transmission we implement 4×4 MIMO processing to overcome modal coupling. Because heterodyning technique is used to save the need for another real-time oscilloscope, a narrow-band optical filter is required for multi-band OFDM signal detection to eliminate the image noise. Due to the unavailability of such a filter we only show single-band transmission (5.3 GHz) in this experiment, but in principle multiband OFDM transmission can be achieved either using a tuneable optical filter in

heterodyne detection, or using intradyne detection setup with two synchronized real-time oscilloscopes.

TABLE 7.3. END-TO-END LOSS OF THE EXPERIMENTAL SETUP

Monitor Node	**Measured loss (dB) back-to-back**	**Measured loss (dB) 4.5-km TMF**
A – C	12.1	13.3
A – D	12.0	13.2
B – C	13.3	14.5
B – D	13.3	14.5
TMF Fibre	0.256 dB/km × 4.5 km	
Mode Converters	1.4 – 2.4 dB	
Mode Strippers	<0.5 dB	

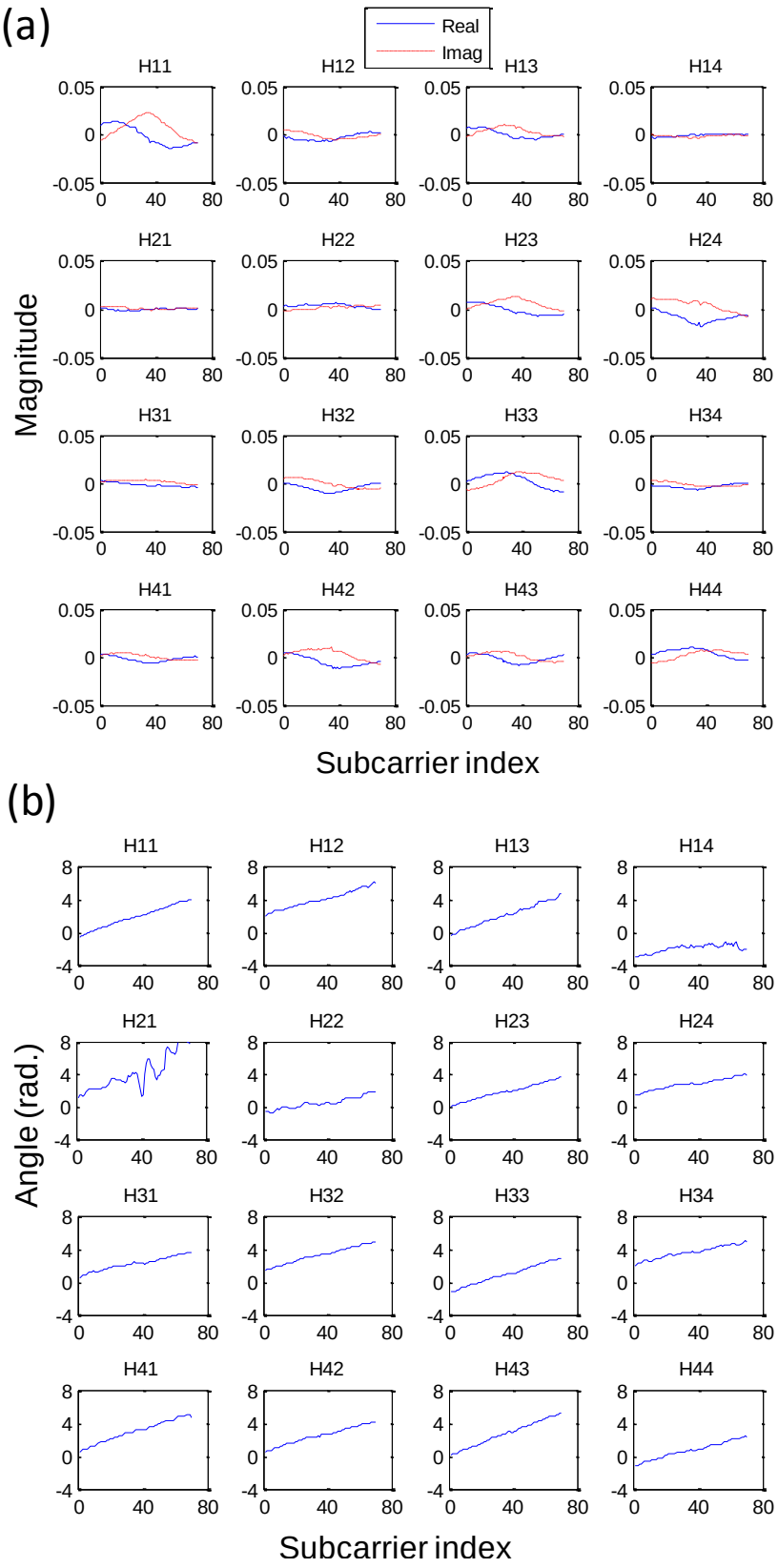

Fig.7.4 Measured channel matrix parameters for the two LP_{11} modes after 4.5-km TMF transmission.(a) Real and imaginary components, and (b) phase of the 4×4 fibre channel matrix. The subcarrier indices are mapped from low to high frequency. The subcarrier index difference of 1 corresponds to frequency spacing of 78 MHz.

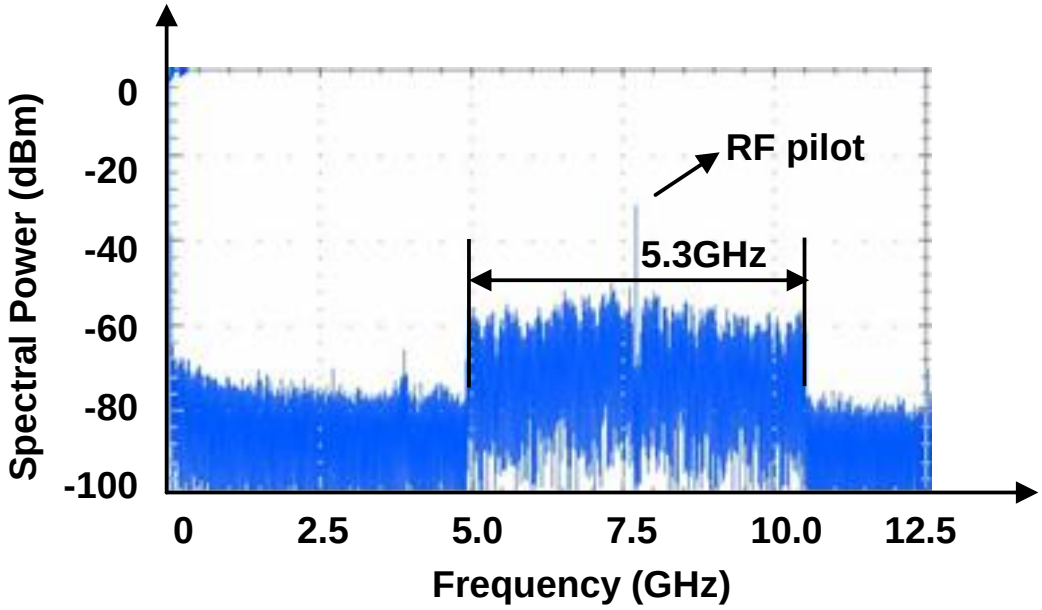

Fig.7.5 Received RF spectrum of one of the four tributaries after 4.5-km TMF transmission. The 5-GHz guard band is intentionally made to avoid intermixing product of signal in heterodyning.

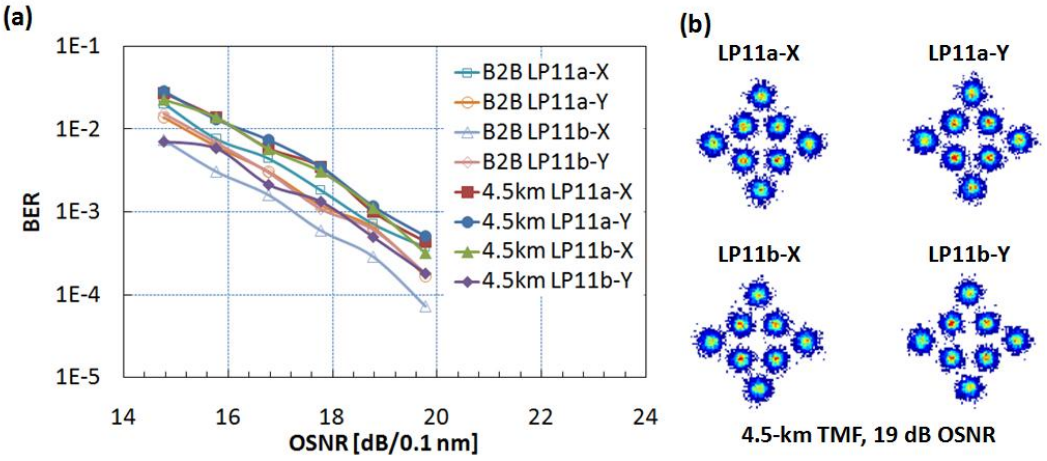

Fig.7.6 (a) Measured OSNR vs. BER performance for 8-QAM 4×4 MIMO-OFDM system for back-to-back (B2B) and 4.5-km TMF transmission configuration. (b) Constellation of received signal after 4.5-km TMF transmission with *OSNR = 19 dB*.

7.3 Transmission of triple-mode (LP_{01}+LP_{11a}+LP_{11b}) MDM-CO-OFDM signal over two-mode fibre

Triple mode transmission over FMF utilizing 6×6 MIMO digital signal processing has already been demonstrated and extensively studied by several groups [109-113]. Here we refer to a most recent progress in [112] that has extended the maximum reach from several tens of km to a significant value of 1,200 km for a 6×20-GBd QPSK signal, thanks to the realization of MM-EDFA and low-DMD FMFs. This long-haul FMF

transmission is emulated by a triple-recirculating loop consists of three parallel routes and switches, while a pair of spatial mode multiplexer (MMUX) and mode de-multiplexer (MDEMUX) based on phase plates [108-110] are used before and after the FMF span, enabling the loop control with single mode components. The longest reach of up to 1,200 km is achieved at -3 dBm for 20% FEC limit (BER= 1×10^{-2}). Due to the limited LP_{01}/LP_{11} modal ER of our free-space mode combiner, however, we did not achieve reasonable result for 6×6 MDM-CO-OFDM transmission of our custom-designed TMF fibre, which we will investigate in the future. The improvement can be made through either the optimization of our free-space mode combiner setup, or the development of novel fused fibre mode coupler with high modal ER [187-188].

7.4 Conclusion

In this chapter, we have shown our up-to-date proof-of-concept lab demonstrations of transmission of MDM-CO-OFDM signal over TMF. Three different transmission schemes are presented and discussed,

1) Transmission of LP_{01}/LP_{11} mode MDM-CO-OFDM signal over 4.5-km two-mode fibre.
2) Transmission of dual-LP_{11} mode MDM-CO-OFDM signal over 4.5-km two-mode fibre using 8QAM modulation.
3) Transmission of triple (LP_{01}+LP_{11a}+LP_{11b}) mode MDM-CO-OFDM signal over two-mode fibre.

The system setup, key components, system parameters, enabling technique and signal processing have been revealed.

8 Conclusions

8.1 Summary of this work

In this thesis, we have elucidated the overall system architecture and critical components and sub-system modules for SDM transmission based on two-mode fibre and presented the up-to-date experimental demonstration of MDM superchannel transmission.

8.1.1 Novel variants of CO-OFDM system

We review the basic concept and principle of conventional Optical OFDM system. We introduce two new variants of the Optical OFDM system called WPT-OFDM and DFTS-OFDM. The system architecture, implementation and performance are discussed.

8.1.2 Few-mode fibre and components for SDM

We focus on the most basic but important element for the SDM transmission system – FMF fibre. The fundamentals of optical fibre and fibre modes are studied. We also show how to design and fabricate a practical two-mode fibre. Furthermore, we have conducted an experiment to characterize the physical property of our custom-designed TMF fibre. After that we investigate the fundamentals of SDM especially the MDM based on MMF or FMF. We show that despite of its disadvantage of high complexity due to the MIMO algorithm, SDM technique based on MMF or FMF has many advantages such as reduced number of devices (amplifier, ROADM), and most importantly, *N* folds increase in channel capacity that facilitates future Terabit and beyond optical networks. Finally, we show a few practical few-mode components which are very critical for few-mode transmission such as mode stripper, mode converter, mode combiner, optical add/drop multiplexer and few-mode amplifiers.

8.1.3 Transmission of MDM-CO-OFDM over Two-mode fibre

With few-mode components and subsystem modules available, the proof-of-concept MDM transmission of CO-OFDM signal over FMF can be realised. We show three experimental demonstrations of MDM transmission over TMF fibre: (1) transmission of LP_{01}/LP_{11} mode MDM-CO-OFDM signal, (2) transmission of dual-LP_{11} mode MDM-CO-OFDM signal, and (3) transmission of triple-mode (LP_{01}+LP_{11a}+LP_{11b}) MDM-CO-OFDM signal over TMF fibre. We present a nonlinear propagation model

for the SDM transmission based on FMF fibre. The information spectral efficiency and channel capacity of FMF based SDM system is derived, and a potential improvement in the nonlinearity performance through constant linear mode coupling is identified.

8.2 Future work and perspectives

It is expected that with the maturity of MDM and CO-OFDM superchannel technique, a high data rate of 100 Gb/s and beyond can be achieved with doubled or even tripled spectral efficiency over existing SMF systems. We identify the following critical enabling components and modules for FMF transmission: low-loss and low-DMD FMF [114], low-loss, high ER and all-fibre based mode MUX/DEMUX [102-113], FMF compatible components (coupler [102,113,187], filter, switch, and ROADM [107]), reliable parameter characterization(DMD, MDL, mode extinction/rejection ratio, nonlinearity) devices, etc, which requires great effort to develop in the future. There are also many other research directions: on the device level in terms of design of low-loss few-mode components, design of few-mode amplifier with even less mode dependence and flatter gain profile; on the system level in terms of multi-dimensional coding, reduction of complexity in DSP algorithm, novel algorithm for crosstalk and impairment mitigation, rigorous modelling of MDM transmission system.

Bibliography

[1] A. G. Bell, "On the production and reproduction of sound by light," Am. J. Sci., vol. **20**, pp. 305–324 (1880).

[2] J. L. Baird, British Patent 285,738, (1928).

[3] C. W. Hansell, U. S. Patent 1,751,584, (1930).

[4] H. Lamm, "Biegsame optische gerate," Z. Instrumenten., vol. **50**, pp. 579 (1930).

[5] A. C. S. van Heel, "A new method of transporting optical images without aberrations," Nature, vol. **173**, pp. 39 (1954).

[6] H. H. Hopkins and N. S. Kapany, "A flexible fiberscope using static scanning," Nature, vol. **173**, pp. 39–41 (1954).

[7] B. O'Brian, U. S. Patent 2,825,260 (1958).

[8] B. I. Hirschowitz, U. S. Patent 3,010,357 (1961).

[9] K. C. Kao and G. A. Hockham, "Dielectric-fiber surface waveguides for optical frequencies," IEE Proc., vol. **113**, pp. 1151 (1966).

[10] W. G. French, J. B. MacChesney, P. B. O'Connor, and G. W. Tasker, "Optical Waveguides with Very Low Losses," Bell Syst. Tech. J., vol. **53**, pp. 951 (1974).

[11] T. Miya, Y. Terunuma, T. Hosaka, and T. Miyashita, "Ultimate low-loss single-mode fiber at 1.55 μm," Electron. Lett., vol. **15**, no. 4, pp. 106–108 (1979).

[12] J. Hecht, City of Light, Oxford University Press, New York, USA, 1999.

[13] X. Zhu, and J.M. Kahn, "Free-space optical communication through atmospheric turbulence channels," Communications, IEEE Transactions on, vol. **50**, no. 8, pp. 1293– 1300 (2002).

[14] D. Qian, M. Huang, E. Ip, Y. Huang, Y. Shao, J. Hu, and T. Wang, "101.7-Tb/s (370×294-Gb/s) PDM-128QAM OFDM Transmission over 3×55-km SSMF using Pilot-based Phase Noise Mitigation," in Optical Fiber Communication Conference (OFC), 2011, paper PDPB5.

[15] A. Sano, T. Kobayashi, S. Yamanaka, A. Matsuura, H. Kawakami, Y. Miyamoto, K. Ishihara, and H. Masuda,"102.3-Tb/s (224 x 548-Gb/s) C- and Extended L-band All-Raman Transmission over 240 km Using PDM-64QAM Single Carrier FDM with Digital Pilot Tone," in Optical Fiber Communication Conference (OFC), 2012, paper PDP5C.3.

[16] S. Hara and R. Prasad, Multicarrier Techniques for 4G Mobile Communications, Artech House, Boston, 2003.

[17] A. J. Lowery, L. Du, and J. Armstrong, "Orthogonal frequency division multiplexing for adaptive dispersion compensation in long haul WDM systems," in Optical Fiber Communication Conference (OFC), 2006, paper PDP39.

[18] W. Shieh and C. Athaudage, "Coherent optical orthogonal frequency division multiplexing," Electron. Lett., vol. **42**, pp. 587–588 (2006).

[19] J. M. Tang, P. M. Lane, and K. A. Shore, "Transmission performance of adaptively modulated optical OFDM signals in multimode fiber links," IEEE Photon. Technol. Lett., vol. **18**, pp. 205–207 (2006).

[20] J. M. Tang, J.M., P.M. Lane, K. A. Shore, "30 Gb/s transmission over 40 km directly modulated DFB laser-based SMF links without optical amplification and dispersion compensation for VSR and metro applications," in Optical Fiber Communication Conference (OFC), 2006, paper JThB8.

[21] A. J. Lowery and J. Armstrong, "10 Gb/s multimode fiber link using power-efficient orthogonal frequency-division multiplexing," Opt. Express, vol. **13**, pp. 10003-10009 (2005).

[22] I. B. Djordjevic and B. Vasic, "Orthogonal frequency division multiplexing for high-speed optical transmission," Opt. Express, vol. **14**, pp. 3767–3775 (2006).

[23] J. Armstrong, "OFDM for Optical Communications," J. Lightwave Technol., vol. **27**, pp. 189–204 (2009).

[24] P. P. Mitra and J. B. Stark, "Nonlinear limits to the information capacity of optical fiber communications," Nature, vol. **411**, pp. 1027–1030 (2001).

[25] Ö. Bulakci, M. Schuster, C. Bunge, B. Spinnler, and N. Hanik, "Wavelet transform based optical OFDM," in Optical Fiber Communication Conference (OFC), 2009, paper OTUO6.

[26] 3rd Generation Partnership Project (3GPP). http://www.3gpp.org/LTE.

[27] K. Fazel and S. Kaiser, Multi-Carrier and Spread Spectrum Systems: From OFDM and MC-CDMA to LTE and WiMAX, Second Edition, John Wiley & Sons Ltd., Chichester, UK (2008).

[28] H. G. Myung, J. Lim, D. and J. Goodman, "Single carrier FDMA for uplink wireless transmission," Vehicular Technology Magazine, IEEE, vol. **1**, no. 3, pp. 30–38 (2006).

[29] T. Hayashi, T. Taru, O. Shimakawa, T. Sasaki, and E. Sasaoka, "Ultra-Low-Crosstalk Multi-Core Fiber Feasible to Ultra-Long-Haul Transmission," in Optical Fiber Communication Conference (OFC), 2011, paper PDPC2.

[30] J. Sakaguchi, Y. Awaji, N. Wada, A. Kanno, T. Kawanishi, T. Hayashi, T. Taru, T. Kobayashi, and M. Watanabe, "109-Tb/s (7×97×172-Gb/s SDM/WDM/PDM) QPSK transmission through 16.8-km homogeneous multi-core fiber," in Optical Fiber Communication Conference (OFC), 2011, paper PDPB6.

[31] J. Sakaguchi, B.J. Puttnam, W. Klaus, Y. Awaji, N. Wada, A. Kanno, T. Kawanishi, K. Imamura, H. Inaba, K. Mukasa, R. Sugizaki, T. Kobayashi, M. Watanabe, "19-core fiber transmission of 19x100x172-Gb/s SDM-WDM-PDM-QPSK signals at 305Tb/s," in Optical Fiber Communication Conference (OFC), 2012, paper PDP5C.1.

[32] R. Ryf, R. Essiambre, A. Gnauch, S. Randel, M.A. Mestre, C. Schmidl, P. Winzer, R. Delbue, P. Pupalaikis, A. Sureka, T. Hayashi, T. Taru, and T. Sasaki, "Space-division Multiplexed Transmission over 4200 km 3-Core mircrosctructured Fiber," in Optical Fiber Communication Conference (OFC), 2012, paper PDP5C.2.

[33] B. Zhu, T. Taunay, M. Fishteyn, X. Liu, S. Chandrasekhar, M. Yan, J. Fini, E. Monberg, and F. Dimarcello, "Space-, Wavelength-, Polarization-Division

Multiplexed Transmission of 56-Tb/s over a 76.8-km Seven-Core Fiber," in Optical Fiber Communication Conference (OFC), 2011, paper PDPB7.

[34] B. Zhu, T.F. Taunay, M. Fishteyn, X. Liu, S. Chandrasekhar, M. F. Yan, J. M. Fini, E. M. Monberg, and F. V. Dimarcello, "112-Tb/s Space-division multiplexed DWDM transmission with 14-b/s/Hz aggregate spectral efficiency over a 76.8-km seven-core fiber," Opt. Express, vol. **19**, pp. 16665–16671 (2011).

[35] S. Berdagué and P. Facq, "Mode division multiplexing in optical fibers," Appl. Opt., vol. **21**, pp. 1950–1955 (1982).

[36] H. R. Stuart, "Dispersive Multiplexing in Multimode Optical Fiber," Science, vol. **289**, pp. 281–283 (2000).

[37] B. C. Thomsen, "MIMO enabled 40 Gb/s transmission using mode division multiplexing in multimode fiber," in Optical Fiber Communication Conference (OFC), 2010, OThM6.

[38] B. Franz, D. Suikat, R. Dischler, F. Buchali, and H. Buelow, "High speed OFDM data transmission over 5 km GI-multimode fiber using spatial multiplexing with 2x4 MIMO processing," in European Conference and Exhibition On Optical Communication (ECOC), 2010, paper Tu3.C.4.

[39] W. Shieh, H. Bao, and Y. Tang, "Coherent optical OFDM: theory and design," Opt. Express, vol. **16**, pp. 841–859 (2008).

[40] Y. Ma, Q. Yang, Y. Tang, S. Chen, and W. Shieh, "1-Tb/s single-channel coherent optical OFDM transmission over 600-km SSMF fiber with subwavelength bandwidth access," Opt. Express, vol. **17**, pp. 9421–9427 (2009).

[41] E. Yamada, A. Sano, and H. Masuda, "1Tb/s (111Gb/s/ch × 10ch) no-guard-interval CO-OFDM transmission over 2100 km DSF," in Opto-Electronics and Communications Conference, 2008 and the 2008 Australian Conference on Optical Fiber Technology. OECC/ACOFT 2008. Joint conference of the, paper PDP6.

[42] S. Chandrasekhar, X. Liu, B. Zhu, and D. W. Peckham, "Transmission of a 1.2-Tb/s 24-carrier no-guard-interval coherent OFDM superchannel over

7200-km of ultra-large-area fiber," in 35th European Conference on Optical Communication (ECOC), 2009, vol. 2009-Supplement, no., pp.1–2, (2009).

[43] A. H. Gnauck, P. Winzer, C. Doerr, and L. Buhl, "10 x 112-Gb/s PDM 16-QAM Transmission over 630 km of Fiber with 6.2-b/s/Hz Spectral Efficiency," in Optical Fiber Communication Conference (OFC), 2009, paper PDPB8.

[44] J. Yu, X. Zhou, M. F. Huang, Y. Shao, D. Qian, T.Wang, M. Cvijetic, P. Magill, L. Nelson, M. Birk, S. Ten, H. B. Matthew, and S. K. Mishra, "17 Tb/s (161x 114 Gb/s) PolMux-RZ-8PSK transmission over 662 km of ultra-low loss fiber using C-band EDFA amplification and digital coherent detection," in 34th European Conference on Optical Communication (ECOC), 2008, paper Th.3.E.2.

[45] A. Sano, H. Masuda, T. Kobayashi, M. Fujiwara, K. Horikoshi, E. Yoshida, Y. Miyamoto, M. Matsui, M. Mizoguchi, H. Yamazaki, Y. Sakamaki, and H. Ishii, "69.1-Tb/s (432 x 171-Gb/s) C- and Extended L-Band Transmission over 240 Km Using PDM-16-QAM Modulation and Digital Coherent Detection," in Optical Fiber Communication Conference (OFC), 2010, paper PDPB7.

[46] A. H. Gnauck, P. J. Winzer, S. Chandrasekhar, X. Liu, B. Zhu, and D. W. Peckham, "10 x 224-Gb/s WDM transmission of 28-Gbaud PDM 16-QAM on a 50-GHz grid over 1,200 km of fiber," in Optical Fiber Communication Conference (OFC), 2012, paper PDPB8.

[47] X. Zhou, J. Yu, M. F. Huang, Y. Shao, T. Wang, L. Nelson, P. D. Magill, M. Birk, P. I. Borel, D. W. Peckham, and R. Lingle, "64-Tb/s (640x 107-Gb/s) PDM-36QAM transmission over 320 km using both pre- and post-transmission digital equalization," in Optical Fiber Communication Conference (OFC), 2010, paper PDPB9.

[48] Y.-K. Huang, E. Ip, M.-F. Huang, B. Zhu, P. N. Ji, Y. Shao, D. W. Peckham, R. Lingle, Y. Aono, T. Tajima, and T. Wang, "10x456-Gb/s DP-16QAM transmission over 8 x 100 km of ULAF using coherent detection with a 30-GHz analog-to-digital converter," in 15th OptoElectronics and Communications Conference (OECC), Sapporo, Japan, Jul. 2010, paper PD3.

[49] M. S. Alfiad, M. Kuschnerov, S. L. Jansen, T. Wuth, D. van den Borne, and H. de Waardt, "11 x 224-Gb/s POLMUX-RZ-16QAM transmission over 670 km of SSMF with 50-GHz channel spacing," IEEE Photon. Technol. Lett., vol. **22**, no. 15, pp. 1150–1152 (2010).

[50] J.-X. Cai, Y. Cai, Y. Sun, C.R. Davidson, D.G. Foursa, A. Lucero, O. Sinkin, W. Patterson, A. Pilipetskii, G. Mohs, and N.S. Bergano, "112x112 Gb/s transmission over 9,360 km with channel spacing set to the baud rate (360% spectral efficiency)," in 36th European Conference and Exposition on Optical Communication (ECOC), 2010, paper PD2.1.

[51] M. Nölle, J. Hilt, L. Molle, M. Seimetz, and R. Freund, "8x224 Gbit/s PDM 16QAM WDM transmission with real-time signal processing at the transmitter," in 36th European Conference and Exposition on Optical Communication (ECOC), 2010, paper We.8.C.4.

[52] H. Ishio, J. Minowa and K. Nosu, "Review and status of wavelength-division-multiplexing technology and its application," J. Lightwave Technol., vol. **2**, no. 4, pp. 448-463 (1984).

[53] N. K. Cheung, K. Nosu and G. Winzer, Eds., "Special issue on dense wavelength division multiplexing techniques for high capacity and multiple access communication systems," IEEE J. Select. Areas Commun., vol. **8**, no. 6, pp. 945–1214 (1990).

[54] C. A. Brackett, "Dense Wavelength division multiplexing networks: Principles and applications," IEEE J. Select. Areas Commun., vol. **8**, no. 6, pp. 948–964 (1990).

[55] ITU-T Recommendation G.694.2, "WDM applications: CWDM wavelength grid," (2003).

[56] A. D. Ellis and F. C. G. Gunning, “Spectral density enhancement using coherent WDM,” IEEE Photon. Technol. Lett. 17, 504–506 (2005).

[57] T. Ohara, H. Takara, I. Shake, K. Mori, K. Sato, S. Kawanishi, S. Mino, T. Yamada, M. Ishii, I. Ogawa, T. Kitoh, K. Magari, M. Okamoto, R. V. Roussev, J. R. kurz, K. R. Parameswaran, and M. M. Fejer, "160-Gb/s OTDM Transmission Using Integrated All-Optical MUX-DEMUX With All-Channel

Modulation and Demultiplexing," Photonics Technology Letters, IEEE, vol. **16**, no. 2, pp. 650–652 (2004).

[58] W. Shieh, X. Yi, Y. Ma, and Y. Tang, "Theoretical and experimental study on PMD-supported transmission using polarization diversity in coherent optical OFDM systems," Optics Express, vol. **15**, pp. 9936–9947 (2007).

[59] W. Shieh, X. Yi, and Y. Tang, "Transmission experiment of multi-gigabit coherent optical OFDM systems over 1000 km SSMF fiber," Electron. Lett., vol. **43**, 183–185 (2007).

[60] S. L. Jansen, I. Morita, N. Takeda, and H. Tanaka, "20-Gb/s OFDM transmission over 4,160-km SSMF enabled by RF-Pilot tone phase noise compensation," in Optical Fiber Communication Conference (OFC), 2007, paper PDP15.

[61] Y. Tang, W. Shieh, X. Yi and R. Evans, "Optimum design for RF-to-optical up-converter in coherent optical OFDM systems," IEEE Photon. Technol. Lett., vol. **19**, pp. 483–485 (2007).

[62] D. S. Ly-Gagnon, S. Tsukarnoto, K. Katoh, and K. Kikuchi, "Coherent detection of optical quadrature phase-shift keying signals with carrier phase estimation," J. Lightwave Technol., vol. **24**, pp. 12–21, 2006.

[63] S. J. Savory, G. Gavioli, R. I. Killey, and P. Bayvel, "Electronic compensation of chromatic dispersion using a digital coherent receiver," Optics Express, vol. **15**, 2120–2126 (2007).

[64] S.B. Cohn and N.P. Weinhouse, "An automatic microwave phase measurement system," Microwave Journal, vol. **7**, pp. 49–56 (1964).

[65] C. A. Hoer and K.C. Roe, "Using an arbitrary six-port junction to measure complex voltage ratios", IEEE Trans. on MTT, vol **MTT-23**, pp. 978–984 (1975).

[66] Y. Tang, W. Chen, W. Shieh, "Study of nonlinearity and dynamic range of coherent optical OFDM receivers," in Optical Fiber Communication Conference (OFC), 2008, paper JWA65.

[67] Q. Pan and R. J. Green, "Bit-error-rate performance of lightwave hybrid AM/OFDM systems with comparison with AM/QAM systems in the presence

of clipping impulse noise," IEEE Photon. Technol. Lett., vol. **8**, 278–280 (1996).

[68] A. J. Lowery and J. Armstrong, "Orthogonal-frequency-division multiplexing for dispersion compensation of long-haul optical systems," Optics Express, vol. **14**, no. 6, pp. 2079–2084 (2006).

[69] J. M. Tang and K. A. Shore, "Maximizing the transmission performance of adaptively modulated optical OFDM signals in multimode-fiber links by optimizing analog-to-digital converters," J. Lightwave Technol., vol. **25**, pp. 787–798 (2007).

[70] X. Q. Jin, J. M. Tang, P. S. Spencer, and K. A. Shore, "Optimization of adaptively modulated optical OFDM modems for multimode fiber-based local area networks," J. Opt. Networking, vol. **7**, pp. 198–214, (2008).

[71] B. J. C. Schmidt, A. J. Lowery and J. Armstrong, "Experimental demonstrations of 20 Gbit/s direct-detection optical OFDM and 12 Gbit/s with a colorless transmitter," in Optical Fiber Communication Conference (OFC), 2007, paper PDP18.

[72] D. F. Hewitt, "Orthogonal frequency division multiplexing using baseband optical single sideband for simpler adaptive dispersion compensation," in Optical Fiber Communication Conference (OFC), 2007, paper OME7.

[73] W. R. Peng, X. Wu, V.R. Arbab, B. Shamee, J. Y. Yang, L. C. Christen, K. M. Feng, A. E. Willner, and S. Chi, "Experimental demonstration of 340 km SSMF transmission using a virtual single sideband OFDM signal that employs carrier suppressed and iterative detection techniques," in Optical Fiber Communication Conference (OFC), 2008, paper OMU1.

[74] W. R. Peng; X. Wu, V. R. Arbab, B. Shamee, L. C. Christen, J. Y. Yang; K. M. Feng, A. E. Willner, and S. Chi, "Experimental demonstration of a coherently modulated and directly detected optical OFDM system using an RF-Tone insertion," in Optical Fiber Communication Conference (OFC), 2008, paper OMU2.

[75] A. J. Lowery, L. B. Du, and J. Armstrong, "Performance of optical OFDM in ultralong-haul WDM lightwave systems," J. Lightwave Technol., vol. **25**, pp. 131–138 (2007).

[76] G. P. Agrawal, Fiber-Optic Communication Systems, Fourth Edition, John Wiley & Sons, Inc., Hoboken, NJ, USA (2010).

[77] N. E. Jolley, H. Kee, P. Pickard, J. Tang, and K. Cordina, "Generation and propagation of a 1550 nm 10 Gbit/s optical orthogonal frequency division multiplexed signal over 1000m of multimode fibre using a directly modulated DFB," in Optical Fiber Communication Conference (OFC), 2005, paper OFP3.

[78] M. Schuster, S. Randel, C. A. Bunge, S. C. J. Lee, F. Breyer, B. Spinnler, and K. Petermann, "Spectrally efficient compatible single-sideband modulation for OFDM transmission with direct detection," IEEE Photon. Technol. Lett., vol. **20**, 670-672 (2008).

[79] A. Cohen and I. Daubechies, "On the Instability of Arbitrary Biorthogonal Wavelet Packets," SIAM J. Math. Anal., pp. 1340-1354 (1993).

[80] R. Coifman and Y. Meyer, "Orthonormal Wave Packet Bases," Technical Report, Dept. of Math., Yale Univ., (1990).

[81] R. Coifman, Y. Meyer, S. Quake and M. V. Wickerhauser, "Signal processing and compression with wavelet packets", NATO ASI Series C Mathematical and Physical Sciences, vol. **442**, pp. 363, (1994).

[82] S. G. Mallat, "Theory for Multiresolution Signal Decomposition: The Wavelet Representation", IEEE transactions on pattern analysis and machine intelligence. vol. **II**, no. 7, pp. 674–693 (1989).

[83] A. N. Akansu and R. A. Haddad, "Multiresolution signal decomposition: transforms, subbands, and wavelets," Second Edition, New Jersey Institute of Technology, Newark, NJ, USA (2001).

[84] G. Strang and T. Nguyen, "Wavelets and filter banks," Wellesley-Cambridge Press, Wellesley MA, USA (1996).

[85] C. S. Burrus, R. A. Gopinath and H. Guo, "Introduction to Wavelets and Wavelet Transforms," Prentice Hall, New Jersey, USA (1998).

[86] Y. Meyer, “Wavelets-algorithms and applications”, Society for Industrial and Applied Mathematics Translation (1993).

[87] A. Haar, “Zur theorie der orthogonalen funktionensysteme”, Mathematische Annalen vol. **69**, pp. 331–371 (1910).

[88] I. Daubechies, Ten Lectures on Wavelets, SIAM Publications, Philadelphia, (1992).

[89] J. D. Johnston, “A filter family designed for use in quadrature mirror filter banks”, in Proc. of the ICASSP’80 Conf., pp. 291-294 (1980).

[90] N. Erdol, F. Bao, and Z. Chen, “Wavelet modulation: a prototype for digital communication systems,” in IEEE Southcon Conference, pp. 168-171 (1995).

[91] I. W. Selesnick, R. G. Baraniuk, and N. G. Kingsbury, “The dual-tree wavelet transform,” IEEE Signal Processing Magazine, vol. **22**, pp. 123-151 (2005).

[92] R. Todd Ogden, “Essential Wavelets for Statistical Applications and Data Analysis”, Birkhauser Boston, 1997.

[93] X. Liu, S. Chandrasekhar, B. Zhu, P. Winzer, A. Gnauck, and D. Peckham, "Transmission of a 448-Gb/s Reduced-Guard-Interval CO-OFDM Signal with a 60-GHz Optical Bandwidth over 2000 Km of ULAF and Five 80-GHz-Grid ROADMs," in Optical Fiber Communication Conference (OFC), 2010, paper PDPC2.

[94] T. Kobayashi, A. Sano, A. Matsuura, M. Yoshida, T. Sakano, H. Kubota, Y. Miyamoto, K. Ishihara, M. Mizoguchi, and M. Nagatani, "45.2Tb/s C-band WDM transmission over 240km using 538Gb/s PDM-64QAM single carrier FDM signal with digital pilot tone," in 37th European Conference and Exposition on Optical Communication (ECOC), 2011, paper Th.13.C6.

[95] W. Shieh and Y. Tang, "Ultrahigh-Speed Signal Transmission Over Nonlinear and Dispersive Fiber Optic Channel: The Multicarrier Advantage," Photonics Journal, IEEE , vol. **2**, no. 3, pp. 276–283 (2010).

[96] Y. Tang, W. Shieh, and B.S. Krongold, "DFT-Spread OFDM for Fiber Nonlinearity Mitigation," IEEE Photon. Technol. Lett., vol. **22**, no. 16, pp.1250–1252 (2010).

[97] X. Chen, A. Li, G. Gao, and W. Shieh, "Experimental Demonstration of Improved Fiber Nonlinearity Tolerance for Unique-word DFT-Spread OFDM Systems," Opt. Express, vol. **19**, pp. 26198–26207 (2011).

[98] A. Li, X. Chen, G. Gao and W. Shieh, "Transmission of 1-Tb/s unique-word DFT-spread OFDM superchannel over 8,000-km SSMF", Proc. SPIE 8309, pp. 830929 (2011).

[99] A. Li, X. Chen, G. Gao, W. Shieh, and B. Krongold, "Transmission of 1.63-Tb/s PDM-16QAM Unique-word DFT-Spread OFDM Signal over 1,010-km SSMF," in Optical Fiber Communication Conference (OFC), 2012, paper OW4C.1.

[100] J. Li, C. Zhao, L. Zhu, F. Zhang, Y. He, and Z. Chen, "Experimental demonstration of ROADM functionality on an optical SCFDM superchannel," IEEE Photon. Technol. Lett., vol. **24**, no. 3, pp. 215–217 (2012).

[101] K. Ishihara, T. Kobayashi, R. Kudo, Y.Takatori, A. Sano, and Y. Miyamoto, "Frequency-domain equalization for coherent optical single-carrier transmission systems," IEICE Trans. Commun., vol. **E92-B**, no. 12, (2009).

[102] N. Hanzawa, K. Saitoh, T. Sakamoto, T. Matsui, S. Tomita, and M. Koshiba, "Demonstration of mode-division multiplexing transmission over 10 km two-mode fiber with mode coupler," in Optical Fiber Communication Conference (OFC), 2011, paper OWA4.

[103] A. Li, A. Al Amin, X. Chen, and W. Shieh, "Reception of Mode and Polarization Multiplexed 107-Gb/s CO-OFDM Signal over a Two-Mode Fiber," in Optical Fiber Communication Conference (OFC), 2012, paper PDPB8.

[104] A. Li, A. A. Amin, X. Chen, and W. Shieh, "Transmission of 107-Gb/s mode and polarization multiplexed CO-OFDM signal over a two-mode fiber," Opt. Express, vol. **19**, pp. 8808–8814 (2011).

[105] A. Li, A. A. Amin, X. Chen, S. Chen, G. Gao, and W. Shieh, "Reception of Dual-Spatial-Mode CO-OFDM Signal Over a Two-Mode Fiber," J. Lightwave Technol., vol. **30**, pp. 634–640 (2012).

[106] A. A. Amin, A. Li, S. Chen, X. Chen, G. Gao, and W. Shieh, "Dual-LP11 mode 4x4 MIMO-OFDM transmission over a two-mode fiber," Opt. Express, vol. **19**, pp. 16672–16679 (2011).

[107] X. Chen, A. Li, J. Ye, A. Al Amin, and W. Shieh, "Reception of Dual-LP11-Mode CO-OFDM Signals through Few-mode Compatible Optical Add/Drop Multiplexer," in Optical Fiber Communication Conference (OFC), 2012, paper PDP5B.4.

[108] M. Salsi, C. Koebele, D. Sperti, P. Tran, P. Brindel, H. Mardoyan, S. Bigo, A. Boutin, F. Verluise, P. Sillard, M. Bigot-Astruc, L. Provost, F. Cerou, and G. Charlet, "Transmission at 2x100Gb/s, over Two Modes of 40km-long Prototype Few-Mode Fiber, using LCOS based Mode Multiplexer and Demultiplexer," in Optical Fiber Communication Conference (OFC), 2011, paper PDPB9.

[109] R. Ryf, S. Randel, A. H. Gnauck, C. Bolle, R. Essiambre, P. Winzer, D. W. Peckham, A. McCurdy, and R. Lingle, "Space-division multiplexing over 10 km of three-mode fiber using coherent 6 × 6 MIMO processing," in Optical Fiber Communication Conference (OFC), 2011, paper PDPB10.

[110] R. Ryf, S. Randel, A. Gnauck, C. Bolle, A. Sierra, S. Mumtaz, M. Esmaeelpour, E. Burrows, R. Essiambre, P. Winzer, D. Peckham, A. McCurdy, and R. Lingle, "Mode-Division Multiplexing Over 96 km of Few-Mode Fiber Using Coherent 6 × 6 MIMO Processing," J. Lightwave Technol., vol. **30**, pp. 521–531 (2012).

[111] N. K. Fontaine, C. R. Doerr, M.A. Mestre, R. Ryf, P. Winzer, L. Buhl, Y. Sun, X. Jiang, and R. Lingle, "Space-division multiplexing and all-optical MIMO demultiplexing using a photonic integrated circuit," in Optical Fiber Communication Conference (OFC), 2012, paper PDP5B.1.

[112] S. Randel, R. Ryf, A. Gnauck, M.A. Mestre, C. Schmidt, R. Essiambre, P. Winzer, R. Delbue, P. Pupalaikis, A. Sureka, Y. Sun, X. Jiang, and R. Lingle, "Mode-multiplexed 6x20-GBd QPSK Transmission over 1200-km DGD-Compensated Few-Mode Fiber," in Optical Fiber Communication Conference (OFC), 2012, paper PDP5C.5.

[113] R. Ryf, M.A. Mestre, A. Gnauck, S. Randel, C. Schmidt, R. Essiambre, P. Winzer, R. Delbue, P. Pupalaikis, A. Sureka, Y. Sun, X. Liang, D. Peckham, A.H. McCurdy, and R. Lingle, "Low-Loss Mode Coupler for Mode-Multiplexed transmission in Few-Mode Fiber," in Optical Fiber Communication Conference (OFC), 2012, paper PDP5B.5.

[114] P. Sillard, M. Astruc, D. Boivin, H. Maerten, and L. Provost, "Few-Mode Fiber for Uncoupled Mode-Division Multiplexing Transmissions," in 37th European Conference and Exposition on Optical Communication (ECOC), 2011, paper Tu.5.LeCervin.7.

[115] L. Gruner-Nielsen, Y. Sun, J. W. Nicholson, D. Jakobsen, R. Lingle, and B. Palsdottir, "Few Mode Transmission Fiber with low DGD, low Mode Coupling and low Loss," in Optical Fiber Communication Conference (OFC), 2012, paper PDP5A.1.

[116] B. Y. Kim, J. N. Blake, H. E. Engan, and H. J. Shaw, "All-fiber acousto-optic frequency shifter," Opt. Lett., vol. **11**, pp. 389–391 (1986).

[117] Y. Yung, S. Alam, Z. Li, A. Dhar, D. Giles, I. Giles, J. Sahu, L. Grüner-Nielsen, F. Poletti, and D. Richardson, "First demonstration of multimode amplifier for spatial division multiplexed transmission systems," in 37th European Conference and Exposition on Optical Communication (ECOC), 2011, paper Th.13.K.4.

[118] E. Ip, N. Bai, Y. Huang, E. Mateo, F. Yaman, S. Bickham, H. Tam, C. Lu, M. Li, S. Ten, A. P. T. Lau, V. Tse, G. Peng, C. Montero, X. Prieto, and G. Li, "88x3x112-Gb/s WDM Transmission over 50-km of Three-Mode Fiber with Inline Multimode Fiber Amplifier," in 37th European Conference and Exposition on Optical Communication (ECOC), 2011, paper Th.13.C.2.

[119] N. Bai, E. Ip, T. Wang, and G. Li, "Multimode fiber amplifier with tunable modal gain using a reconfigurable multimode pump," Opt. Express, vol. **19**, pp. 16601–16611 (2011).

[120] R. Ryf, A. Sierra, R. Essiambre, S. Randel, A. Gnauck, C. A. Bolle, M. Esmaeelpour, P. J. Winzer, R. Delbue, P. Pupalaikis, A. Sureka, D. Peckham, A. McCurdy, and R. Lingle, "Mode-Equalized Distributed Raman

Amplification in 137-km Few-Mode Fiber," in 37th European Conference and Exposition on Optical Communication (ECOC), 2011, paper Th.13.K.5.

[121] C. Koebele, M. Salsi, G. Charlet, and S. Bigo, "Nonlinear Effects in Mode-Division-Multiplexed Transmission Over Few-Mode Optical Fiber," IEEE Photon. Technol. Lett., vol. **23**, no. 18, pp. 1316–1318 (2011).

[122] F. Ferreira, S. Jansen, P. Monteiro, and H. Silva, "Nonlinear Semi-Analytical Model for Simulation of Few-Mode Fiber Transmission," IEEE Photon. Technol. Lett., vol. **24**, no. 4, pp. 240–242 (2012).

[123] X. Chen, A. Li, G. Gao, A. A. Amin, and W. Shieh, "Characterization of Fiber Nonlinearity and Analysis of Its Impact on Link Capacity Limit of Two-Mode Fibers," Photonics Journal, IEEE, vol. **4**, no. 2, pp. 455–460 (2012).

[124] R. Nee and R. Prasad. OFDM for Wireless Multimedia Communications (1st ed.). Artech House, Inc., Norwood, MA, USA, 2000.

[125] S. Hara and R. Prasad, Multicarrier Techniques for 4G Mobile Communications, Artech House, Inc., Norwood, MA, USA, 2003.

[126] R. W. Chang, "Synthesis of band-limited orthogonal signals for multichannel data transmission," Bell Sys. Tech. J., vol. **45**, pp. 1775-1796 (1966).

[127] B. R. Saltzberg, "Performance of an efficient parallel data transmission system," IEEE Trans. Commun., vol. **15**, pp. 805-813 (1967).

[128] W. Shieh and I. Djordjevic, Orthogonal Frequency Division Multiplexing for Optical Communications, Academic Press, 2009.

[129] W. Shieh, H. Bao, and Y. Tang, "Coherent optical OFDM: theory and design," Opt. Express, vol. **16**, pp. 841–859 (2008).

[130] W. Shieh, X. Yi, Y. Ma, and Q. Yang, "Coherent optical OFDM: has its time come? [Invited]," J. Opt. Netw., vol. **7**, pp. 234–255 (2008).

[131] W. Shieh, "PMD-supported coherent optical OFDM systems," IEEE Photon. Technol. Lett. vol. **19**, pp. 134–136 (2007).

[132] Q. Yang, Y. Tang, Y. Ma, and W. Shieh, "Experimental Demonstration and Numerical Simulation of 107-Gb/s High Spectral Efficiency Coherent Optical OFDM," J. Lightwave Technol., vol. **27**, pp. 168–176 (2009).

[133] S. L. Jansen, I. Morita, T. C. W. Schenk, N. Takeda, and H. Tanaka, "Coherent Optical 25.8-Gb/s OFDM Transmission Over 4160-km SSMF," J. Lightwave Technol., vol. **26**, pp. 6–15 (2008).

[134] N. Kaneda, Q. Yang, X. Liu, S. Chandrasekhar, W. Shieh, and Y.-K. Chen, "Real-Time 2.5 GS/s Coherent Optical Receiver for 53.3-Gb/s Sub-Banded OFDM," J. Lightwave Technol. vol. **28**, pp. 494-501 (2010).

[135] I. W. Selesnick, "Hilbert transform pairs of wavelet bases," Signal Processing Letters, IEEE, vol. **8**, no. 6, pp. 170–173, (2001).

[136] I. W. Selesnick, "The design of approximate Hilbert transform pairs of wavelet bases ," Signal Processing, IEEE Transactions on, vol. **50**, no. 5, pp.1144–1152, (2002).

[137] I. W. Selesnick, "The double-density dual-tree DWT," Signal Processing, IEEE Transactions on, vol. **52**, no. 5, pp. 1304–1314 (2004).

[138] I. W. Selesnick, R. G. Baraniuk, and N. G. Kingsbury, "The dual-tree wavelet transform," Signal Processing Magazine, IEEE, vol. **22**, no. 6, pp. 123–151 (2005).

[139] N. Kingsbury, "Complex Wavelets for Shift Invariant Analysis and Filtering of Signals, Applied and Computational Harmonic Analysis," vol. **10**, no. 3, pp. 234–253, (2001).

[140] N. G. Kingsbury, The dual-tree complex wavelet transform: A new technique for shift invariance and directional filters, in Proc. 8th IEEE DSP Workshop, Bryce Canyon, August 1998.

[141] N. G. Kingsbury, "The dual-tree complex wavelet transform: A new efficient tool for image restoration and enhancement," in Proc. EUSIPCO 98, Rhodes, September 1998.

[142] N. G. Kingsbury, "Shift invariant properties of the dual-tree complex wavelet transform," in Proc. ICASSP 99, Phoenix, AZ, paper SPTM 3.6, March 16-19, 1999.

[143] N. G. Kingsbury "Image processing with complex wavelets," Philos. Trans. Roy. Soc. London Ser. A, vol. **357**, pp. 2543–2560, (1999).

[144] N. G. Kingsbury, "A dual-tree complex wavelet transform with improved orthogonality and symmetry properties," Image Processing, 2000. Proceedings. 2000 International Conference on, vol. **2**, pp. 375–378 (2000).

[145] U. Sorger, I. De Broeck, and M. Schnell, "Interleaved FDMA - A New Spread- Spectrum Multiple-Access Scheme," Proc. IEEE ICC '98, Atlanta, GA, pp. 1013-1017, June 1998.

[146] H. G. Myung, J. Lim, and D.J. Goodman, "Peak-to-Average Power Ratio of Single Carrier FDMA Signals with Pulse Shaping," The 17th Annual IEEE International Symposium on Personal, Indoor and Mobile Radio Communications (PIMRC '06), Helsinki, Finland, Sep. 2006.

[147] D. Falconer, S.L. Ariyavisitakul, A. Benyamin-Seeyar, and B. Eidson, "Frequency domain equalization for single-carrier broadband wireless systems," Communications Magazine, IEEE, vol. **40**, no. 4, pp. 58–66 (2002).

[148] H. Witschnig, T. Mayer, A. Springer, A. Koppler, L. Maurer, M. Huemer, and R. Weigel, "A different look on cyclic prefix for SC/FDE," Personal, Indoor and Mobile Radio Communications, 2002. The 13th IEEE International Symposium on, vol. **2**, no., pp. 824–828 (2002).

[149] M. Huemer, H. Witschnig, and J. Hausner, "Unique word based phase tracking algorithms for SC/FDE-systems," Global Telecommunications Conference, 2003. GLOBECOM '03. IEEE, vol. **1**, no., pp. 70–74 (2003).

[150] J. Coon, M. Sandell, M. Beach, and J. McGeehan, "Channel and noise variance estimation and tracking algorithms for unique-word based single-carrier systems," Wireless Communications, IEEE Transactions on, vol. **5**, no. 6, pp. 1488–1496 (2006).

[151] D. Chu, "Polyphase codes with good periodic correlation properties (Corresp.)," Information Theory, IEEE Transactions on, vol. **18**, no. 4, pp. 531- 532 (1972).

[152] H. G. Myung, J. Lim, and D. J. Goodman, "Peak-to-Average Power Ratio of Single Carrier FDMA Signals with Pulse Shaping", The 17th Annual IEEE International Symposium on Personal, Indoor and Mobile Radio Communications (PIMRC '06), Helsinki, Finland (2006).

[153] F. Chang, K. Onohara, and T. Mizuochi, "Forward error correction for 100 G transport networks," Communications Magazine, IEEE, vol. **48**, no. 3, pp. S48–S55 (2010).

[154] T. Mizuochi, Y. Miyata, K. Kubo, T. Sugihara, K. Onohara, and H. Yoshida," Progress in Soft-Decision FEC," in OFC/NFOEC 2011, paper NWC2, (2011).

[155] T. M. Schmidl and D. C. Cox, "Robust frequency and timing synchronization for OFDM," IEEE Trans. Commun., vol. **45**, pp. 1613–1621 (1997).

[156] S. Zhang, P. Y. Kam, C. Yu, and J. Chen, "Decision-aided carrier phase estimation for coherent optical communications," J. Lightwave Technol., vol. **28**, no. 11, pp. 1597–1607 (2010).

[157] S. Zhang, P. Y. Kam, J. Chen, and C. Yu, "Decision-aided maximum likelihood detection in coherent optical phase-shift-keying system," Opt. Express, vol. **17**, pp. 703–715 (2009).

[158] W. Shieh, "Maximum-likelihood phase and channel estimation for coherent optical OFDM," IEEE Photon. Technol. Lett., vol. **20**, pp. 605–607 (2008).

[159] D. Marcuse, Light Transmission Optics, Van Nostrand Reinhold, New York, USA (1982).

[160] A. W. Snyder and J. D. Love, Optical Waveguide Theory, Chapman and Hall, London, UK (1983).

[161] M. J. Adams, An Introduction to Optical Waveguides, Wiley & Sons, Inc., New York, USA, Chap. 7 (1981).

[162] G. P. Agrawal, Nonlinear Fiber Optics, Third Edition, Academic Press, San Diego, CA, USA (2001).

[163] K. Okamoto, Fundamentals of Optical Waveguides, Second Edition, Academic Press, San Diego, CA, USA (2000).

[164] http://www.corning.com/opticalfiber/products/SMF-28e+_fiber.aspx

[165] ITU-T Recommendation G.652, "Transmission Media Characteristics: Characteristics of a Single-Mode Optical Fiber Cable," (2005).

[166] ITU-T Recommendation G.651, Transmission Media Characteristics: Characteristics of a 50/125 M Multimode Graded Index Optical Fiber Cable," (1993).

[167] K. S. Kim, R. H. Stolen, W. A. Reed, and K. W. Quoi, "Measurement of the nonlinear index of silica-core and dispersion-shifted fibers," Opt. Lett., vol. **19**, no. 257–259 (1994).

[168] H. Yokota, G. Tanaka, M. Watanabe, Y. Ishiguro, I. Yoshida, T. Kakii, S. Itoh, Y. Asano, and S. Tanaka, "Transmission characteristics and reliability of pure-silica-core single-mode fibers," J. Lightwave Technol., vol. **4**, no. 8, pp. 1144–1150 (1986).

[169] K. Nagayama, M. Kakui, M. Matsui, I. Saitoh, and Y. Chigusa, "Ultra-low-loss (0.1484 dB/km) pure silica core fiber and extension of transmission distance," Electronics Letters, vol. **38**, no. 20, pp. 1168–1169 (2002).

[170] T. Li (ed.), Optical Fiber Communications: Fiber Fabrication, vol. **1**, Academic Press, San Diego, USA (1985).

[171] U. C. Paek, "High-speed high-strength fiber drawing," J. Lightwave Technol., vol. **LT-4**, pp. 1048–1060 (1986).

[172] B. J. Ainslie, "A review of the fabrication and properties of erbium doped fibers for optical amplifiers," J. Lightwave Technol., vol. **9**, pp. 220–227 (1991).

[173] A. W. Snyder and J. D. Love, Optical Waveguide Theory, Chapman and Hall, London, UK, Chaps. 12–15 (1983).

[174] J. A. Buck, Fundamentals of Optical Fibers, Wiley, New York, USA, Chap. 3 (1995).

[175] B. Y. Kim, J. N. Blake, S. Y. Huang, and H. J. Shaw, "Use of highly elliptical core fibers for two-mode fiber devices," Opt. Lett. vol. **12**, pp. 729–731 (1987).

[176] S. Y. Huang, J. N. Blake, and B. Y. Kim, "Perturbation effects on mode propagation in highly elliptical core two-mode fibers," J. Lightwave Technol., vol. **8**, no. 1, pp. 23–33 (1990).

[177] J. N. Blake, B. Y. Kim, and H. J. Shaw, "Fiber-optic modal coupler using periodic microbending," Opt. Lett., vol. **11**, pp. 177–179 (1986).

[178] J. N. Blake, S. Y. Huang, B. Y. Kim, and H. J. Shaw, "Strain effects on highly elliptical core two-mode fibers," Opt. Lett., vol. **12**, pp. 732–734 (1987).

[179] F. Yaman, N. Bai, Y. Huang, M. Huang, B. Zhu, T. Wang, and G. Li, "10 x 112Gb/s PDM-QPSK transmission over 5032 km in few-mode fibers," Opt. Express, vol. **18**, pp. 21342–21349 (2010).

[180] T. Morioka, Y. Awaji, R. Ryf, P. Winzer, D. Richardson, and F. Poletti, "Enhancing optical communications with brand new fibers," Communications Magazine, IEEE, vol. **50**, no. 2, pp. s31–s42 (2012).

[181] J. Sakai and T. Kimura, "Bending loss of propagation modes in arbitrary-index profile optical fibers," Appl. Opt., vol. **17**, pp. 1499–1506 (1978).

[182] I. K. Hwang, S. H. Yun, and B. Y. Kim, "Long-period fiber gratings based on periodic microbends," Opt. Lett., vol. **24**, pp. 1263–1265 (1999).

[183] R. C. Youngquist, J. L. Brooks, and H. J. Shaw, "Two-mode fiber modal coupler," Opt. Lett., vol. **9**, pp. 177–179 (1984).

[184] S. Savin, M. J. F. Digonnet, G. S. Kino, and H. J. Shaw, "Tunable mechanically induced long-period fiber gratings," Opt. Lett., vol. **25**, pp. 710–712 (2000).

[185] D. D. Davis, T.K. Gaylord, E. N. Glytsis, S. G. Kosinski, S.C. Mettler, and A.M. Vengsarkar, "Long-period fiber grating fabrication with focused CO2 laser pulses," Electronics Letters, vol. **34**, pp. 302–303 (1998).

[186] J. Van Roey, J. van der Donk, and P. Lagasse, "Beam-propagation method: analysis and assessment," J. Opt. Soc. Am., vol. **71**, pp. 803–810 (1981).

[187] A. Li, A. A. Amin and W. Shieh, "Design of a broadband LP11 spatial mode combiner," Proc. SPIE 8309, 83091B (2011).

[188] K. Y. Song, I. K. Hwang, S. H. Yun, and B. Y. Kim, "High performance fused-type mode-selective coupler using elliptical core two-mode fiber at 1550 nm," Photonics Technology Letters, IEEE , vol. **14**, no. 4, pp.501–503 (2002).

[189] W. V. Sorin, B. Y. Kim, and H. J. Shaw, "Highly selective evanescent modal filter for two-mode optical fibers," Opt. Lett. vol. **11**, pp. 581–583 (1986).

[190] A. Yariv, "Coupled-mode theory for guided-wave optics," IEEE J. Quantum Electron, vol. **9**, pp. 919–933 (1973).

[191] D. Marcuse, Theory of dielectric optical waveguides, Academic Press, Inc., New York, USA (1974).

[192] H. Haus, W. Huang, S. Kawakami, N. Whitaker, "Coupled-mode theory of optical waveguides," J. Lightwave Technol., vol. **5**, no. 1, pp. 16–23 (1987).

[193] W.-P. Huang, "Coupled-mode theory for optical waveguides: an overview," J. Opt. Soc. Am. A, vol. **11**, pp. 963-983 (1994).

[194] Y. Ma, Q. Yang, Y. Tang, S. Chen, and W. Shieh, "1-Tb/s Single-Channel Coherent Optical OFDM Transmission with Orthogonal-Band Multiplexing and Subwavelength Bandwidth Access," J. Lightwave Technol., vol. **28**, pp. 308-315, (2010).

Appendix A

Acronyms

ADC	Analogue-to-Digital Converter
ADI	Alternating Direction Implicit
AMO-OFDM	Adaptively Modulated Optical OFDM
AON	All Optical Network
APVD	Advanced Plasma Vapour Deposition
ASE	Amplified Spontaneous Emission
AWG	Arbitrary Waveform Generator
BER	Bit Error Ratio
BF	Bundled Fibre
BPSK	Binary Phase Shift Keying
BR	Balanced Receiver
BS	Beam Splitter
BW	Bandwidth
CCDF	Complementary Cumulative Distribution Function
CCI	Co-Channel Interference
CD	Chromatic Dispersion
CDM	Code Division Multiplexing
CFO	Carrier Frequency Offset
CMT	Coupled Mode Theory
CompSSB	Compatible Single Side Band
CO-OFDM	Coherent Optical OFDM
CP	Cyclic Prefix
CPE	Common Phase Error
CSI	Channel State information
CWDM	Coarse Wavelength Division Multiplexing
DAC	Digital to Analogue Converter
DAML	Decision Aided Maximum Likelihood

DC	Direct Current
DCD	Differential Chromatic Dispersion
DDO-OFDM	Direct Detection Optical OFDM
DEMUX	De-multiplexer
DFB	Distributed Feedback
DFML	Decision Feedback Maximum Likelihood
DFT	Discrete Fourier Transform
DFTS	Discrete Fourier Transform Spread
DGD	Differential Group Delay
DMD	Differential Modal Delay
DS-OFDM	Densely Spaced OFDM
DSP	Digital Signal Processing
DWDM	Dense Wavelength Division Multiplexing
DWPT	Discrete Wavelet packet Transform
DWT	Discrete Wavelet Transform
EA	Effective Area
ECL	External-Cavity Laser
EDFA	Erbium-Doped Fibre Amplifier
ER	Extinction Ratio
ETDM	Electrical Time Division Multiplexing
FBT	Fused Biconic Tapering
FCVD	Furnace Chemical Vapour Deposition
FDE	Frequency Domain Equalization
FDM	Frequency Division Multiplexing
FEC	Forward Error Correction
FMF	Few-Mode Fibre
FT	Fourier Transform
FT-OFDM	Fourier Transform based OFDM
FFT	Fast Fourier Transform
FIR	Finite Impulse Response

FSO	Free-Space Optical communication
FWM	Four-Wave Mixing
GI	Guard Interval
ICI	Inter-Carrier Interference
IDFT	Inverse Discrete Fourier Transform
IDFTS-OFDM	Interleaved Discrete Fourier Transform Spread OFDM
IDWPT	Inverse Discrete Wavelet Packet Transform
IDWT	Inverse Discrete Wavelet Transform
IF	Intermediate Frequency
IFDMA	Interleaved Frequency Division Multiple Access
IFFT	Inverse Fast Fourier Transform
IIR	Infinite Impulse Response
ISI	Inter-Symbol Interference
LAN	Local Area Network
LCoS	Liquid Crystal on Silicon
LDFTS-OFDM	Localized Discrete Fourier Transform Spread OFDM
LFDMA	Localized Frequency Division Multiple Access
LM-DDO-OFDM	Linearly Mapped DDO-OFDM
LO	Local Oscillator
LPF	Low Pass Filter
LP	Linear Polarized
LPFG	Long Period Fibre Grating
MAN	Metropolitan Area Network
MB-DFTS-OFDM	Multi-Band DFTS-OFDM
MC	Mode Converter
MCF	Multi-Core Fibre
MCM	Multi-Carrier Modulation
MCVD	Modified Chemical Vapour Deposition
MDG	Mode Dependant Gain
MDL	Mode Dependant Loss

MDM	Mode Division Multiplexing
MDM-CO-OFDM	Mode Division Multiplexed Coherent Optical OFDM
MEMS	Micro-Electro-Mechanical Systems
MIMO	Multiple Input Multiple Output
MM-EDFA	Multimode Erbium-Doped Fibre Amplifier
MMF	Multimode Fibre
MM-NLSE	Multimode Nonlinear Schrödinger Equation
MMSE	Minimum Mean Square Error
M-PSK	M-ary Phase Shift Keying
M-QAM	M-ary Quadrature Amplitude Modulation
MRA	Multiresolution Analysis
MS	Mode Stripper
MSC	Mode Selective Coupler
MDEMUX	Mode Demultiplexer
MMUX	Mode Multiplexer
MUX	Multiplexer
MZM	Mach-Zehnder Modulator
NF	Noise Figure
NLSE	Nonlinear Schrödinger Equation
NLM-DDO-OFDM	Nonlinearly Mapped DDO-OFDM
OADM	Optical Add/Drop Multiplexer
OFDM	Orthogonal Frequency Division Multiplexing
O-OFDM	Optical OFDM
OSA	Optical Spectrum Analyser
OSNR	Optical Signal to Noise Ratio
OSP	OFDM Symbol Phase
OTDM	Optical Time Division Multiplexing
OTR	Optical To RF
OVD	Outside Vapour Deposition
PAPR	Peak to Average Power Ratio

PBC	Polarization Beam Combiner
PCVD	Plasma activated Chemical Vapour Deposition
PD	Photodiode
PDL	Polarization Dependant Loss
PDM	Polarization Division Multiplexing
PLC	Planar Lightwave Circuit
PMD	Polarization Mode Dispersion
PMF	Polarization Maintaining Fibre
PPLN	Periodically Poled Lithium Niobate
PR	Perfect Reconstruction
PSCF	Pure Silica Core Fibre
PSK	Phase Shift Keying
PSP	Principle State of Polarization
QAM	Quadrature Amplitude Modulation
QMF	Quadrature Mirror Filter
QPSK	Quadrature Phase Shift Keying
RF	Radio Frequency
RIN	Relative Intensity Noise
ROADM	Reconfigurable Optical Add/Drop Multiplexer
RTO	RF To Optical
SC	Single Carrier
SC-FDE	Single Carrier Frequency Domain Equalization
SC-FDM	Single Carrier Frequency Division Multiplexing
SCM	Single-Carrier Modulation
SDH	Synchronous Digital Hierarchy
SDM	Space Division Multiplexing
SE	Spectral Efficiency
SISO	Single Input Single Output
SLM	Spatial Light Modulator
SMC	Spatial Mode Combiner

SMF	Single Mode Fibre
SMS	Spatial Mode Splitter
SNR	Signal to Noise Ratio
SSB	Single Side Band
SSB-OFDM	Single Side Band OFDM
SSFM	Split Step Fourier Method
SSMF	Standard Single Mode Fibre
SW	Switch
TDM	Time Division Multiplexing
TE	Transverse Electric
TM	Transverse Magnetic
TITO	Two Input Two Output
TMF	Two Mode Fibre
TS	Training Sequence
ULAF	Ultra Large Area Fibre
UW	Unique Word
UW-DFTS-OFDM	Unique Word DFTS-OFDM
VAD	Vapour Axial Deposition
WDM	Wavelength Division Multiplexing
WPD	Wavelet Packet Decomposition
WPR	Wavelet Packet Reconstruction
WPT	Wavelet Packet Transform
WPT-OFDM	Wavelet Packet Transform based OFDM
WT	Wavelet Transform
WSS	Wavelength Selective Switch
ZF	Zero Forcing